

**Enhancing Charge Separation on Metal Oxides  
by Space Charge Engineering  
for Photocatalytic Overall Water Splitting**

Submitted in partial fulfillment of the requirements for

the degree of

Doctor of Philosophy

in

Materials Science and Engineering

Mingyi Zhang

B.S., Chemistry, Renmin University of China

M.S., Materials Science and Engineering, Carnegie Mellon University

Carnegie Mellon University  
Pittsburgh, PA

August 2022

© Mingyi Zhang, 2022  
All Rights Reserved

# Acknowledgement

I would like first to thank my advisors, Dr. Gregory Rohrer and Dr. Paul Salvador for their guidance and help in the past five years. They taught me how to design experiments, how to conduct scientific analysis, how to write research paper and how to effectively present experimental results. I enjoy every weekly meeting when I was inspired and encouraged to continue my research. Their influence is not only present in this thesis but in my future career path. I would also like to thank my committee members - Dr. Elizabeth Dickey, Dr. Mohammad Islam, Dr. Stefan Bernhard, and Dr. Frank Osterloh for their valuable suggestions and inspirations to complete this thesis. I want to acknowledge the financial support from National Science Foundation under grant number DMR 1609369 and DMR 2016267.

I also want to express my gratefulness to my friends and colleagues for their help, especially to Dr. Wenjia Song and Dr. Ajay Pisat, who trained me how to use the instruments when I just joined the group. I am also grateful for other group members, including Catherine Zhou, Hokon Kim, Kayla Zitello, Dr. Rubayyat Mahbub, Dr. Xiaoting Zhong, Nnamdi Ene, Andrew Inigo Santiago, William Kent, Alec Sanabria, Cathy Shi and Zipeng Xu. Almost one third of my research was conducted in our Materials Characterization Facility. I would like to acknowledge Dr. Elizabeth Clark, Dr. Adam Wise, Tom Nuhfer, Daniel Flaherty, William Pingitore and Logan Solotky for instrument training. I would like to thank MSE staff Kelly Rockenstein, Jeanna Pekarcik, Suzanne Smith,

and Marygrace Antkowski for their kind administrative help. I also want to express my thank to Brett Riale, who has helped us on equipment maintaining for a countless number of times.

There are people outside our group helped me a lot on completing this thesis. Here, I want to express my thank to Eric Lopato, Jakub Kowalewski and Dr. Stefan Bernhard for their help on building and calibrating the PAPCR, which is one of the most important instruments in my research. I would like to acknowledge Tommy Britt and Dr. P.Chris Pistorius on CLSM experiment and the discussion on the  $\text{SrCl}_2$  melt, Stephen Funni and Dr. Elizabeth Dickey for TEM analysis, Dr. Zhitao Guo and Dr. Andrew Gellman for XPS experiment, Kunyao Jiang and Dr. Lisa Porter for optical measurement, Katrina Ramirez-Meyers and Dr. Jay Whitacre for XRF experiment, Dr. Elaine Zhou from NCSU for XPS experiment.

Finally, I would like to thank my families in China whose support and encouragement accompany me throughout my time at CMU.

## Abstract

Photocatalytic water splitting is a promising technique that can reduce humanity's reliance on fossil fuels by converting solar energy to sustainable hydrogen fuels. However, the commercial application of water splitting is still unavailable due to its low efficiency. Two main factors limiting the efficiency of photocatalytic water splitting are rapid charge recombination processes and surface back reactions. Modifying the space charge region is a promising method to solve this problem. Building internal/external electric fields in the space charge region can provide an opposite driving force for electrons and holes so that they move to different locations on surface, and this could reduce the rate of recombination. Besides, foreign element doping and molten salt treatments can alter charge carrier concentration, compensate defects and reduce recombination centers. Solution pH can also be applied as an external electric field to optimize the reactivity. The long-term goal of this project was to understand the structure-performance relationship of metal oxide photocatalysts and synthesize more efficient photocatalysts by space charge engineering for water splitting.

The first study is on  $\text{La}_2\text{Ti}_2\text{O}_7$ , a material whose photocatalytic reactivity might be affected by surface orientation and ferroelectric domains. By means of a photochemical marker reaction, the orientation dependent photocathodic reactivity has been observed to be greatest on (001) surfaces while surfaces perpendicular to this orientation have the least reactivity. Complex ferroelectric domain structures were observed, but they appeared to have no effect on the photocatalytic reactivity, in contrast to previous observations on other ferroelectrics. These results, together with other recent findings, support the idea that the crystal orientation has a strong influence on reactivity and can be used for charge separation. The following two projects focus on using surface orientation to control reactivity.

The second study is about the effect of pH on the photochemical reactivity of  $\text{SrTiO}_3$ . Using the photochemical reduction of Ag as a marker reaction, the relationship between the solution pH and reactivity of surfaces with three orientations (100), (111) and (110) has been evaluated. For all orientations, in the range of pH 3 to pH 9, the reactivity increases from pH 3, reaches a maximum, and then decreases at high pH. The pH associated with the maximum reactivity depends on the

crystallographic orientation of the surface. The result can be used to optimize the reactivity of SrTiO<sub>3</sub> and the reactor system.

The third study is to investigate the influence of particle shape, particle size, dopant concentration and solution pH on the photocatalytic water splitting reactivity of polygonal Al-doped SrTiO<sub>3</sub> through a high-throughput approach. The result demonstrates that an edge truncated cube exposing {100} and {110} facets at a surface area ratio of 1:1.8 is a suitable shape for Al:SrTiO<sub>3</sub>. Those particles with an average size of 500 nm are more reactive than smaller ones. For all particles, the reactivity was measured as a function of pH from pH 2 to pH 12. The pH dependence was similar to the second study, except that the reactivity increases again at pH 12. The results demonstrate that space charge engineering is an efficient method to optimize the reactivity of particulate photocatalysts. Moreover, the results here show the great potential of the parallelized and automated photochemical reactor (PAPCR) in providing rapid feedback in catalyst engineering schemes.

The fourth and fifth studies are two parts of the investigation on the structure-performance relationship of the SrCl<sub>2</sub> flux synthesized Al-doped SrTiO<sub>3</sub> photocatalyst. In the first part, SrTiO<sub>3</sub> single crystal substrates were heated in the flux and AFM and XPS were used to study the surface before and after the experiment. The results imply that the flux treatment gives rise to a much higher surface hydroxyl group density and an enhanced photoanodic reactivity. Besides, it is found that the potential difference between (100) and (110) surfaces increases from 0.07 V to 0.21 V, leading to a much stronger electric field inside the particle to promote charge separation. In the second part, SrTiO<sub>3</sub> was doped with a series of acceptor cations, including Al<sup>3+</sup>, Mg<sup>2+</sup>, Ga<sup>3+</sup> and Fe<sup>3+</sup>. The photocatalytic hydrogen production rates of these doped SrTiO<sub>3</sub> catalysts have been measured with the PAPCR as a function of doping concentration. Based on simulated Brouwer diagrams, it is thought that these acceptors reduce the free electron concentration, lower the Fermi level, and expand the space charge region. The optimal concentration is close to a situation where the oxygen vacancy donors are fully compensated by the acceptors. In a word, both the SrCl<sub>2</sub> flux and acceptor doping contribute to the reactivity: the flux treatment modifies the surface structure, and the dopants affect the defect chemistry in the bulk.

The last study illustrates a surprising ion exchange between perovskite oxides and molten salts. Using this ion exchange reaction, we synthesized a new type of SrTiO<sub>3</sub> photocatalyst by heating

BaTiO<sub>3</sub> in the molten SrCl<sub>2</sub> flux. The ion-exchanged SrTiO<sub>3</sub> photocatalyst produced hydrogen at about twice the rate of the same material that did not undergo ion exchange. FIB-EDS analysis indicates that Cl<sup>-</sup> is unevenly doped inside the crystals during the flux treatment as a donor defect, creating an internal electric field that can drive more photogenerated charge carriers to the surface for reactions. In addition, under high resolution TEM, lattice fringes with periodicities larger than those expected in SrTiO<sub>3</sub> are observed at the edges of the particles. The orientations of these fringes are consistent with Ruddlesden-Popper phase, which are known to occur in Sr-excess SrTiO<sub>3</sub>. This Sr-rich shell might further compensate charge carrier traps. Moreover, it is found that this reaction can be applied to other materials and that the A-site cations in a ABO<sub>3</sub> perovskite oxide can be exchanged with the cations from a molten salt, suggesting a new strategy to design and synthesize highly reactive photocatalysts for water splitting.

# Table of Contents

<b>Acknowledgement</b> .....	<b>iii</b>
<b>Abstract</b> .....	<b>v</b>
<b>List of Figures</b> .....	<b>xi</b>
<b>List of Tables</b> .....	<b>xxii</b>
<b>List of Publications</b> .....	<b>xxiii</b>
<b>Chapter 2: Background</b> .....	<b>12</b>
2.1 Semiconductor based photocatalysis .....	12
2.2 Space charge engineering .....	21
2.3 The effect of crystallographic orientation on photocatalytic reactivity.....	24
2.4 The effect of ferroelectric domains on photocatalytic reactivity.....	29
2.5 The effect of pH on photocatalytic reactivity.....	33
2.6 The effect of foreign ion incorporation.....	37
2.7 References .....	39
<b>Chapter 3: Experimental Methods</b> .....	<b>49</b>
3.1 Atomic force microscopy (AFM).....	49
3.2 Piezo force microscopy (PFM).....	50
3.3 X-ray diffraction (XRD) .....	51
3.4 Scanning electron microscopy (SEM).....	52
3.5 Electron backscatter diffraction (EBSD) .....	54
3.6 Transmission electron microscope (TEM).....	55
3.7 BET surface area analysis .....	57
3.8 X-ray photoelectron spectroscopy (XPS).....	57
3.9 UV-vis diffuse reflectance spectroscopy (UV-vis DRS) .....	59
3.10 Photochemical marker reaction.....	60
3.11 Parallelized and automated photochemical reactor (PAPCR).....	62
3.12 References .....	63
<b>Chapter 4: Influence of Orientation and Ferroelectric Domains on the Photochemical Reactivity of <math>\text{La}_2\text{Ti}_2\text{O}_7</math></b> .....	<b>67</b>
4.1 Introduction .....	67
4.2 Experimental Methods.....	70
4.3 Results.....	72

4.4 Discussion .....	79
4.5 Conclusion.....	82
4.6 References .....	82
<b>Chapter 5: Influence of pH and Surface Orientation on the Photochemical Reactivity of SrTiO<sub>3</sub></b> .....	<b>90</b>
5.1 Introduction .....	90
5.2 Experimental Methods.....	92
5.3 Results.....	95
5.4 Discussion .....	105
5.5 Conclusion.....	109
5.6 References .....	109
<b>Chapter 6: Influence of Particle Size and Shape on the Rate of Hydrogen Produced by Al-doped SrTiO<sub>3</sub> Photocatalysts</b> .....	<b>117</b>
6.1 Introduction .....	117
6.2 Experimental Methods.....	120
6.3 Results.....	124
6.4 Discussion .....	131
6.5 Conclusion.....	134
6.6 References .....	135
<b>Chapter 7: Influence of the Molten SrCl<sub>2</sub> Flux Treatment on the Surface Structure and Photochemical Reactivities of SrTiO<sub>3</sub></b> .....	<b>141</b>
7.1 Introduction .....	141
7.2 Experimental Methods.....	142
7.3 Results.....	144
7.4 Discussion .....	155
7.5 Conclusion.....	159
7.6 References .....	159
<b>Chapter 8: Space Charge Engineering via Defect Compensation for Enhanced Photocatalytic Reactivity</b> .....	<b>164</b>
8.1 Introduction .....	164
8.2 Experimental Methods.....	165
8.3 Results.....	167
8.4 Discussion .....	175
8.5 Conclusion.....	181

8.6 References .....	182
<b>Chapter 9: Ion Exchange between Perovskite Oxides and Molten Salts: A Potential Strategy to Synthesize Highly Efficient Photocatalysts for Water Splitting .....</b>	<b>187</b>
9.1 Introduction .....	187
9.2 Experimental Methods.....	189
9.3 Results.....	191
9.4 Discussion .....	201
9.5 Conclusion.....	208
9.6 References .....	208
<b>Chapter 10: Integrated Discussion and Future Work .....</b>	<b>216</b>
<b>Appendix I: Determining the Effect of Surface Orientation on Photochemical Reactivity using Photochemical Marker Reactions .....</b>	<b>219</b>
<b>Appendix II: Investigating the Effect of High Temperature Photochromism Treatment on the Photochemical Properties of Fe-doped SrTiO<sub>3</sub>.....</b>	<b>239</b>
<b>Appendix III: Synthesizing AgNb<sub>x</sub>Ta<sub>1-x</sub>O<sub>3</sub> Solid Solution for Visible Light Driven Water Splitting .....</b>	<b>246</b>
<b>Appendix IV: Parallelized and Automated Photochemical Reactor (PAPCR) .....</b>	<b>249</b>

# List of Figures

Figure 2-1: Schematic photoexcitation in a solid followed by deexcitation events are presented in panel (A) and (B), modified from ref. <sup>2</sup> Panel (C) presents the energy barrier of an overall water splitting reaction. ....	<b>12</b>
Figure 2-2: Scheme of photocatalytic (A) overall water splitting; (B) proton reduction half reactions with CH <sub>3</sub> OH as sacrificial reagent; (C) water oxidation half reaction with Ag <sup>+</sup> as sacrificial reagent. ....	<b>13</b>
Figure 2-3: Experimentally measured exchange current for hydrogen evolution over different metal surfaces plotted as a function of the calculated hydrogen chemisorption energy per atom. Taken from ref. <sup>19</sup> .....	<b>16</b>
Figure 2-4: (a) Proposed mechanism for the photocatalytic cyclooctane dehydrogenation using Rh <sup>I</sup> (PMe <sub>3</sub> ) <sub>2</sub> (CO)Cl. (b) Proposed reactions involved in the photocatalytic production of H <sub>2</sub> from aqueous HCl solutions using Ir <sup>III</sup> Cl <sub>6</sub> <sup>3-</sup> . (c) A schematic of three component systems. Adapted from ref. <sup>26</sup> .....	<b>20</b>
Figure 2-5: Energy band diagrams of metal and n-type semiconductor contact, reproduced from ref. <sup>33</sup> E <sub>c</sub> and E <sub>v</sub> correspond to energy of conduction band and valance band edges. φ <sub>m</sub> and φ <sub>s</sub> correspond to work functions of metal and semiconductor. E <sub>vac</sub> , vacuum energy. χ <sub>s</sub> , electron affinity of the semiconductor. ....	<b>22</b>
Figure 2-6: Schematic diagrams showing the energy levels and free charge densities for a n-type semiconductor. The blue dotted line labeled the space charge region with a thickness of D. n <sub>i</sub> = intrinsic carrier density; n <sub>e</sub> = electron density; n <sub>h</sub> = hole density. Reproduced from reference. <sup>33</sup> .....	<b>23</b>
Figure 2-7: A band diagram with tunable band edge energies for two crystal surfaces (red and blue). Dashed arrows describe the motions of photogenerated electrons and holes. ....	<b>25</b>
Figure 2-8: Left: I-V curves from the {100}, {110} and {111} facets of Cu <sub>2</sub> O crystals. Right: Band structure of Cu <sub>2</sub> O for different orientations. Reproduced from ref. <sup>49</sup> .....	<b>26</b>
Figure 2-9: (a) Dark-field optical microscopy images of the α-Fe <sub>2</sub> O <sub>3</sub> surface after the photochemical reduction of Ag. (b) Orientation dependent reactivity of 547 grains plotted on the standard stereographic triangle for a hexagonal crystal. Reproduced from ref. <sup>50</sup> .....	<b>26</b>
Figure 2-10: (a) Schematic representation of the structure of the bands closest to the Fermi level for SrTiO <sub>3</sub> , reproduced from ref. <sup>55</sup> (b) SEM image of photo deposition of Ag on faceted SrTiO <sub>3</sub> particles. (c) SEM image of photo deposition of MnO <sub>2</sub> on faceted SrTiO <sub>3</sub> particles. ....	<b>28</b>
Figure 2-11: Schematic illustration of the relationship among piezoelectricity, pyroelectricity and ferroelectricity. ....	<b>29</b>
Figure 2-12: (a) PbTiO <sub>3</sub> has a cubic structure (Pm3m) in paraelectric phase. (b) PbTiO <sub>3</sub> has a tetragonal structure (P4/mmm) in ferroelectric phase. (c) Schematic illustration of formation of 90° domain walls and 180° domain walls in PbTiO <sub>3</sub> . ....	<b>30</b>

Figure 2-13: Topographic AFM images of the same location from a (001) BaTiO <sub>3</sub> single crystal surface under illumination in (a) 0.115M AgNO <sub>3</sub> solution and (b) 0.0115M Pb(Ac) <sub>2</sub> solution. Reproduced from ref. <sup>64</sup> (c) Out of plane PFM image of a (001) BiFeO <sub>3</sub> grain. Dark contrast in the image corresponds to regions with positive polarization and bright regions correspond to a region with negative polarization. (d) Topographic AFM image of the same location after reduction of Ag. Reproduced from ref. <sup>76</sup> .....	<b>32</b>
Figure 2-14: Schematic of measurement of standard potential of M/M <sup>z+</sup> .....	<b>33</b>
Figure 2-15: Pourbaix diagram of water. The shadow region corresponds to the equilibrium condition of water. ....	<b>34</b>
Figure 2-16: Pourbaix diagrams for (a) Sr and (b) Ti in aqueous solution. Surface Pourbaix diagrams showing the thermodynamic stability for SrTiO <sub>3</sub> at (c) pH 1 and (d) pH 12. Taken from ref. <sup>78</sup> .....	<b>35</b>
Figure 2-17: Simulated voltage dependence of electron (J <sub>n</sub> ) and hole (J <sub>p</sub> ) current densities at the surface of a 20 nm TiO <sub>2</sub> film on BaTiO <sub>3</sub> . A* represents Richardson constant. V <sub>oc</sub> represents open-circuit potential. Reproduced from ref. <sup>78</sup> .....	<b>36</b>
Figure 2-18: Schematic representation of equilibrium defect model for undoped and acceptor doped SrTiO <sub>3</sub> . Reproduced from ref. <sup>80</sup> .....	<b>38</b>
Figure 3-1: SEM image of an AFM silicon cantilever and tip with a length of 450 μm (left). An AFM schematic (right). Reproduced from ref. <sup>3</sup> .....	<b>49</b>
Figure 3-2: Sketch of Piezo Force Microscopy set-up in scanning probe microscope. Reproduced from the application note of NT-MDT Spectrum Instruments. ....	<b>51</b>
Figure 3-3: Schematic diagram of diffraction of X-rays by a crystal. Reproduced from ref. <sup>8</sup> .....	<b>52</b>
Figure 3-4: Structure of scanning electron microscope (SEM). Reproduced from ref. <sup>9</sup> .....	<b>53</b>
Figure 3-5: Schematic of the typical EBSD geometry. Reproduced from ref. <sup>13</sup> .....	<b>54</b>
Figure 3-6: Schematic of the (A) diffraction mode and (B) image mode in TEM. Taken from ref. <sup>14</sup> .....	<b>56</b>
Figure 3-7: Schematic of an electron ejected from a sulfur atom induced by X-ray. ....	<b>58</b>
Figure 3-8: Schematic illustration of a typical setup for a marker reaction.....	<b>60</b>
Figure 3-9: (a) SEM image of surface of γ –WO <sub>3</sub> after photooxidation of Mn <sup>2+</sup> . Adapted from ref. <sup>23</sup> (b) Topographic AFM image of (Bi <sub>1-0.5x</sub> Na <sub>0.5x</sub> )(V <sub>1-x</sub> Mo <sub>x</sub> )O <sub>4</sub> (x=0.05) surface after Ag <sup>+</sup> reduction. Adapted from ref. <sup>24</sup> .....	<b>61</b>
Figure 3-10: Image of H <sub>2</sub> detect film is shown in (a) before reaction and (b) after an experiment of 18 h. (c) The amount of H <sub>2</sub> evolved (μmol) versus time (h) for each vial has been calculated and shown. ....	<b>63</b>
Figure 4-1: Crystal structure of La <sub>2</sub> Ti <sub>2</sub> O <sub>7</sub> with TiO <sub>6</sub> octahedra shown. The polarization direction is along [010] axis.....	<b>69</b>

Figure 4-2: Black line corresponds to the XRD pattern of the  $\text{La}_2\text{Ti}_2\text{O}_7$  powder synthesized with molten salt method in this work. Red line corresponds to a calculated pattern of the  $\text{La}_2\text{Ti}_2\text{O}_7$ . (ICSD IDs: 5416 1950).....70

Figure 4-3: (a) SE image after silver reduction. (b) Orientation map of the same area with a color key at bottom left. The field of view is about  $50\ \mu\text{m} \times 60\ \mu\text{m}$ . Six grains have been outlined to illustrate the correspondence between the two images. ....73

Figure 4-4: (a) A higher resolution SEM image after reaction for the large grain labeled “H” at left top of Figure 4-3(a), which is “near red” (near (001)) in Figure 4-3(b). (b) SEM images of the same grain after reaction with a larger magnification. The sample has been kept for years so that the reactivity reduced. ....73

Figure 4-5: SEM images of  $\text{La}_2\text{Ti}_2\text{O}_7$  surfaces after the photochemical reduction of silver. High-reactivity grains are labeled with "H" while low-reactivity grains are labeled with "L". ....74

Figure 4-6: Orientations of  $\text{La}_2\text{Ti}_2\text{O}_7$  grains with high reactivity and low reactivity are labeled in (a) and (b), respectively. Each point corresponds to a grain and the points are plotted in the standard stereographic projection for monoclinic crystals.....75

Figure 4-7: The orientation distribution of grains with high reactivity (red circles) and low reactivity (blue squares) for the photochemical reduction of silver. The units are multiples of a random distribution (MRD). ....76

Figure 4-8: A  $\text{La}_2\text{Ti}_2\text{O}_7$  grain imaged with different modalities. (a) a PFM out-of-plane amplitude image. (b) a PFM out-of-plane phase image. A meandering black line in (a), marked by the arrow, corresponds to a change from light to dark contrast in the phase image. The dark (light) contrast corresponds to regions with  $-180^\circ$  ( $0^\circ$ ) phase shift. (c & d) SEM images of the grain before (c) and after (d) photochemical silver reduction. ....77

Figure 4-9: (a) an SEM image before reaction. (b) an SEM image of the same grain after silver reduction. (c) a PFM out-of-plane amplitude image of the same grain. (d) a PFM out-of-plane phase image of the same grain. Darker regions correspond to domains with positive polarizations, and brighter regions correspond to domains with negative polarizations. Arrows in (c) and (d) mark artifacts caused by a tip issue (see text). ....78

Figure 4-10: (a) SE image of a surface after photochemical silver reduction. The surface orientation of the grain in the middle is  $17.6^\circ$  from (010). (b) PFM out-of-plane image of the same area on sample. Positive domains are labeled with "+" while negative domains are labeled with "-". ....79

Figure 4-11: Schematic energy level diagram at the  $\text{La}_2\text{Ti}_2\text{O}_7$ /solution interface for a (001) oriented grain (left) and a (010) oriented grain (right), assuming the flat band condition. The energy scale is in Volts.  $E_v$ ,  $E_F$ , and  $E_c$  are the valence band edge, the Fermi level, and the conduction band edge, respectively.....81

Figure 5-1: Illustration of the method used to quantify the excess volume in this work. AFM images of a  $\text{SrTiO}_3$  surface before reaction are shown in (a) and (b), as 2D and 3D versions, respectively. The same surface is plotted again in (c), using Originlab and the xyz data extracted from AFM image. AFM images of the same surface after photochemical reaction are shown in

(d) and (e), as 2D and 3D versions, respectively. The surface is plotted again in (f), using Originlab and the xyz data extracted from AFM image. The difference of the integral value between (f) and (c) represents the excess value that was used to quantify the silver product volume and reactivity.....**95**

Figure 5-2: Topographic AFM images of the same location on a (100) SrTiO<sub>3</sub> single crystal surface (a) before and (b)–(h) after photochemical reaction with an aqueous silver nitrate solution having pH values between pH 3-9, as indicated. The dark to light vertical contrast is (a) 1 nm (b) 20 nm (c) 20 nm (d) 20 nm (e) 40 nm (f) 10 nm (g) 5 nm, and (h) 5 nm.....**96**

Figure 5-3: Excess volume of reduced Ag on the SrTiO<sub>3</sub>(100) surface as a function of pH. Units are μm, computed by dividing the volume (μm<sup>3</sup>) by the area (μm<sup>2</sup>). The point is the mean and the bars represent the standard deviation from three measurements. The uncertainty in the silver volume is estimated to be 8 %. The right-hand vertical axis quantifies the value relative to the maximum value at pH 6.....**97**

Figure 5-4: (a) and (b) show topographic AFM images of the same location of a SrTiO<sub>3</sub> (100) crystal after the reduction of silver the oxidation of lead. (a) has been immersed in neutral 10<sup>-4</sup> M AgNO<sub>3</sub> solution and illuminated under 40 W UV light for 15 min and (b) has been immersed in neutral 10<sup>-3</sup> M Pb(CH<sub>3</sub>COO)<sub>2</sub> solution and illuminated under 100 W UV light for 30 min. ....**98**

Figure 5-5: Topographic AFM images of the same location on a SrTiO<sub>3</sub> (110) single crystal surface (a) before and (b)–(h) after photochemical reaction in aqueous silver nitrate solution having pH values between pH 3-9, as indicated. The dark-to-white contrast shown is 5 nm for (a), (b), and (h), 10 nm for (c), (e), and (g) and 15 nm for (d) and (f). ....**99**

Figure 5-6: Excess volume of reduced Ag on the SrTiO<sub>3</sub>(110) surface as a function of pH. Units are μm, computed by dividing the volume (μm<sup>3</sup>) by the area (μm<sup>2</sup>). The uncertainty in the silver volume is estimated to be 6 %. The point is the mean and the bars represent the standard deviation from three measurements. The right-hand vertical axis quantifies the value relative to the maximum value at pH 7.....**99**

Figure 5-7: Topographic AFM images of the same location on a (111) SrTiO<sub>3</sub> single crystal surface (a) before and (b)–(h) after photochemical reaction in an aqueous silver nitrate solution having pH values between pH 3-9, as indicated. The dark-to-white contrast is 18 nm for (a), (g), and (h), and 30 nm for (b), (c), and (d) and 25 nm for (e) and (f). ....**100**

Figure 5-8: Excess volume of reduced Ag on the SrTiO<sub>3</sub>(111) surface as a function of pH. Units are μm, computed by dividing the volume (μm<sup>3</sup>) by the area (μm<sup>2</sup>). The point is the mean and the bars represent the standard deviation from three measurements. The uncertainty in the silver volume is estimated to be 9 %. The right-hand vertical axis quantifies the value relative to the maximum value at pH 4.....**101**

Figure 5-9: AFM image of a SrTiO<sub>3</sub>(111) crystal after immersing in 10<sup>-5</sup> M AgNO<sub>3</sub> solution with a neutral pH (pH ≈ 6) and illuminated under 300 W UV light for 30min. The blue dash line marks the boundary of cathodic and anodic surfaces. ....**101**

Figure 5-10: An orientation map of the polycrystal SrTiO<sub>3</sub> sample. Selected grains near low index orientations are marked with a red circle (100), a blue triangle (111), and a green box (110). **102**

Figure 5-11: Topographic AFM images of the same area on a near (100) orientated grain shown in (a) before and (b)-(h) after photochemical reaction in an aqueous silver nitrate solution having pH values between pH 3-9, as indicated. The dark-to-white contrast in all images is 30 nm..... **103**

Figure 5-12: Topographic AFM images of the same area on a (110) grain shown in (a) before and after photochemical reaction in aqueous silver nitrate solutions with pH values of 3-9 (as indicated). The vertical range from dark to bright is 35 nm in all images. .... **103**

Figure 5-13: Topographic AFM images of the same area on a (111) grain shown in (a) before and after photochemical in aqueous silver nitrate solutions with pH values of 3-9 (as indicated). The vertical range from dark to bright is 15 nm in all images..... **104**

Figure 5-14: Excess volume as a function of pH on the polycrystalline sample for (a) the near (100) surface, (b) the near (110) surface, and (c) the near (111) surface. Units are  $\mu\text{m}$ , computed by dividing the volume ( $\mu\text{m}^3$ ) by the area ( $\mu\text{m}^2$ ). Note that the vertical scales vary in each. In each case, the point is the mean and the bars represent the standard deviation. The right-hand vertical axis quantifies the value relative to the maximum average value in each plot. .... **105**

Figure 5-15: Comparison of the volume of reduced silver as a function of pH on the (100), (110), and (111) single crystal surfaces. Units are  $\mu\text{m}$ , computed by dividing the volume ( $\mu\text{m}^3$ ) by the area ( $\mu\text{m}^2$ ). .... **106**

Figure 5-16: Schematic electronic energy levels for the bands in  $\text{SrTiO}_3$ . The conduction band ( $E_C$ ), valence band ( $E_V$ ), Fermi level ( $E_F$ ), and the silver reduction potential ( $\text{Ag}/\text{Ag}^+$ ) are marked. The upward band bending increase with pH. (c) At high pH, holes are more easily transported to the surface than electrons (indicated by the thickness and length of the arrows). (b) As the pH is reduced and band bending decreases, the barrier for electron transport to the surface remains, but the much higher concentration of electrons in the n-type semiconductor results in comparable electron and hole currents. (a) At the lowest pH, the overall reaction is limited by the transport of holes (minority carriers) to the surface. The energy scale is estimated based on known values for the band gap and silver reduction levels using the method outlined by Morrison.<sup>50</sup> ..... **107**

Figure 6-1: Schematic diagram illustrating the route of the formation of Al-doped  $\text{SrTiO}_3$  catalysts in the presence of different surfactants. .... **122**

Figure 6-2: Schematic illustration of the parallelized and automated photochemical reactor (PAPCR). .... **124**

Figure 6-3: SEM images as well as schematic diagrams for  $\text{SrTiO}_3$  nanocrystals with different shape and treated in melts with different Al concentrations. Scale bar is 200 nm..... **125**

Figure 6-4: XRD patterns of type A, B, C and D crystals treated in  $\text{SrCl}_2$  flux with (a) 1%, (b) 2%, (c) 3% and (d) 5% aluminum added..... **126**

Figure 6-5: Mass specific rate of hydrogen generation from suspensions with 16 types of powders in DI water whose pH is in range of pH 2 to pH 12. All powders are of the type designated as Large (450 nm). The bars represent standard deviations..... **127**

Figure 6-6: UV-vis diffuse reflectance spectra of four types of Al-doped SrTiO <sub>3</sub> with 1% Al doped. .....	<b>128</b>
Figure 6-7: SEM images as well as schematic diagrams for type A and B SrTiO <sub>3</sub> crystals with large, medium, and small size. Scale bar = 200 nm. ....	<b>129</b>
Figure 6-8: Mass specific rate of hydrogen production ( $\mu\text{mol g}^{-1}\text{h}^{-1}$ ) from suspensions with crystal type A-L, A-M and A-S under different pH are shown in (a), (b) and (c), respectively. Mass specific rate of hydrogen production ( $\mu\text{mol g}^{-1}\text{h}^{-1}$ ) from suspensions with crystal type B-L, B-M and B-S under different pH are shown in (d), (e) and (f), respectively. The bars represent standard deviation. ....	<b>129</b>
Figure 6-9: Absolute rate ( $\mu\text{mol m}^{-2}\text{h}^{-1}$ ) of (a) type B-L crystals loaded with 0.1 wt% Rh and Cr cocatalysts, (b) type B-M crystals loaded with 0.2 wt% Rh and Cr cocatalysts and (c) type B-S crystals loaded with 0.3 wt% Rh and Cr cocatalysts as a function of pH.....	<b>130</b>
Figure 6-10: SEM images of the type A-L-Al ((a) and (b)) and B-L ((c) and (d)) SrTiO <sub>3</sub> nanocrystals with photo-deposition of Ag and MnO <sub>2</sub> . Scale bar represents 200 nm. The purpose of using A-L-Al instead of A-L is to show that, for type A crystals, {100} facets serve as both reduction sites and oxidation sites while {111} facets do not participate into reactions. ....	<b>132</b>
Figure 6-11: Schematic illustration of the spatial distribution of photogenerated electrons and holes on (a) {100} facets dominated, (b) optimal ratio of {100} to {110} facets, (c) {110} facet dominated conditions. Red surface and blue surface represent {100} and {110} facets. Yellow balls and blue balls represent to electrons and holes. ....	<b>133</b>
Figure 7-1: (a) SEM images of Hydro1% and Hydro2% crystals and the resulting crystals after modifying by SrCl <sub>2</sub> flux in an aluminum crucible. The scale bar represents 400 nm. (b) and (c) show mass specific rates ( $\mu\text{mol g}^{-1}\text{h}^{-1}$ ) of H <sub>2</sub> generation for Hydro1% and Hydro2% crystals before and after SrCl <sub>2</sub> treatment, respectively. The bars represent the standard deviation. ...	<b>146</b>
Figure 7-2: Topographic AFM image and KFM surface potential image of an air annealed SrTiO <sub>3</sub> (110) surface are given in (a) and (b). The average potential is 0.11 V. Images of the surface after photoreduction of Ag <sup>+</sup> and photooxidation of Mn <sup>2+</sup> are shown in (c) and (d). The dark-to-light vertical contrast is (a): 0 to 3.8 nm, (b): 0.091V to 0.164V, (c): 0 to 5.7 nm, (d): 0 to 8 nm. ....	<b>147</b>
Figure 7-3: Topographic AFM images of air annealed SrTiO <sub>3</sub> (110) single crystal surfaces after treating in molten (a) SrCl <sub>2</sub> flux and (e) KCl flux. Surface potential images were recorded on the same sample, but different locations are shown in (b) and (f). The average potential is determined to be (b): -0.27 V and (f): -0.032 V. Panel (c) and (d) show AFM images of the SrCl <sub>2</sub> treated (110) surface after Ag <sup>+</sup> photoreduction and Mn <sup>2+</sup> photo-oxidation. Panel (g) and (h) show AFM images of the KCl treated (110) surface after Ag <sup>+</sup> photoreduction and Mn <sup>2+</sup> photo-oxidation. The dark-to-light vertical contrast is (a): 0 to 4 nm, (b): -0.33 to -0.22 V, (c): 0 to 15 nm, (d): 0 to 5.4 nm, (e): 0 to 4.7 nm, (f): -0.055 to 0.024 V, (g): 0 to 9 nm, (h): 0 to 7 nm.....	<b>148</b>
Figure 7-4: Topographic AFM image and KFM surface potential image of an air annealed SrTiO <sub>3</sub> (100) surface are given in (a) and (b). The average potential is 0.18 V. Images of the surface after photoreduction of Ag <sup>+</sup> and photooxidation of Mn <sup>2+</sup> are shown in (c) and (d). The dark-to-	

light vertical contrast is (a): 0 to 2.3 nm, (b): 0.15 V to 0.219 V, (c): 0 to 7 nm, (d): 0 to 4.5 nm.  
 ..... **149**

Figure 7-5: Topographic AFM images of air annealed SrTiO<sub>3</sub> (100) single crystal surfaces after treating in molten (a) SrCl<sub>2</sub> flux and (e) KCl flux. Surface potential images were recorded on the same sample, but different locations are shown in (b) and (f). The average potential is determined to be (b): -0.063 V and (f): 0.12v. Panel (c) and (d) show AFM images of the SrCl<sub>2</sub> treated (100) surface after Ag<sup>+</sup> photoreduction and Mn<sup>2+</sup> photo-oxidation. Panel (g) and (h) show AFM images of the KCl treated (100) surface after Ag<sup>+</sup> photoreduction and Mn<sup>2+</sup> photo-oxidation. The dark-to-light vertical contrast is (a): 0 to 2.3 nm, (b): -0.078 to 0.005 V, (c): 0 to 7.2 nm, (d): 0 to 4.7 nm, (e): 0 to 7.4 nm, (f): 0.099 to 0.13 V, (g): 0 to 16.6 nm, (h): 0 to 11 nm.  
 ..... **150**

Figure 7-6: Summaries of the photochemical reactivities and surface potentials of the six samples in Table 7-1..... **151**

Figure 7-7: High resolution O 1s XPS spectra of air annealed (a) (100) and (d) (110) single crystal surfaces, SrCl<sub>2</sub> flux treated (b) (100) and (e) (110) single crystal surfaces and KCl flux treated (c) (100) and (f) (110) single crystal surfaces. The peaks for oxygen atoms bonded in Ti-O and -OH are filled in red and blue, respectively. .... **152**

Figure 7-8: High resolution Sr 3d XPS spectra of air annealed (a) (100) and (d) (110) single crystal surfaces, SrCl<sub>2</sub> flux treated (b) (100) and (e) (110) single crystal surfaces and KCl flux treated (c) (100) and (f) (110) single crystal surfaces. The peaks for strontium atoms bonded in 3d<sub>5/2</sub> and -3d<sub>3/2</sub> are filled in purple and orange, respectively..... **153**

Figure 7-9: High resolution Ti 2p XPS spectra of air annealed (a) (100) and (d) (110) single crystal surfaces, SrCl<sub>2</sub> flux treated (b) (100) and (e) (110) single crystal surfaces and KCl flux treated (c) (100) and (f) (110) single crystal surfaces. The peaks for oxygen atoms bonded in 2p<sub>3/2</sub> and 2p<sub>1/2</sub> are filled in green and brown, respectively..... **154**

Figure 7-10: Images of a (100) SrTiO<sub>3</sub> crystal in molten SrCl<sub>2</sub> flux in a Pt crucible captured with a confocal laser scanning microscope. .... **155**

Figure 7-11: XRD patterns of the resulting materials by heating SrCl<sub>2</sub> in (a) an alumina crucible and (b) a platinum crucible at 1150 °C for 10 h. The materials were collected by centrifugation using deionized water. .... **156**

Figure 7-12: Phase diagram of SrCl<sub>2</sub>-SrO system. Replotted from ref.<sup>25</sup> ..... **157**

Figure 7-13: (a) Surface hydroxyl groups concentrations (shown in bars) and surface potential (shown in dots) of the six samples. (b) Schematic illustration of the change of surface potential induced by the molten SrCl<sub>2</sub> and KCl flux treatment. (c) Schematic illustration of the two possible mechanisms of the hydroxyl group-rich surface..... **158**

Figure 8-1: SEM images of hydrothermally synthesized pure SrTiO<sub>3</sub> particles, denoted as “undoped”. The particles were then treated in a molten SrCl<sub>2</sub> flux in an alumina crucible, a platinum crucible, and a magnesia crucible, denoted as “undoped-sA”, “undoped-sP” and “undoped-sM”. Scale bars represent 500 nm. .... **168**

Figure 8-2: SEM images of Al-doped particles that have been treated in the SrCl<sub>2</sub> flux in a platinum crucible (-sP), an alumina crucible (-sA) and a magnesia crucible (-sM). The numbers represent Al dopant additions. The scale bar represents 500 nm. ....169

Figure 8-3: Photocatalytic maximum hydrogen production rates of Al-doped SrTiO<sub>3</sub> crystals in (a) pH 7 DI water and (b) 10% methanol as a function of Al addition. The crystals have been treated in the molten SrCl<sub>2</sub> flux in an alumina crucible, a magnesia crucible, or a platinum crucible. The bars represent standard deviations. ....170

Figure 8-4: SEM images of Mg-doped particles that have been treated in the SrCl<sub>2</sub> flux in a platinum crucible (-sP), an alumina crucible (-sA) and a magnesia crucible (-sM). The numbers represent Mg dopant additions. The scale bar represents 500 nm. ....171

Figure 8-5: Photocatalytic maximum hydrogen production rates of Mg-doped SrTiO<sub>3</sub> crystals in (a) pH 7 DI water and (b) 10% methanol as a function of Mg addition. The crystals have been treated in the molten SrCl<sub>2</sub> flux in an alumina crucible, a magnesia crucible, or a platinum crucible. The bars represent standard deviations. ....171

Figure 8-6: SEM images of Ga-doped particles that have been treated in the SrCl<sub>2</sub> flux in a platinum crucible (-sP), an alumina crucible (-sA) and a magnesia crucible (-sM). The numbers represent Ga dopant additions. The scale bar represents 500 nm. ....172

Figure 8-7: Photocatalytic maximum hydrogen production rates of Ga-doped SrTiO<sub>3</sub> crystals in (a) pH 7 DI water and (b) 10% methanol as a function of Ga addition. The crystals have been treated in the molten SrCl<sub>2</sub> flux in an alumina crucible, a magnesia crucible, or a platinum crucible. The bars represent standard deviations. ....173

Figure 8-8: Photocatalytic maximum hydrogen production rates in DI water of Al-doped, Mg-doped, and Ga-doped SrTiO<sub>3</sub> crystals as a function of doping concentration. The undoped samples flux treated in an alumina crucible is plotted as an empty square. The rest of the samples were flux treated in a platinum crucible. The measured points are labeled with arrows. ....175

Figure 8-9: Brouwer diagrams of undoped SrTiO<sub>3</sub> and 0.07% Al-doped SrTiO<sub>3</sub> at 1150 °C and 100 °C. The calculation employed a python code modified from the code on co-doping BaTiO<sub>3</sub> developed by Ryu et al.<sup>26,27</sup> ....178

Figure 8-10: Schematic illustration of how the incorporation of Al<sup>3+</sup>, Mg<sup>2+</sup> and Ga<sup>3+</sup> influences the space charge of SrTiO<sub>3</sub>. ....179

Figure 9-1: (a) SEM images of molten SrCl<sub>2</sub> flux treated SrTiO<sub>3</sub>, BaTiO<sub>3</sub>, PbTiO<sub>3</sub>, CaTiO<sub>3</sub>, rutile and anatase TiO<sub>2</sub>. Scale bar: 2 μm. (b) XRD patterns of the six flux treated samples with a standard SrTiO<sub>3</sub> pattern plotted as black droplines (ICDD: 01-074-1296). (c) Photocatalytic maximum H<sub>2</sub> production rates from the six samples in 10% methanol solution, pH 2 water, pH 7 water and pH 12 water under 380 nm illumination. ....192

Figure 9-2: (a) XRD patterns of BaTiO<sub>3</sub> treated in the molten SrCl<sub>2</sub> flux for a variety of temperature and time combinations. (b) Lattice parameters refined from the XRD patterns. The bars represent standard deviations. (c) Photocatalytic H<sub>2</sub> production rates of the samples in pH 7 DI water. (d) Photocatalytic H<sub>2</sub> production rates of the samples in pH 12 DI water. ...194

Figure 9-3: SEM images of BaTiO<sub>3</sub> treated in molten SrCl<sub>2</sub> flux in an alumina crucible or a platinum crucible are shown in (a) and (b), respectively. Scale bars are shown in the images. Maximum H<sub>2</sub> production rates measured with the PAPCR of BaTiO<sub>3</sub> treated in the molten SrCl<sub>2</sub> flux with different amount of Al added in an alumina crucible or a platinum crucible are shown in (c) and (d). The concentration of Al<sup>3+</sup> and Cl<sup>-</sup> are determined with EDS and shown in the images in a different axis.....**196**

Figure 9-4: SEM images of BaTiO<sub>3</sub> treated in the SrCl<sub>2</sub> flux in an alumina crucible with different amount of Al added. ....**197**

Figure 9-5: SEM images of BaTiO<sub>3</sub> treated in the molten SrCl<sub>2</sub> flux in a platinum crucible with different amount of Al added. ....**197**

Figure 9-6: XRD patterns of BaTiO<sub>3</sub> treated in the molten SrCl<sub>2</sub> flux with different amount of Al<sub>2</sub>O<sub>3</sub> added in an alumina crucible or a platinum crucible are shown in (a) and (b), respectively. A magnified image of the (110) reflection is given in a separated panel in both (a) and (b). Lattice parameters have been refined with HighScore and given in (c) and (d). The bars represent standard deviations. Note that the minor peaks at 38.6°, 44.9° and 65.3° are attribute to the (111), (200) and (220) reflections of the Al sample stage in the diffractometer but not from the samples.....**198**

Figure 9-7: High resolution XPS spectra of Sr 3d region in (a) pristine SrTiO<sub>3</sub>, (b) STO-sA, (c) BTO-sA; Ti 2p region in (d) pristine SrTiO<sub>3</sub>, (e) STO-sA, (f) BTO-sA; and O 1s scan in (g) pristine SrTiO<sub>3</sub>, (h) STO-sA, (i) BTO-sA.....**200**

Figure 9-8: (a) SEM images of BTO-sA particle cross section samples prepared via FIB milling. (b) EDS element maps of the box region in (a).....**201**

Figure 9-9: SEM images of particle cross section samples of (a) PTO-sA and (b) CTO-sA. Kirkendall pores are observed in both samples. Scale bars are shown in the images. Note that the small particles in (b) correspond to redeposition during ion milling. ....**202**

Figure 9-10: (a) High resolution TEM image of a particle edge of BTO-sA. (b) SAED pattern recorded on the lattice in (a). Bright field and dark field images on the same particle edge are shown in (c) and (d). Scale bars are given in the images.....**203**

Figure 9-11: (a) FFT pattern of the lattice fringes in Fig. 9-10(a). (b) Inverse-FFT pattern by selecting the split spots in (a). ....**205**

Figure 9-12: A high resolution TEM image of a BTO-sA particle edge is given in (a) with its corresponding (b) SAED pattern and (c) FFT pattern. (d) Inverse-FFT pattern by selecting the split spots in (c).....**205**

Figure 9-13: (a) Photocatalytic maximum H<sub>2</sub> production rates of PTO-sA and the same sample that has been soaked in 10% methanol solution, pH 2 water, pH 7 water and pH 12 water for 1 or 2 weeks. The illumination is provided by 380 nm LEDs. (b) Photocatalytic maximum H<sub>2</sub> production rates of CaTiO<sub>3</sub> that have been treated in the SrCl<sub>2</sub> flux for one or two times. The rates are measured in 10% methanol, pH 2 water, pH 7 water and pH 12 water under 380 nm illumination. ....**207**

Figure 11-1: SEM images of the surface of (a) bare BiVO <sub>4</sub> , and the surface after photodepositing (b) Au, (c) Pt, (d) Ag, (e) MnO <sub>2</sub> , (f) PbO <sub>2</sub> . Scale bar, 500 nm. Reproduced from ref. <sup>6</sup> .....	<b>219</b>
Figure 11-2: Surface atomic structure of anatase (a) (010), (b) (001) and (c) (010) surface. ....	<b>220</b>
Figure 11-3: DFT calculated band structure and density of states (DOS) of BiOBr (a) (001), (110) and (c) (010), (102) facets. Crystal structure of BiOBr (001) and BiOBr (010) are illustrated in (b) and (d). ((e) (f)) SEM images of BiOBr-(001) after in situ photodeposited with Pt and MnO <sub>x</sub> . ((h) (i)) SEM images of BiOBr-(010) after in situ photodeposited with Pt and MnO <sub>x</sub> . Schematic illustration of photoexcited charge distributions on BiOBr-(001) and BiOBr-(010) are shown in (g) and (j). Adapted from Ref. <sup>11</sup> .....	<b>222</b>
Figure 11-4: (a) Orientation map of an α-Fe <sub>2</sub> O <sub>3</sub> ceramic surface. (b) Dark-field optical microscopy images of the α-Fe <sub>2</sub> O <sub>3</sub> surface after the photochemical reduction of Ag. The brighter contrasts correspond to silver products. (c) The average relative potential value measured by KFM (for 167 grains from 16 different images) plotted versus orientation on a stereographic projection broken into 39 regions. (d) A similar plot of the average activity measured from DF-OM images. Adapted from ref. <sup>22</sup> .....	<b>224</b>
Figure 11-5: (a–c) Tungsten probes contacting single Cu <sub>2</sub> O crystals for their electrical conductivity measurements. (d) Schematic illustration of the measurement set up. (e) I–V curves for the (100), (110), and (111) faces of Cu <sub>2</sub> O crystals. (f) Modified general band diagram of Cu <sub>2</sub> O crystals accounting for their observed optical size and facet effects. Adapted from ref. <sup>23,24,26</sup> .....	<b>225</b>
Figure 11-6: (a) UV-visible spectra of anatase TiO <sub>2</sub> particles exposing 18% (001) facets and 72% (001) facets, reproduced from ref. <sup>31</sup> (b) UV-vis diffusive reflectance spectra of Ag <sub>3</sub> PO <sub>4</sub> nano cubes and rhombic dodecahedrons, adapted from ref. <sup>32</sup> (c) A plot summarizing the volume variation of Cu <sub>2</sub> O octahedra and cubes with respect to their UV–vis absorption band positions reproduced from ref. <sup>34</sup> (d) Plots of (αhν) <sup>1/2</sup> versus photon energy (hν) of CeO <sub>2</sub> nanocrystals, reproduced from ref. <sup>35</sup> .....	<b>226</b>
Figure 11-7: Schematic of a (a) faceted particle and the same particle after (b) photoreduction of Ag <sup>+</sup> and (c) photo-oxidation of Pb <sup>2+</sup> .....	<b>228</b>
Figure 11-8: Illustration of EBSD analysis process of Ba <sub>0.8</sub> Sr <sub>0.2</sub> TiO <sub>3</sub> ceramic surface. The pattern was collected and processed through OIM Collection software. ....	<b>229</b>
Figure 11-9: Topographic AFM image of the BiVO <sub>4</sub> surface after a photochemical reaction (a) after reduction and (d) after oxidation. The corresponding orientation maps are shown in (b) and (e). Orientations of grains on the BiVO <sub>4</sub> surface that were classified as low and high reactivity for the photochemical oxidation of (c) Ag <sup>+</sup> reduction and (f) Pb <sup>2+</sup> oxidation. Each point corresponds to an observed grain and the points are plotted in stereographic projection. Reproduced from Ref. <sup>38</sup> .....	<b>230</b>
Figure 12-1: UV-vis spectra of undoped SrTiO <sub>3</sub> single crystal and Fe-doped SrTiO <sub>3</sub> single crystal with and without the photochromism treatment. ....	<b>240</b>
Figure 12-2: Photoreduction of Ag <sup>+</sup> on the surface of a Fe-doped SrTiO <sub>3</sub> single crystal that has undergone a photochromism treatment. The maker reaction was carried out under UV	

illumination for (a) and (b) and visible light illumination for (c) and (d). The dark to bright contrast is (a): 30 nm, (b): 30 nm, (c): 10 nm, (d): 6 nm. ....241

Figure 12-3: SEM images of 0.01%, 0.02%, 0.05% and 0.1% Fe doped SrTiO<sub>3</sub>. The samples were prepared with a solid-state method and then heated in the molten SrCl<sub>2</sub> flux. ....242

Figure 12-4: Photocatalytic hydrogen production rates of SrCl<sub>2</sub> flux treated Fe-doped SrTiO<sub>3</sub> with different Fe additions in (a) 10% methanol solutions and (b) pure water. ....243

Figure 13-1: (a) XRD pattern and (b) photocatalytic hydrogen generation under 380 nm light from the prepared AgNbO<sub>3</sub> powders. ....247

Figure 13-2: Photocatalytic hydrogen generation from AgNb<sub>x</sub>Ta<sub>1-x</sub>O<sub>3</sub> solid solutions under 380 nm illumination.....247

Figure 14-1: Schematic illustration of the PAPCR. ....250

Figure 14-2: Pictures of the reactor array taken after injecting specific amount of hydrogen. .252

Figure 14-3: (a) The linear fitting for the average normalized intensity in the range of 0 to 31% hydrogen. The average of the 15 vials are represented by the black dots, and standard deviation are represented by the yellow and the purple lines, and the orange line shows the best fit. (b) Plot of the hydrogen production versus reaction time from one of the vials. ....253

Figure 14-4: Hydrogen production from Ru(bpy)<sub>3</sub>(PF<sub>6</sub>)<sub>2</sub> catalysts in the identical experiment..254

## List of Tables

Table 4-1: Details of population analysis in Fig. 4-7. ....	<b>76</b>
Table 6-1: Summary of synthesis route and conditions for all samples. ....	<b>121</b>
Table 6-2: BET data of undoped SrTiO <sub>3</sub> crystals. ....	<b>131</b>
Table 7-1: Photochemical reactivities and surface potential of the six SrTiO <sub>3</sub> single crystal surfaces. ....	<b>151</b>
Table 7-2: Sr/Ti ratios and surface hydroxyl groups concentrations of the six samples determined with the XPS spectra. ....	<b>154</b>
Table 8-1: Molar ratios determined by ICP-OES of selected SrTiO <sub>3</sub> crystals. ....	<b>173</b>
Table 8-2: Molar ratios of the 15 hydrothermally doped SrTiO <sub>3</sub> crystals estimated from the data in Table 8-1. These crystals were not treated in the SrCl <sub>2</sub> flux. ....	<b>174</b>
Table 9-1: Refined lattice parameters and unit cell volumes (refined with HighScore) of the six samples in Figure 9-1. The reference lattice parameter of SrTiO <sub>3</sub> (ICDD: 01-073-0661) is 3.9050 Å. ....	<b>192</b>
Table 9-2: BET surface areas, Al <sup>3+</sup> and Ba <sup>2+</sup> concentrations determined by ICP-OES, Cl <sup>-</sup> concentrations determined by XRF of STO-sA and BTO-sA. ....	<b>195</b>
Table 9-3: Surface Compositions and Chemical State of Sr, Ti and O of pristine SrTiO <sub>3</sub> , STO-sA and BTO-sA determined from XPS spectra. ....	<b>200</b>
Table 9-4: Summary of ion exchange materials in this work. ....	<b>208</b>
Table 11-1: Summary of photocatalysts with orientation dependent photochemical reactivities. ....	<b>227</b>
Table 14-1: The volume (ml) of hydrogen injected for calibration and the corresponding percentage of hydrogen (H <sub>2</sub> %) as well as the amount of hydrogen (μmol) calculated. ....	<b>251</b>

## List of Publications

1. Mingyi Zhang, Paul A. Salvador, Gregory S. Rohrer. Influence of pH and Surface Orientation on the Photochemical Reactivity of SrTiO<sub>3</sub>. *ACS Applied Materials & Interfaces* **2020** 12 (20), 23617-23626. <https://dx.doi.org/10.1021/acsami.0c04351>
2. Mingyi Zhang, Paul A. Salvador, Gregory S. Rohrer. Influence of Orientation and Ferroelectric Domains on the Photochemical Reactivity of La<sub>2</sub>Ti<sub>2</sub>O<sub>7</sub>. *Journal of the European Ceramic Society* **2021** 41 (1), 319-325. <https://doi.org/10.1016/j.jeurceramsoc.2020.09.020>
3. Mingyi Zhang, Paul A. Salvador, Gregory S. Rohrer. Influence of Particle Size and Shape on the Rate of Hydrogen Produced by Al-doped SrTiO<sub>3</sub> Photocatalysts. *Journal of the American Ceramic Society* **2022** 105 (8). 5336-5346. <https://doi.org/10.1111/jace.18488>

Note that Chapter 4, 5 and 6 in this thesis were slightly modified from the publications 1, 2 and 3 listed above.

# Chapter 1: Introduction

## 1.1 Motivation

Energy is a critical component of our everyday needs. On account of the exhaustion of cheap oil and the impact of greenhouse emissions, people are forced to seek environmentally clean alternative energy resources.<sup>1,2</sup> Solar energy is a potential substitute for fossil fuels because of its sustainability and environmental friendliness.<sup>3</sup> In 2021, Americans used 97.3 quads (quadrillion BTU) of energy but among them solar energy only made up 1.5 quad.<sup>4</sup> To harvest energy from the sun, a promising strategy is photocatalytic water splitting, a technique that converts water into hydrogen and oxygen with the help of solar illumination. Hydrogen is an ideal fuel for its high energy density and minimal air pollution. Furthermore, since water and sun light are abundant, endless, and renewable, all we need is to design a stable photocatalyst that can split water efficiently.

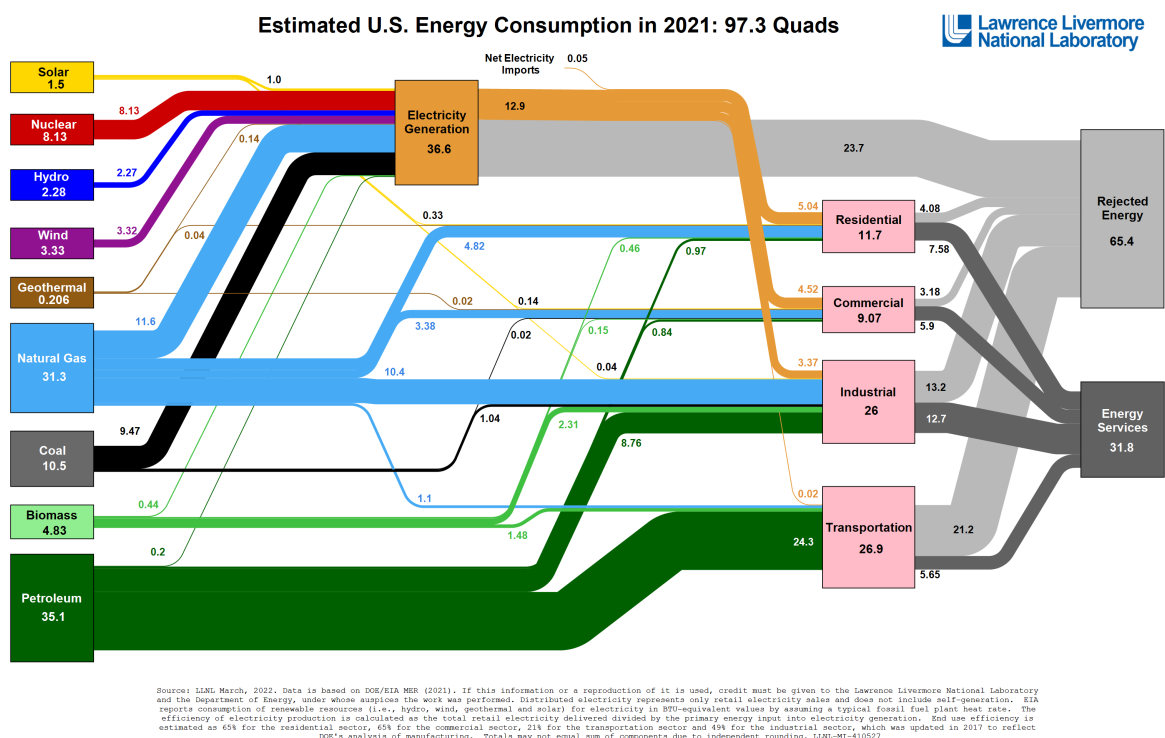
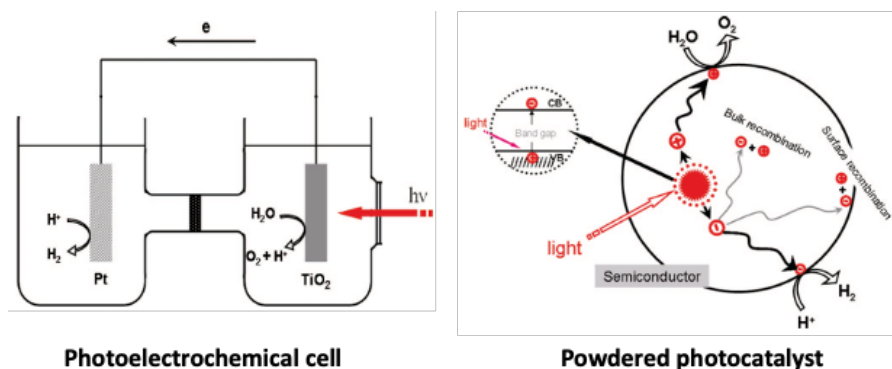


Figure 1-1: The 2021 energy flow chart released by Lawrence Livermore National Laboratory.<sup>4</sup>

There are two major categories of water splitting. The first category is to use photoelectrochemical cells (PECs).<sup>5,6</sup> In a PEC system, there will be two electrodes, such as TiO<sub>2</sub> and Pt, immersed in

an electrolyte and connected to an external electric circuit. Under illumination, electron-hole pairs are generated and separated by an electric field to drive proton reduction and water oxidation. However, the durability of electrode is poor, and this might increase its cost.<sup>7</sup>

The second category is photocatalysis using a colloidal suspension of powdered catalysts.<sup>8,9</sup> A particulate catalyst could be considered as a smart PEC, where different regions of the powder surface serve as photoanodes and photocathodes. Those powders have the potential to be fabricated at lower costs than PECs, but they have relatively poor efficiencies. Two of the most significant problems for particulate photocatalysts are the high rate of photogenerated carrier recombination and the back reaction of intermediate chemical species.



**Figure 1-2:** Simple schematic of photoelectrochemical cell (left), reproduced from ref.<sup>10</sup> Schematic of powdered photocatalyst (right), reproduced from ref.<sup>11</sup>

A tremendous amount of research has focused on reducing the rate of charge recombination and back reactions. In this thesis, two primary strategies are tested to enhance the separation of photogenerated electron-hole pairs. The first one is to develop catalysts with an internal electric field in the space charge region. An internal field may arise from polarization of ferroelectric or ferroelastic domains,<sup>12,13</sup> phase boundaries,<sup>14</sup> polar surface terminations<sup>15,16</sup> and surface orientations.<sup>17,18</sup> With such fields, electrons and holes will be attracted to different locations of the catalyst surface for reduction and oxidation so that an enhancement of charge separation is achieved. Hence, the overall photocatalytic efficiency should increase.

The second strategy is to apply an external electric field to the space charge region. Since the two half reactions need to proceed at the same rate to keep charge neutral, the overall reaction rate depends on the slower one of the two half reactions. If one applies a potential to increase the rate

of the slower reaction, it will decrease the faster reaction; the maximum overall rate is achieved at a potential where the rates of the photocathodic and photoanodic reactions are equal. pH is a good candidate to provide an external field. The solution pH influences the amount of charge adsorbed on the surface, the surface potential, the band bending in the semiconductor, and, therefore, the concentration of available charge carriers at the surface. Because the photochemical reactivity is directly proportional to the amount of available charge carriers, the pH serves as an external field and affects the overall reaction rate.

## 1.2 Objectives

The work described here has three major goals. As we have mentioned in Section 1.1, an internal electric field in the space charge region could influence the photochemical reactivity.  $\text{La}_2\text{Ti}_2\text{O}_7$  is a ferroelectric material with a layered perovskite structure. Many materials have been found to exhibit anisotropic catalytic reactivity such that some orientations are more photocathodic while other orientations are more photoanodic, and this effect originates from the different degree of band bending in the space charge region as well as the different surface potential. If one can prepare shape-controlled particles exhibiting specific facets, photo reduction and photo oxidation will thus occur on different locations of the particle, hence the overall photocatalytic efficiency would be enhanced.  $\text{La}_2\text{Ti}_2\text{O}_7$  has a strong anisotropic structure and simulations imply that there is a significant difference in the band edge positions perpendicular and parallel to the perovskite layers,<sup>19</sup> so that we assume that its photocatalytic reactivity is influenced by surface orientation. Besides,  $\text{La}_2\text{Ti}_2\text{O}_7$  has a polarization in ferroelectric domains with a magnitude of  $5 \mu\text{C}/\text{cm}^2$ , which is similar to  $\text{BiFeO}_3$  ( $6 \mu\text{C}/\text{cm}^2$ ). Thus, we assume that they should behave similarly with the reactivity being influenced by ferroelectric domains. With the two assumptions, the first goal of this work is to test the photochemical reactivity of  $\text{La}_2\text{Ti}_2\text{O}_7$  by means of marker reactions and investigate the relative importance of surface orientation and ferroelectric domains. We found that, in this case, surface orientation plays a more important role in photocatalytic reactivities.

I then turned my attention to  $\text{SrTiO}_3$ , which can split water under UV illumination and has an orientation dependent photocatalytic reactivity.<sup>20,21</sup> My second goal was to test the pH effect on the photochemical reactivity on surfaces of  $\text{SrTiO}_3$  with different orientations. Solution pH can influence the surface charge and surface potential. Increasing pH, more negative charges ( $\text{OH}^-$ )

will adsorb to surface and bend the bands upward. Also, it is expected that the pH effect may vary in different crystallographic orientations because of the anisotropic transport and chemical properties on SrTiO<sub>3</sub>. If one could establish a model for band bending as a function of solution pH, it will be useful for us to understand pH effect and apply it to more catalyst systems.

The third goal is to explore other feasible tools to modify the space charge region for better reactivity. Doping foreign elements is a widely used method to improve the properties of photocatalysts. The dopants usually serve as donors or acceptors, alter the charge carrier concentration, and shift the Fermi level. For example, doping aluminum into SrTiO<sub>3</sub> was found to reduce the number of free electrons and shift the Fermi level anodically.<sup>22</sup> Determining a suitable dopant with an optimized doping concentration is necessary to prepare a highly efficient photocatalyst. Additionally, particle size may influence band structure too. If the particle is too large, charge carriers generated in the center flat band region are unable to migrate to the surface. If the particle is smaller than twice the length of space charge region, the band bending will be reduced so that the electric field in the space charge region will be smaller and photogenerated carriers are more difficult to separate. Therefore, determining a suitable size for particulate photocatalysts is also a crucial task. Finally, catalyst synthesis route is also critical. It is known that materials prepared in molten salt methods and hydrothermal methods might have a higher crystallinity than those prepared with solid-state methods, which results in a lower concentration of charge carrier traps and better reactivity.

The long-term objective of this project is to develop a series of shape-controlled particle photocatalysts exposing specific facets serving as photoanodes and photocathodes. By separating the location of the two half reactions, the rate of charge recombination and back reaction should be regulated for such particles. Next, the optimal particle size, dopant concentration and synthesizing route will be employed. Finally, the solution pH will be adjusted to find the pH value associated with maximum reactivity.

### **1.3 Hypothesis**

**Question 1:** What are the influences of surface orientation and ferroelectric polarization on the photochemical reactivity on La<sub>2</sub>Ti<sub>2</sub>O<sub>7</sub>?

*Hypothesis 1*

*La<sub>2</sub>Ti<sub>2</sub>O<sub>7</sub> is a ferroelectric material with a layered perovskite structure. The photocatalytic reactivity of La<sub>2</sub>Ti<sub>2</sub>O<sub>7</sub> is influenced by both surface orientation and ferroelectric domains.*

The spontaneous polarization within a ferroelectric creates an electric field driving photogenerated carriers to move in opposite directions, which causes reduction and oxidation to occur at different locations. For a positive domain, there will be a potential drop across the domain, bending the band downwards and electrons can easily move to the surface to react with species in solution. On the contrary, for a negative domain, the polarization will bend the band upwards and holes can easily move to surface. The polarization in La<sub>2</sub>Ti<sub>2</sub>O<sub>7</sub> domains is of 5  $\mu\text{C}/\text{cm}^2$ ,<sup>23</sup> which is similar to BiFeO<sub>3</sub> (6  $\mu\text{C}/\text{cm}^2$ ).<sup>24</sup> The photochemical reactivity of BiFeO<sub>3</sub> depends on ferroelectric domains,<sup>25</sup> so we expect that La<sub>2</sub>Ti<sub>2</sub>O<sub>7</sub> should behave similarly. Meanwhile, surface orientations usually affect photochemical reactivity, too. La<sub>2</sub>Ti<sub>2</sub>O<sub>7</sub> has a strong anisotropic structure. Simulations by Bruyer et al. show significant differences in the band edge positions perpendicular and parallel to the layers.<sup>19</sup> Therefore, the photocatalytic reactivity of La<sub>2</sub>Ti<sub>2</sub>O<sub>7</sub> is also supposed to depend on orientations. Hence, we expect that the reactivity of La<sub>2</sub>Ti<sub>2</sub>O<sub>7</sub> depends on both orientation and ferroelectric domains. In order to investigate which factor is dominant, we carried out experiments described in Chapter 4.

**Question 2:** What is the interplay between crystallographic orientations and solution pH on the photochemical reactivity of SrTiO<sub>3</sub>?

*Hypothesis 2*

*Adjusting the aqueous solution pH can control surface charge and the rates of the two half reactions to influence the overall photochemical reaction rate of SrTiO<sub>3</sub>. Because of different potentials at different surfaces, the pH effect is likely to vary with surface orientation.*

pH can be considered as an external electric field to adjust photocatalytic reactivity since it could control the relative rates of oxidation and reduction reactions, leading to a change in the overall reaction rate. In a low pH environment (higher H<sup>+</sup> concentration), there will be more positive charge on the surface, leading to a downward band bending (or reduced upward band bending), so that electrons will be transported to the surface, but holes will be repelled, and photo reduction is favored. In a high pH environment (higher OH<sup>-</sup> concentration), there will be more negative charge on the surface, leading to increased upward band bending, so that holes will be transported to the

surface, but electrons will be repulsed, and photo oxidation is favored. Since the overall reaction rate depends on the slower one of the two half reactions, the maximum reactivity should be achieved at an intermediate pH value. Because of different potentials at different surfaces, the pH effect is likely to differ on (100), (110), and (111) surfaces.

**Question 3:** Is it feasible to develop an anisotropic faceted Al:SrTiO<sub>3</sub> particle catalyst with an enhanced charge separation for overall water splitting? And how will solution pH affect the reactivity?

#### *Hypothesis 3*

*An Al:SrTiO<sub>3</sub> particle exposing {100} and {110} facets should have better photocatalytic reactivity than particles with only {100} facets. By tailoring the fraction of the two types of facets, the photocatalytic reactivity will be optimized.*

Based on previous study, in SrTiO<sub>3</sub>, {100} surfaces are more photocathodic while {110} surfaces are more photoanodic,<sup>26,27</sup> hence, a separation of photogenerated carries occurs between the two surfaces. Dong et al. introduced a hydrothermal method to prepare faceted SrTiO<sub>3</sub> nano particles exposing {100} and {110} facets and the percentage of the two types of facets could be adjusted by changing surfactants.<sup>28</sup> Also, Al-doped SrTiO<sub>3</sub> (Al:SrTiO<sub>3</sub>) loaded with RhCrO<sub>x</sub> (rhodium chromium oxide) cocatalysts splits water with an apparent efficiency (quantum yield greater than 50% at 365 nm).<sup>29-31</sup> In my research, I combined the two works, developing shape-controlled Al-doped SrTiO<sub>3</sub> and finding the best shape by adjusting the ratio of {100} and {110} facets for photocatalytic water splitting. The most suitable doping ratio and crystal size have been determined. The solution pH was adjusted to optimize the reactivity.

**Question 4:** What is the specific role of Al<sup>3+</sup> dopants on the photocatalytic reactivity of SrTiO<sub>3</sub>? Is it possible to replace it with other elements?

#### *Hypothesis 4*

*Al<sup>3+</sup> serves as an acceptor dopant in SrTiO<sub>3</sub>, lowers the free electron concentration and expands the space charge region. Mg<sup>2+</sup>, Ga<sup>3+</sup> and Fe<sup>3+</sup> also serve as acceptor dopants since they occupy Ti sites, so they should behave like Al<sup>3+</sup> and contribute to the photocatalytic reactivity.*

Introducing aliovalent dopants into a host material would alter the free charge carrier concentration. SrTiO<sub>3</sub> is a n-type semiconductor because of intrinsic oxygen vacancies.<sup>32</sup> Al<sup>3+</sup> is an acceptor dopant that can provide positive charge and compensate oxygen vacancy donors. The reduced free electron concentration would expand the space charge region, contributing to the improved transport of photogenerated charge carriers. At the same time, this will lower the Fermi level and reduce the potential difference between the semiconductor and the solution, leading to a lower degree of band bending. If so, there should be an optimal doping concentration that can balance the two factors. In this study, I investigated the effect of introducing foreign elements (Al<sup>3+</sup>, Mg<sup>2+</sup>, Ga<sup>3+</sup>, Fe<sup>3+</sup>) on the photocatalytic reactivity of SrTiO<sub>3</sub> as a function of doping concentration. A defect compensation model is provided to understand the doping effect.

**Question 5:** Is the molten SrCl<sub>2</sub> flux treatment a necessary step to prepare highly reactive SrTiO<sub>3</sub> photocatalysts? If so, what happens when we soak SrTiO<sub>3</sub> in this molten salt?

*Hypothesis 5*

*Al-doped SrTiO<sub>3</sub> photocatalysts prepared in the molten SrCl<sub>2</sub> flux are more reactive than those prepared in other methods. The flux treatment modifies the surface structure and surface chemistry to a condition that is more favorable to photochemical reactions.*

Nearly all high-performance Al-doped SrTiO<sub>3</sub> photocatalysts employed the molten SrCl<sub>2</sub> flux treatment. But its mechanism is still not clear. Previous report assumes that SrTiO<sub>3</sub> dissolves and recrystallizes in the melt so that the crystallinity is improved.<sup>30,33</sup> Based on my previous results, it is less likely that the particle completely dissolves and recrystallizes. My assumption is the surface slightly dissolves in the flux and the newly formed surface is more reactive. To test this, I carried out the flux treatment on large SrTiO<sub>3</sub> single crystal substrates and studied the surface with AFM and XPS before and after the treatment.

## 1.4 References

- (1) Dresselhaus, M. S.; Thomas, I. L. Alternative Energy Technologies. *Nature* **2001**, *414* (6861), 332–337. <https://doi.org/10.1038/35104599>.
- (2) Kamat, P. V. Meeting the Clean Energy Demand: Nanostructure Architectures for Solar

- Energy Conversion. *J. Phys. Chem. C* **2007**, *111* (7), 2834–2860. <https://doi.org/10.1021/jp066952u>.
- (3) Crabtree, G. W.; Lewis, N. S. Solar Energy Conversion. *Phys. Today* **2007**, *60* (3), 37–42. <https://doi.org/10.1063/1.2718755>.
- (4) Laboratory, L. L. N. US Energy Flow Trends-2019. **2019**.
- (5) Osterloh, F. E. Inorganic Nanostructures for Photoelectrochemical and Photocatalytic Water Splitting. *Chem. Soc. Rev.* **2013**, *42* (6), 2294–2320. <https://doi.org/10.1039/C2CS35266D>.
- (6) Tryk, D. A.; Fujishima, A.; Honda, K. Recent Topics in Photoelectrochemistry: Achievements and Future Prospects. *Electrochim. Acta* **2000**, *45* (15), 2363–2376. [https://doi.org/10.1016/S0013-4686\(00\)00337-6](https://doi.org/10.1016/S0013-4686(00)00337-6).
- (7) Li, Z.; Luo, W.; Zhang, M.; Feng, J.; Zou, Z. Photoelectrochemical Cells for Solar Hydrogen Production: Current State of Promising Photoelectrodes, Methods to Improve Their Properties, and Outlook. *Energy Environ. Sci.* **2013**, *6* (2), 347–370. <https://doi.org/10.1039/C2EE22618A>.
- (8) Kudo, A.; Miseki, Y. Heterogeneous Photocatalyst Materials for Water Splitting. *Chem. Soc. Rev.* **2009**, *38* (1), 253–278. <https://doi.org/10.1039/B800489G>.
- (9) Wang, Z.; Li, C.; Domen, K. Recent Developments in Heterogeneous Photocatalysts for Solar-Driven Overall Water Splitting. *Chem. Soc. Rev.* **2019**, *48* (7), 2109–2125. <https://doi.org/10.1039/C8CS00542G>.
- (10) Fujishima, A.; Honda, K. Electrochemical Photolysis of Water at a Semiconductor Electrode. *Nature* **1972**, *238* (5358), 37+. <https://doi.org/10.1038/238037a0>.
- (11) Linsebigler, A. L.; Lu, G.; Yates, J. T. Photocatalysis on TiO<sub>2</sub> Surfaces: Principles, Mechanisms, and Selected Results. *Chem. Rev.* **1995**, *95* (3), 735–758. <https://doi.org/10.1021/cr00035a013>.
- (12) Dunn, S.; Jones, P. M.; Gallardo, D. E. Photochemical Growth of Silver Nanoparticles on

- C- and C+ Domains on Lead Zirconate Titanate Thin Films. *J. Am. Chem. Soc.* **2007**, *129* (28), 8724–8728. <https://doi.org/10.1021/ja071451n>.
- (13) Pisat, A. S.; Rohrer, G. S.; Salvador, P. A. Spatial Selectivity of Photodeposition Reactions on Polar Surfaces of Centrosymmetric Ferroelastic Gamma-WO<sub>3</sub>. *J. Mater. Chem. A* **2017**, *5* (18), 8261–8266. <https://doi.org/10.1039/c7ta00842b>.
- (14) Wang, X.; Xu, Q.; Li, M.; Shen, S.; Wang, X.; Wang, Y.; Feng, Z.; Shi, J.; Han, H.; Li, C. Photocatalytic Overall Water Splitting Promoted by an  $\alpha$ - $\beta$  Phase Junction on Ga<sub>2</sub>O<sub>3</sub>. *Angew. Chemie Int. Ed.* **2012**, *51* (52), 13089–13092. <https://doi.org/10.1002/anie.201207554>.
- (15) Zhu, Y.; Salvador, P. A.; Rohrer, G. S. Controlling the Relative Areas of Photocathodic and Photoanodic Terraces on the SrTiO<sub>3</sub>(111) Surface. *Chem. Mater.* **2016**, *28* (14), 5155–5162. <https://doi.org/10.1021/acs.chemmater.6b02205>.
- (16) Zhu, Y.; Salvador, P. A.; Rohrer, G. S. Controlling the Termination and Photochemical Reactivity of the SrTiO<sub>3</sub>(110) Surface. *Phys. Chem. Chem. Phys.* **2017**, *19* (11), 7910–7918. <https://doi.org/10.1039/C6CP08608J>.
- (17) Huang, M. H. Facet-Dependent Optical Properties of Semiconductor Nanocrystals. *Small* **2019**, *15* (7), 1804726. <https://doi.org/10.1002/sml.201804726>.
- (18) Li, R.; Zhang, F.; Wang, D.; Yang, J.; Li, M.; Zhu, J.; Zhou, X.; Han, H.; Li, C. Spatial Separation of Photogenerated Electrons and Holes among {010} and {110} Crystal Facets of BiVO<sub>4</sub>. *Nat. Commun.* **2013**, *4*. <https://doi.org/10.1038/ncomms2401>.
- (19) Bruyer, E.; Sayede, A. Density Functional Calculations of the Structural, Electronic, and Ferroelectric Properties of High-k Titanate Re<sub>2</sub>Ti<sub>2</sub>O<sub>7</sub> (Re=La and Nd). *J. Appl. Phys.* **2010**, *108* (5), 53705. <https://doi.org/10.1063/1.3459891>.
- (20) Giocondi, J. L.; Salvador, P. A.; Rohrer, G. S. The Origin of Photochemical Anisotropy in SrTiO<sub>3</sub>. *Top. Catal.* **2007**, *44* (4), 529–533. <https://doi.org/10.1007/s11244-006-0101-y>.
- (21) Mu, L.; Zhao, Y.; Li, A.; Wang, S.; Wang, Z.; Yang, J.; Wang, Y.; Liu, T.; Chen, R.; Zhu, J.; et al. Enhancing Charge Separation on High Symmetry SrTiO<sub>3</sub> Exposed with Anisotropic

- Facets for Photocatalytic Water Splitting. *Energy Environ. Sci.* **2016**, *9* (7), 2463–2469. <https://doi.org/10.1039/C6EE00526H>.
- (22) Zhao, Z.; Goncalves, R. V.; Barman, S. K.; Willard, E. J.; Byle, E.; Perry, R.; Wu, Z.; Huda, M. N.; Moulé, A. J.; Osterloh, F. E. Electronic Structure Basis for Enhanced Overall Water Splitting Photocatalysis with Aluminum Doped SrTiO<sub>3</sub> in Natural Sunlight. *Energy Environ. Sci.* **2019**, *12* (4), 1385–1395. <https://doi.org/10.1039/C9EE00310J>.
- (23) Yamamoto, J. K.; Bhalla, A. S. Piezoelectric Properties of Layered Perovskite A<sub>2</sub>Ti<sub>2</sub>O<sub>7</sub> (A=La and Nd) Single-crystal Fibers. *J. Appl. Phys.* **1991**, *70* (8), 4469–4471. <https://doi.org/10.1063/1.349078>.
- (24) Teague, J. R.; Gerson, R.; James, W. J. Dielectric Hysteresis in Single Crystal BiFeO<sub>3</sub>. *Solid State Commun.* **1970**, *8* (13), 1073–1074.
- (25) Schultz, A. M.; Zhang, Y.; Salvador, P. A.; Rohrer, G. S. Effect of Crystal and Domain Orientation on the Visible-Light Photochemical Reduction of Ag on BiFeO<sub>3</sub>. *ACS Appl. Mater. Interfaces* **2011**, *3* (5), 1562–1567. <https://doi.org/10.1021/am200127c>.
- (26) Mu, L.; Zhao, Y.; Li, A.; Wang, S.; Wang, Z.; Yang, J.; Wang, Y.; Liu, T.; Chen, R.; Zhu, J.; et al. Enhancing Charge Separation on High Symmetry SrTiO<sub>3</sub> Exposed with Anisotropic Facets for Photocatalytic Water Splitting. *Energy Environ. Sci.* **2016**, *9* (7), 2463–2469. <https://doi.org/10.1039/c6ee00526h>.
- (27) Pisat, A. S.; Salvador, P. A.; Rohrer, G. S. The Facet Structure and Photochemical Reactivity of Arbitrarily Oriented Strontium Titanate Surfaces. *Adv. Mater. Interfaces* **2019**, *6* (16), 1900731. <https://doi.org/10.1002/admi.201900731>.
- (28) Dong, L.; Shi, H.; Cheng, K.; Wang, Q.; Weng, W.; Han, W. Shape-Controlled Growth of SrTiO<sub>3</sub> Polyhedral Submicro/Nanocrystals. *Nano Res.* **2014**, *7* (9), 1311–1318. <https://doi.org/10.1007/s12274-014-0495-y>.
- (29) Lyu, H.; Hisatomi, T.; Goto, Y.; Yoshida, M.; Higashi, T.; Katayama, M.; Takata, T.; Minegishi, T.; Nishiyama, H.; Yamada, T.; et al. An Al-Doped SrTiO<sub>3</sub> Photocatalyst Maintaining Sunlight-Driven Overall Water Splitting Activity for over 1000 h of Constant

- Illumination. *Chem. Sci.* **2019**, *10* (11), 3196–3201. <https://doi.org/10.1039/C8SC05757E>.
- (30) Ham, Y.; Hisatomi, T.; Goto, Y.; Moriya, Y.; Sakata, Y.; Yamakata, A.; Kubota, J.; Domen, K. Flux-Mediated Doping of SrTiO<sub>3</sub> Photocatalysts for Efficient Overall Water Splitting. *J. Mater. Chem. A* **2016**, *4* (8), 3027–3033. <https://doi.org/10.1039/C5TA04843E>.
- (31) Chiang, T. H.; Lyu, H.; Hisatomi, T.; Goto, Y.; Takata, T.; Katayama, M.; Minegishi, T.; Domen, K. Efficient Photocatalytic Water Splitting Using Al-Doped SrTiO<sub>3</sub> Coloaded with Molybdenum Oxide and Rhodium–Chromium Oxide. *ACS Catal.* **2018**, *8* (4), 2782–2788. <https://doi.org/10.1021/acscatal.7b04264>.
- (32) Shi, T.; Chen, Y.; Guo, X. Defect Chemistry of Alkaline Earth Metal (Sr/Ba) Titanates. *Prog. Mater. Sci.* **2016**, *80*, 77–132. <https://doi.org/10.1016/j.pmatsci.2015.10.002>.
- (33) Yamakata, A.; Yeilin, H.; Kawaguchi, M.; Hisatomi, T.; Kubota, J.; Sakata, Y.; Domen, K. Morphology-Sensitive Trapping States of Photogenerated Charge Carriers on SrTiO<sub>3</sub> Particles Studied by Time-Resolved Visible to Mid-IR Absorption Spectroscopy: The Effects of Molten Salt Flux Treatments. *J. Photochem. Photobiol. A Chem.* **2015**, *313*, 168–175. <https://doi.org/10.1016/j.jphotochem.2015.05.016>.

## Chapter 2: Background

Water splitting is a process that can produce hydrogen by directly decomposing water under illumination. Since the first report on a  $\text{TiO}_2$  electrode by Fujishima and Honda in 1972,<sup>1</sup> extensive research has been carried out to achieve water splitting with a great number of photocatalyst materials. In this chapter, an overview of fundamental principles of water splitting will be provided. Next, a brief explanation of why commercial application of water splitting is restricted is discussed. Finally, I will introduce how to improve the photocatalyst performance by modifying the space charge region, including surface orientation effect, ferroelectric polarization effect, solution effect and doping effect.

### 2.1 Semiconductor based photocatalysis

#### 2.1.1 Fundamental principles of semiconductor photocatalysis

The photocatalytic properties of semiconductor photocatalysts depend on the surface properties and electronic band structure. In a typical reaction, there are three major steps: (1) a semiconductor absorbs a photon of energy higher than its band gap ( $E > E_{Bg}$ ) to excite an electron from the valance band to the conduction band, leaving a positively charged hole in the valance band; (2) electron hole pairs are separated and migrate to the semiconductor surface; (3) electrons and holes are trapped with species in solutions and drive reactions.

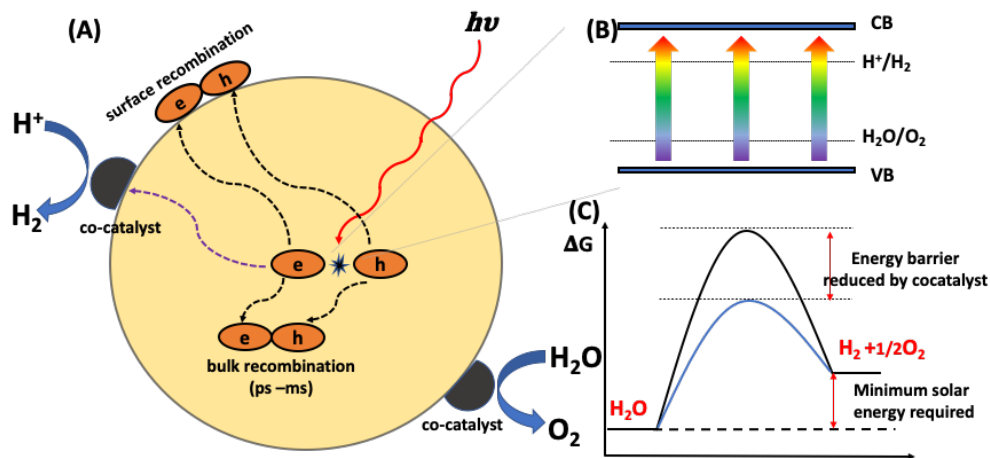
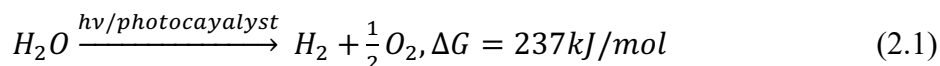


**Figure 2-1:** Schematic photoexcitation in a solid followed by deexcitation events are presented in panel (A) and (B), modified from ref.<sup>2</sup> Panel (C) presents the energy barrier of an overall water splitting reaction.

In overall water splitting, H<sub>2</sub> and O<sub>2</sub> are produced in a stoichiometric ratio 2:1. From the perspective of thermodynamics, the overall water splitting is classified as an “up-hill” reaction, as illustrated in Figure 2.1 (C), with a large positive change in Gibbs free energy ( $\Delta G^0 = +237 \text{ kJ/mol}$ , 2.46 eV per molecule).



For overall photocatalytic water splitting to occur, the bottom of semiconductor conduction band must exceed the proton reduction potential (0.0 V vs. NHE at pH 0), the top of valance band must exceed the oxidation potential of water (1.23 V vs. NHE at pH 0). Hence, the minimum band gap for overall water splitting is ~1.23 eV. With the assistance of scavengers, semiconductors that are unsuitable for overall splitting can produce either H<sub>2</sub> or O<sub>2</sub>, as illustrated in Figure 2-2. For the proton reduction half reaction, CH<sub>3</sub>OH, SO<sub>3</sub><sup>2-</sup>, EDTA<sup>4-</sup> can be used as hole scavenger. For the water oxidation half reaction, Ag<sup>+</sup>, Fe<sup>3+</sup> and IO<sub>3</sub><sup>-</sup> can be used as electron scavengers.

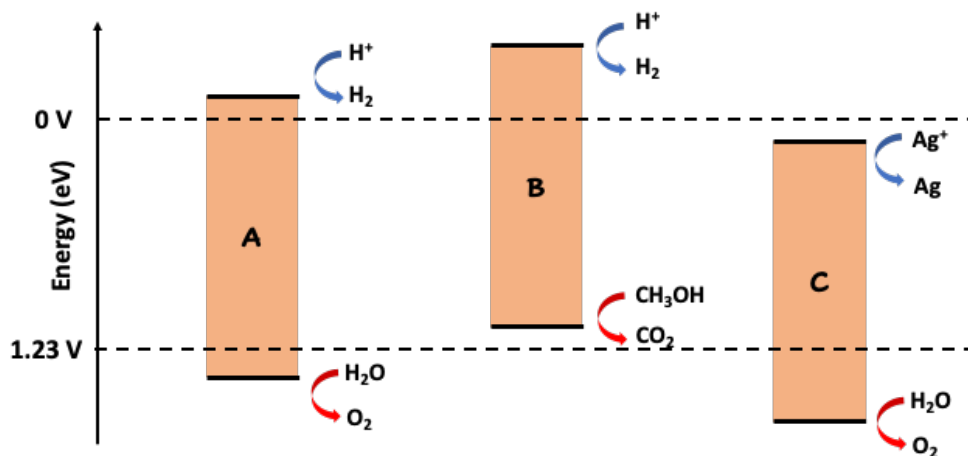


**Figure 2-2:** Scheme of photocatalytic (A) overall water splitting; (B) proton reduction half reactions with CH<sub>3</sub>OH as sacrificial reagent; (C) water oxidation half reaction with Ag<sup>+</sup> as sacrificial reagent.

The chemical reduction and oxidation reactions for overall water splitting are listed in Eq. (2.2) and (2.3), respectively:



The chemical reduction and oxidation reactions for the proton reduction half reaction with  $\text{CH}_3\text{OH}$  as a hole scavenger are listed in Eq. (2.4) and (2.5), respectively:



The chemical reduction and oxidation reactions for the water oxidation half reaction with  $\text{Ag}^+$  as an electron scavenger are listed in Eq. (2.6) and (2.7), respectively:



### 2.1.2 Types of photocatalysis

Apart from water splitting, photocatalysis is widely applied in green chemistry and organic synthesis. Actually, photocatalysis might refer to any reaction that requires the simultaneous presence of a catalyst and light. In this section, selected applications will be briefly introduced, and representative research works will be provided.

#### *photocatalytic degradation of organic pollutants*

With the speeding up of human industry, large amounts of toxic organic pollutants have been discharged into nature, leading to a negative consequence in the lives of humans. Semiconductor based photocatalysis appears to be a promising way to remove these pollutants. Benefits of semiconductor catalysts include non-toxic, low cost, easy to recycle. The process of organic degradation is similar to water splitting. Under suitable illumination, electrons and holes migrate to the semiconductor surface and participate in the reduction-oxidation reactions. It is found that radical intermediates always participate in organic degradation. For instance, an  $\text{O}_2$  molecule can scavenge an electron forming a superoxide radical ( $\cdot\text{O}_2^-$ ). Next, this superoxide radical reacts with a proton forming a hydroperoxide radical ( $\cdot\text{HO}_2$ ).<sup>3</sup> The hydroperoxide radical has a redox potential of +2.27 V vs. SHE at pH 7, which is enough to oxidize most organic compounds.<sup>4</sup>

### *photocatalytic CO<sub>2</sub> reduction*

As a greenhouse gas, excessive CO<sub>2</sub> emission has dramatically changed our environment. The International Panel on Climate Change predicted that the global temperature will rise 1.9 °C in mean value if CO<sub>2</sub> rises to 590 ppm by 2100.<sup>5</sup> Among many technologies mitigating CO<sub>2</sub> emissions, photocatalytic CO<sub>2</sub> reduction is preferred for its convenience and relatively low cost. A highly efficient photocatalytic CO<sub>2</sub> reduction method has been reported by Kuang et al. with CsPbBr<sub>3</sub> perovskite quantum dot /graphene oxide composite catalyzing CO<sub>2</sub> reduction at a rate of 23.7 μmol g<sup>-1</sup>h<sup>-1</sup> with a selectivity over 99.3%.<sup>6</sup>

CO<sub>2</sub> is a very stable molecule, and its reduction needs to overcome a huge energy barrier. In general, for a typical CO<sub>2</sub> reduction, the molecule is first activated by adsorption into electron rich oxygen vacancy defect sites or gain electrons from a semiconductor directly,<sup>7,8</sup> and then, transferred into reactive CO<sub>2</sub><sup>δ-</sup>. This intermediate can further get converted into CO, CH<sub>4</sub>, CH<sub>2</sub>O, CH<sub>3</sub>OH. For instance, one could convert CO<sub>2</sub> and H<sub>2</sub>O into CH<sub>4</sub> and O<sub>2</sub> under illumination. This is usually defined as photocatalytic CO<sub>2</sub> methanation:



As the main constituent of natural gas, CH<sub>4</sub> is a widely used fuel for heating and electricity generating. Since the natural gas we are using now is fossil-based, photocatalytic CO<sub>2</sub> methanation provides us with a method to synthesize natural gas. CO<sub>2</sub> methanation might be helpful to reduce the emission of CO<sub>2</sub> to lighten greenhouse effect. Meanwhile, the high abundance and relatively low cost of raw material, CO<sub>2</sub> and H<sub>2</sub>O, making this synthetic natural gas a significantly value-added product.<sup>8</sup>

### *Photocatalysis in synthesis*

Photocatalysis is a helpful tool in organic synthesis, too. The principle mode of action in photocatalysis is to induce an electron transfer to or from a substrate, thus generating anions, cations, or neutral radicals.<sup>9</sup> In organic synthesis, photocatalysis can be roughly divided into photoreduction and photooxidation, depending on the specific reactions. In the traditional way, bringing a stable organic molecule such as an alkane to an oxidized state needs strong oxidizing

agent and drastic reaction conditions. Photocatalysis is able to activate the reagent under mild conditions, allowing a better control of the intermediates generated.<sup>10</sup>

### 2.1.3 Roles of cocatalysts

In photocatalytic water splitting, semiconductor photocatalysts are always loaded with specific cocatalysts. In most of the cases, those cocatalysts are necessary if one would like a satisfactory overall water splitting performance. They serve as reaction sites and accelerate the reactions, promote the separation of photogenerated charge<sup>11</sup> and decrease the activation energy.<sup>12</sup>

Cocatalysts are usually loaded for the two half reactions separately. For the H<sub>2</sub> evolution half reaction, noble metals, like Pt, are selected as cocatalysts. Firstly, since noble metals usually have larger work functions than semiconductors, they are able to trap electrons from the semiconductor. Pt has the largest work functions among noble metals, so that it is regarded as the most suitable H<sub>2</sub> evolution cocatalyst. Secondly, noble metals have good stability and are less likely degraded in water. Thirdly, Trasatti et al.<sup>13</sup> found a volcano relationship between the exchange current for H<sub>2</sub> evolution and the metal-hydrogen bond strength during electrochemical reaction (see Figure 2-3). Pt is at the top of the volcano, which means it needs the lowest activation energy to catalyze the reaction. Representative works employing Pt as cocatalysts are TiO<sub>2</sub>,<sup>14,15</sup> PbTiO<sub>3</sub>,<sup>16</sup> La<sub>2</sub>TiO<sub>2</sub>N,<sup>17</sup> CdS.<sup>18</sup> Apart from Pt, people sometimes select Rh, Au or Ir as H<sub>2</sub> evolution cocatalysts as well.

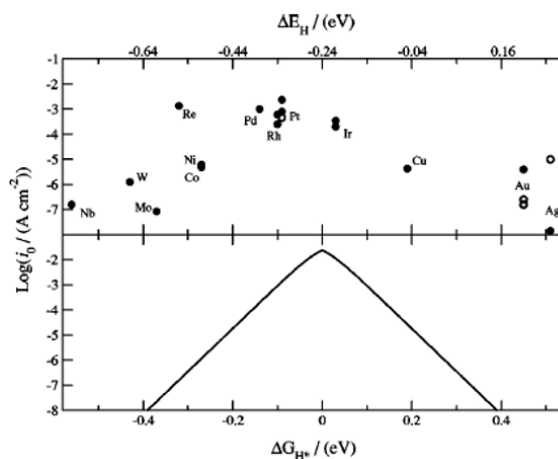


**Figure 2-3:** Experimentally measured exchange current for hydrogen evolution over different metal surfaces plotted as a function of the calculated hydrogen chemisorption energy per atom. Taken from ref.<sup>19</sup>

For the O<sub>2</sub> evolution half reactions, cocatalysts are also crucial. Since the two half reactions must proceed at the same rate to maintain charge neutrality, the overall reaction rate is limited by the slower one, usually the water oxidation. The corresponding materials should have low work functions that can trap holes. And those O<sub>2</sub> evolution cocatalysts are always metal oxides, such as CoO<sub>x</sub>,<sup>12</sup> NiO,<sup>20</sup> RuO<sub>2</sub>.<sup>21</sup> Past research has shown that loading both cocatalysts for reduction and oxidation has better performance than loading only one cocatalyst. However, in most catalyst systems, reduction cocatalysts are necessary even if people believe that the photo oxidation is the rate limiting half reaction. Loading only reduction cocatalysts or both cocatalysts promote the reactivity. But loading only oxidation cocatalysts is not always useful.

To load cocatalysts on semiconductors, there are two main approaches. The first approach is the impregnation method, where the cocatalysts are uniformly deposited on photocatalyst particle. As a result, the two half reactions may occur at the same location. The second approach is photo deposition, if different surface orientations have different work functions, then the cocatalysts might deposit at different locations. Hence, photo reduction and photo oxidation may occur on different locations on the surface of photocatalyst, which is beneficial to the separation of charge.

#### **2.1.4 Factors limiting the efficiency of photocatalysis and how to overcome them**

Works on photocatalytic water splitting revolve around efficiency. If one can develop a catalyst with a satisfactory efficiency, the commercial application of water splitting will become reality. A widely used efficiency is quantum efficiency, defining the number of electrons participating in reactions relative to the number of photons incident to the system. The number of reacted electrons equals twice the number of evolved H<sub>2</sub> molecules or four times the number of evolved O<sub>2</sub> molecules. And the number of incident photons could be measured by a photodiode.<sup>22</sup>

Hence, the external quantum efficiency (EQE) is defined as:

$$\begin{aligned}
 EQE (\%) &= \frac{\# \text{ of reacted electrons}}{\# \text{ of incident photons}} \times 100\% \\
 &= \frac{2 \times \# \text{ of evolved H}_2 \text{ molecules}}{\# \text{ of incident photons}} \times 100\% \quad (2.9)
 \end{aligned}$$

The internal quantum efficiency (IQE) is slightly different from EQE in that it specifies the number of electrons participating in reactions relative to the number of photons absorbed in the system. The equation is defined as:

$$\begin{aligned}
 IQE (\%) &= \frac{\# \text{ of reacted electrons}}{\# \text{ of absorbed photons}} \times 100\% \\
 &= \frac{2 \times \# \text{ of evolved } H_2 \text{ molecules}}{\# \text{ of absorbed photons}} \times 100\%
 \end{aligned}
 \tag{2.10}$$

Obviously, IQE is always higher than EQE. Since it is hard to determine how many photons have been absorbed, the external quantum efficiency is commonly used. Another standard efficiency is solar-to-hydrogen (STH) efficiency, which is convenient to determine the performance of a photocatalyst:

$$STH = \frac{\text{energy of evolved } H_2}{\text{energy of incident photons}} = \frac{r_{H_2} \times \Delta G}{P_{sun} \times S} \times 100\%
 \tag{2.11}$$

$r_{H_2}$  corresponds to the rate of hydrogen generation (mmol/s),  $\Delta G$  corresponds to the Gibbs free energy (J/mol) of the water splitting reaction,  $P_{sun}$  corresponds to the light energy flux (mW/cm<sup>2</sup>), and S is the irradiation area (cm<sup>2</sup>).

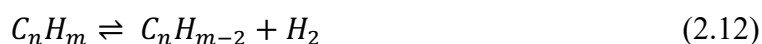
Recall that earlier, the three major steps of photocatalytic water splitting are: light absorption, photogenerated charge generation, separation and migration, surface reaction. The two factors that limit the efficiency of water splitting the most are the recombination of electron-hole pairs and back reactions on surface, as shown in Figure 2-1. Improving the charge separation efficiency has been a critical topic in photocatalytic water splitting for a long time. Many strategies are available to increase the charge separation. Decreasing the particle size could decrease the migration distance so that charge carriers are more likely to reach surface.<sup>23</sup> Developing a highly crystalline catalyst is another approach because defects in the bulk/surface usually serve as recombination centers. Removing these centers will help suppress the rate of charge recombination. Moreover, building internal/external electric fields in the space charge region for separating electrons and holes is also a popular method and this is also the main point of my research.<sup>24</sup> More details of this method will be discussed later.

## 2.1.5 Molecular Photocatalysts

Photocatalytic hydrogen production can also be carried out using homogeneous molecular catalysts. Although its mechanism is quite different from semiconductor-based catalysts, it is still worth a discussion since it could help us understand the reaction sites. The molecules employed here are usually complexes with a transition metal cation coordination center that can store solar energy with their excited states, accompanied by protonation and dehydrogenation cycles with the assistance of certain substrates.<sup>25-27</sup> In this section, a few represented catalyst mechanisms will be discussed:

### *Alkane dehydrogenation*

Alkane dehydrogenation can be expressed in the following equation:



Photocatalytic alkane dehydrogenation has been reported using Ir, Rh, and Pt complexes, and the driving force of the reaction can be supplied by a photon. Herein, I use  $Rh^I(PR_3)_2(CO)Cl$  ( $R = Me, Et, Ph$ ) as an example,<sup>28</sup> as illustrated in Figure 2-4(a): Activated by the photons, the CO dissociates and the  $Rh^I(PR_3)_2Cl$  intermediate forms. This intermediate forms C-H bonds by adding cyclohexane as a substrate and generates a dihydrido alkane complex via  $\beta$ -hydride elimination. After the alkene dissociation and CO coordination, it will regenerate the starting complex by emitting a hydrogen molecule.<sup>29</sup> Photocatalytic dehydrogenation can also occur in other substrates, such as the dehydrogenation of alcohols to ketones or aldehydes.

### *Hydrogen production from acidic solutions*

Inorganic acids usually have a much lower energy compared with alkane substrates, so it usually needs higher energy photons to activate the reactions. For example,  $Ir^{III}Cl_6^{3-}$  can produce  $H_2$  and  $Cl_2$  in a stoichiometric ratio in HCl solutions under 254 nm UV light. The proposed mechanism is given in Figure 2-4(b). The radiation will convert  $HIr^{III}Cl_6^{2-}$  to its excited state  $[HIr^{III}Cl_6^{2-}]^*$ , and then it decomposes into  $Ir^{IV}Cl_6^{2-}$  and a H radical. This resulted H radical might react with a another  $HIr^{III}Cl_6^{2-}$  to form  $Ir^{IV}Cl_6^{2-}$  and a  $H_2$  molecule. Meanwhile, the irradiation can excite  $Ir^{IV}Cl_6^{2-}$  to  $[Ir^{IV}Cl_6^{2-}]^*$ , then reduced by a  $Cl^-$  anion forming  $Ir^{III}Cl_6^{3-}$  and a Cl radical. Two Cl radicals can

form a  $\text{Cl}_2$  molecule and revert  $\text{Ir}^{\text{III}}\text{Cl}_6^{3-}$  to  $\text{Ir}^{\text{IV}}\text{Cl}_6^{2-}$ . Similar catalytic reactions can also occur be conducted using  $\text{Pt}^{2+}$ ,<sup>30</sup>  $\text{Eu}^{2+}$ ,<sup>31</sup>  $\text{Fe}^{2+}$ ,<sup>32</sup> etc.

### Three component systems

This scheme consists of three parts: a photosensitizer that can absorb photons, a mediator that can be reversibly reduced by electrons, and a catalyst that can reduce protons to hydrogen. So, we may see that this is pretty similar to the Z-scheme semiconductor heterojunction catalysts. Here I talk about  $\text{Ru}^{\text{II}}(\text{bpy})_3^{2+}$ , a common photosensitizer, which is also the material we used in the normalization calibration of our photoreactor (see Appendix 4). Induced by a photon,  $\text{Ru}^{\text{II}}(\text{bpy})_3^{2+}$  goes to the excited state  $\text{Ru}^{\text{II}}(\text{bpy})_3^{2+*}$  and then forms  $\text{Ru}^{\text{III}}(\text{bpy})_3^{3+}$  by transferring electron to the mediator. This electron will then transfer to the catalyst, like colloidal Pt, and reduce protons to hydrogen.  $\text{Ru}^{\text{III}}(\text{bpy})_3^{3+}$  will be reduced to the ground state  $\text{Ru}^{\text{II}}(\text{bpy})_3^{2+}$  by a sacrificial donor. A schematic of the reaction is given in Figure 2-4(c).

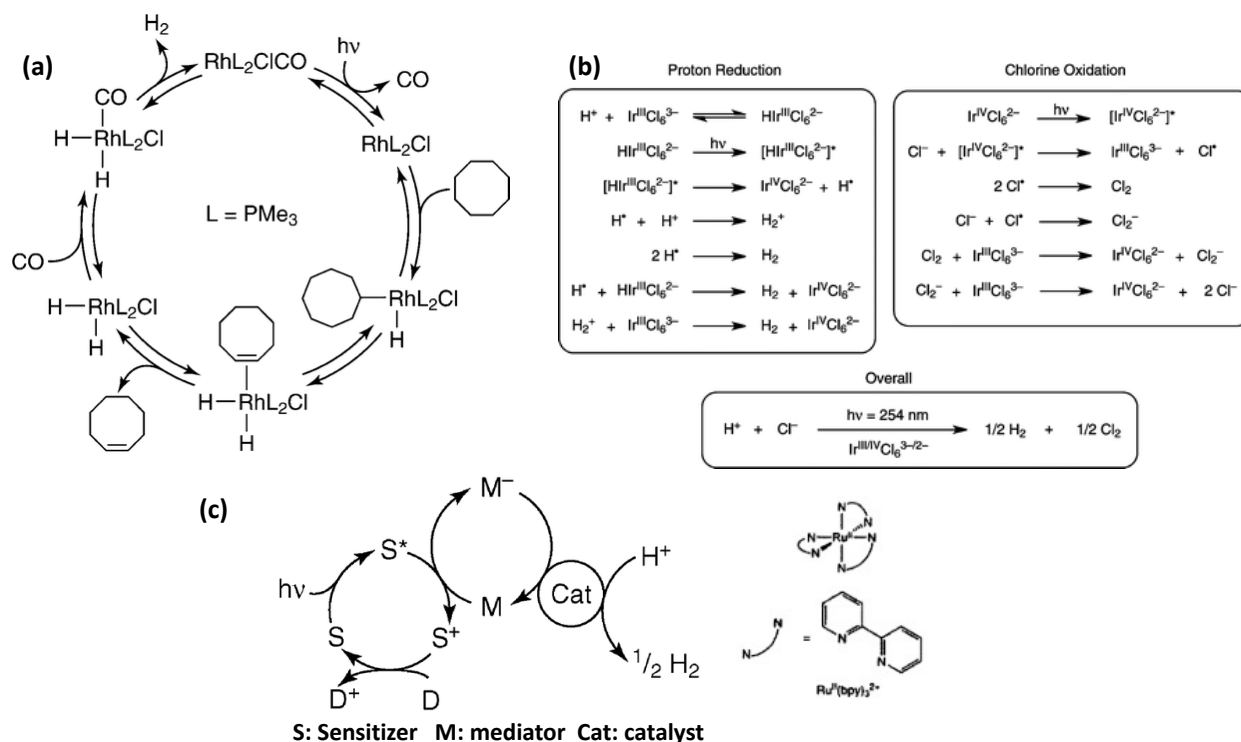


**Figure 2-4:** (a) Proposed mechanism for the photocatalytic cyclooctane dehydrogenation using  $\text{Rh}^{\text{I}}(\text{PMe}_3)_2(\text{CO})\text{Cl}$ . (b) Proposed reactions involved in the photocatalytic production of  $\text{H}_2$  from aqueous  $\text{HCl}$  solutions using  $\text{Ir}^{\text{III}}\text{Cl}_6^{3-}$ . (c) A schematic of three component systems. Adapted from ref.<sup>26</sup>

## 2.2 Space charge engineering

### 2.2.1 Metal-Semiconductor Interface

Materials generally have different work functions, which is defined as the energy difference between the vacuum level and the Fermi energy and denoted as  $\phi$ . When a metal and a semiconductor contact with each other, electrons will flow from the low work function side to the high work function side. For an n-type semiconductor, if the Fermi level of the semiconductor is higher than the Fermi level of the metal, electrons will flow from the semiconductor to the metal until the two Fermi levels are aligned. This is shown in Figure 2-5 (left). At equilibrium, the metal side will be negatively charged while the semiconductor is positively charged. This causes the free charge carrier concentration near the semiconductor surface (space charge region) to be lower than in the bulk, and this named a depletion layer. Here, the energy band edges will also shift due to the electric field at the interface region between the metal and the semiconductor. When  $\phi_m > \phi_s$ , the energy band bends upwards as electrons in semiconductors are repulsed by the negatively charged Helmholtz layer located in the metal. When  $\phi_m < \phi_s$ , electrons will flow from the metal to the semiconductor, leading to an accumulation layer at the surface of semiconductor. Now, the semiconductor energy bands bend downwards as electrons in semiconductors are attracted by the positively charged Helmholtz layer in the metal, shown in Figure 2-5 (right).

The degree of band bending is equal to the work function difference between metal and semiconductor:

$$V_{BB} = |\phi_m - \phi_s| \quad (2.13)$$

When  $\phi_m > \phi_s$ , there will be a Schottky barrier forming at the interface, defined as:

$$\phi_{BB} = (\phi_m - \chi_s) \quad (2.14)$$

$\chi_s$  is the electron affinity of semiconductor. If  $\phi_m < \phi_s$ , there will be no Schottky barrier formed but an ohmic contact.

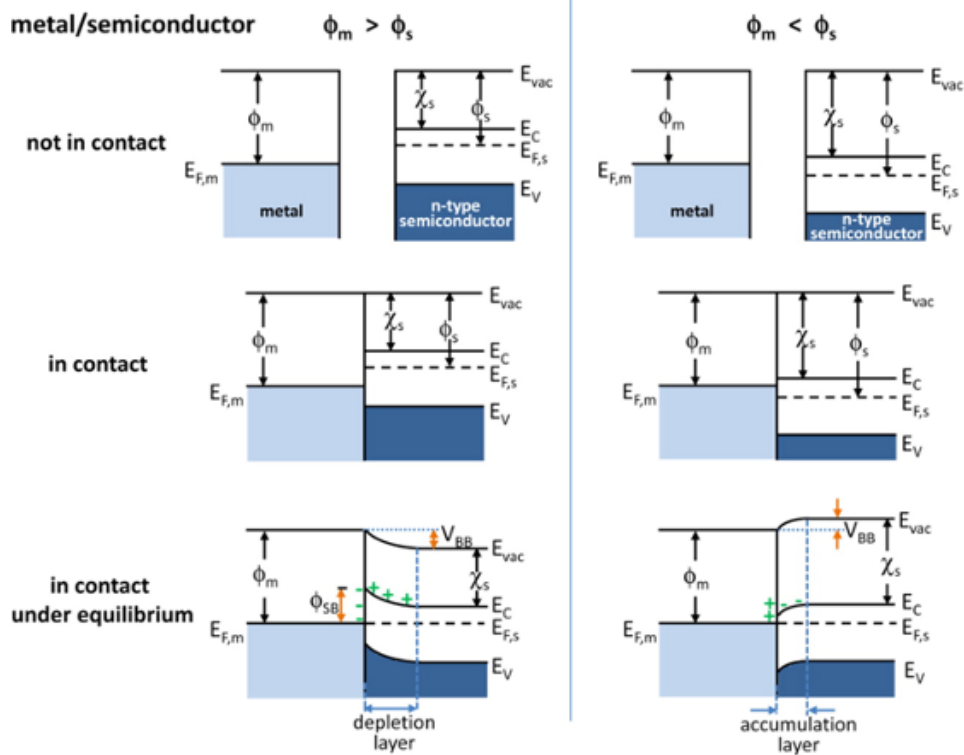


**Figure 2-5:** Energy band diagrams of metal and n-type semiconductor contact, reproduced from ref.<sup>33</sup>  $E_c$  and  $E_v$  correspond to energy of conduction band and valance band edges.  $\phi_m$  and  $\phi_s$  correspond to work functions of metal and semiconductor.  $E_{vac}$ , vacuum energy.  $\chi_s$ , electron affinity of the semiconductor.

## 2.2.2 Space charge region

Space charge regions result from field inhomogeneities. When a bulk semiconductor is in contact with another semiconductor, metal, or electrolyte, a space charge region will form at the interface to equalize the Fermi levels.<sup>34,35</sup> Here, charge carriers flow from high carrier density region to low carrier density region, leaving uncompensated donors and acceptors forming a series of electric dipoles. The potential created by these dipoles finally gives rise to band bending.

Figure 2-6 illustrates three kinds of space charge regions for a n-type semiconductor. The first column corresponds to the flat band condition where no space charge region exists. For downward band bending, negative charges accumulate at the surface of the semiconductor due to the attraction of outside positive charges, forming an accumulation layer. For upward band bending, positive charges accumulate at the surface, causing the decrease of electron concentration, forming a depletion layer. There is a possibility that if the degree of upward band bending is large enough,

as shown in the fourth column of Figure 2-6, the hole concentration becomes larger than the electron concentration, converting the semiconductor from n-type to p-type at surface. In this case, the space charge region is called an inversion layer.

Most reactions will occur on semiconductor surface and the band structure in the space charge region will have a strong influence on the reaction rate. Therefore, space charge engineering is a promising approach to improve the efficiency of photocatalysis.

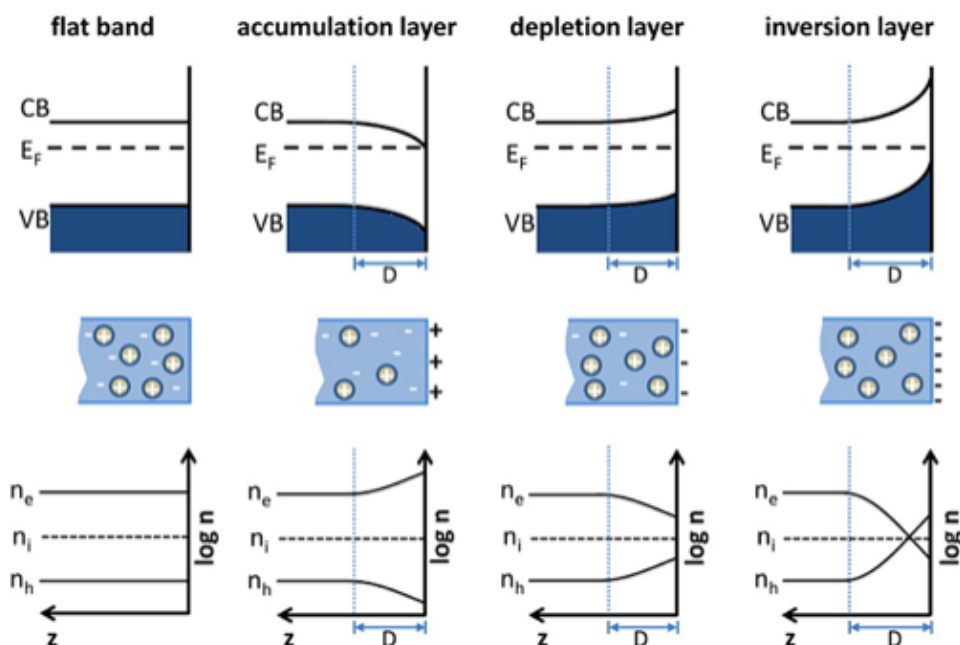


**Figure 2-6:** Schematic diagrams showing the energy levels and free charge densities for a n-type semiconductor. The blue dotted line labeled the space charge region with a thickness of  $D$ .  $n_i$  = intrinsic carrier density;  $n_e$  = electron density;  $n_h$  = hole density. Reproduced from reference.<sup>33</sup>

### 2.2.3 How is band bending induced?

The band bending concept was originated by Schottky and Mott to explain the properties of metal-semiconductor interfaces.<sup>36-39</sup> Apart from what we have discussed in 2.2.2, band bending could be induced by many other factors. For instance, an external field can induce band bending near the semiconductor surface.<sup>40</sup> In an ideal system where a semiconductor and a metal contact with each other, we assume that they have the same work function and no charge carriers flow. Adding a voltage will break this balance. By adding a positive voltage ( $V > 0$ ), the electric field will cause electrons to accumulate near the surface and bend the bands downward. On the contrary, adding a negative voltage ( $V < 0$ ) will bend the band upward.

Band bending could be induced by surface states as well.<sup>41</sup> Surface states form as a result of the broken lattice symmetry at the surface. Composed of unpaired electrons in dangling bonds, surface states usually have a different Fermi level compared with the bulk. These states act as either donors (dangling electrons being excited to the conduction band) or acceptors (electrons being captured to pair with electrons in dangling bonds).<sup>42</sup> Hence, charge carriers will transfer between the bulk and the surface, causing band bending. A similar case is that transition metal oxides usually have partially occupied d-orbitals which could serve as donors or acceptors as well.<sup>43</sup> Moreover, the adsorption of molecules can induce band bending.<sup>44</sup> A molecule with unfilled molecular orbital may accept electrons from the semiconductor and lead an upward band bending. Some molecules may serve as donors and lead a downward band bending.

Solution pH can alter band bending by controlling surface charge on the semiconductor and this is a feasible tool to optimize the photocatalytic reactivity. Details about this effect will be discussed in section 2.5.

## **2.3 The effect of crystallographic orientation on photocatalytic reactivity**

### **2.3.1 The origin of the orientation effect**

The reactivity of a photocatalyst is influenced by its surface atomic structure and its linked electronic structure. Band gaps, band edges, surface potential, and electronic conductivity are likely to vary with crystallographic orientations. Thus, different surface orientations may have different photochemical reactivities.

Figure 2-7 explains how photogenerated charge carriers are separated to different orientations. Two orientations with different band edges are represented by the red and blue curves. Owing to different degrees of band bending, the blue band edges are higher than the red band edges, providing a driving force for the separation of electrons and holes. Electrons tend to move along the red band: on the contrary, holes move along the blue edges. Photo reduction and photo oxidation will occur on a red surface and a blue surface, respectively. Hence, the overall photochemical reactivity should be enhanced because of the inhibition of charge recombination and back reactions.

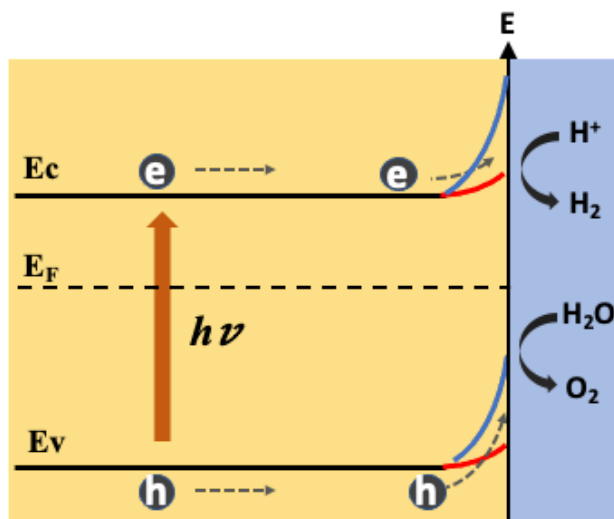


**Figure 2-7:** A band diagram with tunable band edge energies for two crystal surfaces (red and blue). Dashed arrows describe the motions of photogenerated electrons and holes.

### 2.3.2 Selected examples of orientation effect

Surface orientation has been reported to have a significant influence on the photochemical properties of  $Cu_2O$  nanoparticles. The electric conductivity has been measured on a  $\{100\}$ -bound cube, a  $\{110\}$ -bound rhombic dodecahedra and a  $\{111\}$ -bound octahedra with tungsten probes connected to a nanomanipulator.<sup>45,46</sup> From the I-V curves obtained, they found that a  $Cu_2O$  octahedron is highly conductive, a cube is moderately conductive, and a rhombic dodecahedron is non-conductive. It is proposed that the anisotropic electric conductivity comes from the different degrees of band bending in the three crystallographic orientations, as shown in Figure 2-8. The  $\{110\}$  face has the largest band bending so that it has the biggest energy barrier when in contact with W. The  $\{111\}$  face has the smallest band bending as well as the smallest resistivity. This is reasonable since electronic conductivity in a solid is proportional to density of free charge carriers. While employing these  $Cu_2O$  as photocatalysts for degradation of methyl orange, the rhombic dodecahedra are highly active, the cubes are moderately active and the octahedra are less,<sup>47,48</sup> which indicates the power of the orientation effects on photocatalysis. The large degree of band bending in the  $\{110\}$  faces provides a driving force to separate photogenerated electron-hole pairs.

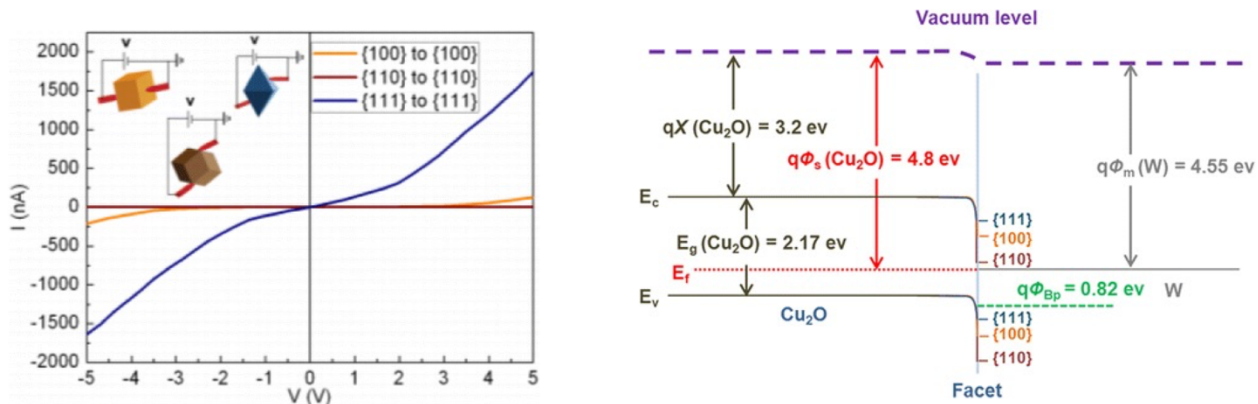


**Figure 2-8:** Left: I-V curves from the {100}, {110} and {111} facets of  $\text{Cu}_2\text{O}$  crystals. Right: Band structure of  $\text{Cu}_2\text{O}$  for different orientations. Reproduced from ref.<sup>49</sup>

Figure 2-9 presents a similar orientation effect observed on  $\alpha\text{-Fe}_2\text{O}_3$ .<sup>50</sup>  $\alpha\text{-Fe}_2\text{O}_3$  is a promising photocatalyst with a bandgap of 2.2 eV.<sup>51</sup> Ag marker reactions were carried out on polycrystalline  $\alpha\text{-Fe}_2\text{O}_3$  ceramic surface. They found that grains oriented within  $30^\circ$  of the  $(1\bar{1}02)$  plane were far more reactive than other orientations. Using KFM, the surface potential of highly reactive grains was determined to be more positive than other grains. Because the  $(1\bar{1}02)$  surface has the largest positive charge, it has greatest downward band bending and more effectively attracts electrons, leading to the highest photocathodic reactivity.

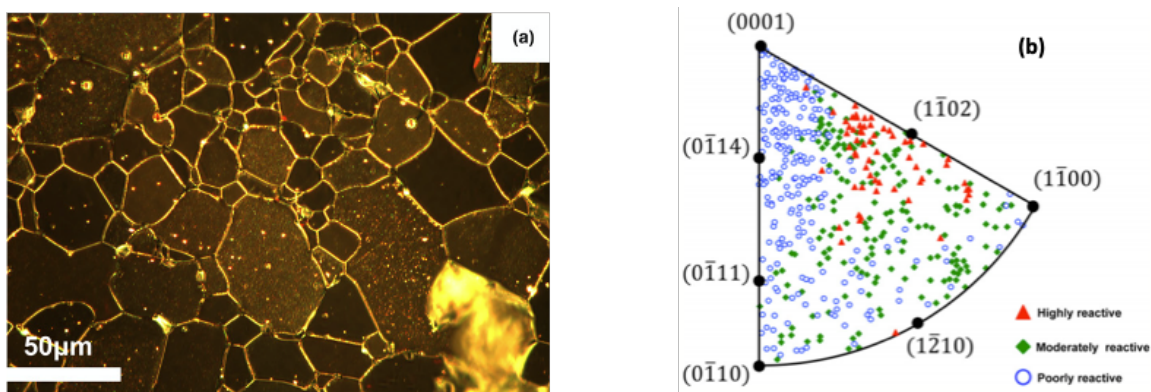


**Figure 2-9:** (a) Dark-field optical microscopy images of the  $\alpha\text{-Fe}_2\text{O}_3$  surface after the photochemical reduction of Ag. (b) Orientation dependent reactivity of 547 grains plotted on the standard stereographic triangle for a hexagonal crystal. Reproduced from ref.<sup>50</sup>

Another representative material is  $\text{BiVO}_4$ , which is a potential photocatalyst under visible light. Li et al. first discovered that the photo deposition of metal/metal oxides are facet selective on monoclinic  $\text{BiVO}_4$  particles.<sup>52,53</sup> The {100} facets are photo reductive while {110} facets are photo

oxidative. The author indicates that the different energy levels of the two orientations contributes to this spatial selectivity. More examples on the orientation effect are presented in Appendix 1.

### 2.3.3 Orientation dependence of photochemical reactivity on SrTiO<sub>3</sub>

The photochemical activity of SrTiO<sub>3</sub> has been studied thoroughly and the orientation dependence has been observed on different kinds of SrTiO<sub>3</sub> crystals. In 2003, Giocondi et al. photochemically reduced silver cations from an aqueous solution on a SrTiO<sub>3</sub> polycrystal with surfaces bounded by {110}, {111} and {100} planes.<sup>54</sup> After reaction, all highly reactive grains contained a facet inclined by about 20° from {100}. Thus, they concluded that SrTiO<sub>3</sub> surfaces near {100} have the highest relative photocathodic reactivity. In 2007, Giocondi et al. prepared faceted SrTiO<sub>3</sub> microcrystals and carried out photochemical reactions to deposit insoluble products on the surface to study the anisotropic reactivity of SrTiO<sub>3</sub>.<sup>55</sup> It is found that silver products are formed preferentially on {100} surfaces after photochemical silver reductions. The electronic band structure was used to explain the results. Based on the diagram shown in Figure 2-10(a), the band is relatively flat in [100] direction (Γ to X) compared with band in [110] direction (Γ to M) and [111] direction (Γ to R). So, higher energy is needed to excite all states in [110] direction (about 5 eV) and [111] directions (about 6 eV). Therefore, electron hole pairs with momentum in the [100] direction could be excited by lower energy light, which contributes to the higher reactivity of the {100} surface. Another indication from the band structure is when {100} surface and {110} surfaces coexist, holes are likely to migrate to {110} surface while electrons migrate to {100} surface. This is because holes will migrate to the highest points in the valance band; one such point is the M position, at {110}. Besides band structure, surface termination and chemistry vary with orientations, contributing to this anisotropic reactivity. In 2019, Pisat et al. found the similar results between {110} and {100} facets within the same grain on ceramic surfaces.<sup>56</sup> A special treatment can tune SrTiO<sub>3</sub> polycrystals with arbitrary orientations show single crystal-like grains with a combination of {110} and {100} facets. After photochemical reactions, {100} facets appear to be uniformly photocathodic and serve as reduction sites; {110} facets appear to be photoanodic and serve as oxidation sites.

Knowing that {100} surfaces are photocathodic and {110} surfaces are photoanodic, it is possible to synthesize SrTiO<sub>3</sub> particulate catalysts bounded by the two facets, boosting the rate of charge

separation and overall photochemical reactivity. Dong et al. introduced a hydrothermal method to prepare shape-controlled SrTiO<sub>3</sub> polyhedral submicron crystals.<sup>57</sup> By using a series of surfactants, particle shape could be adjusted from isotropic facets (6-facet SrTiO<sub>3</sub>) to anisotropic facets (12-facet SrTiO<sub>3</sub>) with the percentage of {110} facets compared to {100} facets increasing. By means of this synthesis route, Li et al. and Huang et al. found that SrTiO<sub>3</sub> particles exposing both {100} and {110} facets show significant enhancement of photocatalytic reactivity than those only exposing {100} facets.<sup>58,59</sup> It is indicated that the good reactivity of anisotropic faceted SrTiO<sub>3</sub> is attributed to the charge separation between {100} facets and {110} facets. Recently, Domen et al. selectively photodeposited Rh/Cr<sub>2</sub>O<sub>3</sub> and CoOOH and {100} and {110} facets of Al doped SrTiO<sub>3</sub>, respectively, obtaining a quantum efficiency as high as 96% under illumination between 350 nm and 360 nm.<sup>60</sup>

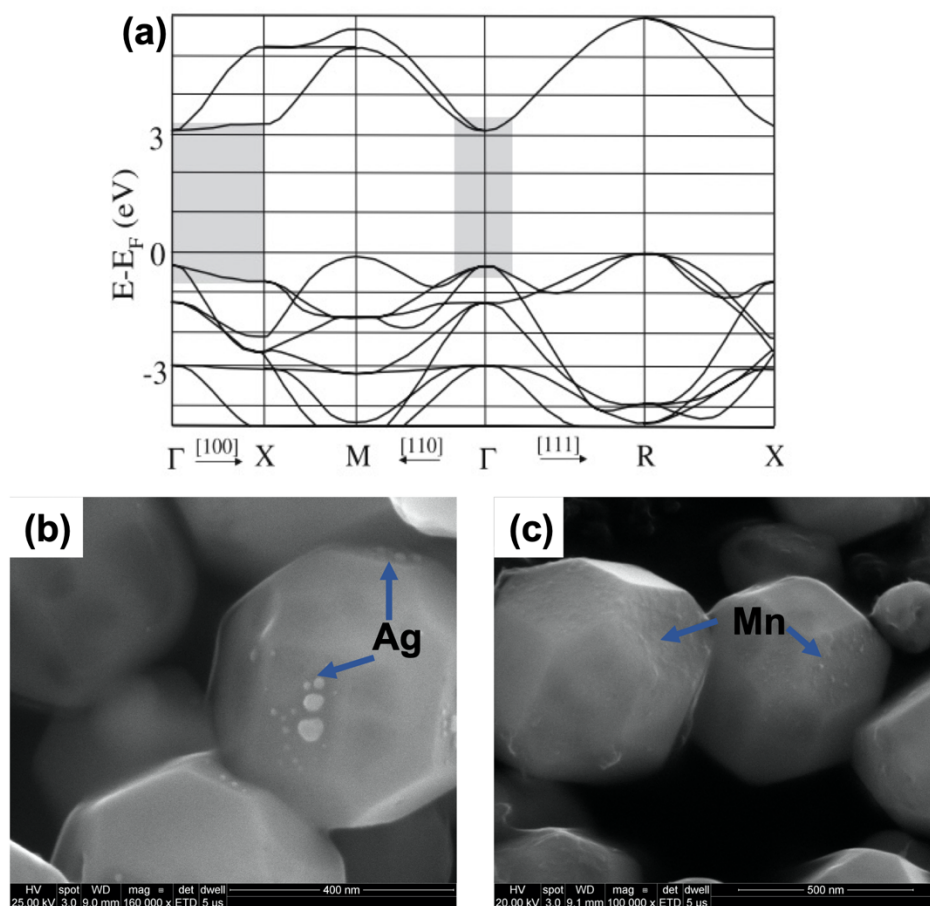


**Figure 2-10:** (a) Schematic representation of the structure of the bands closest to the Fermi level for SrTiO<sub>3</sub>, reproduced from ref.<sup>55</sup> (b) SEM image of photo deposition of Ag on faceted SrTiO<sub>3</sub> particles. (c) SEM image of photo deposition of MnO<sub>2</sub> on faceted SrTiO<sub>3</sub> particles.

## 2.4 The effect of ferroelectric domains on photocatalytic reactivity

### 2.4.1 What is ferroelectricity

Ferroelectricity is a subclass of pyroelectricity, and pyroelectricity is a subclass of piezoelectricity. The concepts and properties of piezoelectricity, pyroelectricity and ferroelectricity are related to crystal structures. There are 32 classes of crystals (crystallographic point group) in total. Among them, 11 crystal classes are centrosymmetric, nonpolar and exhibiting no piezoelectric effect. The other 21 classes are non-centrosymmetric with one displaying no piezoelectricity and the other 20 showing piezoelectricity, from which we will observe the appearance of electric potential by applying a mechanical stress and the crystal will be polarized. Among the 20 piezoelectric classes, 10 of them are pyroelectric, exhibiting a temperature dependent spontaneous polarization. Among pyroelectric materials, if the polarization could be switched by an external electric field, it is distinguished as ferroelectric.

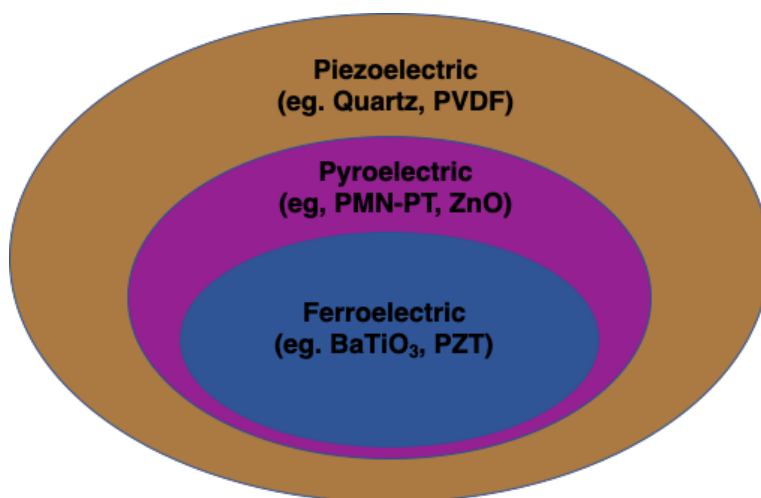


**Figure 2-11:** Schematic illustration of the relationship among piezoelectricity, pyroelectricity and ferroelectricity.

The first characteristic of a ferroelectric material is that it exhibits a spontaneous polarization in the absence of an external electric field. This polarization vector usually possesses at least two stable orientations and could be switched between those orientations by an external electric field. The polarization usually arises from the displacement of atoms, for example, the Ti and O ions in Figure 2-12(b) shifts upward compared with Figure 2-12(a). Secondly, most ferroelectric materials undergo a phase transformation from ferroelectric to paraelectric (order to disorder) from

low temperature to high temperature, where the transition temperature is defined as the Curie temperature ( $T_C$ ). The third feature is that ferroelectric domains usually form to minimize the electrostatic energy associated with depolarization fields and the elastic energy from the mechanical stress. In  $\text{PbTiO}_3$ , as shown in Figure 2-12(c),  $90^\circ$  domain walls form to reduce both the elastic energy and electrostatic energy while  $180^\circ$  domain walls only reduce electrostatic energy.

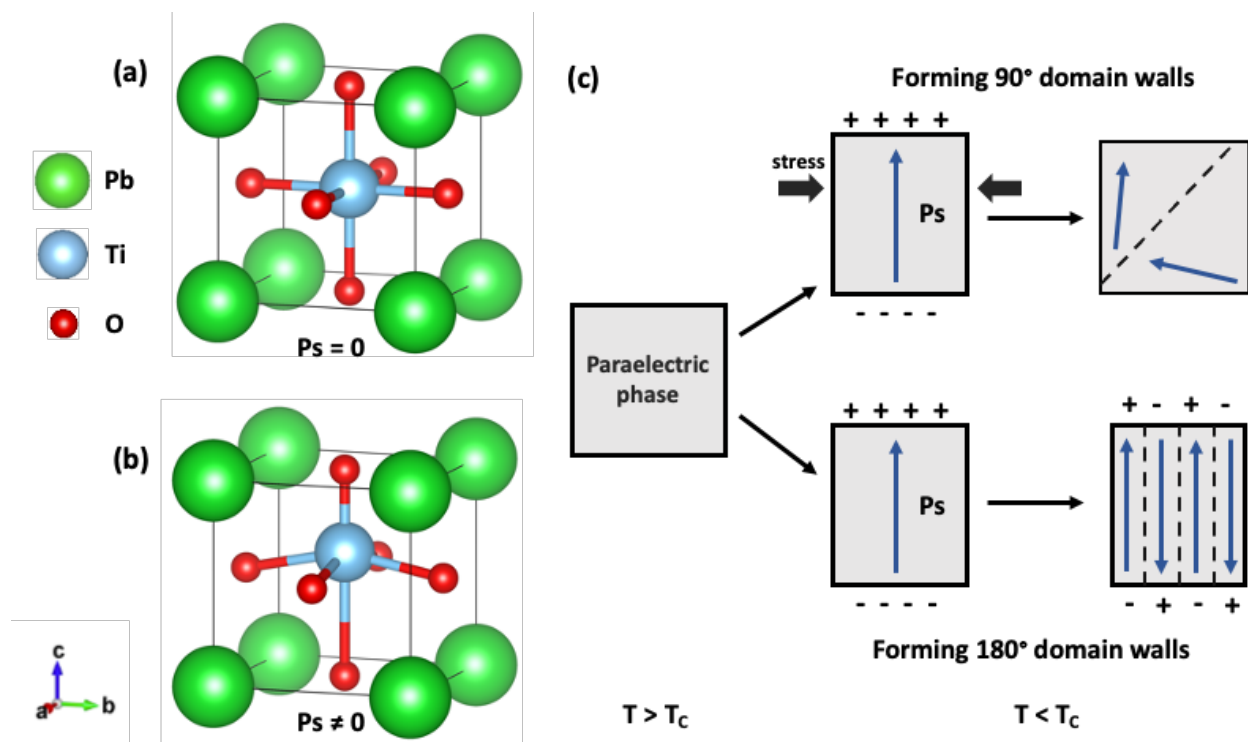


**Figure 2-12:** (a)  $\text{PbTiO}_3$  has a cubic structure ( $Pm\bar{3}m$ ) in paraelectric phase. (b)  $\text{PbTiO}_3$  has a tetragonal structure ( $P4/mmm$ ) in ferroelectric phase. (c) Schematic illustration of formation of  $90^\circ$  domain walls and  $180^\circ$  domain walls in  $\text{PbTiO}_3$ .

## 2.4.2 How do ferroelectric domains contribute to photochemistry?

The internal dipolar field of ferroelectric materials creates charged surfaces and induces band bending in space charge region with magnitudes of several hundred meV or greater.<sup>24,61</sup> The band bending will be upward in a negative domain and downward in a positive domain. As a result, photogenerated electrons and holes tend to move in opposite directions and the two half reactions will occur on different locations on the surface.

A photochemical marker reaction is an effective method to observe this effect.<sup>62</sup> (Details about marker reactions will be discussed in Chapter 3). By employing marker reactions, it is possible to selectively photo-deposit metals and metal oxides and identify the reaction sites for photoreduction and photooxidation, respectively.<sup>63–67</sup> Figure 2-13 gives two examples to the ferroelectric effect. BaTiO<sub>3</sub> is a famous ferroelectric material with spontaneous polarization along the [001] orientation, which has a magnitude of 26  $\mu\text{C}/\text{cm}^2$ . In Figure 2-12 (a) and (b), after photochemical marker reactions, Ag and PbO<sub>2</sub> accumulate on different locations of the surface, corresponding to the positive domains and negative domains, respectively.<sup>64</sup> This observation indicates that the electric field within ferroelectric domains drives electrons and holes migrating in different directions, providing a potential method to reduce the rate of charge recombination. The second example is BiFeO<sub>3</sub>, a ferroelectric semiconductor photocatalyst with a band gap about 2.5 eV.<sup>68,69</sup> Polycrystalline BiFeO<sub>3</sub> ceramics have a polarization of 6.1  $\mu\text{C}/\text{cm}^2$  along  $\langle 111 \rangle_p$  direction. Figure 2-12 (c) shows a PFM phase image showing the domain polarization map. Domains with positive out-of-plane polarizations appear dark and domains with negative polarizations appear bright. The AFM image of the same location after photochemical silver reduction is shown in Figure 2-12 (d). The distribution of silver deposits is consistent with the PFM images. Silver mainly appears on positive domains, indicating that electrons and holes are moving to different locations of the surface. This spatial selectivity has been observed on other ferroelectric materials, such as PbTiO<sub>3</sub>,<sup>70</sup> LiNbO<sub>3</sub>,<sup>71</sup> Ba<sub>x</sub>Sr<sub>1-x</sub>TiO<sub>3</sub>.<sup>72</sup>

The applications of ferroelectric materials on photocatalytic water splitting and organic dye degradation have been reported, showing enhanced reactivity. BaTiO<sub>3</sub>/TiO<sub>2</sub> core shell particles have been studied by Li<sup>73</sup> and Song.<sup>74</sup> Catalysts with macro-size BaTiO<sub>3</sub> cores have greater performance compared with catalysts with nano-size cores. Considering the space charge region of BaTiO<sub>3</sub> is about 162 nm,<sup>72</sup> the potential drop induced by ferroelectric polarization within the space charge region in smaller cores was not as great as in the larger cores. Nam et al. found that the photocatalytic reactivity of ferroelectric K<sub>0.5</sub>Na<sub>0.5</sub>NbO<sub>3</sub> after poling is 7.4 times higher than unpoled ones, owing to the internal dipole field.<sup>75</sup>

It seems that ferroelectric domains could contribute to separation of photogenerated charge carriers, however, is this always true? I will further discuss this and give a counter example in Chapter 4.

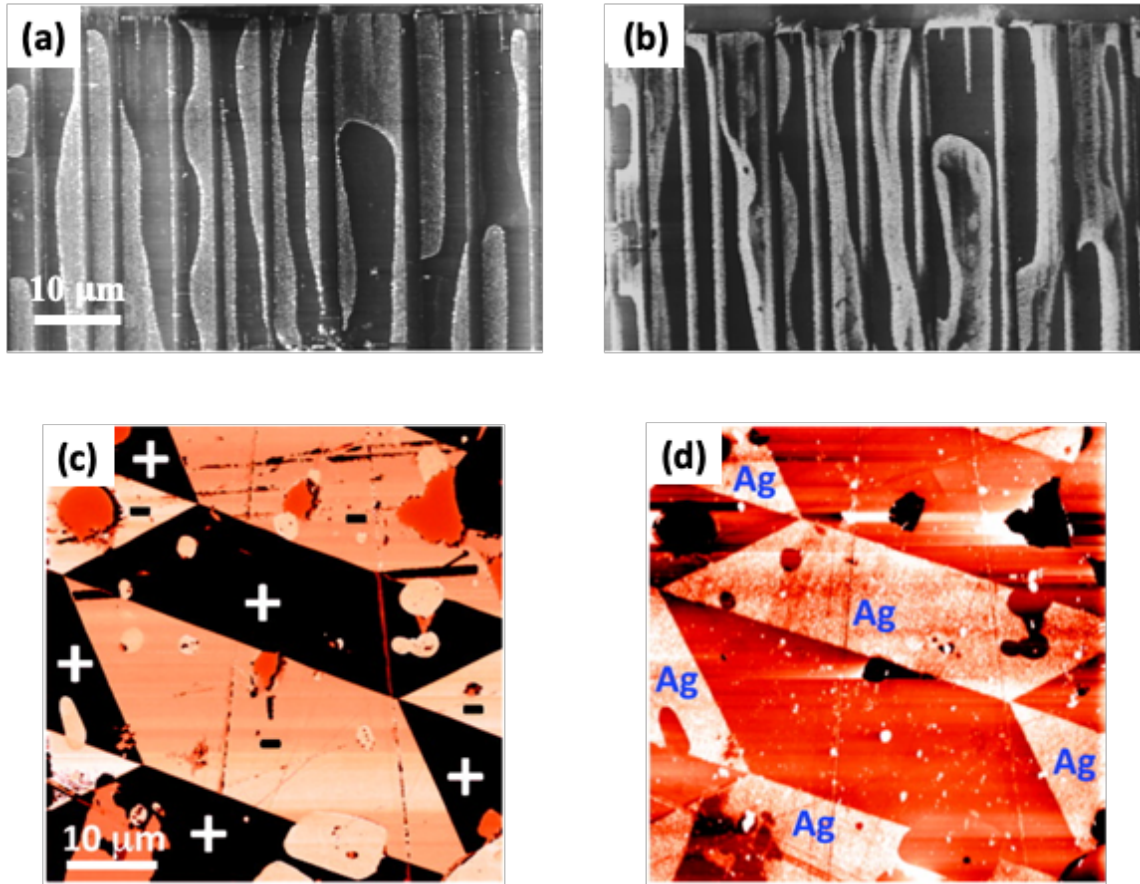


**Figure 2-13:** Topographic AFM images of the same location from a (001) BaTiO<sub>3</sub> single crystal surface under illumination in (a) 0.115M AgNO<sub>3</sub> solution and (b) 0.0115M Pb(Ac)<sub>2</sub> solution. Reproduced from ref.<sup>64</sup> (c) Out of plane PFM image of a (001) BiFeO<sub>3</sub> grain. Dark contrast in the image corresponds to regions with positive polarization and bright regions correspond to a region with negative polarization. (d) Topographic AFM image of the same location after reduction of Ag. Reproduced from ref.<sup>76</sup>

## 2.5 The effect of pH on photocatalytic reactivity

### 2.5.1 Energy levels for ions in solution

The energy potential levels for ions in solution represents their tendency to accept or give electrons when approaching an electrode. The lower the potential, the more the species is likely to oxidize. For example,  $\text{Na}/\text{Na}^+$  has a standard potential of  $-2.7 \text{ V/NHE}$ , meaning that Na metal is really unstable and easily loses an electron forming  $\text{Na}^+$  ions.  $\text{Au}/\text{Au}^{3+}$  has a standard potential of  $1.5\text{V/NHE}$ , meaning Au metal is stable and hard to be oxidized. Immersing the metal M electrode into electrolyte containing  $\text{M}^{z+}$  ions, there will be an equilibrium reaction:



To measure this potential, this metal electrode is connected with a hydrogen reference electrode whose Fermi energy is defined as zero. The hydrogen reference electrode energy is considered to be very close to  $4.5 \text{ eV}$  below  $E^{\circ}$ , the energy of an electron at infinity.<sup>77</sup> As shown in Figure 2-14, the voltage between the two electrodes is defined as the standard redox potential.

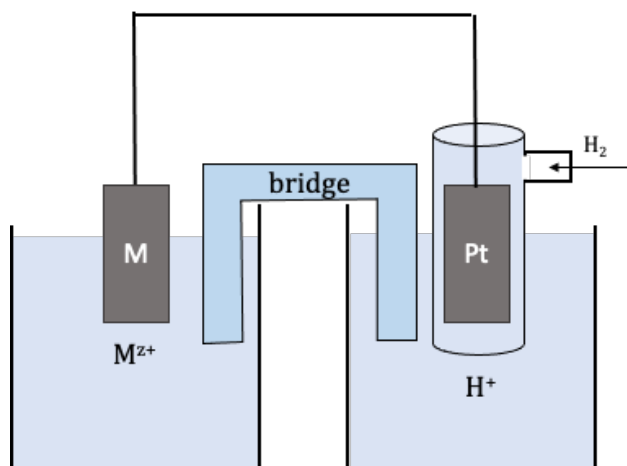


**Figure 2-14:** Schematic of measurement of standard potential of  $\text{M}/\text{M}^{z+}$ .

### 2.5.2 Nernst equation

In a reverse process, the electrode potential depends on the activity of each red-ox species, which can be described in the Nernst equation:

$$E = E^{\circ} - \frac{RT}{nF} \ln \left( \frac{a_{\text{Red}}}{a_{\text{Ox}}} \right) \quad (2.16)$$

where  $E^0$  is the standard redox potential.  $R$  is the gas constant,  $8.314\text{J/mol K}$ .  $T$  is temperature.  $F$  is Faraday constant,  $96485\text{ C/mol}$ .  $n$  represents the stoichiometric number of electrons exchanged in the reaction.  $a_{\text{Red}}$  and  $a_{\text{Ox}}$  represents the activity of reduced species and oxidized species, respectively.

Considering the reduction of a proton, the Nernst equation can be written as:

$$= E_{H^+/H_2}^{\circ} + \frac{RT}{nF} \ln \left( \frac{[a_{H^+}]^2}{P_{H_2}} \right) \quad (2.17)$$

At room temperature  $25\text{ }^{\circ}\text{C}$  and unit partial pressure, the equation above will be:

$$E_{H^+/H_2} = E_{H^+/H_2}^{\circ} - 0.059\text{pH} = -0.059\text{pH} \quad (2.18)$$

A similar approach could be applied for the oxidation of water:

$$E_{O_2/H_2O} = E_{O_2/H_2O}^{\circ} - 0.059\text{pH} = 1.23 - 0.059\text{pH} \quad (2.19)$$

Using the above equations, one can get the Pourbaix diagram of water as shown in Figure 2-15. Molecular  $\text{H}_2\text{O}$  is stable in the gray region. Above the upper boundary, water can be oxidized into oxygen. Below the under boundary, water can be reduced to hydrogen. The boundary is a function of  $\text{pH}$ .

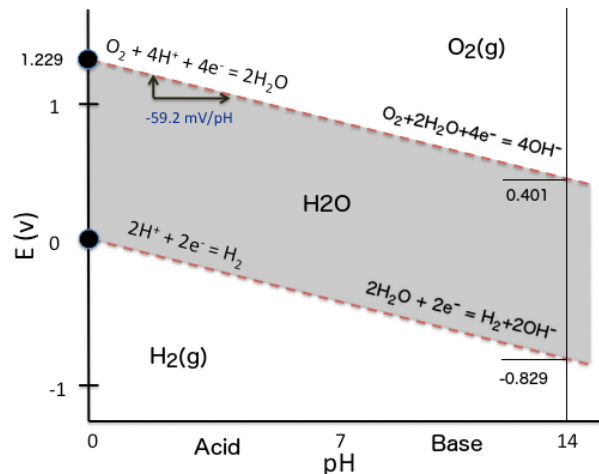


**Figure 2-15:** Pourbaix diagram of water. The shadow region corresponds to the equilibrium condition of water.

Solution pH would also affect the materials stability as materials would dissolve in strong acidic or alkali conditions. The Pourbaix diagram of SrTiO<sub>3</sub> have been computed by Raman et al. and shown in Figure 2-16. The bulk/solvent equilibrium of Sr and Ti is shown in (a) and (b), indicating that the two atoms tend to exist in Sr<sup>2+</sup> and TiO<sub>2</sub> at mild pH. (c) and (d) show the surface Pourbaix diagram of SrTiO<sub>3</sub> at pH 1 and pH 12. It is found that SrTiO<sub>3</sub> is overall stable in both conditions, while strontium vacancies form at highly oxidizing potentials. At high pH, the surface is more likely to be hydroxylated, and this change of surface chemistry affects the photochemical properties.

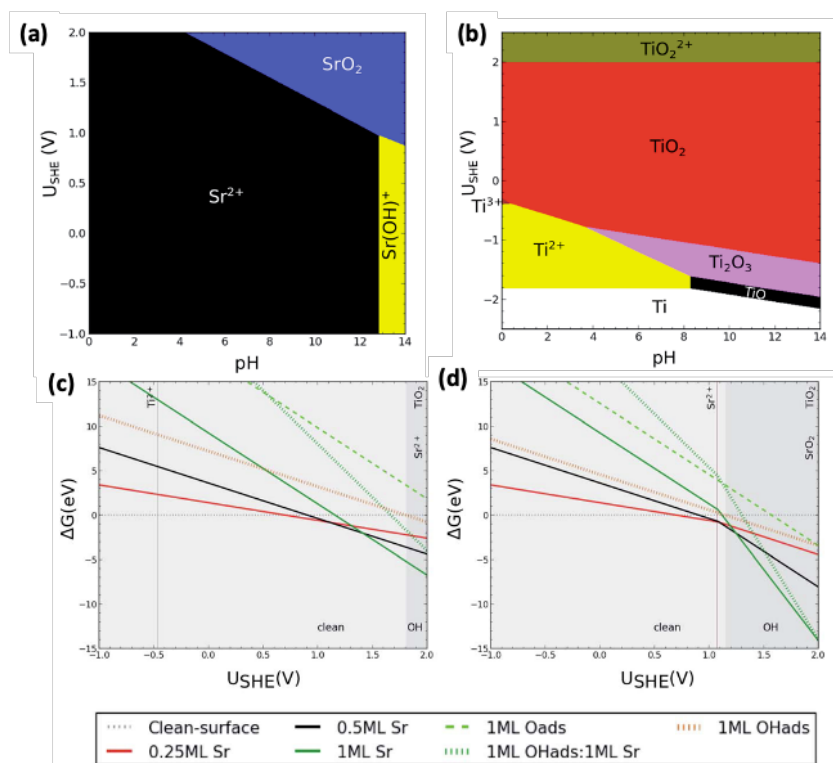


**Figure 2-16:** Pourbaix diagrams for (a) Sr and (b) Ti in aqueous solution. Surface Pourbaix diagrams showing the thermodynamic stability for SrTiO<sub>3</sub> at (c) pH 1 and (d) pH 12. Taken from ref.<sup>78</sup>

### 2.5.3 pH effect on photochemistry

pH can not only adjust the potential of chemical species but also the energy levels of semiconductors. In fact, solution pH can tailor the surface charge, influence the band bending and the potential of the surface changes by  $\approx 59$  mV for each unit of pH.<sup>42</sup> At low pH, the net charge on the surface will be positive, leading to a downward band bending in the space charge region. Holes will be repelled to the surface and the overall reaction is limited by the photoanodic reaction.

At high pH, the net charge on the surface will be negative, bending the band upward in the space charge region. Electrons will have to overcome a high energy barrier to move to the surface. The photocathodic half reaction will be the limiting factor. Because the reaction rate of overall reaction depends on the slower one of the two half reactions, the maximum reaction rate should appear at some intermediate pH. We believe this pH is related to isoelectric point (IEP), which is the point of zero zeta potential. If the photoanodic reaction is the limiting half reaction, this ideal pH should be greater than IEP to favor the oxidation reaction. If the photocathodic reaction is the limiting reaction, the suitable pH associated with maximum reactivity should be less than IEP to promote the reduction reaction. Note that IEP should not be confused with point of zero charge (PZC). PZC just describes a pH where an equal number of  $H^+$  and  $OH^-$  are adsorbed. In pure water, IEP and PZC are equal. But if there are ions other than  $H^+$  and  $OH^-$ , the two points will be different. The effect of pH on photochemistry has been studied on  $BaTiO_3$ . In a simulation work on  $TiO_2$  coated  $BaTiO_3$ , current density for electrons and holes changed as a function of applied voltage, as shown in Figure 2-17.<sup>78</sup> In reality, the voltage can be applied by changing solution pH and the optimized pH value for the reaction is calculated to be greater than 7. In an experimental work on  $BaTiO_3$  polycrystal grains, the photochemical reactivity is low at a pH between 4 and 5 and reaches a maximum value between pH 7 and 8.<sup>79</sup> This result is consistent with the simulation work.

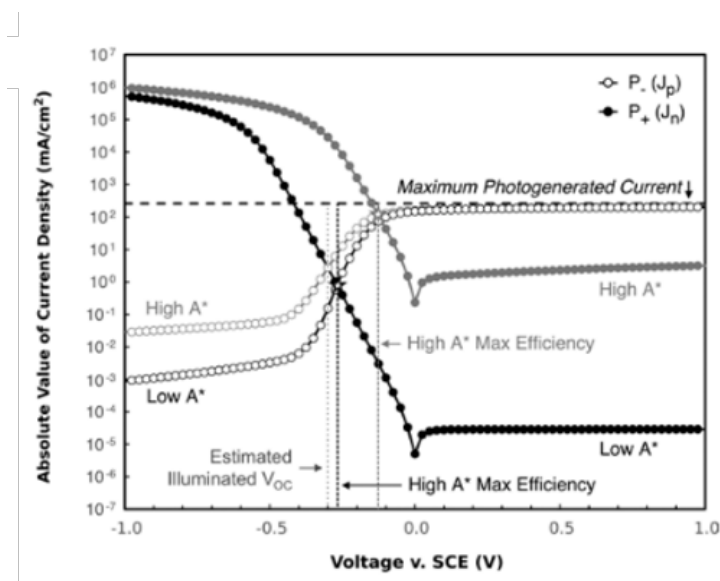


**Figure 2-17:** Simulated voltage dependence of electron ( $J_n$ ) and hole ( $J_p$ ) current densities at the surface of a 20 nm  $TiO_2$  film on  $BaTiO_3$ .  $A^*$  represents Richardson constant.  $V_{oc}$  represents open-circuit potential. Reproduced from ref.<sup>78</sup>

## **2.6 The effect of foreign ion incorporation**

### **2.6.1 Semiconductor doping**

Doping is another commonly used method to improve photocatalyst performance. We should first distinguish doping and alloying from a materials science perspective. Doping usually means adding a small number of foreign materials to the host materials and it may not change the crystal structure significantly. Such dopants can be considered as defects such as interstitials or substitutionals. Alloying usually means adding a large number of foreign materials to form a solid solution, and this will change the material structure significantly. In this section, I will focus on doping effect and explore how a little number of dopants influence the photocatalytic reactivity.

Doping atoms with different valence into the lattice can introduce excess electrons or holes. A semiconductor that is doped with a donor impurity is called an n-type semiconductor in which donor atoms provide excess free electrons, increase the Fermi level, and improve the electric conductivity. A semiconductor that is doped with an acceptor impurity is called a p-type semiconductor, acceptor atoms provide excess free holes, lower the Fermi level, and improve the electric conductivity.

### **2.6.2 The effect of doping on space charge**

Considering that most of oxides have intrinsic defects, the influence of dopants on charge carrier density might be complex. Here I focus on SrTiO<sub>3</sub>, a widely studied electroceramic, which is also the most important material in my graduate study. SrTiO<sub>3</sub> is generally agreed to be an intrinsic n-type semiconductor because of oxygen vacancies. There might be some background impurities acting as acceptor dopants, such as Na and K on the A-site or Fe and Al on the B-site. But the concentration of background impurities cannot overcome the oxygen vacancy concentration so that it is overall n-type. A Brouwer diagram of SrTiO<sub>3</sub> at 1000 °C is shown in Figure 2-18.

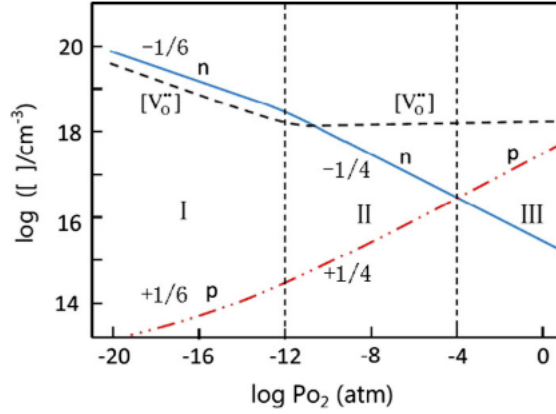


**Figure 2-18:** Schematic representation of equilibrium defect model for undoped and acceptor doped SrTiO<sub>3</sub>. Reproduced from ref.<sup>80</sup>

In the intrinsic region (low  $P_{O_2}$ ), oxygen vacancies are the predominant ionic defects balanced by free electrons. The electroneutrality condition is:

$$n \approx 2[V_O^{\bullet\bullet}] \quad (2.20)$$

In the extrinsic region (intermediate and high  $P_{O_2}$ ), free electron density decreases, and oxygen vacancies are compensated by acceptors. Note that the strontium vacancy concentration is negligibly small at this temperature. The electroneutrality condition is:

$$[A'] \approx 2[V_O^{\bullet\bullet}] \quad (2.21)$$

Note that at the point where  $n = p$ , the semiconductor is fully compensated. And the compensation point can be tuned by adjusting the doping concentration. For example, adding acceptor will lower the free electron concentration, moving the compensation point to the low  $P_{O_2}$  region. Therefore, at an ideal doping concentration, SrTiO<sub>3</sub> will become intrinsic (semi-insulating), leading to a much longer space charge region and longer photogenerated charge carrier's lifetime. Given the identical light penetration depth, more photogenerated charge carriers will be generated inside the space charge region, and they can be separated by the field and are less likely to recombine. This might explain why the majority of high performance SrTiO<sub>3</sub> photocatalysts that have been reported are acceptor doped, and what the optimal doping concentration might correspond to. More discussion will be given in Chapter 7, where I will compare Al with Mg and Ga as acceptor dopants for SrTiO<sub>3</sub> and discuss how they influence the photocatalytic reactivity.

### 2.6.3 The effect of foreign ion incorporation on optical property

By introducing foreign atoms, it is possible to create an impurity band in the forbidden gap region, and this might allow charge carriers to transit between VB/CB to the impurity band. When the doping concentration is low, this effect is very weak. But if one introduced a large quantity of impurities to the host (e.g., solid solution), this effect will influence the optical properties and narrow the band gap. In the case of metal oxides, the valence band edge is usually composed of  $O_{2p}$  orbitals. The formation of a new band with a more negative level than  $O_{2p}$  orbital induced by the dopants will reduce the band gap.<sup>81</sup> For example, Mn-, Ru-, Rh-, and Ir- doped  $SrTiO_3$  exhibit absorption spectra with shoulders in the visible light region, corresponding to the impurity states.<sup>82</sup> Among them, Rh-  $SrTiO_3$  is a photocathode that can produce hydrogen in aqueous methanol solutions under visible light irradiation.

## 2.7 References

- (1) Fujishima, A.; Honda, K. Electrochemical Photolysis of Water at a Semiconductor Electrode. *Nature* **1972**, *238* (5358), 37+. <https://doi.org/10.1038/238037a0>.
- (2) Linsebigler, A. L.; Lu, G.; Yates, J. T. Photocatalysis on  $TiO_2$  Surfaces: Principles, Mechanisms, and Selected Results. *Chem. Rev.* **1995**, *95* (3), 735–758. <https://doi.org/10.1021/cr00035a013>.
- (3) Chatterjee, D.; Dasgupta, S. Visible Light Induced Photocatalytic Degradation of Organic Pollutants. *J. Photochem. Photobiol. C Photochem. Rev.* **2005**, *6* (2), 186–205. <https://doi.org/10.1016/j.jphotochemrev.2005.09.001>.
- (4) Tryk, D. A.; Fujishima, A.; Honda, K. Recent Topics in Photoelectrochemistry: Achievements and Future Prospects. *Electrochim. Acta* **2000**, *45* (15), 2363–2376. [https://doi.org/10.1016/S0013-4686\(00\)00337-6](https://doi.org/10.1016/S0013-4686(00)00337-6).
- (5) Change, I. P. C. *Climate Change 2007 - Mitigation of Climate Change: Working Group III Contribution to the Fourth Assessment Report of the IPCC*; Assessment report (Intergovernmental Panel on Climate Change): Working Group; Cambridge University Press, 2007.

- (6) Xu, Y.-F.; Yang, M.-Z.; Chen, B.-X.; Wang, X.-D.; Chen, H.-Y.; Kuang, D.-B.; Su, C.-Y. A CsPbBr<sub>3</sub> Perovskite Quantum Dot/Graphene Oxide Composite for Photocatalytic CO<sub>2</sub> Reduction. *J. Am. Chem. Soc.* **2017**, *139* (16), 5660–5663. <https://doi.org/10.1021/jacs.7b00489>.
- (7) Kar, P.; Farsinezhad, S.; Mahdi, N.; Zhang, Y.; Obuekwe, U.; Sharma, H.; Shen, J.; Semagina, N.; Shankar, K. Enhanced CH<sub>4</sub> Yield by Photocatalytic CO<sub>2</sub> Reduction Using TiO<sub>2</sub> Nanotube Arrays Grafted with Au, Ru, and ZnPd Nanoparticles. *Nano Res.* **2016**, *9* (11), 3478–3493. <https://doi.org/10.1007/s12274-016-1225-4>.
- (8) Zeng, S.; Kar, P.; Thakur, U. K.; Shankar, K. A Review on Photocatalytic CO<sub>2</sub> reduction Using Perovskite Oxide Nanomaterials. *Nanotechnology* **2018**, *29* (5), 52001. <https://doi.org/10.1088/1361-6528/aa9fb1>.
- (9) König, B. Photocatalysis in Organic Synthesis – Past, Present, and Future. *European J. Org. Chem.* **2017**, *2017* (15), 1979–1981. <https://doi.org/10.1002/ejoc.201700420>.
- (10) Ravelli, D.; Dondi, D.; Fagnoni, M.; Albini, A. Photocatalysis. A Multi-Faceted Concept for Green Chemistry. *Chem. Soc. Rev.* **2009**, *38* (7), 1999–2011. <https://doi.org/10.1039/B714786B>.
- (11) Yang, J.; Wang, D.; Han, H.; Li, C. Roles of Cocatalysts in Photocatalysis and Photoelectrocatalysis. *Acc. Chem. Res.* **2013**, *46* (8), 1900–1909. <https://doi.org/10.1021/ar300227e>.
- (12) Wang, D.; Li, R.; Zhu, J.; Shi, J.; Han, J.; Zong, X.; Li, C. Photocatalytic Water Oxidation on BiVO<sub>4</sub> with the Electrocatalyst as an Oxidation Cocatalyst: Essential Relations between Electrocatalyst and Photocatalyst. *J. Phys. Chem. C* **2012**, *116* (8), 5082–5089. <https://doi.org/10.1021/jp210584b>.
- (13) Trasatti, S. Work Function, Electronegativity, and Electrochemical Behaviour of Metals: III. Electrolytic Hydrogen Evolution in Acid Solutions. *J. Electroanal. Chem. Interfacial Electrochem.* **1972**, *39* (1), 163–184. [https://doi.org/10.1016/S0022-0728\(72\)80485-6](https://doi.org/10.1016/S0022-0728(72)80485-6).
- (14) Abe, R.; Sayama, K.; Domen, K.; Arakawa, H. A New Type of Water Splitting System

- Composed of Two Different TiO<sub>2</sub> Photocatalysts (Anatase, Rutile) and a IO<sup>3-</sup>/I<sup>-</sup> Shuttle Redox Mediator. *Chem. Phys. Lett.* **2001**, *344* (3), 339–344. [https://doi.org/10.1016/S0009-2614\(01\)00790-4](https://doi.org/10.1016/S0009-2614(01)00790-4).
- (15) Abe, R.; Sayama, K.; Sugihara, H. Development of New Photocatalytic Water Splitting into H<sub>2</sub> and O<sub>2</sub> Using Two Different Semiconductor Photocatalysts and a Shuttle Redox Mediator IO<sup>3-</sup>/I<sup>-</sup>. *J. Phys. Chem. B* **2005**, *109* (33), 16052–16061. <https://doi.org/10.1021/jp0528481>.
- (16) Kim, H. G.; Becker, O. S.; Jang, J. S.; Ji, S. M.; Borse, P. H.; Lee, J. S. A Generic Method of Visible Light Sensitization for Perovskite-Related Layered Oxides: Substitution Effect of Lead. *J. Solid State Chem.* **2006**, *179* (4), 1214–1218. <https://doi.org/10.1016/j.jssc.2006.01.024>.
- (17) Kasahara, A.; Nukumizu, K.; Hitoki, G.; Takata, T.; Kondo, J. N.; Hara, M.; Kobayashi, H.; Domen, K. Photoreactions on LaTiO<sub>2</sub>N under Visible Light Irradiation. *J. Phys. Chem. A* **2002**, *106* (29), 6750–6753. <https://doi.org/10.1021/jp025961+>.
- (18) Darwent, J. R. H<sub>2</sub> Production Photosensitized by Aqueous Semiconductor Dispersions. *J. Chem. Soc., Faraday Trans. 2* **1981**, *77* (9), 1703–1709. <https://doi.org/10.1039/F29817701703>.
- (19) Nørskov, J. K.; Bligaard, T.; Logadottir, A.; Kitchin, J. R.; Chen, J. G.; Pandelov, S.; Stimming, U. Trends in the Exchange Current for Hydrogen Evolution. *J. Electrochem. Soc.* **2005**, *152* (3), J23. <https://doi.org/10.1149/1.1856988>.
- (20) Kudo, A.; Kato, H. Effect of Lanthanide-Doping into NaTaO<sub>3</sub> Photocatalysts for Efficient Water Splitting. *Chem. Phys. Lett.* **2000**, *331* (5), 373–377. [https://doi.org/10.1016/S0009-2614\(00\)01220-3](https://doi.org/10.1016/S0009-2614(00)01220-3).
- (21) Maeda, K.; Saito, N.; Lu, D.; Inoue, Y.; Domen, K. Photocatalytic Properties of RuO<sub>2</sub>-Loaded β-Ge<sub>3</sub>N<sub>4</sub> for Overall Water Splitting. *J. Phys. Chem. C* **2007**, *111* (12), 4749–4755. <https://doi.org/10.1021/jp067254c>.
- (22) Sayama, K.; Arakawa, H. Effect of Carbonate Salt Addition on the Photocatalytic

- Decomposition of Liquid Water over Pt–TiO<sub>2</sub> Catalyst. *J. Chem. Soc., Faraday Trans.* **1997**, *93* (8), 1647–1654. <https://doi.org/10.1039/A607662I>.
- (23) Marschall, R. Semiconductor Composites: Strategies for Enhancing Charge Carrier Separation to Improve Photocatalytic Activity. *Adv. Funct. Mater.* **2014**, *24* (17), 2421–2440. <https://doi.org/10.1002/adfm.201303214>.
- (24) Li, L.; Salvador, P. A.; Rohrer, G. S. Photocatalysts with Internal Electric Fields. *Nanoscale* **2014**, *6* (1), 24–42. <https://doi.org/10.1039/c3nr03998f>.
- (25) Gray, H. B.; Maverick, A. W. Solar Chemistry of Metal Complexes. *Science (80-. )*. **1981**, *214* (4526), 1201–1205. <https://doi.org/10.1126/science.214.4526.1201>.
- (26) Esswein, A. J.; Nocera, D. G. Hydrogen Production by Molecular Photocatalysis. *Chem. Rev.* **2007**, *107* (10), 4022–4047. <https://doi.org/10.1021/cr050193e>.
- (27) Dobereiner, G. E.; Crabtree, R. H. Dehydrogenation as a Substrate-Activating Strategy in Homogeneous Transition-Metal Catalysis. *Chem. Rev.* **2010**, *110* (2), 681–703. <https://doi.org/10.1021/cr900202j>.
- (28) Nomura, K.; Saito, Y. N-Alkene and Dihydrogen Formation from n-Alkanes by Photocatalysis Using Carbonyl(Chloro)Phosphine–Rhodium Complexes. *J. Chem. Soc., Chem. Commun.* **1988**, No. 3, 161–162. <https://doi.org/10.1039/C39880000161>.
- (29) Maguire, J. A.; Boese, W. T.; Goldman, A. S. Photochemical Dehydrogenation of Alkanes Catalyzed by Trans-Carbonylchlorobis(Trimethylphosphine)Rhodium: Aspects of Selectivity and Mechanism. *J. Am. Chem. Soc.* **1989**, *111* (18), 7088–7093. <https://doi.org/10.1021/ja00200a030>.
- (30) Jones, R. F.; Cole-Hamilton, D. J. The Photochemical Decomposition of Sulphuric Acid Catalysed by [HPt(PEt<sub>3</sub>)<sub>3</sub>]<sup>+</sup>. *J. Chem. Soc., Chem. Commun.* **1981**, No. 24, 1245–1246. <https://doi.org/10.1039/C39810001245>.
- (31) Collinson, E.; Dainton, F. S.; Malati, M. A. The Photo-Oxidation of Chromous Ions in Aqueous Solution at 25°C. *Trans. Faraday Soc.* **1959**, *55* (0), 2096–2106. <https://doi.org/10.1039/TF9595502096>.

- (32) Heidt, L. J.; Mullin, M. G.; Martin, W. B.; Beatty, A. M. J. Gross and Net Quantum Yields At 2537 Å. For Ferrous to Ferric in Aqueous Sulfuric Acid and the Accompanying Reduction of Water to Gaseous Hydrogen<sup>1</sup>. *J. Phys. Chem.* **1962**, *66* (2), 336–341. <https://doi.org/10.1021/j100808a034>.
- (33) Zhang, Z.; Yates, J. T. Band Bending in Semiconductors: Chemical and Physical Consequences at Surfaces and Interfaces. *Chem. Rev.* **2012**, *112* (10), 5520–5551. <https://doi.org/10.1021/cr3000626>.
- (34) Soga, T. Chapter 1 - Fundamentals of Solar Cell; Soga, T. B. T.-N. M. for S. E. C., Ed.; Elsevier: Amsterdam, 2006; pp 3–43. <https://doi.org/10.1016/B978-044452844-5/50002-0>.
- (35) Böer, K. W. *Introduction to Space Charge Effects in Semiconductors*; Springer-Verlag Berlin Heidelberg, 2010. <https://doi.org/10.1007/978-3-642-02236-4>.
- (36) Schottky, W. Halbleitertheorie Der Sperrschicht. *Naturwissenschaften* **1938**, *26* (52), 843. <https://doi.org/10.1007/BF01774216>.
- (37) Mott, N. F. The Theory of Crystal Rectifiers. *Proc. R. Soc. London. Ser. A. Math. Phys. Sci.* **1939**, *171* (944), 27–38. <https://doi.org/10.1098/rspa.1939.0051>.
- (38) Mott, N. F. Note on the Contact between a Metal and an Insulator or Semi-Conductor. *Math. Proc. Cambridge Philos. Soc.* **1938**, *34* (4), 568–572. <https://doi.org/DOI:10.1017/S0305004100020570>.
- (39) Apostol, N. G.; Teodorescu, C.-M. Band Bending at Metal-Semiconductor Interfaces, Ferroelectric Surfaces and Metal-Ferroelectric Interfaces Investigated by Photoelectron Spectroscopy BT - Surface Science Tools for Nanomaterials Characterization; Kumar, C. S. S. R., Ed.; Springer Berlin Heidelberg: Berlin, Heidelberg, 2015; pp 405–461. [https://doi.org/10.1007/978-3-662-44551-8\\_11](https://doi.org/10.1007/978-3-662-44551-8_11).
- (40) Bardeen, J. Nobel Lecture. In *NobelPrize.org. Nobel Media AB 2020*; 1956.
- (41) Zangwill, A. *Physics at Surfaces*; Cambridge University Press, 1988. <https://doi.org/10.1017/CBO9780511622564>.

- (42) Morrison, S. R. *Electrochemistry at Semiconductor and Oxidized Metal Electrodes*. **1980**.
- (43) Surfaces, W. on E. on N.; Franklin, A. D.; States., U.; Standards., N. B. of; (U.S.), N. S. F.; States., U.; Administration., E. R. and D. *Electrocatalysis on Non-Metallic Surfaces : Proceedings of a Workshop Held at the National Bureau of Standards, Gaithersburg, Maryland, December 9-12, 1975; U.S. Dept. of Commerce, the Bureau : [For sale by the Supt. of Docs., U.S. Govt. Print. Off.]: [Washington], 1976.*
- (44) Zhang, Z.; Yates, J. T. Effect of Adsorbed Donor and Acceptor Molecules on Electron Stimulated Desorption: O<sub>2</sub>/TiO<sub>2</sub>(110). *J. Phys. Chem. Lett.* **2010**, *1* (14), 2185–2188. <https://doi.org/10.1021/jz1007559>.
- (45) Kuo, C.-H.; Yang, Y.-C.; Gwo, S.; Huang, M. H. Facet-Dependent and Au Nanocrystal-Enhanced Electrical and Photocatalytic Properties of Au–Cu<sub>2</sub>O Core–Shell Heterostructures. *J. Am. Chem. Soc.* **2011**, *133* (4), 1052–1057. <https://doi.org/10.1021/ja109182y>.
- (46) Tan, C.-S.; Hsu, S.-C.; Ke, W.-H.; Chen, L.-J.; Huang, M. H. Facet-Dependent Electrical Conductivity Properties of Cu<sub>2</sub>O Crystals. *Nano Lett.* **2015**, *15* (3), 2155–2160. <https://doi.org/10.1021/acs.nanolett.5b00150>.
- (47) Wang, W.-C.; Lyu, L.-M.; Huang, M. H. Investigation of the Effects of Polyhedral Gold Nanocrystal Morphology and Facets on the Formation of Au–Cu<sub>2</sub>O Core–Shell Heterostructures. *Chem. Mater.* **2011**, *23* (10), 2677–2684. <https://doi.org/10.1021/cm200708q>.
- (48) Zheng, Z.; Huang, B.; Wang, Z.; Guo, M.; Qin, X.; Zhang, X.; Wang, P.; Dai, Y. Crystal Faces of Cu<sub>2</sub>O and Their Stabilities in Photocatalytic Reactions. *J. Phys. Chem. C* **2009**, *113* (32), 14448–14453. <https://doi.org/10.1021/jp904198d>.
- (49) Huang, M. H. Facet-Dependent Optical Properties of Semiconductor Nanocrystals. *Small* **2019**, *15* (7), 1804726. <https://doi.org/10.1002/sml.201804726>.
- (50) Zhu, Y.; Schultz, A. M.; Rohrer, G. S.; Salvador, P. A. The Orientation Dependence of the Photochemical Activity of  $\alpha$ -Fe<sub>2</sub>O<sub>3</sub>. *J. Am. Ceram. Soc.* **2016**, *99* (7), 2428–2435.

<https://doi.org/10.1111/jace.14201>.

- (51) Lin, Y.; Yuan, G.; Sheehan, S.; Zhou, S.; Wang, D. Hematite-Based Solar Water Splitting: Challenges and Opportunities. *Energy Environ. Sci.* **2011**, *4* (12), 4862–4869. <https://doi.org/10.1039/C1EE01850G>.
- (52) Li, R.; Zhang, F.; Wang, D.; Yang, J.; Li, M.; Zhu, J.; Zhou, X.; Han, H.; Li, C. Spatial Separation of Photogenerated Electrons and Holes among {010} and {110} Crystal Facets of BiVO<sub>4</sub>. *Nat. Commun.* **2013**, *4*. <https://doi.org/10.1038/ncomms2401>.
- (53) Li, R.; Han, H.; Zhang, F.; Wang, D.; Li, C. Highly Efficient Photocatalysts Constructed by Rational Assembly of Dual-Cocatalysts Separately on Different Facets of BiVO<sub>4</sub>. *Energy Environ. Sci.* **2014**, *7* (4), 1369–1376. <https://doi.org/10.1039/C3EE43304H>.
- (54) Giocondi, J. L.; Rohrer, G. S. Structure Sensitivity of Photochemical Oxidation and Reduction Reactions on SrTiO<sub>3</sub> Surfaces. *J. Am. Ceram. Soc.* **2003**, *86* (7), 1182–1189. <https://doi.org/10.1111/j.1151-2916.2003.tb03445.x>.
- (55) Giocondi, J. L.; Salvador, P. A.; Rohrer, G. S. The Origin of Photochemical Anisotropy in SrTiO<sub>3</sub>. *Top. Catal.* **2007**, *44* (4), 529–533. <https://doi.org/10.1007/s11244-006-0101-y>.
- (56) Pisat, A. S.; Salvador, P. A.; Rohrer, G. S. The Facet Structure and Photochemical Reactivity of Arbitrarily Oriented Strontium Titanate Surfaces. *Adv. Mater. Interfaces* **2019**, *6* (16), 1900731. <https://doi.org/10.1002/admi.201900731>.
- (57) Dong, L.; Shi, H.; Cheng, K.; Wang, Q.; Weng, W.; Han, W. Shape-Controlled Growth of SrTiO<sub>3</sub> Polyhedral Submicro/Nanocrystals. *Nano Res.* **2014**, *7* (9), 1311–1318. <https://doi.org/10.1007/s12274-014-0495-y>.
- (58) Mu, L.; Zhao, Y.; Li, A.; Wang, S.; Wang, Z.; Yang, J.; Wang, Y.; Liu, T.; Chen, R.; Zhu, J.; et al. Enhancing Charge Separation on High Symmetry SrTiO<sub>3</sub> Exposed with Anisotropic Facets for Photocatalytic Water Splitting. *Energy Environ. Sci.* **2016**, *9* (7), 2463–2469. <https://doi.org/10.1039/c6ee00526h>.
- (59) Hsieh, P.-L.; Naresh, G.; Huang, Y.-S.; Tsao, C.-W.; Hsu, Y.-J.; Chen, L.-J.; Huang, M. H. Shape-Tunable SrTiO<sub>3</sub> Crystals Revealing Facet-Dependent Optical and Photocatalytic

- Properties. *J. Phys. Chem. C* **2019**, *123* (22), 13664–13671. <https://doi.org/10.1021/acs.jpcc.9b02081>.
- (60) Takata, T.; Jiang, J.; Sakata, Y.; Nakabayashi, M.; Shibata, N.; Nandal, V.; Seki, K.; Hisatomi, T.; Domen, K. Photocatalytic Water Splitting with a Quantum Efficiency of Almost Unity. *Nature* **2020**, *581* (7809), 411–414. <https://doi.org/10.1038/s41586-020-2278-9>.
- (61) Morris, M. R.; Pendlebury, S. R.; Hong, J.; Dunn, S.; Durrant, J. R. Effect of Internal Electric Fields on Charge Carrier Dynamics in a Ferroelectric Material for Solar Energy Conversion. *Adv. Mater.* **2016**, *28* (33), 7123–7128. <https://doi.org/10.1002/adma.201601238>.
- (62) Lowekamp, J. B.; Rohrer, G. S.; Morris Hotsenpiller, P. A.; Bolt, J. D.; Farneth, W. E. Anisotropic Photochemical Reactivity of Bulk TiO<sub>2</sub> Crystals. *J. Phys. Chem. B* **1998**, *102* (38), 7323–7327. <https://doi.org/10.1021/jp982721e>.
- (63) Wenderich, K.; Mul, G. Methods, Mechanism, and Applications of Photodeposition in Photocatalysis: A Review. *Chem. Rev.* **2016**, *116* (23), 14587–14619. <https://doi.org/10.1021/acs.chemrev.6b00327>.
- (64) Giocondi, J. L.; Rohrer, G. S. Spatial Separation of Photochemical Oxidation and Reduction Reactions on the Surface of Ferroelectric BaTiO<sub>3</sub>. *J. Phys. Chem. B* **2001**, *105* (35), 8275–8277. <https://doi.org/10.1021/jp011804j>.
- (65) Song, W.; Salvador, P. A.; Rohrer, G. S. Influence of the Magnitude of Ferroelectric Domain Polarization on the Photochemical Reactivity of BaTiO<sub>3</sub>. *ACS Appl. Mater. Interfaces* **2018**, *10* (48), 41450–41457. <https://doi.org/10.1021/acsami.8b16983>.
- (66) Dunn, S.; Jones, P. M.; Gallardo, D. E. Photochemical Growth of Silver Nanoparticles on C- and C+ Domains on Lead Zirconate Titanate Thin Films. *J. Am. Chem. Soc.* **2007**, *129* (28), 8724–8728. <https://doi.org/10.1021/ja071451n>.
- (67) Giocondi, J. L.; Rohrer, G. S. The Influence of the Dipolar Field Effect on the Photochemical Reactivity of Sr<sub>2</sub>Nb<sub>2</sub>O<sub>7</sub> and BaTiO<sub>3</sub> Microcrystals. *Top. Catal.* **2008**, *49* (1),

18. <https://doi.org/10.1007/s11244-008-9067-2>.
- (68) Choi, T.; Lee, S.; Choi, Y. J.; Kiryukhin, V.; Cheong, S.-W. Switchable Ferroelectric Diode and Photovoltaic Effect in BiFeO<sub>3</sub>. *Science* (80-. ). **2009**, *324* (5923), 63–66. <https://doi.org/10.1126/science.1168636>.
- (69) Basu, S. R.; Martin, L. W.; Chu, Y. H.; Gajek, M.; Ramesh, R.; Rai, R. C.; Xu, X.; Musfeldt, J. L. Photoconductivity in BiFeO<sub>3</sub> Thin Films. *Appl. Phys. Lett.* **2008**, *92* (9), 91905. <https://doi.org/10.1063/1.2887908>.
- (70) Li, R.; Zhao, Y.; Li, C. Spatial Distribution of Active Sites on a Ferroelectric PbTiO<sub>3</sub> Photocatalyst for Photocatalytic Hydrogen Production. *Faraday Discuss.* **2017**, *198*, 463–472. <https://doi.org/10.1039/c6fd00199h>.
- (71) Liu, X.; Kitamura, K.; Terabe, K.; Hatano, H.; Ohashi, N. Photocatalytic Nanoparticle Deposition on LiNbO<sub>3</sub> Nanodomain Patterns via Photovoltaic Effect. *Appl. Phys. Lett.* **2007**, *91* (4), 44101. <https://doi.org/10.1063/1.2759472>.
- (72) Bhardwaj, A.; Burbure, N. V.; Rohrer, G. S. Enhanced Photochemical Reactivity at the Ferroelectric Phase Transition in Ba<sub>1-x</sub>Sr<sub>x</sub>TiO<sub>3</sub>. *J. Am. Ceram. Soc.* **2010**, *93* (12), 4129–4134. <https://doi.org/10.1111/j.1551-2916.2010.04002.x>.
- (73) Li, L.; Liu, X.; Zhang, Y.; Salvador, P. A.; Rohrer, G. S. Heterostructured (Ba,Sr)TiO<sub>3</sub>/TiO<sub>2</sub> Core/Shell Photocatalysts: Influence of Processing and Structure on Hydrogen Production. *Int. J. Hydrogen Energy* **2013**, *38* (17), 6948–6959. <https://doi.org/10.1016/j.ijhydene.2013.03.130>.
- (74) Song, W.; Lopato, E. M.; Bernhard, S.; Salvador, P. A.; Rohrer, G. S. High-Throughput Measurement of the Influence of pH on Hydrogen Production from BaTiO<sub>3</sub>/TiO<sub>2</sub> Core/Shell Photocatalysts. *Appl. Catal. B Environ.* **2020**, *269*, 118750. <https://doi.org/10.1016/j.apcatb.2020.118750>.
- (75) Park, S.; Lee, C. W.; Kang, M.-G.; Kim, S.; Kim, H. J.; Kwon, J. E.; Park, S. Y.; Kang, C.-Y.; Hong, K. S.; Nam, K. T. A Ferroelectric Photocatalyst for Enhancing Hydrogen Evolution: Polarized Particulate Suspension. *Phys. Chem. Chem. Phys.* **2014**, *16* (22),

10408–10413. <https://doi.org/10.1039/C4CP01267D>.

- (76) Schultz, A. M.; Zhang, Y.; Salvador, P. A.; Rohrer, G. S. Effect of Crystal and Domain Orientation on the Visible-Light Photochemical Reduction of Ag on BiFeO<sub>3</sub>. *ACS Appl. Mater. Interfaces* **2011**, *3* (5), 1562–1567. <https://doi.org/10.1021/am200127c>.
- (77) Battisti, A.; Trasatti, S. Medium Effects: Implications in Studies of Adsorption of Organic Substances at Electrodes\_A Theoretical Approach. *J. Electroanal. Chem.* **1974**, *54*, 1–17.
- (78) Raman, A. S.; Patel, R.; Vojvodic, A. Surface Stability of Perovskite Oxides under OER Operating Conditions: A First Principles Approach. *Faraday Discuss.* **2021**, *229* (0), 75–88. <https://doi.org/10.1039/C9FD00146H>.
- (79) Glickstein, J. J.; Salvador, P. A.; Rohrer, G. S. Computational Model of Domain-Specific Reactivity on Coated Ferroelectric Photocatalysts. *J. Phys. Chem. C* **2016**, *120* (23), 12673–12684. <https://doi.org/10.1021/acs.jpcc.6b03875>.
- (80) Song, W.; Salvador, P. A.; Rohrer, G. S. The Effect of pH on the Photochemical Reactivity of BaTiO<sub>3</sub>. *Surf. Sci.* **2018**, *675*, 83–90. <https://doi.org/10.1016/j.susc.2018.04.021>.
- (81) Chan, N.-H.; Sharma, R. K.; Smyth, D. M. Nonstoichiometry in SrTiO<sub>3</sub>. *J. Electrochem. Soc.* **1981**, *128* (8), 1762–1769. <https://doi.org/10.1149/1.2127727>.
- (82) Yamaguchi, Y.; Kudo, A. Visible Light Responsive Photocatalysts Developed by Substitution with Metal Cations Aiming at Artificial Photosynthesis. *Front. Energy* **2021**, *15* (3), 568–576. <https://doi.org/10.1007/s11708-021-0774-8>.
- (83) Konta, R.; Ishii, T.; Kato, H.; Kudo, A. Photocatalytic Activities of Noble Metal Ion Doped SrTiO<sub>3</sub> under Visible Light Irradiation. *J. Phys. Chem. B* **2004**, *108* (26), 8992–8995. <https://doi.org/10.1021/jp049556p>.

## Chapter 3: Experimental Methods

*In this chapter, I am going to present the experimental methods employed in the photochemistry studies. The sample preparation routes will be detailed introduced in the following chapters. Here, I focus on sample characterization techniques and the two approaches to evaluate the catalyst performance.*

### 3.1 Atomic force microscopy (AFM)

Atomic force microscopy (AFM), invented in 1986, is a widely used technique for imaging the surface of samples.<sup>1</sup> It could be applied to almost all type of samples, including metals, ceramics, polymers and composites. Besides topography, AFM can even measure other signals, such as magnetic force, adhesion force, surface potential and mechanical properties.<sup>2</sup> AFM makes use of a sharp tip which is about 10–20 nm in diameter attached to a cantilever. The cantilever will bend under force. When the tip is close to a surface, an electrostatic force from the surface deflects the cantilever and this deflection is detected as a change in the direction of the laser reflected from the back of the cantilever.

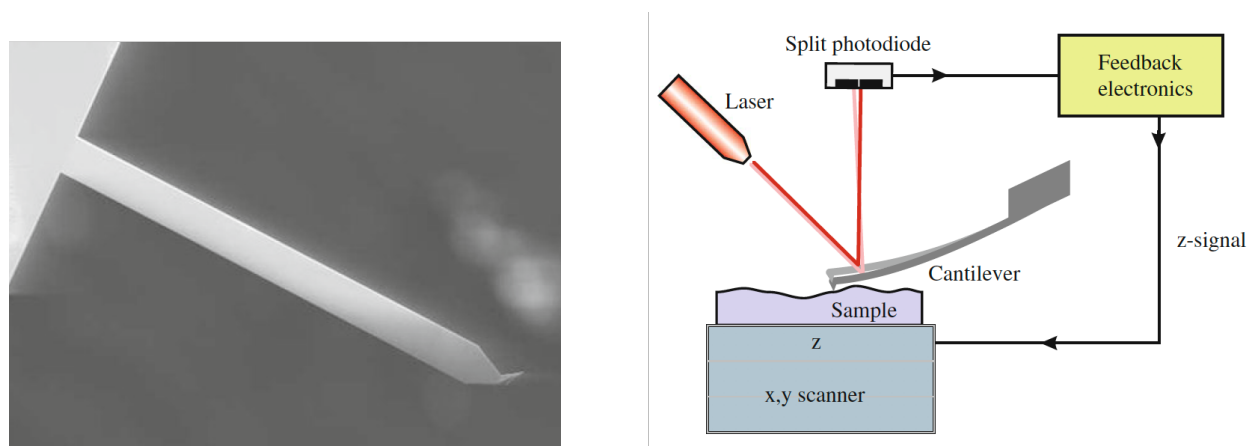


**Figure 3-1:** SEM image of an AFM silicon cantilever and tip with a length of 450  $\mu\text{m}$  (left). An AFM schematic (right). Reproduced from ref.<sup>3</sup>

AFM has two common modes. The first mode is contact mode. The AFM tip contacts the surface, and the cantilever deflection is held constant. Therefore, the force between the tip and surface will be constant as well. To maintain this constant deflection, the z-position of the tip must be changed,

and the z-position changes are recorded as topographical signal. A schematic illustration of this mode is shown in Figure 3-1. However, the mode is not suitable for soft samples, like polymer chains, since the sample might be damaged by the tip under contact mode.

The second mode is tapping mode. The AFM cantilever is vibrated above the sample surface so that the tip is in contact with the surface only intermittently. In this mode, the cantilever vibrates close to its free resonance frequency. When the tip is close to surface, the interaction between the tip and surface will affect the amplitude of the cantilever vibration. The changes in the vertical position needed to maintain constant amplitude are recorded as the topographic signals.

At present, the force sensitivity and thermal stability (drift) of AFM limit the precision of characterization.<sup>4</sup> Developing ultra-stable AFM with high positional stability and high force precision will definitely help scientists study more complex surface systems. In my research, AFM is mainly used in photochemical marker reactions, which will be discussed in section 3.10. The topographic images of the sample surface will be recorded by AFM before and after the marker reactions, so that we could study the distribution of the photochemical products as well as the photochemical reactivity.

## **3.2 Piezo force microscopy (PFM)**

Piezo force microscopy is an important offspring of AFM that can detect the tiny displacement of samples caused by electric field excitation. This method provides a possibility to determine the domain structure as well as the hysteresis loops of ferroelectrics and piezoelectrics. A conventional method to characterize such domain structures is optical or electrical microscopy on etched surface. PFM is obviously more convenient because the sample won't be damaged.

The application of PFM is based on the converse piezoelectric effect. Owing to the converse piezoelectric effect, applying an oscillating electric field to a ferroelectric sample leads to a surface vibration. The polarization state can be determined by measuring the magnitude and phase of this vibration signal.<sup>5</sup> In a typical PFM setup, a conductive probe is set to contact the sample with a voltage applied between the tip and the sample, and this results in a periodical displacement of the sample. The amplitude and phase of the tip displacement will be recorded by the amplifiers. For example, if the polarization vector is perpendicular to the applied electric field, the sample will

extend itself along the ferroelectric vector, providing horizontal displacements. If the polarization is parallel to the applied electric field, there will be a vertical displacement in the sample. The PFM probe tip, usually conducted in contact mode, will move along with the surface displacement and causes the cantilever to deflect.<sup>6</sup> Because the deflections are different for domains with different polarizations, the contrast in this signal can be correlated to the domain structure.

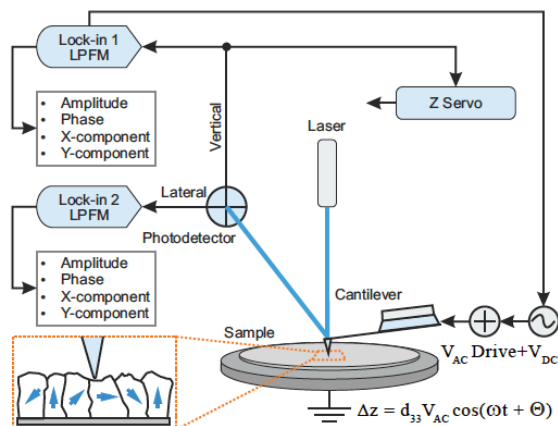


**Figure 3-2:** Sketch of Piezo Force Microscopy set-up in scanning probe microscope. Reproduced from the application note of NT-MDT Spectrum Instruments.

In my research, PFM is used to investigate the domain structure of  $\text{La}_2\text{Ti}_2\text{O}_7$ . Because we assume that the photocatalytic reactivity of  $\text{La}_2\text{Ti}_2\text{O}_7$  is influenced by the ferroelectric polarization, employing PFM is a straight way to determine the whether the distribution of the photochemical products is correlated to ferroelectric domains.

### 3.3 X-ray diffraction (XRD)

X-ray diffraction is a powerful tool to characterize the structure and purity of crystalline materials. For small samples, it could also be applied to determine sample crystallinity.<sup>7</sup> X-rays are a form of light with energies ranging from about 100 eV to 10 MeV with wavelengths on the order of nanometers. This length is in the same order of the spacing between atoms in crystals. X-rays are usually produced when the electrons released by a hot cathode accelerate to a high velocity and collide with a metal target (Cu, Fe, Mo), the anode. Then the X-ray will be filtered to produce monochromatic X-rays.

The X-rays are directed at the sample at various angles, and the diffracted X-rays are collected. In crystals with periodic arrangement of atoms, the diffraction follows the Bragg Law:

$$2d\sin\theta = n\lambda \quad (3.1)$$

where  $n$  is the number of wavelengths in the path difference between diffracted X-rays. Given incident angle  $\theta$  and X-ray wavelength, we can determine the  $d$  spacing between different crystal planes. If we repeat this measurement on many sets of planes, we could determine the lattice constant of the unit cell.

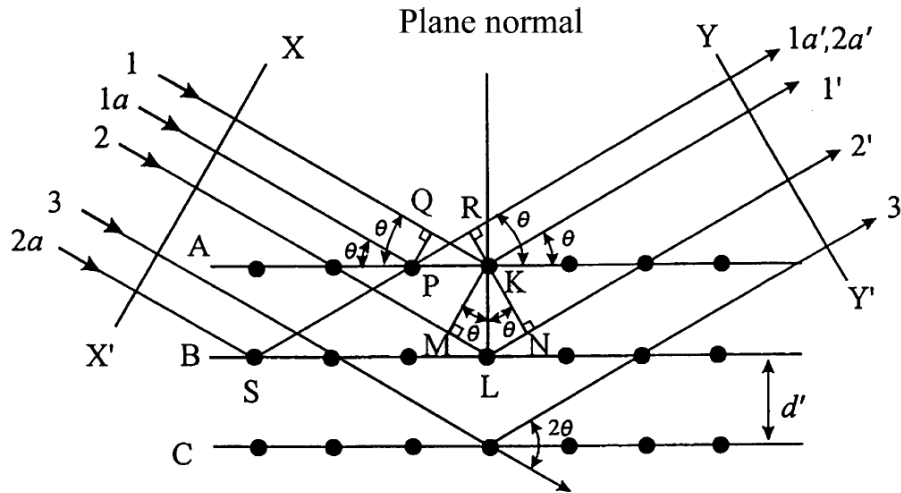


**Figure 3-3:** Schematic diagram of diffraction of X-rays by a crystal. Reproduced from ref.<sup>8</sup>

In my research, XRD is usually employed to determine the lattice parameters of doped samples. It is also useful for phase identification and sample purity examination.

### 3.4 Scanning electron microscopy (SEM)

Scanning electron microscopy is a powerful tool to explore surface structure and morphological features. Besides, it is also able to provide information on sample size, composition, crystallography, and other physical properties. It makes use of a focused electron beam to scan the sample surface and provides information of surface structure. Different from TEM, SEM has a large depth of field, which contributes to a three-dimensional appearance of the image.

The electron beam used is typically in the range of 0.1 kV to 30 kV. After emitting from the source, the beam will be modified by apertures, magnetic lenses and electromagnetic coils.<sup>9</sup> There are two major types of scattered electrons after the beam interact with specimen: secondary electrons (SEs) and backscattered electrons (BSEs), which escape from different locations in the specimen. Secondary electrons come from inelastic scattering and are from the near surface region, with a

depth of 5-50 nm,<sup>10</sup> corresponding to topographical signal. Backscattered electrons originate from elastic scattering with energy similar to the incident electrons, so that BSEs might come from a much deeper region, about 50-300 nm. BSEs are mainly responsible to compositional contrast. And BSEs can also help determine the orientation contrasts for domains and grains. Besides, the interaction between surface and specimen also generates characteristic X-ray, which is useful to elemental identical.

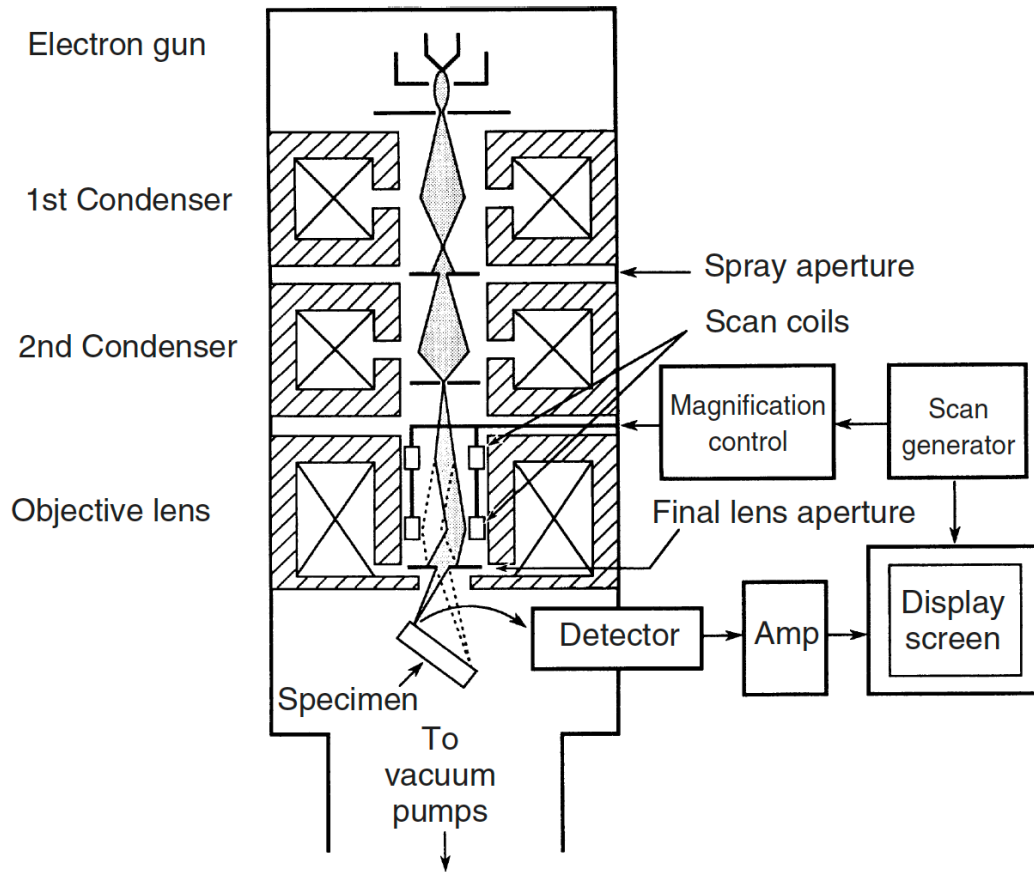


**Figure 3-4:** Structure of scanning electron microscope (SEM). Reproduced from ref.<sup>9</sup>

In my research, SEM is mainly used to characterize the surface morphology of both polycrystalline ceramic samples and single crystal powders. After photochemical marker reactions, SEM images can be used as a supplement to determine the distribution of the photo deposits. Besides, in the work of Al:SrTiO<sub>3</sub> (Chapter 6), we are studying the effect of crystal shape on the photocatalytic reactivity, and SEM is used to determine the particle shape and size.

### 3.5 Electron backscatter diffraction (EBSD)

Electron backscatter diffraction (EBSD) can be performed on SEM to determine grain orientation and local texture.<sup>13</sup> EBSD pattern is generated by backscattered electrons coming from approximately 20 nm deep in the material and collected by a phosphor screen. This pattern is based on the Kikuchi diffraction patterns obtained in a transmission electron microscope.<sup>11,12</sup> An EBSD pattern consists of regular arrangement of bands representing the projection of crystal lattice on the screen. By analyzing the bands, we can calculate the interplanar spacing and angles and determine surface orientation accordingly.

The whole EBSD Kikuchi pattern consist of pairs of parallel lines. Each pair of bands are known as a Kikuchi band with a distinct width and correspond to a distinct crystallographic plane; the intersection of bands correspond to zone axis (pole). By indexing the poles and bands in the pattern, it is feasible to get the crystallographic orientation of the surface. In most cases, the pattern indexation can be completed in an automated fashion through commercial software, by applying a Hough transformation.

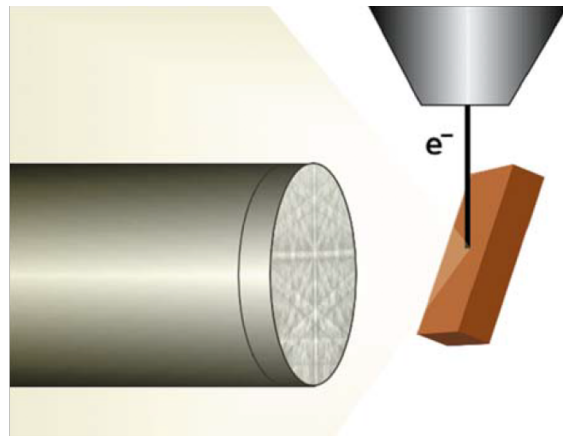


**Figure 3-5:** Schematic of the typical EBSD geometry. Reproduced from ref.<sup>13</sup>

Before an EBSD experiment, the sample surface must be flattened and polished. The sample stage needs to be inclined at 70 degrees to increase both the contrast in the diffraction pattern and the fraction of electrons scattered from the sample. Using an electron beam, electrons backscattered by lattice will be recorded by the phosphorous screen. The phosphorous screen converts electrons

into light detected by a CCD camera. Finally, the image could be analyzed and indexed to characterize the local orientation.

In my work on  $\text{La}_2\text{Ti}_2\text{O}_7$  (Chapter 4), we are going to determine the orientation effect on the reactivity. A total of 90 grains on a ceramic sample surface have been studied and EBSD was used to determine the orientation of these grains. In the work on the  $\text{SrTiO}_3$  (Chapter 5), the pH effects were first determined on single crystals with orientations of (100), (110) and (111). In order to confirm these results, we prepared a polycrystal sample. Using EBSD, we find three grains that were close to (100), (110), and (111) orientations and these grains were used to study the pH effect. Note that a specific example is provided in Appendix 1 to explain how to use EBSD to study the orientation effect of photochemical reactivity.

### **3.6 Transmission electron microscope (TEM)**

In Chapter 9, TEM is used to determine the structure of the special  $\text{SrTiO}_3$  crystals using  $\text{BaTiO}_3$  as precursor and investigate how it differs from the normal  $\text{SrTiO}_3$ . TEM employs a high energy electron beam thus it can provide very high-resolution image. Unlike SEM, the electron beam transmits through the sample and interacts with the mass of the sample. The beam emitted from the electron gun is first shaped by the condenser lens and the condenser aperture, focused by the objective lens, and the image is magnified and positioned by the intermediate lens and the projector lens (see Figure 3-6). TEM has two main operational modes: image mode and diffraction mode. In fact, the diffraction pattern and image are simultaneously formed in the microscope. The diffraction pattern is formed at the back focal plane by the objective lens with the electrons diffracted from the sample, and the image is generated by combining the diffracted electron beams. By adjusting the strength of the intermediate lens, we can switch which of them to show on the screen. Illustrations of the two operation modes are given in Figure 3-6. The contrast of the recorded image might arise from many properties of the sample like mass, thickness, atomic number, and crystal defects.

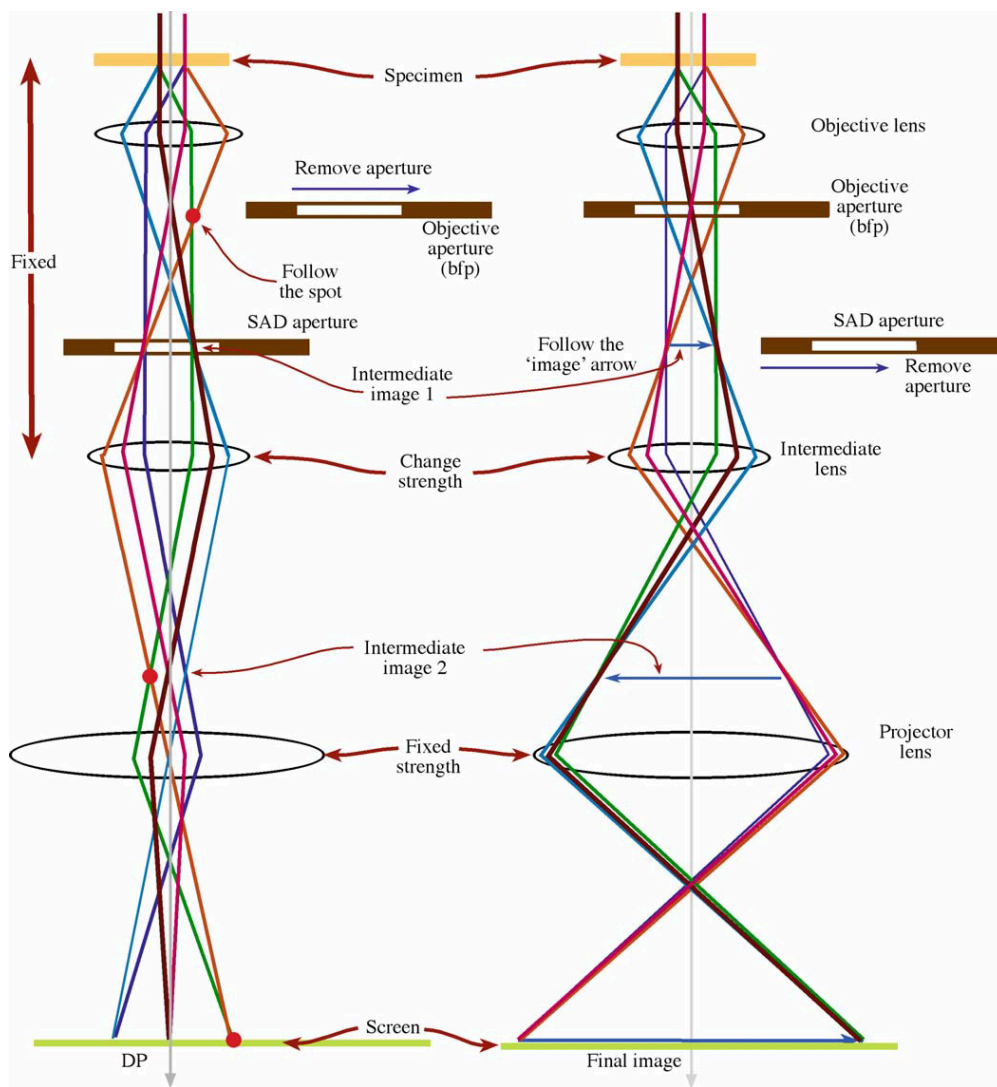


**Figure 3-6:** Schematic of the (A) diffraction mode and (B) image mode in TEM. Taken from ref.<sup>14</sup>

TEM is very useful to characterize the structure of photocatalysts. For example, bright/dark field images can help identify the location of cocatalysts. Bright field images are formed by the direct unscattered electrons, while dark field are formed by a certain group of scattered electrons selected by the objective aperture. If we select the beam diffracted by the cocatalysts (e.g., Pt), the Pt cocatalysts will have much brighter contrast in the dark field image. Besides, diffraction patterns can help us determine the orientation of a specific crystal facet, which is very important when we study the orientation effect on photocatalysis. Note that the thickness of a good TEM specimen is usually less than 100 nm, and sometimes the catalyst particle might be too large, and the beam cannot transmit the particle. One solution is to tilt the sample and look at the particle edge.

### 3.7 BET surface area analysis

The BET (Brunauer, Emmett and Teller) theory is commonly used to evaluate the gas adsorption data and generate a specific surface area result in units of area per mass of sample ( $\text{m}^2/\text{g}$ ). The theory was developed by Stephen Brunauer, Paul Emmett and Edward Teller,<sup>15</sup> which is extended from the Langmuir theory.<sup>16</sup> The conventional Langmuir theory considers monolayer adsorbates, and the BET theory extends this to multilayers, which is closer to what actually happens.

Prior to the analysis, the sample should be degassed to remove any adsorbed water and other contaminations on the surface, which is very important for hydrothermally synthesized powders since there will always be a lot of residual water. The analysis is usually conducted using  $\text{N}_2$  because of its strong interaction with most solids, and the surface area is determined by measuring how much gas is adsorbed. Because the physisorption between the solid and gas is very weak, the sample is cooled with liquid  $\text{N}_2$  and to create a detectable adsorption level. In a typical experiment: the degassed sample is put in a test tube, known amounts of nitrogen ( $P/P_0$ ) is stepwise released to the tube, achieved by creating partial vacuum, and the pressure change induced by the adsorption is monitored, through which we can get an adsorption isotherm. The isotherm is then converted to the surface area information. In my work, BET is employed to measure the surface area ratio of my powder catalysts. It is generally agreed that a higher surface area ratio provides more reaction sites and better reactivity, thus we need to consider its influence when we compare different catalysts. Note that the hydrogen rate measured by the reactor is in the form of  $\mu\text{mol h}^{-1}$ , which is known as the absolute rate. After normalizing it by the sample weight, we get the mass specific rate ( $\mu\text{mol h}^{-1}\text{g}^{-1}$ ). To exclude the influence of surface area, we normalize the mass specific rate with the BET surface area ratio ( $\text{m}^2/\text{g}$ ) and get the surface area specific rate ( $\mu\text{mol h}^{-1}\text{m}^{-2}$ ). In Chapter 6, I will discuss the particle size effect, the interplay between surface area ratio and space charge length, and BET is the approach to compare the surface area of different sized particles.

### 3.8 X-ray photoelectron spectroscopy (XPS)

XPS is a type of electron spectroscopy that can detect the material surface chemistry, such as surface composition and element electronic state. The spectrum is obtained by irradiating the

material with a high energy X-ray beam, and the electrons ejected from the surface are recorded as a function of kinetic energy. Although the X-ray can penetrate into the bulk of the material, the electrons can only escape from the near surface region, the method is then highly sensitive to surface. The information depth of XPS is generally in the range of 1 to 10 nm.

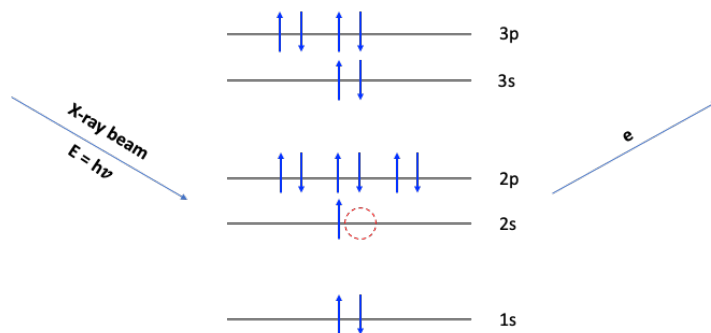


**Figure 3-7:** Schematic of an electron ejected from a sulfur atom induced by X-ray.

Figure 3-7 shows the orbitals of a sulfur atom. An electron from the 2s orbital is ejected from the atom by the incident X-ray, and its binding energy can be expressed as:

$$E_{2s} = E_{photon} - (E_{kinetic} + \varphi) \quad (3.2)$$

In this equation, photon energy and work function are known, and the kinetic energy of the emitted electron is measured by the detector. So, we could use these numbers to measure the binding energy of an atom originated from the 2s orbital. The binding energy (and the relative intensity of the spectrum peak) serves as the fingerprint of all elements (except H and He), enables us to quantify the element composition of the material. The binding energy is sensitive to the distribution of the valence electron. Considering a carbon atom bonded to a fluorine atom, the 2p electrons are attracted by the fluorine due to its high electronegativity. This will reduce the screening of the 1s electrons by the 2p electrons and increases the binding energy of the 1s electrons, which is known as chemical shift.

In Chapter 7 and Chapter 9, I will discuss the effect of the SrCl<sub>2</sub> flux treatment on SrTiO<sub>3</sub>. And, XPS is applied to determine the change of surface chemistry by the flux.

### 3.9 UV-vis diffuse reflectance spectroscopy (UV-vis DRS)

Band gap energy is one of the most important properties of photocatalyst as it determines how much light that can be absorbed from the solar spectrum. UV-vis diffuse reflectance spectroscopy (UV-vis DRS) is the primary technique used to measure the semiconductor band gap. For liquids, we can measure the light intensity before and after the transmission through the sample and then determine how much light is absorbed. However, for solid materials, it is relatively difficult for light to penetrate the sample especially when the sample is thick or opaque. Therefore, instead of measuring its transmission, one can measure its reflection, assuming that the incident light is either reflected or absorbed. Diffuse reflection corresponds to the incident light scattered in different directions, and it is measured by a special attachment called “integrating sphere”.

The Tauc method<sup>17</sup> describes the relationship between absorption coefficient  $\alpha$  and band gap energy:

$$(\alpha \cdot hv)^{\frac{1}{\gamma}} = B(hv - E_g) \quad (3.3)$$

The factor  $\gamma$  is 0.5 or 2 for direct semiconductor and indirect semiconductor, respectively. B is a constant. Since we cannot directly measure the absorption coefficient, we can use the Kubelka-Munk function instead.<sup>18</sup> The equation is written as:

$$F(R_{\infty}) = \frac{(1-R_{\infty})^2}{2R_{\infty}} \quad (3.4)$$

Where  $R_{\infty}$  represents the reflectance of an infinitely thick specimen. We could put  $F(R_{\infty})$  in the Tauc equation:

$$(F(R_{\infty}) \cdot hv)^{\frac{1}{\gamma}} = B(hv - E_g) \quad (3.5)$$

After plotting  $(F(R_{\infty}) \cdot hv)^{\frac{1}{\gamma}}$  as a function of energy, the band gap energy is determined by extrapolating the linear region of the plot to the x-axis.<sup>19</sup>

### 3.10 Photochemical marker reaction

Photochemical marker reactions are effective to study the photocatalytic properties of materials and are really helpful to determine reaction sites for photoreduction and photo-oxidation. It usually makes use of half reactions with a series of metal salts as electron/hole scavengers. After reaction, insoluble products will deposit on the surface that can be characterized by SEM or AFM.<sup>20-22</sup>

In a typical setup, as shown in Figure 3-8, the sample is placed on a substrate. Next, an O ring is placed on the top of the sample, containing selected metal salt solution. A quartz cover is used to seal the solution without bubbles. The sample will be illuminated, then rinsed in deionized water and dried by a stream of nitrogen. Intensity of illumination and the distance between lamp and the surface can be adjusted. Note that the sample surface must be well polished for a satisfactory microscope image. By observing the distribution of metal deposits, we could determine whether a location on the surface is more photocathodic or photoanodic. By measuring the volume/height of the deposits, one can estimate the relative reactivity of the sample. After one experiment, the sample will be cleaned by a cotton swipe and ultrasonically washed in methanol and acetone. Before running a second experiment, SEM is used to determine whether most of the deposits have been removed.

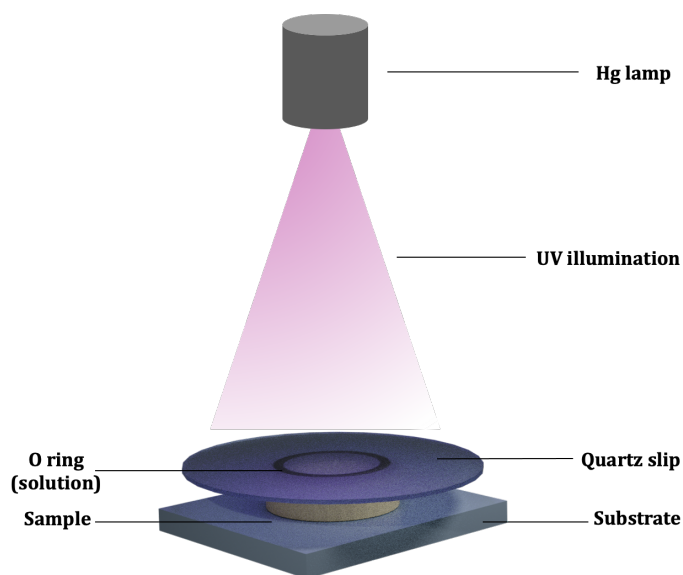
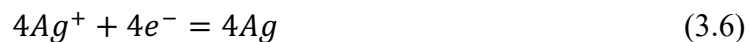
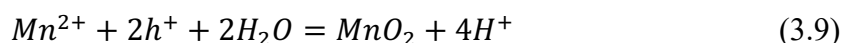
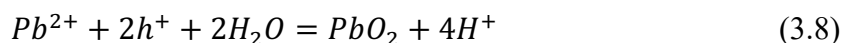


**Figure 3-8:** Schematic illustration of a typical setup for a marker reaction.

To study photocathodic reactivity,  $\text{AgNO}_3$  is the most commonly used salt. The whole reaction will be:



In order to study photoanodic reactivity,  $\text{Pb}(\text{CH}_3\text{COO})_2$  or  $\text{MnSO}_4$  are usually selected. The corresponding reactions will be:



Note that to get a satisfactory experimental result, one needs to find a suitable salt concentration as well as illumination condition. If the concentration is too low or the illumination is not strong enough, there will be few deposits on surface and it will be difficult to analyze them. If the solution concentration is too high, the surface will be overreacted, and we cannot determine the distribution of products. Figure 3-9 presents the surface morphology of two catalysts after photochemical marker reactions under microscope.

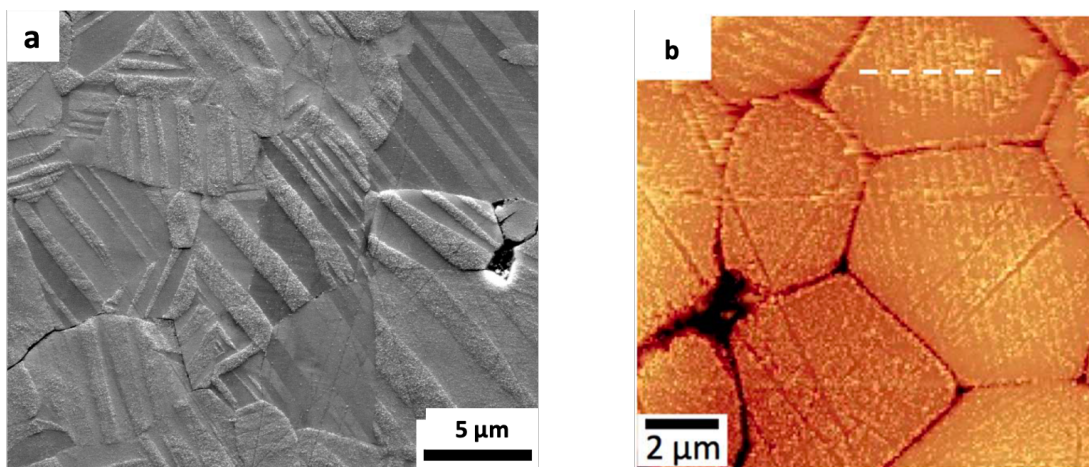


**Figure 3-9:** (a) SEM image of surface of  $\gamma\text{-WO}_3$  after photooxidation of  $\text{Mn}^{2+}$ . Adapted from ref.<sup>23</sup> (b) Topographic AFM image of  $(\text{Bi}_{1-0.5x}\text{Na}_{0.5x})(\text{V}_{1-x}\text{Mo}_x)\text{O}_4$  ( $x=0.05$ ) surface after  $\text{Ag}^+$  reduction. Adapted from ref.<sup>24</sup>

### 3.11 Parallelized and automated photochemical reactor (PAPCR)

A conventional method to measure the efficiency of photocatalytic water splitting is based on gas chromatography. This method is highly accurate, and one could measure the evolution of other types of gas, such as oxygen. Considering the limit of time and manpower, it is impossible to study a large amount of catalysts in a short time period by this method. Fortunately, the parallelized and automated photochemical reactor (PAPCR), a new type of photoreactor developed by Bernhard's lab, provides a route to a high-throughput screening of a large number of photocatalysts.<sup>25</sup>

The reactor consists of 108 1 ml glass shell vials whose headspace is covered by a film of H<sub>2</sub> detection tape (DetecTape, Midsun Specialty Products). Suspensions of particulate catalysts and solution will be added into these small volume vials so that 108 samples can be studied in one experiment. Two 100 W LED chips are placed in the bottom of reactor providing illumination for the reaction. A camera is fixed on the top, taking pictures of the H<sub>2</sub> detection tape every several minutes. The color of the tape will change from light to dark when exposed H<sub>2</sub>.<sup>25</sup> The relationship between tape darkness and local H<sub>2</sub> concentration has been calibrated. In this way, we may calculate the amount of H<sub>2</sub> generated at each time step, as well as the reaction rate, for each of the 108 vials.

Figure 3-10 shows a typical result from an experiment using PAPCR. Fig. 3-10 (a) is the image of the hydrogen tape before the reaction. Each circle corresponds to a vial. There are three stripes of tapes on the top of the vials and the two horizontal lines correspond to the edges of the tapes. After an experiment of 18 h, the color of the tapes changed, as shown in Fig. 3-10 (b). The darker the color, the higher the concentration of H<sub>2</sub> is of the headspace. Because the camera takes an image every six minutes, we have a total of 180 images. For each image, the hydrogen production is calculated for each vial using the relationship determined in the calibration experiment. The hydrogen productions from each vial as a function of reaction time for each vial are shown in Fig. 3-10 (c). The ranges of the x-axis and y-axis are (0 to 18 h) and (0 to 35  $\mu\text{mol}$ ). The three labels on the y-axis are 4  $\mu\text{mol}$ , 8  $\mu\text{mol}$  and 12  $\mu\text{mol}$ . The data in Fig. 3-10 (c) is consistent with our direct observation of on Fig. 3-10 (b). To process the data, these curves are fitted with a logarithmic model because the rate of back reactions increase with the pressure in the head space.

The maximum slope of the logarithmic fitted curve is used as the generation rate. A detailed illustration of the reactor setup, calibration and operation is provided in Appendix 4.

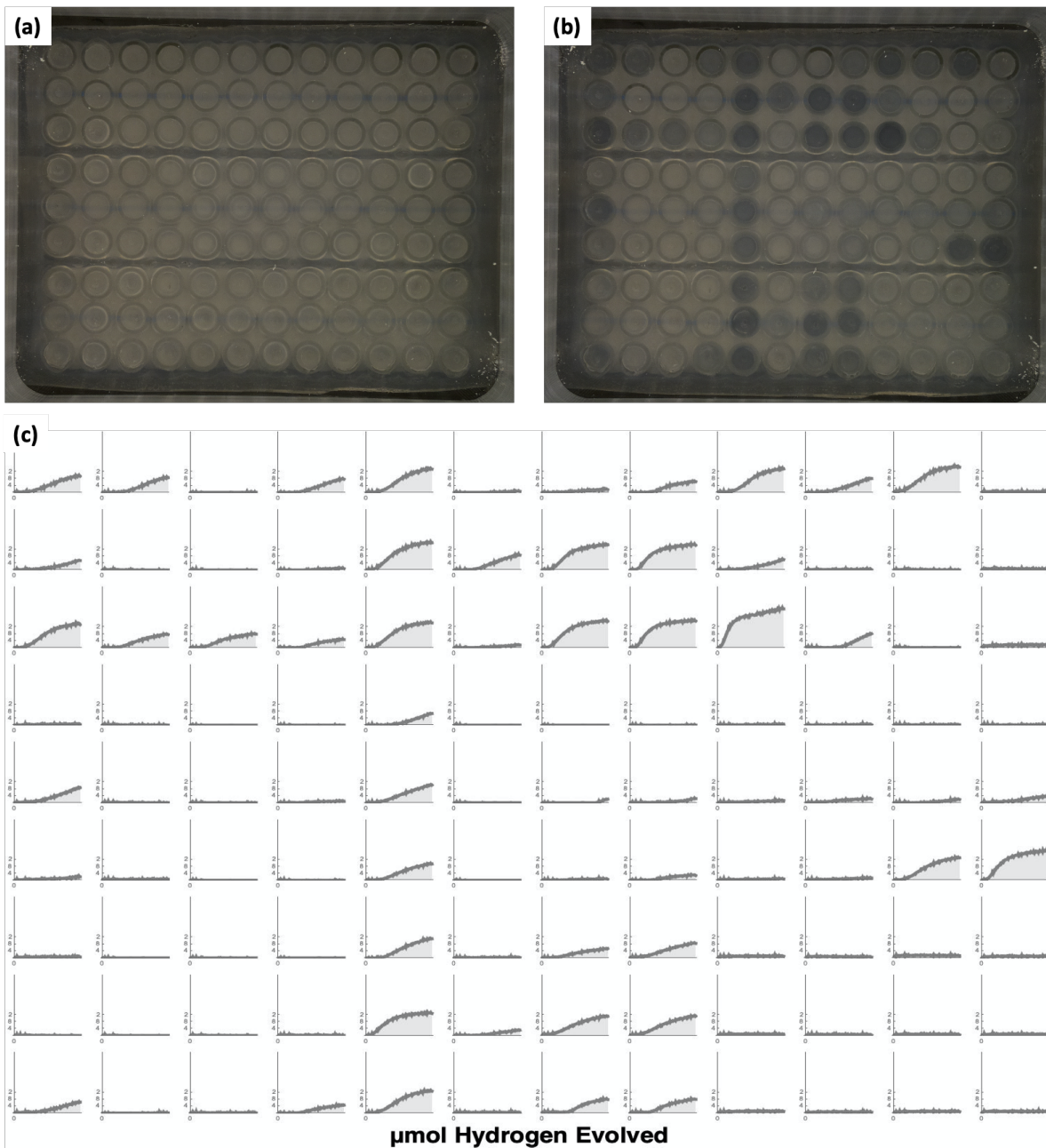


**Figure 3-10:** Image of H<sub>2</sub> detect film is shown in (a) before reaction and (b) after an experiment of 18 h. (c) The amount of H<sub>2</sub> evolved ( $\mu\text{mol}$ ) versus time (h) for each vial has been calculated and shown.

### 3.12 References

- (1) Binnig, G.; Quate, C. F.; Gerber, C. Atomic Force Microscope. *Phys. Rev. Lett.* **1986**, *56*

- (9), 930–933. <https://doi.org/10.1103/PhysRevLett.56.930>.
- (2) Sinha Ray, S. 3 - Structure and Morphology Characterization Techniques. In *Clay-Containing Polymer Nanocomposites*; Sinha Ray, S., Ed.; Elsevier: Amsterdam, 2013; pp 39–66. <https://doi.org/10.1016/B978-0-444-59437-2.00003-X>.
- (3) Voigtländer, B. *Scanning Probe Microscopy*; Springer, Berlin, Heidelberg, 2015. <https://doi.org/10.1007/978-3-662-45240-0>.
- (4) Dufrêne, Y. F.; Ando, T.; Garcia, R.; Alsteens, D.; Martinez-Martin, D.; Engel, A.; Gerber, C.; Müller, D. J. Imaging Modes of Atomic Force Microscopy for Application in Molecular and Cell Biology. *Nat. Nanotechnol.* **2017**, *12* (4), 295–307. <https://doi.org/10.1038/nnano.2017.45>.
- (5) Gruverman, A.; Alexe, M.; Meier, D. Piezoresponse Force Microscopy and Nanoferroic Phenomena. *Nat. Commun.* **2019**, *10* (1), 1661. <https://doi.org/10.1038/s41467-019-09650-8>.
- (6) Alexe, M.; Gruverman, A. *Nanoscale Characterisation of Ferroelectric Materials*; Springer, Berlin, Heidelberg, 2004. <https://doi.org/10.1007/978-3-662-08901-9>.
- (7) Holder, C. F.; Schaak, R. E. Tutorial on Powder X-Ray Diffraction for Characterizing Nanoscale Materials. *ACS Nano* **2019**, *13* (7), 7359–7365. <https://doi.org/10.1021/acsnano.9b05157>.
- (8) Waseda, Y.; Matsubara, E.; Shinoda, K. *X-Ray Diffraction Crystallography: Introduction, Examples and Solved Problems*; Springer, 2011.
- (9) Goldstein, J.; Goldshtain, Y.; Goldstein, J. A.; Media, S. S.; Newbury, D. E.; Joy, D. C.; Echlin, P.; Lyman, C. E.; E, D.; others. *Scanning Electron Microscopy and X-Ray Microanalysis: Third Edition*; Scanning Electron Microscopy and X-ray Microanalysis; Springer US, 2003.
- (10) Scanning Electron Microscopy. In *Materials Characterization*; John Wiley & Sons, Ltd, 2013; pp 127–161. <https://doi.org/10.1002/9783527670772.ch4>.

- (11) Nishikawa, S.; Kikuchi, S. Diffraction of Cathode Rays by Calcite. *Nature* **1928**, *122* (3080), 726. <https://doi.org/10.1038/122726a0>.
- (12) Nishikawa, S.; Kikuchi, S. Diffraction of Cathode Rays by Mica. *Nature* **1928**, *121* (3061), 1019–1020. <https://doi.org/10.1038/1211019a0>.
- (13) Schwartz, A. J.; Kumar, M.; Adams, B. L.; Field, D. P. *Electron Backscatter Diffraction in Materials Science*; Springer US, 2010.
- (14) Williams, D. B.; Carter, C. B. *Transmission Electron Microscopy: A Textbook for Materials Science*; Cambridge library collection; Springer, 2009.
- (15) Brunauer, S.; Emmett, P. H.; Teller, E. Adsorption of Gases in Multimolecular Layers. *J. Am. Chem. Soc.* **1938**, *60* (2), 309–319. <https://doi.org/10.1021/ja01269a023>.
- (16) Langmuir, I. The Adsorption of Gases on Plane Surfaces of Glass, Mica And Platinum. *J. Am. Chem. Soc.* **1918**, *40* (9), 1361–1403. <https://doi.org/10.1021/ja02242a004>.
- (17) Tauc, J.; Grigorovici, R.; Vancu, A. Optical Properties and Electronic Structure of Amorphous Germanium. *Phys. status solidi* **1966**, *15* (2), 627–637. <https://doi.org/10.1002/pssb.19660150224>.
- (18) Kubelka, P.; Munk, F. An Article on Optics of Paint Layers. *Z. Tech. Phys* **1931**, *12*, 593–601.
- (19) Makuła, P.; Pacia, M.; Macyk, W. How To Correctly Determine the Band Gap Energy of Modified Semiconductor Photocatalysts Based on UV–Vis Spectra. *J. Phys. Chem. Lett.* **2018**, *9* (23), 6814–6817. <https://doi.org/10.1021/acs.jpcclett.8b02892>.
- (20) Giocondi, J. L.; Rohrer, G. S. Spatial Separation of Photochemical Oxidation and Reduction Reactions on the Surface of Ferroelectric BaTiO<sub>3</sub>. *J. Phys. Chem. B* **2001**, *105* (35), 8275–8277. <https://doi.org/10.1021/jp011804j>.
- (21) Giocondi, J. L.; Rohrer, G. S. Orientation Dependence of Photochemical Reduction Reactions on SrTiO<sub>3</sub> Surfaces. *MRS Proc.* **2002**, *751*, Z2.4. <https://doi.org/10.1557/PROC-751-Z2.4>.

- (22) Giocondi, J. L.; Rohrer, G. S. The Influence of the Dipolar Field Effect on the Photochemical Reactivity of  $\text{Sr}_2\text{Nb}_2\text{O}_7$  and  $\text{BaTiO}_3$  Microcrystals. *Top. Catal.* **2008**, *49* (1), 18. <https://doi.org/10.1007/s11244-008-9067-2>.
- (23) Pisat, A. S.; Rohrer, G. S.; Salvador, P. A. Spatial Selectivity of Photodeposition Reactions on Polar Surfaces of Centrosymmetric Ferroelastic Gamma- $\text{WO}_3$ . *J. Mater. Chem. A* **2017**, *5* (18), 8261–8266. <https://doi.org/10.1039/c7ta00842b>.
- (24) Munprom, R.; Salvador, P. A.; Rohrer, G. S. Ferroelastic Domains Improve Photochemical Reactivity: A Comparative Study of Monoclinic and Tetragonal  $(\text{Bi}_{1-0.5x}\text{Na}_{0.5x})(\text{V}_{1-x}\text{Mo}_x)\text{O}_4$  Ceramics. *J. Mater. Chem. A* **2016**, *4* (8), 2951–2959. <https://doi.org/10.1039/c5ta05551b>.
- (25) Lopato, E. M.; Eikey, E. A.; Simon, Z. C.; Back, S.; Tran, K.; Lewis, J.; Kowalewski, J. F.; Yazdi, S.; Kitchin, J. R.; Ulissi, Z. W.; et al. Parallelized Screening of Characterized and DFT-Modeled Bimetallic Colloidal Cocatalysts for Photocatalytic Hydrogen Evolution. *ACS Catal.* **2020**, *10* (7), 4244–4252. <https://doi.org/10.1021/acscatal.9b05404>.

## Chapter 4: Influence of Orientation and Ferroelectric Domains on the Photochemical Reactivity of $\text{La}_2\text{Ti}_2\text{O}_7$

*Previous studies indicate that the distribution of photogenerated charge carriers on the surface is influenced by the ferroelectric polarization. However, is this always true? In this chapter, I am going to introduce a counter example.  $\text{La}_2\text{Ti}_2\text{O}_7$  is a ferroelectric material, and it also has a strongly anisotropic structure. In this study, complex domain structures were observed within the grains, but they appeared to have no effect on the photocathodic reduction of silver, in contrast to previous observations on other ferroelectrics.  $\text{La}_2\text{Ti}_2\text{O}_7$  is an example of a ferroelectric oxide in which the crystal orientation has a greater influence on the photochemical reactivity than polarization from the internal domain structure.*

### 4.1 Introduction

Metal oxide semiconductors can be used to split water<sup>1,2</sup> and degrade organic pollutants<sup>3,4</sup>. Hydrogen derived from water splitting could be used as a fuel that would not increase the concentration of atmospheric  $\text{CO}_2$ . Since the discovery that water could be split using a  $\text{TiO}_2$  photoanode and a Pt cathode,<sup>5</sup> many other metal oxides have been shown to be able to split water.<sup>6,7</sup> However, none of the materials studied so far are able to produce hydrogen at rates that make it economically competitive with producing hydrogen by the conventional steam reforming of methane.<sup>8</sup> This has motivated studies of reaction mechanisms and sources of efficiency losses with the hope that improved catalysts can be developed.<sup>9</sup>

One line of inquiry has been directed at determining the orientation dependence of the photochemical reactivity with the goal of designing ideal particle shapes that maximize reactivity. For example, the orientation dependence of the reactivity has been determined for rutile<sup>10</sup> and anatase<sup>11</sup>  $\text{TiO}_2$ ,  $\text{BiVO}_4$ ,<sup>12,13</sup>  $\text{Fe}_2\text{O}_3$ ,<sup>14</sup>  $\text{CaTiO}_3$ ,<sup>15</sup> and  $\text{SrTiO}_3$ .<sup>16-18</sup> There are two main findings from these studies. The first is that surfaces with different crystallographic orientations can have very different reactivities. The second is that some orientations are (relatively) more photocathodic and others are more photoanodic. This provides a mechanism for charge carrier separation, making it possible to localize the reduction reaction on one surface and the oxidation reaction on another. This is thought to reduce recombination and lead to improved efficiency.<sup>19</sup>

A second line of inquiry has been to use the positively and negatively charged domains of ferroelectrics to spatially separate the oxidation and reduction reactions and therefore improve efficiency.<sup>20</sup> For example, domain selective oxidation and reduction reactions have been reported on  $\text{Pb}(\text{Zr},\text{Ti})\text{O}_3$ ,<sup>21-23</sup>  $\text{BaTiO}_3$ ,<sup>24</sup> and  $\text{BiFeO}_3$ <sup>25</sup> surfaces. Considering these two lines of inquiry, the question arises: how do the influence of crystal orientation and the presence of ferroelectric domains interact to influence reactivity? Previously, we have examined the combined influence of orientation and charged ferroelastic (rather than ferroelectric) domains, and found that orientation was the more important parameter.<sup>13,15</sup> We have also examined the combined influence of orientation and charged surface terminations and also found that orientation was the more important parameter.<sup>18</sup> However, the combined effects of ferroelectric polarization and orientation have not been explored in detail. Studies of  $\text{BaTiO}_3$ <sup>26</sup> and  $\text{BiFeO}_3$ <sup>25</sup> suggested that orientation is less important than the domain structure, but these studies were based on a relatively small number of observations.

Here we study the combined influence of ferroelectric domains and crystal orientation in  $\text{La}_2\text{Ti}_2\text{O}_7$ , a ferroelectric with the  $(110)_p$  layered perovskite structure.<sup>27,28</sup> Throughout this chapter, directions in the layered perovskite structure will be denoted with a subscript "p". The crystal structure, illustrated in Figure 4-1, has layers along  $[001]$  within which  $\text{TiO}_6$  octahedra share corners along  $[100]$  and  $[011]$ , as in the perovskite structure. Materials with this structure have the distinction of having very high Curie temperatures ( $T_C$ ), which make them candidate materials for applications as high temperature piezoelectrics. Examples include,  $\text{La}_2\text{Ti}_2\text{O}_7$  ( $T_C \sim 1500$  °C),<sup>29</sup>  $\text{Sr}_2\text{Nb}_2\text{O}_7$  ( $T_C \sim 1330$  °C),<sup>30</sup> and  $\text{Pr}_2\text{Ti}_2\text{O}_7$  ( $T_C \sim 1750$  °C).<sup>31</sup>  $\text{Sr}_2\text{Nb}_2\text{O}_7$  and  $\text{La}_2\text{Ti}_2\text{O}_7$  have been reported to split water under ultraviolet (UV) illumination.<sup>32</sup> Consistent with this observation,  $\text{La}_2\text{Ti}_2\text{O}_7$  has a band gap of 3.2-3.8 eV<sup>32-35</sup> and band edge positions suitable to for the photocathodic reduction and photoanodic oxidation of  $\text{H}_2\text{O}$ .  $\text{La}_2\text{Ti}_2\text{O}_7$  has a monoclinic structure with space group  $\text{P}2_1$  ( $a = 7.811$  Å,  $b = 5.547$  Å,  $c = 13.019$  Å,  $\beta = 98.28^\circ$ ) and its ferroelectric polarization is along the  $[010]$  axis.<sup>31,36</sup>

Following the observation that  $\text{La}_2\text{Ti}_2\text{O}_7$  could split water, efforts have been made to modify its photochemical properties through doping and the formation of heterostructures. For example, Nashim et al.<sup>37</sup> have fabricated an n- $\text{La}_2\text{Ti}_2\text{O}_7$ /p- $\text{LaCrO}_3$  heterostructure with an enhanced photoactivity.  $\text{La}_2\text{Ti}_2\text{O}_7/\text{In}_2\text{O}_3$  heterojunction nanocomposites synthesized by Hu et al.<sup>38</sup> had an

improved rate of hydrogen generation compared to the individual materials. Meng et al.<sup>39</sup> doped  $\text{La}_2\text{Ti}_2\text{O}_7$  nanosheets with nitrogen and narrowed the band gap, extending the light absorption into visible light ( $\sim 495$  nm). Hwang et al.<sup>33</sup> investigated the effect of Cr and Fe doping and produced hydrogen in the presence of methanol using visible light irradiation ( $\sim 420$  nm).

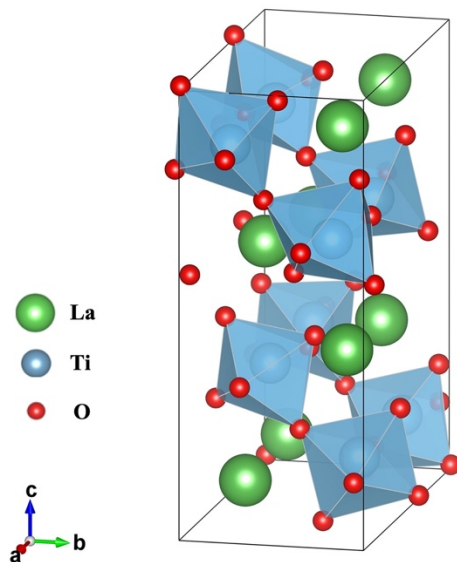


**Figure 4-1:** Crystal structure of  $\text{La}_2\text{Ti}_2\text{O}_7$  with  $\text{TiO}_6$  octahedra shown. The polarization direction is along  $[010]$  axis.

The purpose of this chapter is to describe the relative importance of crystal orientation and ferroelectric domain orientation on the photochemical properties of  $\text{La}_2\text{Ti}_2\text{O}_7$ . The polarization of the ferroelectric domains in  $\text{La}_2\text{Ti}_2\text{O}_7$  ( $5 \mu\text{C}/\text{cm}^2$ )<sup>36,40</sup> is similar to that of  $\text{BiFeO}_3$  ( $6 \mu\text{C}/\text{cm}^2$ ), so one might assume that would behave similarly. On the other hand, the  $(110)_p$  layered perovskite structure of  $\text{La}_2\text{Ti}_2\text{O}_7$  is much more anisotropic than  $\text{BiFeO}_3$ , so the orientation is also likely to influence reactivity. To quantify these effects, we have produced dense polycrystalline  $\text{La}_2\text{Ti}_2\text{O}_7$  ceramics and measured grain orientations by electron backscatter diffraction (EBSD). The domain structure in the grains was also measured by piezo-force microscopy (PFM). After performing a photochemical marker reaction that leaves insoluble silver at the reaction<sup>10,41</sup> it is possible to compare the patterns of reaction products to the grain orientation and domain structure. It has been found that the patterns of photochemically reduced silver are not correlated to the domain structure, but are correlated to the crystal orientation.

## 4.2 Experimental Methods

**Sample preparation.**  $\text{La}_2\text{Ti}_2\text{O}_7$  powder was synthesized using a molten salt method.<sup>42</sup> Reagent-grade  $\text{La}_2\text{O}_3$  (99.99 %, Alfa Aesar) and  $\text{TiO}_2$  (99.9 %, CERAC) were mixed with a 1:2 ratio in deionized water. A salt with 50 mol % NaCl (Fisher) and 50 mol % KCl (Alfa Aesar) was then added to the mixture, constituting 50 wt % of the total reaction mixture. Then the mixture was ball-milled overnight in a plastic bottle with yttria stabilized zirconia as the grinding media. After ball milling, the mixture was dried in air at 80 °C and then heated to 1150 °C for 6 h in air in an alumina crucible. The cooled mass was washed with deionized water until the Powder X-ray diffraction (XRD) pattern showed that it was single phase  $\text{La}_2\text{Ti}_2\text{O}_7$  (see Figure 4-2).

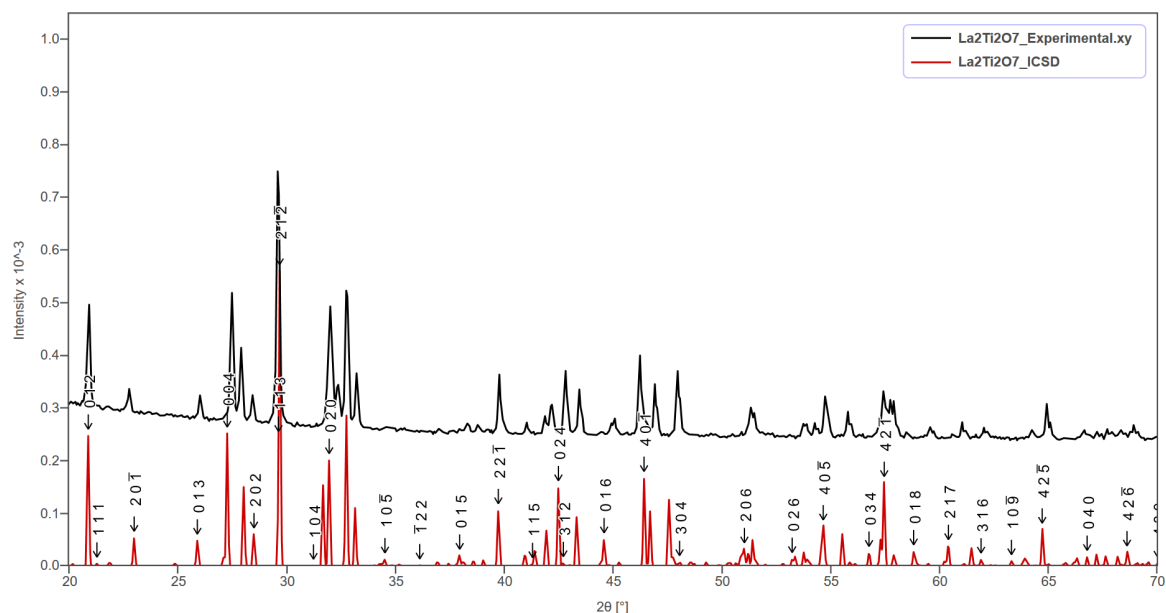


**Figure 4-2:** Black line corresponds to the XRD pattern of the  $\text{La}_2\text{Ti}_2\text{O}_7$  powder synthesized with molten salt method in this work. Red line corresponds to a calculated pattern of the  $\text{La}_2\text{Ti}_2\text{O}_7$ . (ICSD IDs: 5416 1950)

Polycrystalline ceramics were prepared from the  $\text{La}_2\text{Ti}_2\text{O}_7$  powder. Disk-shaped samples were formed by pressing the powders in a die, with a few drops of PVA as binder, using 130 MPa of pressure from a hydraulic press. The resulting disks had a diameter of 1 cm and a thickness of 3 mm. The samples were then put in an alumina crucible with some excess powder to ensure that the pellet did not contact the crucible. The samples were calcined at 900 °C for 8 h, sintered at

1350 °C for 10 h, and coarsened at 1550 °C for 3 h. A flat surface was achieved by grinding with 600, 800, and 1200 grit silicon carbide abrasive papers (Buehler), and polishing with a series of diamond suspensions (Buehler) with a final suspension of 0.05 μm. The polished samples were then annealed at 1300 °C for 6 h to repair polishing damage and thermally etch the grain boundaries. After annealing, the microstructure consisted of randomly oriented plate-shaped grains with apparent grain diameters in the two-dimensional section plane ranging from 2 to 50 μm. The large range of apparent grain sizes arises from differently oriented sections through the anisotropically shaped grains. Finally, XRD was used to verify that the sample remained single phase La<sub>2</sub>Ti<sub>2</sub>O<sub>7</sub>.

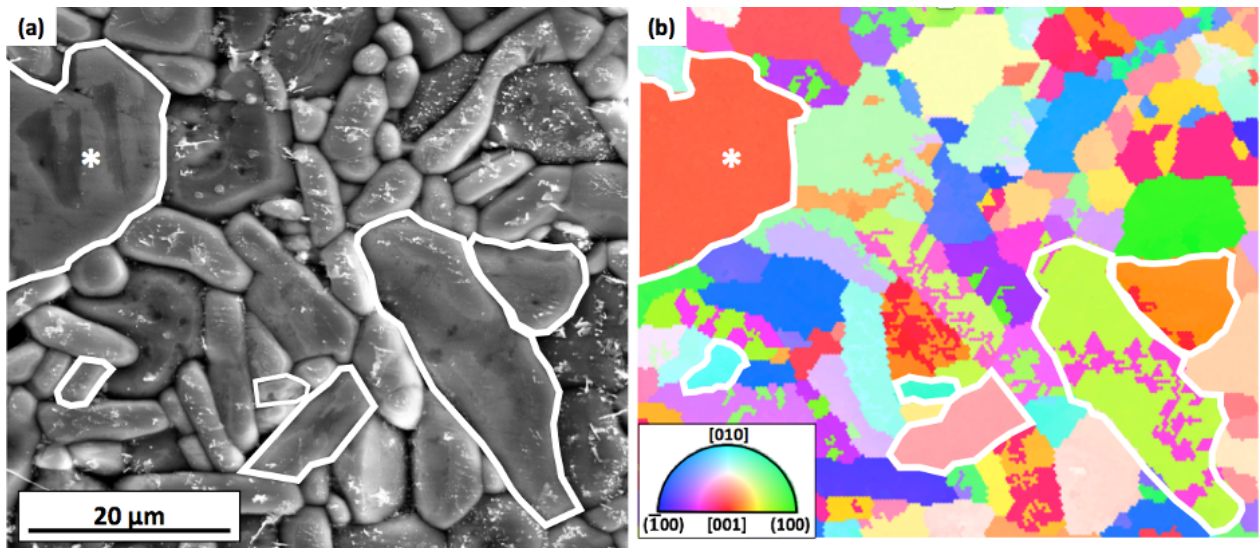
**Characterization.** EBSD was used to measure the orientations of the crystals at the surface of the La<sub>2</sub>Ti<sub>2</sub>O<sub>7</sub> ceramic with a FEI Quanta 200 scanning electron microscope (SEM) operated in low vacuum mode. EBSD patterns were recorded with a step size of ~ 0.5 μm and indexed by the TSL orientation imaging microscopy (OIM) software using the P2<sub>1</sub> monoclinic Pr<sub>2</sub>Ti<sub>2</sub>O<sub>7</sub> structure as a reference,<sup>35</sup> but with the lattice parameter adjusted to La<sub>2</sub>Ti<sub>2</sub>O<sub>7</sub> ( $a = 7.8114 \text{ \AA}$ ,  $b = 5.5474 \text{ \AA}$ ,  $c = 13.0185 \text{ \AA}$ ,  $\beta = 98.719^\circ$ ). The data was then processed in OIM Analysis Software. A grain dilation clean-up was applied using a 5° tolerance angle, a 10-pixel minimum grain size and a multiple row requirement. All of the orientations segmented to be part of a single grain were then used to determine a single average orientation for each grain.

A NT-MDT Solver NEXT atomic force microscope (AFM) was used to record topographic and PFM images. Images were formed using conductive probes with a Pt/Ir coating from Nanoworld (ARROW-EFM). An AC bias of 4 V with a frequency of approximately 350 kHz was used where the first contact resonance was observed. Because of the sample's low electronic conductivity, it had to be thinned to less than 1.5 mm in thickness and copper contacts had to be applied to the top and bottom of the sample. The sample was cleaned with acetone before and after the PFM measurements. The samples were then used to reduce Ag<sup>+</sup> with photochemical marker reactions. An O-ring was placed on the top of the sample, and a few drops of 0.115 M AgNO<sub>3</sub> (Acros) aqueous solution were added to fill the O-ring, and a quartz slip was placed on the top to seal the liquid. The sample was then illuminated by a mercury lamp (Newport) operated at 150 W for 20 min. After illumination, the sample was rinsed in DI water and dried with a stream from an aero duster (Miller-Stephenson). The locations of silver deposits were determined using an FEI Quanta 200 SEM with a 20 kV beam with a spot size of 4. Before any subsequent reaction, the sample

was wiped with cotton swabs and ultrasonically cleaned in methanol and acetone. SEM was used to make sure the silver deposits on the surfaces had been removed. It was not always possible to remove all of the silver that accumulated at the bottoms of pores or grain boundary grooves; data from these regions were not interpreted and did not influence the results.

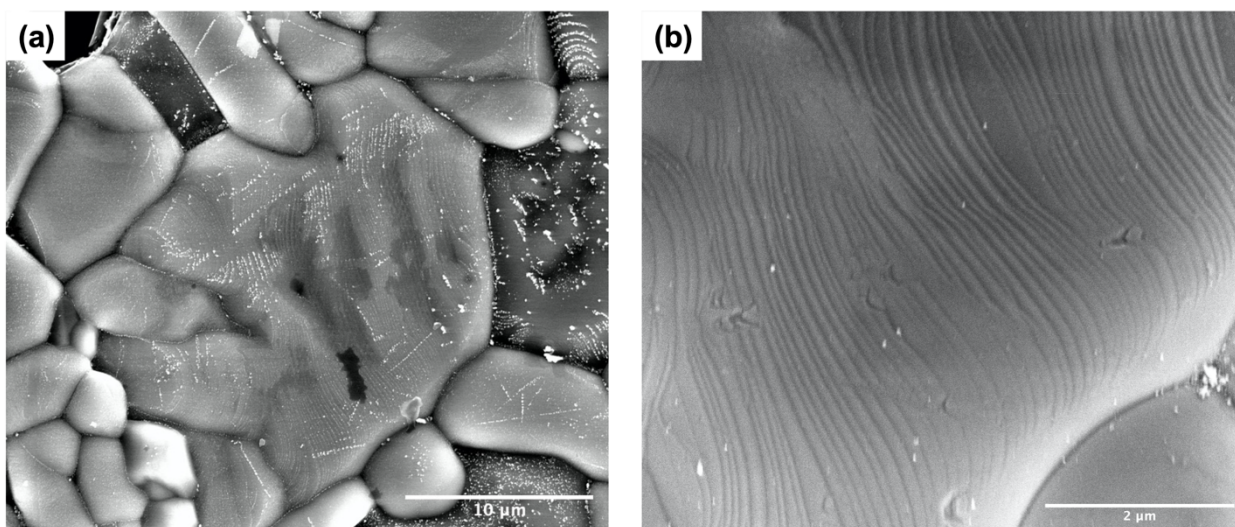
### 4.3 Results

Figure 4-3(a) shows a SEM image of the surface after the photodeposition of silver. For comparison, an EBSD orientation map of the same region is shown in Figure 4-3(b). To make it easier to find the same grains in the two images, six grains are surrounded by thick white lines. Note that in this two-dimensional section, some grains are elongated while others are more equiaxed. This results from the fact that the grains are relatively plate-shaped, with large (001) faces; sections parallel to (001) appear more equiaxed (red colored grains in Figure 4-3(b)) and perpendicular sections appear elongated. Also, within some grains, two distinct colors appear that correspond to two different orientations. Because the local structure within the  $a$ - $b$  planes is similar to perovskite, the [100] and [010] directions are sometimes incorrectly assigned by the indexing software. In these cases, we assumed the majority assignment was correct. The OIM Analysis Software assigns a 'confidence index' (CI) to each grain orientation and it was assumed that the orientations of grains with a  $CI \geq 0.1$  are correct.



**Figure 4-3:** (a) SE image after silver reduction. (b) Orientation map of the same area with a color key at bottom left. The field of view is about  $50\ \mu\text{m} \times 60\ \mu\text{m}$ . Six grains have been outlined to illustrate the correspondence between the two images.

The SEM image in Figure 4-3(a) does not have sufficient resolution to determine the amount of reduced silver. To illustrate this, the image in Figure 4-4 shows a higher resolution image of the region around the large [001] oriented (red) grain in the upper left-hand quadrant of Figure 4-3 (this grain is labeled with an asterisk). High densities of small particles of reduced silver, especially at steps, that are invisible in Figure 4-3(a) are clearly imaged in Figure 4-4 (a). Fig. 4-4(b) show that SEM image of the same grain with a higher magnification. It is found that silver particles prefer to accumulate on terraces but near the step edges. Note that when Fig. 4-4 (b) was captured, the sample has been kept for years so that the reactivity reduced significantly under the same experiment condition.



**Figure 4-4:** (a) A higher resolution SEM image after reaction for the large grain labeled “H” at left top of Figure 4-3(a), which is “near red” (near (001)) in Figure 4-3(b). (b) SEM images of the same grain after reaction with a larger magnification. The sample has been kept for years so that the reactivity reduced.

To quantitatively determine the amount of silver on each grain, the number of silver deposits were counted on high resolution images (see Figure 4-5) using the linear intercept method; several test lines are plotted on each grain and we count the number of deposits intercepted by each line. The average number of intercepts from all lines on a single grain is taken as the number of deposits on each grain. The data was then discretized into two categories: low reactivity (average deposits <

5) or high reactivity (average deposits > 5). Grains with high reactivity usually have a relatively dense uniform coverage of silver deposits. Grains with low reactivity usually have an inhomogeneous silver coverage with a few large deposits on part of the surface. While the reason for this difference is not known, one might speculate that the many particles on the high reactivity grains have limited growth because they compete for silver cations in the vicinity. Examples of high and low reactivity grains are shown in Figure 4-5. Note that the orientation determined by EBSD is the average grain orientation with respect to the macroscopic surface orientation. The surfaces of the grains are actually curved, so the local orientation is not always the same as the macroscopic grain orientation and this accounts for the local variations in the amount of silver. The rationale for discretizing the results into only two categories is to avoid some of the uncertainties associated with orientation measurement and local surface curvature.

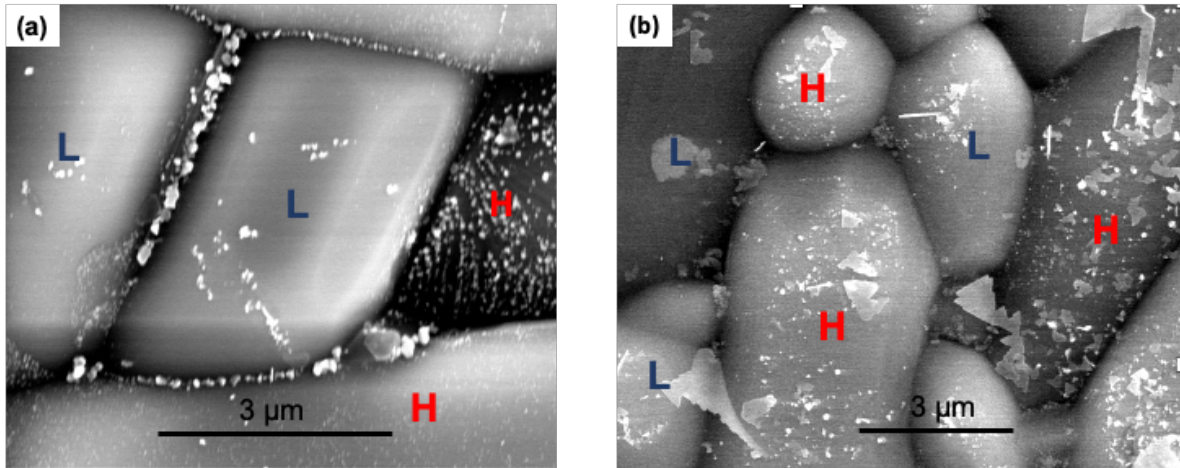


**Figure 4-5:** SEM images of  $\text{La}_2\text{Ti}_2\text{O}_7$  surfaces after the photochemical reduction of silver. High-reactivity grains are labeled with "H" while low-reactivity grains are labeled with "L".

To determine the orientation dependence of silver reduction, the numbers of silver deposits were measured on about 90 grains. Figure 4-6 summarize the results, where the orientations of the high and low reactivity grain are plotted in Figures 4-6(a) and 4-6(b), respectively. High-reactivity grains appear to be clustered near (001), and the number of these grains decreases with inclination from (001). The low reactivity grains have an approximately opposite distribution. There are no low reactivity grains within  $30^\circ$  of (001), and an increasing number of them are found further from the (001) orientation. Note that [010] is the polar axis and there is no evidence that this is a high-reactivity orientation.

The distributions of high and low reactivity orientations in Figure 4-6 suggest that the results can be discriminated by a single variable, the inclination from the (001) orientation. This is similar to the method used by Munprom et al.<sup>13</sup> to understand the results from monoclinic BiVO<sub>4</sub>. Here, the angles of inclination of the grains from (001) are classified in bins that are 10° wide. By analyzing a large number of randomly generated orientations, we can determine the fraction of observations that should be found in each bin, if the grains were randomly oriented. The fraction of the observations found in each bin, divided by the fraction expected in a random distribution, quantifies the population in units of multiples of a random distribution (MRD), as illustrated in Figure 4-7. The data for this calculation are shown in Table 4-1. These results clearly show low reactivity orientations occur at a frequency greater than random for grains inclined by more than 60° from (001). Similarly, high reactivity orientations occur with a greater than random frequency within 30° of (001) and no low reactivity grains are found in this orientation domain. Note that correlating the relative reactivity to a single orientation parameter (the inclination from (001)) ameliorates problems stemming from the difficulty of distinguishing the [100] and [010] axes from the EBSD patterns.

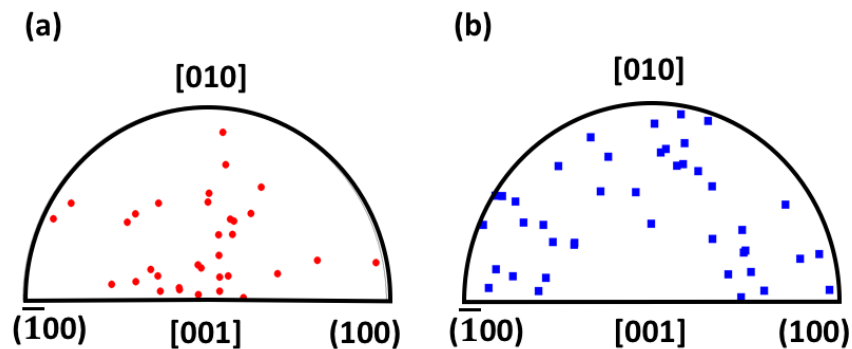


**Figure 4-6:** Orientations of La<sub>2</sub>Ti<sub>2</sub>O<sub>7</sub> grains with high reactivity and low reactivity are labeled in (a) and (b), respectively. Each point corresponds to a grain and the points are plotted in the standard stereographic projection for monoclinic crystals.

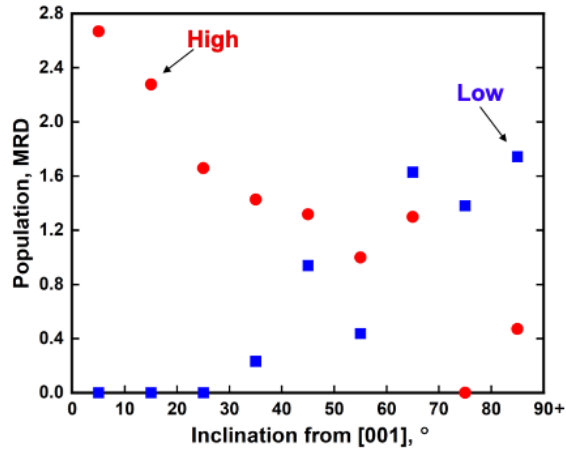


**Figure 4-7:** The orientation distribution of grains with high reactivity (red circles) and low reactivity (blue squares) for the photochemical reduction of silver. The units are multiples of a random distribution (MRD).

**Table 4-1:** Details of population analysis in Fig. 4-7.

	Total Grains (#)	Random Population	High Reactivity (#)	High Reactivity (MRD)	Low Reactivity (#)	Low Reactivity (MRD)
0°~10°	2	0.015298	2	2.66808	0	0
10°~20°	5	0.044812	5	2.27707	0	0
20°~30°	6	0.073812	6	1.65893	0	0
30°~40°	8	0.10015	7	1.42643	1	0.23221
40°~50°	13	0.12384	8	1.31835	5	0.93895
50°~60°	10	0.14309	7	0.99837	3	0.48758
60°~70°	21	0.15710	10	1.29906	11	1.62835
70°~80°	10	0.16841	0	0	10	1.3809
80°~90+°	17	0.17349	4	0.47053	13	1.74261

To investigate whether ferroelectric domains influenced local reactivity, PFM was used to image grains whose orientation and relative reactivity were already measured. Out-of-plane PFM amplitude and phase images from the same grain are shown in Figure 4-8(a) and (b), respectively. The amplitude image in Figure 4-8(a) shows clear bright / dark contrast, indicative of domains with complex shapes. The PFM phase image in Figure 4-8(b) shows strong white/black contrast on the two sides of the boundary, indicating that this is a 180° domain boundary, consistent with our expectation for  $\text{La}_2\text{Ti}_2\text{O}_7$  that domains that have polarization vectors of identical strength and opposite directions along  $[0\pm 10]$ .<sup>30,36</sup> This particular grain was oriented 30.1° from the polar  $[010]$  axis. While this is not very close to the polar axis, our previous work indicates that there should

still be a measurable polarization (though lower than along the polar axis) normal to the surface, consistent with the PFM observations.<sup>43</sup> The meandering structure of the domain wall is similar to that observed in single crystals, even though the feature size is smaller in the grains of the polycrystal.<sup>36</sup> The domains observed in  $\text{La}_2\text{Ti}_2\text{O}_7$  thin films are usually smaller than  $1\ \mu\text{m}$  and do not have the same meandering structure.<sup>44,45</sup>

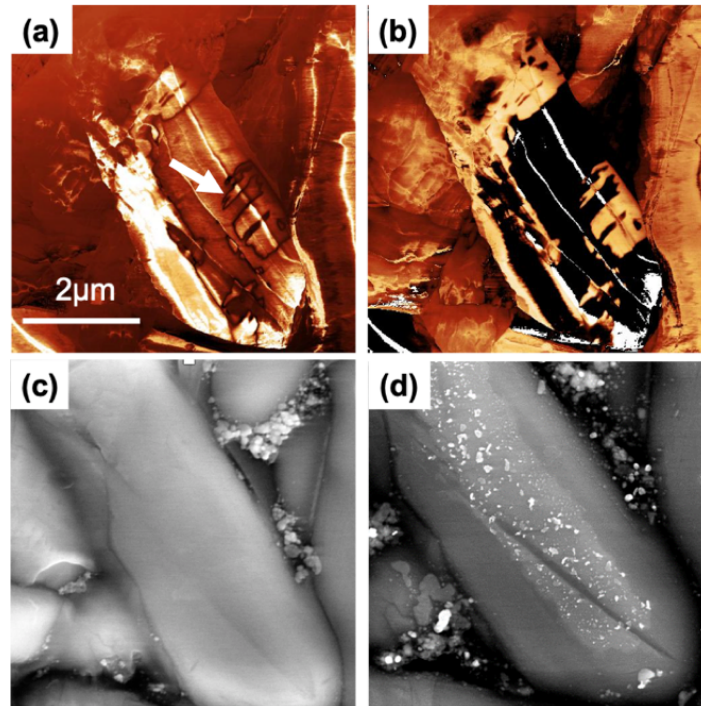


**Figure 4-8:** A  $\text{La}_2\text{Ti}_2\text{O}_7$  grain imaged with different modalities. (a) a PFM out-of-plane amplitude image. (b) a PFM out-of-plane phase image. A meandering black line in (a), marked by the arrow, corresponds to a change from light to dark contrast in the phase image. The dark (light) contrast corresponds to regions with  $-180^\circ$  ( $0^\circ$ ) phase shift. (c & d) SEM images of the grain before (c) and after (d) photochemical silver reduction.

SEM images of the same grain shown in PFM images are shown in Figure 4-8(c) and (d), before and after photochemical silver reduction, respectively. The brightest contrast in Figure 4-8(d) corresponds to silver deposits. The silver deposition is non-uniform; in this case it accumulates mainly on the central part of the grain and in the grain boundary grooves (silver in the grooved regions is not counted). Note that the grain surface is curved because of the grain boundary grooves. The central part is flat and has the macroscopic orientation measured by EBSD, while the periphery slopes downward at an angle of approximately  $10^\circ$ . In other words, the periphery of the grain has a different surface orientation and, therefore, a different reactivity. More importantly,

the patterns of deposited Ag in Figure 4-8(d) do not correlate with the patterns of PFM contrast. Figure 4-9 shows images of a grain (running from top left to bottom right through the center of all images) whose orientation is inclined by about  $48^\circ$  from the polar [010] axis. Figures 4-9(a) and 4-9(b) are SE images showing the surface before and after the photochemical reduction of silver, respectively. Figures 4-9(c) and 4-9(d) are PFM out-of-plane images, respectively of the amplitude and phase, of the same grain. Similar to the results shown in Figure 4-8, silver did not deposit uniformly and there is no correlation between silver pattern and PFM pattern. Note that there is an artifact in the PFM image where the complex shape of the domain is repeated; this results from the sloped surface, which sometimes causes the image to be formed from different areas of the tip. Ferroelectric domains in this ceramic sample have sizes as large as several micrometers. The absence of a correlation between the deposited silver and PFM contrast contradicts prior studies of ferroelectrics including  $\text{BaTiO}_3$ ,<sup>26</sup>  $\text{Pb}(\text{Zr},\text{Ti})\text{O}_3$ ,<sup>23</sup> and  $\text{BiFeO}_3$ ,<sup>25</sup> in which domain selective reactivity was routinely observed.

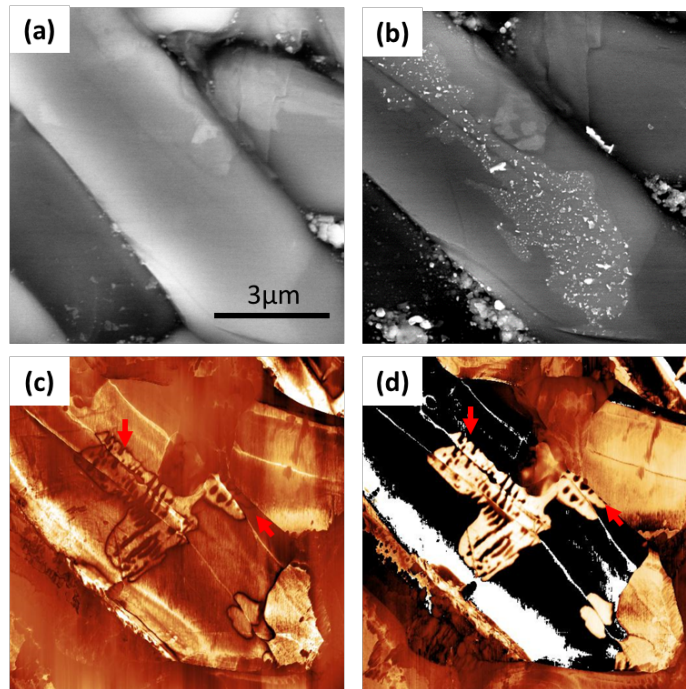


**Figure 4-9:** (a) an SEM image before reaction. (b) an SEM image of the same grain after silver reduction. (c) a PFM out-of-plane amplitude image of the same grain. (d) a PFM out-of-plane phase image of the same grain. Darker regions correspond to domains with positive polarizations, and brighter regions correspond to domains with negative polarizations. Arrows in (c) and (d) mark artifacts caused by a tip issue (see text).

Figures 4-10(a) and 4-10(b) show an example of the reactivity and domain structure of a grain that is closer to the (010) orientation. In this case, the grain normal is inclined by  $17.6^\circ$  from the polar axis. Positive domains, which have bright contrast, are marked with a "+" and negative domains, which have dark contrast, are marked with a "-". In contrast with the surrounding grains, the grain near (010) reduces a very small amount of silver (see Figure 4-10(a)), regardless of which domain is considered. Therefore, the domain structure has no observable influence on the reduction of silver (or absence thereof).

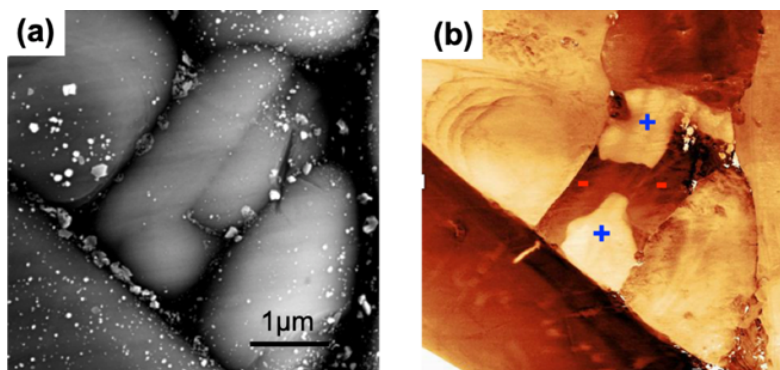


**Figure 4-10:** (a) SE image of a surface after photochemical silver reduction. The surface orientation of the grain in the middle is  $17.6^\circ$  from (010). (b) PFM out-of-plane image of the same area on sample. Positive domains are labeled with "+" while negative domains are labeled with "-".

## 4.4 Discussion

The  $\text{La}_2\text{Ti}_2\text{O}_7$  structure is anisotropic, being made up of two-dimensional slabs of the perovskite structure (with four  $\text{LaTiO}_3$  perovskite layers) truncated along the  $[110]$  cubic perovskite direction (referred to as  $[110]_p$ ). These slabs are layered parallel to the  $\text{La}_2\text{Ti}_2\text{O}_7$  (001) planes, with excess oxygen ( $\text{O}_2$ ) in the interlayer space between the slabs (and a concomitant relaxation of La into the region between the slabs). Hwang et al.<sup>46</sup> and Bruyer et al.<sup>47</sup> have calculated the electronic structure of  $\text{La}_2\text{Ti}_2\text{O}_7$  and found that it has a direct band gap. Because materials that have direct band gaps absorb light efficiently, they suggested that this is one of the reasons it is a good water splitting catalyst. Hwang et al.<sup>46</sup> also suggested that the photocatalytic properties benefitted from the energetic separation of the empty Ti 3d levels, near the conduction band edge, from the empty La 4f levels, which might act as trap states.

Takata et al.<sup>48</sup> suggested that it was the layer structure that was responsible for the remarkable photocatalytic properties of  $\text{La}_2\text{Ti}_2\text{O}_7$ . Specifically, they suggested that the layers between the  $[110]_p$  oriented slabs provided additional active sites for the oxidation of water. If this were so, one would expect the orientations perpendicular to the  $[001]$  direction to appear active for oxidation. While we did not study the oxidation half of the reaction, we do know that these orientations are not active for reduction. When we compare the current results to the orientation dependent reactivity of other titanates with the perovskite and perovskite-related structures, there is little similarity, suggesting that the anisotropic layered structure influences the properties more than the local structural similarities with the perovskite structure. For example, to a first approximation, the (001) surface is structurally comparable to the  $(110)_p$  surface (the similarity depends specifically on which chemical plane is chosen). The results here show that for  $\text{La}_2\text{Ti}_2\text{O}_7$ , the photocathodic reaction occurs preferentially on the (001) surface, but in the perovskites  $\text{BaTiO}_3$ ,<sup>24</sup>  $\text{SrTiO}_3$ ,<sup>18</sup> and  $\text{CaTiO}_3$ ,<sup>15</sup> the comparable  $(110)_p$  orientation has the lowest photocathodic reactivity. The atomic structure of  $\text{La}_2\text{Ti}_2\text{O}_7$  surfaces has not, to our knowledge, been studied. The present study found that the surfaces are not faceted. However, for surfaces orientated near (001), steps were observed and this is consistent with previous studies.<sup>49,50</sup>

Calculations of the band structure reported by Bruyer et al.<sup>47</sup> indicate that the layered structure leads to significant differences in the band edge positions perpendicular and parallel to the layers. Specifically, they show that the conduction band edge in the  $[001]$  direction is about 0.3 eV lower in energy than the conduction band energy in the  $[010]$  direction (and the band gap differs by a similar amount). A schematic energy level diagram, illustrating the relative energies of the band edges perpendicular to the (001) and (010) planes, in the flat band condition, is illustrated in Figure 4-11. Based on this energy difference, there is a thermodynamic driving force for electrons, which promote the photocathodic reaction, to migrate toward the (001) surface; this is consistent with the observation that the (001) surface has the maximum photocathodic reactivity.

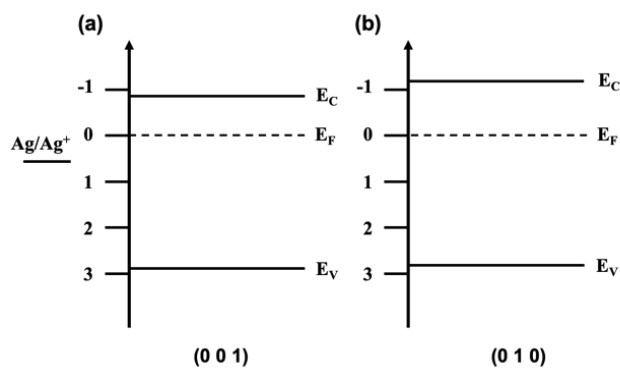


**Figure 4-11:** Schematic energy level diagram at the  $\text{La}_2\text{Ti}_2\text{O}_7$ /solution interface for a (001) oriented grain (left) and a (010) oriented grain (right), assuming the flat band condition. The energy scale is in Volts.  $E_V$ ,  $E_F$ , and  $E_C$  are the valence band edge, the Fermi level, and the conduction band edge, respectively.

One aspect of the findings that is surprising is that the reactivity appears to be unaffected by the presence of ferroelectric domains, unlike nearly all of the previous ferroelectric compounds studied. One exception is that a previous study of  $\text{Sr}_2\text{Nb}_2\text{O}_7$  (which is isostructural with  $\text{La}_2\text{Ti}_2\text{O}_7$ ): it also showed no clear evidence for spatially selective reactivity arising from ferroelectric domains.<sup>24</sup> However, that study was not conclusive because it was not possible to image domains to verify their existence and shape. Here, we can visualize the structure of the domains and see that silver is not deposited in patterns related to the domain structure. The most likely reason for this is that the surface band bending originating from the surface charge of the ferroelectric domains is not large enough to overcome the intrinsic difference in the band edge positions at different surfaces. Based on the 0.3 eV difference in the band edge positions calculated by Bruyer et al.<sup>47</sup>, the ferroelectric domains on the (010) surface would have to bend the conduction band downward from its flat band position by at least this amount before the (010) surface could compete with the (001) surface for electrons. In comparison, the energy of the conduction band in the rhombohedral phase of  $\text{BiFeO}_3$ , which does show domain specific reactivity and has a similar ferroelectric polarization to  $\text{La}_2\text{Ti}_2\text{O}_7$ , does not depend as strongly on orientation.<sup>51-53</sup> In other words, it is plausible that the more isotropic electronic structure of  $\text{BiFeO}_3$  makes it possible to observe domain selective reduction of Ag while the anisotropic electronic structure of  $\text{La}_2\text{Ti}_2\text{O}_7$  overwhelms the effects of the domains.

On the other hand, it is also plausible that a difference in the band edge positions of 0.3 eV could be overcome by band bending arising from the domain polarization. Apostol et al.<sup>54</sup> used XPS to

determine a binding energy shift of about 1 eV between the positive and negative domains on Pb(Zr,Ti)O<sub>3</sub> surfaces and Höfer et al.<sup>55</sup> used photoemission electron microscopy to determine an energy difference of 1.3 V between the positive and negative domains on BaTiO<sub>3</sub> surfaces. However, these measurements were in vacuum and screening in an aqueous solution by the chemisorption of water (the conditions of our experiments) is expected to significantly reduce these values. For example, in the ambient atmosphere, Morris et al.<sup>56</sup> measured the band bending in BaTiO<sub>3</sub> to be in the range of 0.3-0.5 eV during illumination. Furthermore, some amount of this band bending would occur on the neutral surface and the fraction that stems from the ferroelectric polarization is not known. The exact amount of band bending on La<sub>2</sub>Ti<sub>2</sub>O<sub>7</sub> will depend on the orientation, the surface composition, and the reaction environment. Although accurate information about the band edge positions is currently unavailable, the observations are consistent with the idea that the anisotropy of the electronic structure is more influential than the charge associated with the ferroelectric domains.

## 4.5 Conclusion

Measurements of the orientation dependence of the reactivity of La<sub>2</sub>Ti<sub>2</sub>O<sub>7</sub> show that the photocathodic reduction of the silver is favored on the (001) surface while perpendicular surfaces reduce much less silver. This result is consistent with what is known about the anisotropy of the electronic structure, which favors the transport of electrons to the (001) surface. Ferroelectric domains on the surface were also characterized by PFM. The domains were found to have irregular shapes and there was no correlation between the pattern of silver reduction and the domain shape. The results indicated that the ferroelectric polarization of La<sub>2</sub>Ti<sub>2</sub>O<sub>7</sub> does not alter the reactivity enough to overcome the influence of the anisotropic crystal structure.

## 4.6 References

- (1) Qu, Y.; Duan, X. Progress, Challenge and Perspective of Heterogeneous Photocatalysts. *Chem. Soc. Rev.* **2013**, *42* (7), 2568–2580. <https://doi.org/10.1039/C2CS35355E>.
- (2) Wang, Z.; Li, C.; Domen, K. Recent Developments in Heterogeneous Photocatalysts for Solar-Driven Overall Water Splitting. *Chem. Soc. Rev.* **2019**, *48* (7), 2109–2125. <https://doi.org/10.1039/C8CS00542G>.

- (3) Gong, M.; Xiao, S.; Yu, X.; Dong, C.; Ji, J.; Zhang, D.; Xing, M. Research Progress of Photocatalytic Sterilization over Semiconductors. *RSC Adv.* **2019**, *9* (34), 19278–19284. <https://doi.org/10.1039/C9RA01826C>.
- (4) Luo, J.; Zhang, S.; Sun, M.; Yang, L.; Luo, S.; Crittenden, J. C. A Critical Review on Energy Conversion and Environmental Remediation of Photocatalysts with Remodeling Crystal Lattice, Surface, and Interface. *ACS Nano* **2019**, *13* (9), 9811–9840. <https://doi.org/10.1021/acsnano.9b03649>.
- (5) Fujishima, A.; Honda, K. Electrochemical Photolysis of Water at a Semiconductor Electrode. *Nature* **1972**, *238* (5358), 37+. <https://doi.org/10.1038/238037a0>.
- (6) Osterloh, F. E. Inorganic Materials as Catalysts for Photochemical Splitting of Water. *Chem. Mater.* **2008**, *20* (1), 35–54. <https://doi.org/10.1021/cm7024203>.
- (7) Osterloh, F. E. Inorganic Nanostructures for Photoelectrochemical and Photocatalytic Water Splitting. *Chem. Soc. Rev.* **2013**, *42* (6), 2294–2320. <https://doi.org/10.1039/C2CS35266D>.
- (8) Pinaud, B. A.; Benck, J. D.; Seitz, L. C.; Forman, A. J.; Chen, Z.; Deutsch, T. G.; James, B. D.; Baum, K. N.; Baum, G. N.; Ardo, S.; et al. Technical and Economic Feasibility of Centralized Facilities for Solar Hydrogen Production via Photocatalysis and Photoelectrochemistry. *Energy Environ. Sci.* **2013**, *6* (7), 1983–2002. <https://doi.org/10.1039/C3EE40831K>.
- (9) Hisatomi, T.; Domen, K. Reaction Systems for Solar Hydrogen Production via Water Splitting with Particulate Semiconductor Photocatalysts. *Nat. Catal.* **2019**, *2* (5), 387–399. <https://doi.org/10.1038/s41929-019-0242-6>.
- (10) Lowekamp, J. B.; Rohrer, G. S.; Morris Hotsenpiller, P. A.; Bolt, J. D.; Farneth, W. E. Anisotropic Photochemical Reactivity of Bulk TiO<sub>2</sub> Crystals. *J. Phys. Chem. B* **1998**, *102* (38), 7323–7327. <https://doi.org/10.1021/jp982721e>.

- (11) Ohno, T.; Sarukawa, K.; Matsumura, M. Crystal Faces of Rutile and Anatase TiO<sub>2</sub> Particles and Their Roles in Photocatalytic Reactions. *New J. Chem.* **2002**, *26* (9), 1167–1170. <https://doi.org/10.1039/B202140D>.
- (12) Li, R.; Zhang, F.; Wang, D.; Yang, J.; Li, M.; Zhu, J.; Zhou, X.; Han, H.; Li, C. Spatial Separation of Photogenerated Electrons and Holes among {010} and {110} Crystal Facets of BiVO<sub>4</sub>. *Nat. Commun.* **2013**, *4*. <https://doi.org/10.1038/ncomms2401>.
- (13) Munprom, R.; Salvador, P. A.; Rohrer, G. S. The Orientation Dependence of the Photochemical Reactivity of BiVO<sub>4</sub>. *J. Mater. Chem. A* **2015**, *3* (5), 2370–2377. <https://doi.org/10.1039/c4ta06045h>.
- (14) Zhu, Y.; Schultz, A. M.; Rohrer, G. S.; Salvador, P. A. The Orientation Dependence of the Photochemical Activity of  $\alpha$ -Fe<sub>2</sub>O<sub>3</sub>. *J. Am. Ceram. Soc.* **2016**, *99* (7), 2428–2435. <https://doi.org/10.1111/jace.14201>.
- (15) Zitello, K. E.; Salvador, P. A.; Rohrer, G. S. Influence of Surface Orientation on the Photochemical Reactivity of CaTiO<sub>3</sub>. *J. Am. Ceram. Soc.* **2020**, *103* (8), 4498–4506. <https://doi.org/10.1111/jace.17107>.
- (16) Giocondi, J. L.; Salvador, P. A.; Rohrer, G. S. The Origin of Photochemical Anisotropy in SrTiO<sub>3</sub>. *Top. Catal.* **2007**, *44* (4), 529–533. <https://doi.org/10.1007/s11244-006-0101-y>.
- (17) Mu, L.; Zhao, Y.; Li, A.; Wang, S.; Wang, Z.; Yang, J.; Wang, Y.; Liu, T.; Chen, R.; Zhu, J.; et al. Enhancing Charge Separation on High Symmetry SrTiO<sub>3</sub> Exposed with Anisotropic Facets for Photocatalytic Water Splitting. *Energy Environ. Sci.* **2016**, *9* (7), 2463–2469. <https://doi.org/10.1039/c6ee00526h>.
- (18) Pisat, A. S.; Salvador, P. A.; Rohrer, G. S. The Facet Structure and Photochemical Reactivity of Arbitrarily Oriented Strontium Titanate Surfaces. *Adv. Mater. Interfaces* **2019**, *6* (16), 1900731. <https://doi.org/10.1002/admi.201900731>.
- (19) Takata, T.; Jiang, J.; Sakata, Y.; Nakabayashi, M.; Shibata, N.; Nandal, V.; Seki, K.; Hisatomi, T.; Domen, K. Photocatalytic Water Splitting with a Quantum Efficiency of

- Almost Unity. *Nature* **2020**, *581* (7809), 411–414. <https://doi.org/10.1038/s41586-020-2278-9>.
- (20) Li, L.; Salvador, P. A.; Rohrer, G. S. Photocatalysts with Internal Electric Fields. *Nanoscale* **2014**, *6* (1), 24–42. <https://doi.org/10.1039/c3nr03998f>.
- (21) Inoue, Y.; Okamura, M.; Sato, K. A Thin-Film Semiconducting Titanium Dioxide Combined with Ferroelectrics for Photoassisted Water Decomposition. *J. Phys. Chem.* **1985**, *89* (24), 5184–5187. <https://doi.org/10.1021/j100270a013>.
- (22) Inoue, Y.; Sato, K.; Sato, K.; Miyama, H. Photoassisted Water Decomposition by Ferroelectric Lead Zirconate Titanate Ceramics with Anomalous Photovoltaic Effects. *J. Phys. Chem.* **1986**, *90* (13), 2809–2810. <https://doi.org/10.1021/j100404a006>.
- (23) Dunn, S.; Jones, P. M.; Gallardo, D. E. Photochemical Growth of Silver Nanoparticles on C- and C+ Domains on Lead Zirconate Titanate Thin Films. *J. Am. Chem. Soc.* **2007**, *129* (28), 8724–8728. <https://doi.org/10.1021/ja071451n>.
- (24) Giocondi, J. L.; Rohrer, G. S. The Influence of the Dipolar Field Effect on the Photochemical Reactivity of Sr<sub>2</sub>Nb<sub>2</sub>O<sub>7</sub> and BaTiO<sub>3</sub> Microcrystals. *Top. Catal.* **2008**, *49* (1), 18. <https://doi.org/10.1007/s11244-008-9067-2>.
- (25) Schultz, A. M.; Zhang, Y.; Salvador, P. A.; Rohrer, G. S. Effect of Crystal and Domain Orientation on the Visible-Light Photochemical Reduction of Ag on BiFeO<sub>3</sub>. *ACS Appl. Mater. Interfaces* **2011**, *3* (5), 1562–1567. <https://doi.org/10.1021/am200127c>.
- (26) Burbure, N. V.; Salvador, P. A.; Rohrer, G. S. Photochemical Reactivity of Titania Films on BaTiO<sub>3</sub> Substrates: Influence of Titania Phase and Orientation. *Chem. Mater.* **2010**, *22* (21), 5831–5837. <https://doi.org/10.1021/cm1018019>.
- (27) Levin, I.; Bendersky, L. A. Symmetry Classification of the Layered Perovskite-Derived A<sub>n</sub>B<sub>n</sub>X<sub>3n+2</sub> Structures Structures. *Acta Crystallogr. Sect. B* **1999**, *55* (6), 853–866. <https://doi.org/10.1107/S0108768199005479>.

- (28) Levin, I.; Bendersky, L. A.; Vanderah, T. A. A Structural Study of the Layered Perovskite-Derived  $\text{Sr}_n(\text{Ti},\text{Nb})_n\text{O}_{3n+2}$  Compounds by Transmission Electron Microscopy. *Philos. Mag. A* **2000**, *80* (2), 411–445. <https://doi.org/10.1080/01418610008212060>.
- (29) Yamamoto, J. K.; Bhalla, A. S. Piezoelectric Properties of Layered Perovskite  $\text{A}_2\text{Ti}_2\text{O}_7$  (A=La and Nd) Single-crystal Fibers. *J. Appl. Phys.* **1991**, *70* (8), 4469–4471. <https://doi.org/10.1063/1.349078>.
- (30) Satoshi, N.; Masakazu, K.; Tsutomu, K. Crystallographic and Dielectric Properties of Ferroelectric  $\text{A}_2\text{B}_2\text{O}_7$  (A=Sr, B=Ta, Nb) Crystals and Their Solid Solutions. *J. Phys. Soc. Japan* **1975**, *38* (3), 817–824. <https://doi.org/10.1143/JPSJ.38.817>.
- (31) Gao, Z. P.; Yan, H. X.; Ning, H. P.; Reece, M. J. Ferroelectricity of  $\text{Pr}_2\text{Ti}_2\text{O}_7$  Ceramics with Super High Curie Point. *Adv. Appl. Ceram.* **2013**, *112* (2), 69–74. <https://doi.org/10.1179/1743676112Y.0000000030>.
- (32) Kim, H. G.; Hwang, D. W.; Kim, J.; Kim, Y. G.; Lee, J. S. Highly Donor-Doped (110) Layered Perovskite Materials as Novel Photocatalysts for Overall Water Splitting. *Chem. Commun.* **1999**, No. 12, 1077–1078. <https://doi.org/10.1039/a902892g>.
- (33) Hwang, D. W.; Kim, H. G.; Lee, J. S.; Kim, J.; Li, W.; Oh, S. H. Photocatalytic Hydrogen Production from Water over M-Doped  $\text{La}_2\text{Ti}_2\text{O}_7$  (M = Cr, Fe) under Visible Light Irradiation ( $\lambda > 420$  nm). *J. Phys. Chem. B* **2005**, *109* (6), 2093–2102. <https://doi.org/10.1021/jp0493226>.
- (34) Nashim, A.; Martha, S.; Parida, K. M. Heterojunction Conception of N- $\text{La}_2\text{Ti}_2\text{O}_7$ /p-CuO in the Limelight of Photocatalytic Formation of Hydrogen under Visible Light. *RSC Adv.* **2014**, *4* (28), 14633–14643. <https://doi.org/10.1039/C3RA47037G>.
- (35) Patwe, S. J.; Katari, V.; Salke, N. P.; Deshpande, S. K.; Rao, R.; Gupta, M. K.; Mittal, R.; Achary, S. N.; Tyagi, A. K. Structural and Electrical Properties of Layered Perovskite Type  $\text{Pr}_2\text{Ti}_2\text{O}_7$ : Experimental and Theoretical Investigations. *J. Mater. Chem. C* **2015**, *3* (17), 4570–4584. <https://doi.org/10.1039/c5tc00242g>.

- (36) Nanamatsu, S.; Kimura, M.; Doi, K.; Matsushita, S.; Yamada, N. New Ferroelectric -  $\text{La}_2\text{Ti}_2\text{O}_7$ . *Ferroelectrics* **1974**, *8* (1–2), 511–513. <https://doi.org/10.1080/00150197408234143>.
- (37) Nashim, A.; Parida, K. N- $\text{La}_2\text{Ti}_2\text{O}_7$ /p- $\text{LaCrO}_3$ : A Novel Heterojunction Based Composite Photocatalyst with Enhanced Photoactivity towards Hydrogen Production. *J. Mater. Chem. A* **2014**, *2* (43), 18405–18412. <https://doi.org/10.1039/c4ta02401j>.
- (38) Hu, S.; Chi, B.; Pu, J.; Jian, L. Novel Heterojunction Photocatalysts Based on Lanthanum Titanate Nanosheets and Indium Oxide Nanoparticles with Enhanced Photocatalytic Hydrogen Production Activity. *J. Mater. Chem. A* **2014**, *2* (45), 19260–19267. <https://doi.org/10.1039/C4TA04177A>.
- (39) Meng, F.; Hong, Z.; Arndt, J.; Li, M.; Zhi, M.; Yang, F.; Wu, N. Visible Light Photocatalytic Activity of Nitrogen-Doped  $\text{La}_2\text{Ti}_2\text{O}_7$  Nanosheets Originating from Band Gap Narrowing. *Nano Res.* **2012**, *5* (3), 213–221. <https://doi.org/10.1007/s12274-012-0201-x>.
- (40) Teague, J. R.; Gerson, R.; James, W. J. Dielectric Hysteresis in Single Crystal  $\text{BiFeO}_3$ . *Solid State Commun.* **1970**, *8* (13), 1073–1074.
- (41) Wenderich, K.; Mul, G. Methods, Mechanism, and Applications of Photodeposition in Photocatalysis: A Review. *Chem. Rev.* **2016**, *116* (23), 14587–14619. <https://doi.org/10.1021/acs.chemrev.6b00327>.
- (42) Fuierer, P. A.; Newnham, R. E.  $\text{La}_2\text{Ti}_2\text{O}_7$  Ceramics. *J. Am. Ceram. Soc.* **1991**, *74* (11), 2876–2881. <https://doi.org/10.1111/j.1151-2916.1991.tb06857.x>.
- (43) Song, W.; Salvador, P. A.; Rohrer, G. S. Influence of the Magnitude of Ferroelectric Domain Polarization on the Photochemical Reactivity of  $\text{BaTiO}_3$ . *ACS Appl. Mater. Interfaces* **2018**, *10* (48), 41450–41457. <https://doi.org/10.1021/acsami.8b16983>.
- (44) Shao, Z.; Saitzek, S.; Roussel, P.; Ferri, A.; Bruyer, E.; Sayede, A.; Rguiti, M.; Mentre, O.; Desfeux, R. Microstructure and Nanoscale Piezoelectric/Ferroelectric Properties in  $\text{La}_2\text{Ti}_2\text{O}_7$  Thin Films Grown on (110)-Oriented Doped Nb: $\text{SrTiO}_3$  Substrates. *Adv. Eng. Mater.* **2011**, *13* (10), 961–969. <https://doi.org/10.1002/adem.201100105>.

- (45) Kaspar, T. C.; Hong, S.; Bowden, M. E.; Varga, T.; Yan, P.; Wang, C.; Spurgeon, S. R.; Comes, R. B.; Ramuhalli, P.; Henager Jr., C. H. Tuning Piezoelectric Properties through Epitaxy of  $\text{La}_2\text{Ti}_2\text{O}_7$  and Related Thin Films. *Sci. Rep.* **2018**, *8*. <https://doi.org/10.1038/s41598-018-21009-5>.
- (46) Hwang, D. W.; Lee, J. S.; Li, W.; Oh, S. H. Electronic Band Structure and Photocatalytic Activity of  $\text{Ln}_2\text{Ti}_2\text{O}_7$  (Ln = La, Pr, Nd). *J. Phys. Chem. B* **2003**, *107* (21), 4963–4970. <https://doi.org/10.1021/jp034229n>.
- (47) Bruyer, E.; Sayede, A. Density Functional Calculations of the Structural, Electronic, and Ferroelectric Properties of High-k Titanate  $\text{Re}_2\text{Ti}_2\text{O}_7$  (Re=La and Nd). *J. Appl. Phys.* **2010**, *108* (5), 53705. <https://doi.org/10.1063/1.3459891>.
- (48) Takata, T.; Furumi, Y.; Shinohara, K.; Tanaka, A.; Hara, M.; Kondo, J. N.; Domen, K. Photocatalytic Decomposition of Water on Spontaneously Hydrated Layered Perovskites. *Chem. Mater.* **1997**, *9* (5), 1063–1064. <https://doi.org/10.1021/cm960612b>.
- (49) Cai, X.; Zhu, M.; Elbanna, O. A.; Fujitsuka, M.; Kim, S.; Mao, L.; Zhang, J.; Majima, T. Au Nanorod Photosensitized  $\text{La}_2\text{Ti}_2\text{O}_7$  Nanosteps: Successive Surface Heterojunctions Boosting Visible to Near-Infrared Photocatalytic  $\text{H}_2$  Evolution. *ACS Catal.* **2018**, *8* (1), 122–131. <https://doi.org/10.1021/acscatal.7b02972>.
- (50) Orum, A.; Takatori, K.; Hori, S.; Ikeda, T.; Yoshimura, M.; Tani, T. Atomic Force Microscopy Surface Analysis of Layered Perovskite  $\text{La}_2\text{Ti}_2\text{O}_7$  particles Grown by Molten Flux Method. *Jpn. J. Appl. Phys.* **2016**, *55* (8S1), 08NB08. <https://doi.org/10.7567/jjap.55.08nb08>.
- (51) Tütüncü, H. M.; Srivastava, G. P. Electronic Structure and Zone-Center Phonon Modes in Multiferroic Bulk  $\text{BiFeO}_3$ . *J. Appl. Phys.* **2008**, *103* (8), 83712. <https://doi.org/10.1063/1.2908865>.
- (52) Wang, H.; Zheng, Y.; Cai, M.-Q.; Huang, H.; Chan, H. L. W. First-Principles Study on the Electronic and Optical Properties of  $\text{BiFeO}_3$ . *Solid State Commun.* **2009**, *149* (15), 641–644. <https://doi.org/10.1016/j.ssc.2009.01.023>.

- (53) Sagar, E.; Mahesh, R.; Kumar, N. Pavan; Reddy, P. Venugopal. Investigation of Structural and Multiferroic Properties of Three Phases of BiFeO<sub>3</sub> Using Modified Becke Johnson Potential Technique. *J. Phys. Chem. Solids* **2017**, *110*, 316–326. <https://doi.org/10.1016/j.jpcs.2017.06.023>.
- (54) Apostol, N. G.; Stoflea, L. E.; Lungu, G. A.; Tache, C. A.; Popescu, D. G.; Pintilie, L.; Teodorescu, C. M. Band Bending at Free Pb(Zr,Ti)O<sub>3</sub> Surfaces Analyzed by X-Ray Photoelectron Spectroscopy. *Mater. Sci. Eng. B* **2013**, *178* (19), 1317–1322. <https://doi.org/10.1016/j.mseb.2013.02.007>.
- (55) Höfer, A.; Fechner, M.; Duncker, K.; Hölzer, M.; Mertig, I.; Widdra, W. Persistence of Surface Domain Structures for a Bulk Ferroelectric above T<sub>C</sub>. *Phys. Rev. Lett.* **2012**, *108* (8), 87602. <https://doi.org/10.1103/PhysRevLett.108.087602>.
- (56) Morris, M. R.; Pendlebury, S. R.; Hong, J.; Dunn, S.; Durrant, J. R. Effect of Internal Electric Fields on Charge Carrier Dynamics in a Ferroelectric Material for Solar Energy Conversion. *Adv. Mater.* **2016**, *28* (33), 7123–7128. <https://doi.org/10.1002/adma.201601238>.

## Chapter 5: Influence of pH and Surface Orientation on the Photochemical Reactivity of SrTiO<sub>3</sub>

*Solution pH is an external electric field that can alter the surface charge and band bending of photocatalysts. In this chapter, I measured the photochemical Ag<sup>+</sup> reduction rates on SrTiO<sub>3</sub> surface as a function of pH. It is found that the photochemical reactivity is strongly influenced by solution pH, and the effect depends on surface orientation. The observations are then interpreted with a band-bending model.*

### 5.1 Introduction

Heterogeneous photochemical reactions on semiconductor surfaces have been studied for decades for their potential applications as catalysts for water splitting and the degradation of organic pollutants.<sup>1-5</sup> When photogenerated electrons and holes migrate to semiconductor surfaces, they can drive reduction and oxidation reactions. However, commercial applications are limited by low efficiency.<sup>6,7</sup> Two of the most significant problems are the high rate of photogenerated carrier recombination<sup>8</sup> and the back-reaction of intermediate chemical species.<sup>9</sup> The spatial separation of electrons and holes by internal fields or charged surfaces has been suggested as a potential method to increase the overall photochemical reactivity.<sup>10</sup> For example, a surface domain with a negative (positive) charge will attract holes (electrons) and therefore promote the photoanodic (photocathodic) reaction. As long as the surface contains both photoanodic and photocathodic domains, the overall reaction will be promoted. Internal fields and charged surfaces may arise from phase boundaries,<sup>11,12</sup> ferroelectric polarizations,<sup>13,14</sup> or polar surface terminations.<sup>15,16</sup> Experimental evidence supports the assertion that internal fields and charged surfaces can be used to improve the photochemical reactivity.<sup>17-22</sup>

Because the two half reactions must proceed at the same rate to maintain charge neutrality, the overall reaction rate is limited by the slower one. If one applies a potential to increase the rate of the slower reaction, it will decrease the faster reaction; the maximum overall rate is achieved at a potential where neither of the two half reactions limit the overall rate. For particles in a solution, the potential can be changed by adjusting the pH. The solution pH influences the amount of charge adsorbed on the surface, the surface potential, the band bending in the semiconductor, and,

therefore, the concentration of available charge carriers at the surface. Because the photochemical reactivity is directly proportional to the amount of available charge carriers, the pH will affect the overall reaction rate. For example, Zhong et al.<sup>23</sup> made a photochemical water splitting device comprised of a SrTiO<sub>3</sub> membrane separating solutions of different pH. The gradient in pH created a "chemical bias" so that H<sub>2</sub> was produced on the low pH side of the device and O<sub>2</sub> was produced at the high pH side.

Past studies have shown that pH has a strong influence on the photochemical reaction rate for a variety of catalysts. The effect of pH and the rationale for the effect vary with the catalyst and the reaction. Ohtani et al.<sup>24</sup> measured the pH dependence of the photocatalytic activity of TiO<sub>2</sub> powders in silver nitrate solutions from pH 2 to 8. The reactivity is negligible at low pH and increases as the pH increases. The rationale provided by the authors was that the positive surface charge at low pH inhibits the adsorption of Ag<sup>+</sup>, decreasing the reactivity. The rate of photochemical reduction of Cr<sup>4+</sup> by TiO<sub>2</sub> decreased as the pH changed from pH 1 to 6, which is opposite what was reported for Ag<sup>+</sup> reduction.<sup>25</sup> Oosawa and Grätzel<sup>26</sup> showed that removing surface OH<sup>-</sup> from TiO<sub>2</sub> (presumably making the surface more positive) increased the rate of the oxygen evolution reaction. Guo et al.<sup>27</sup> reported the pH-dependence of photo-deposition of a series of metals and metal oxides on faceted BiOBr particles. With increasing pH, there was a reversal of surface charge so that the photocathodic facets became photoanodic and the photoanodic facets become photocathodic.

In the present work, we measure the rate of Ag<sup>+</sup> reduction by SrTiO<sub>3</sub> in the range of pH 3 to 9. SrTiO<sub>3</sub> is a well-known perovskite photocatalyst that can split water under UV-light illumination.<sup>28-30</sup> SrTiO<sub>3</sub> surfaces have the interesting feature of having terraces with different chemical terminations and different electrochemical potentials that have been measured by atomic force microscopy (AFM).<sup>16,31,32</sup> On the (111) and (110) surface, the different potentials lead to photocathodic and photoanodic terraces. The reactivities of the terraces with different chemical terminations on the (100) surface have not yet been explored. The presence of photoanodic and photocathodic surface domains on the SrTiO<sub>3</sub> surface is analogous to the photoanodic and photocathodic surface domains found on BaTiO<sub>3</sub> surfaces because of bulk ferroelectric domains.<sup>14</sup> It has been shown that the rate of Ag<sup>+</sup> photoreduction on BaTiO<sub>3</sub> surfaces increases as the pH increases from pH 2 to 8.<sup>33</sup> and Song et al.<sup>34</sup> recently showed that hydrogen production from

BaTiO<sub>3</sub>/TiO<sub>2</sub> core/shell photocatalysts varied with pH and exhibited a local maximum in reactivity at pH 9. The rationale for these observations was that increasing negative charge on the surface (with increasing pH) increased upward band bending and increased the rate of the photoanodic reaction, increasing the overall rate of reaction; this mechanism is consistent with simulations of the process.<sup>35</sup> In contrast to this earlier work, here we investigate the photochemical reactivity of non-ferroelectric, cubic SrTiO<sub>3</sub> surfaces. We measure the pH dependence on surfaces of known orientation, because it is known that photochemical reactivity can vary with orientation.<sup>14,36–38</sup>

The purpose of this work is to evaluate the relationship between the solution pH and the photochemical reactivity of three low index SrTiO<sub>3</sub> surfaces: (100), (110), and (111). These three facets are commonly found on small catalyst particles<sup>37,39</sup> and they are also part of the equilibrium shape of SrTiO<sub>3</sub> at some temperatures.<sup>40</sup> We use both single crystal surfaces and crystals at the surface of ceramics whose orientations have been measured by electron backscatter diffraction (EBSD). The single crystals show what happens when the surface is almost exclusively a single orientation while the vicinal surfaces identified in the polycrystal show what happens for more realistic surfaces where the principal orientation is combined with smaller facets of other orientations. The photochemical reactivity is determined from topographic AFM images by measuring the volume of silver deposits on the surface after reaction. The observations are then interpreted with a band bending model. The results imply that to create catalysts with optimized reactivity, it is necessary to control particle shape, chemical termination, and the pH.

## 5.2 Experimental Methods

**Sample preparation.** The experimental approach is based on photochemical "marker reactions" that leave an insoluble product on the surface at the site of reaction.<sup>14,15,41–43</sup> The reactivity of single crystals, with nearly ideal low index orientations, and grains in a ceramic, with surfaces vicinal to the ideal orientation, were measured as a function of pH and compared. Details of the sample preparation and photochemical marker reactions are given below.

Chemical-mechanical polished (100), (110), and (111) oriented SrTiO<sub>3</sub> single crystals (MTI Corporation, Richmond, 0.5 cm × 0.5 cm, roughness < 5 Å) were sonicated in a methanol bath for 10 min and then placed in a covered alumina crucible and annealed in a muffle furnace at 1100 °C for 6 h (ramp rates were 5 °C/min). After annealing, atomically flat terraces were observed by

AFM (Solver-Next, NT-MDT, Russia). Note that this surface treatment defines a mixed termination that contains both photoanodic and photocathodic terraces.<sup>14,16,32</sup>

Polycrystalline SrTiO<sub>3</sub> ceramics were prepared by uniaxially compacting commercially available powder (99 %, Alfa Aesar) in a cylindrical die with a pressure of 150 MPa. A few drops of PVA were added as a binder to form disk-shaped samples with a thickness of 3 mm and a diameter of 1 cm. The samples were placed in an alumina crucible, on top of excess SrTiO<sub>3</sub> powder, heated to 900 °C (ramp rates were 5 °C/min) for 12 h to remove any residual organics, sintered for 10 h at 1360 °C (ramp rates were 10 °C/min), and annealed for 6 h at 1470 °C (ramp rates were 10 °C/min) to increase the grain size to about 20 μm. The sample was then cooled in furnace at a rate of 10 °C/min. The annealed surface was ground with SiC abrasive papers and consecutively polished with a series of diamond suspensions, with a final suspension of 0.25 μm diamond. The polished sample was then annealed at 1150 °C for 6 h to repair polishing damage and thermally etch the grain boundaries. All the heating processes were carried out in air. The crystallographic orientations of individual grains in the polycrystalline sample were determined using an FEI Quanta 200 SEM equipped with an electron backscatter diffraction (EBSD) system. Three grains, close to low index orientations, were selected for comparison to the single crystals.

***Photochemical Ag marker reaction.*** The photo-reduction of aqueous Ag<sup>+</sup> leaves metallic silver on the surface at the site of the reaction. Reaction conditions were selected so that the surface was only partially covered with silver and the underlying surface structure was still obvious so that it was possible to determine the volume of silver. The reaction was carried out using and 10<sup>-5</sup> M aqueous AgNO<sub>3</sub> solution prepared from AgNO<sub>3</sub> (Acros) and deionized water. The low concentration was chosen to avoid precipitation.<sup>44</sup> The pH of the solution was controlled through the addition of acetic acid (Fisher Chemical) or NaOH (Acros Organics) and measured using pH test paper (Hydriion). Next, an O-ring was placed on the top of sample and the interior volume was filled with the silver bearing solution. A quartz cover slip was then placed on the top of the O-ring to seal the solution without air bubbles. Next, a 300 W mercury lamp (Newport, Irvine, CA) was used to illuminate the single crystal sample for 30 min. Some single crystal samples were immersed in 10<sup>-4</sup> M aqueous AgNO<sub>3</sub> solution and illuminated for 15 min, which gives a similar distribution of silver deposits. When the polycrystals were reacted using the same conditions as the single crystal, so much silver was deposited that it was not possible to see the

underlying surface structure. Because the polycrystal was more reactive than the single crystal, the lamp power was reduced to 150 W, and the exposure was reduced to 15 min. After illumination, the pH value of the solution was measured again, and no obvious change was observed. The sample was then rinsed in deionized water and dried using an aero duster (Miller-Stephenson). Before the next reaction, the sample surface was wiped with cotton swabs and ultrasonically cleaned in methanol and acetone, respectively for 10 min. An XL30 scanning electron microscope (Phillips) was used to make sure that visible deposits were removed. Any amount of Ag that may remain and contaminate the surface is much smaller than what is measured as a product of the reaction. Furthermore, this Ag contamination should be roughly constant throughout the measurements. Unfortunately, a more aggressive cleaning procedure would destroy the surface features that we are using for comparison. For the photooxidation of  $\text{Pb}^{2+}$ , the sample was immersed in  $10^{-3}$  M aqueous  $\text{Pb}(\text{CH}_3\text{COO})_2$  solution prepared from  $\text{Pb}(\text{CH}_3\text{COO})_2$  (Acros) and deionized water. The lamp was operated at 100 W and the sample was illuminated for 30 min. All other procedures were the same as for the reduction of  $\text{Ag}^+$ .

Topographic images of the same area of the surface before and after reaction were obtained by AFM in semi-contact mode. The Gwyddion software package,<sup>45</sup> MATLAB, and OriginLab were used to process and analyze the data. To estimate the amount of silver deposited on the surface by the reaction, the images before and after the reaction are compared and the excess volume after the reaction is determined. This is illustrated schematically in Fig. 5-1. The position and height data from the same area before and after the reaction is extracted from the images. To define a constant plane, three points from the clean surface, where no silver is present, are selected in each image (as nearly as possible the same points in each image). A plane is then fit to the three points in each image and this plane is taken as a reference. Next, the volume is calculated for each image and the excess volume after the reaction is taken to be a measure of the relative amount of silver deposited. For each experiment, the excess volume was measured three times to estimate the variability. To assess tip related errors, the before images were recorded with three different tips and the results were compared.

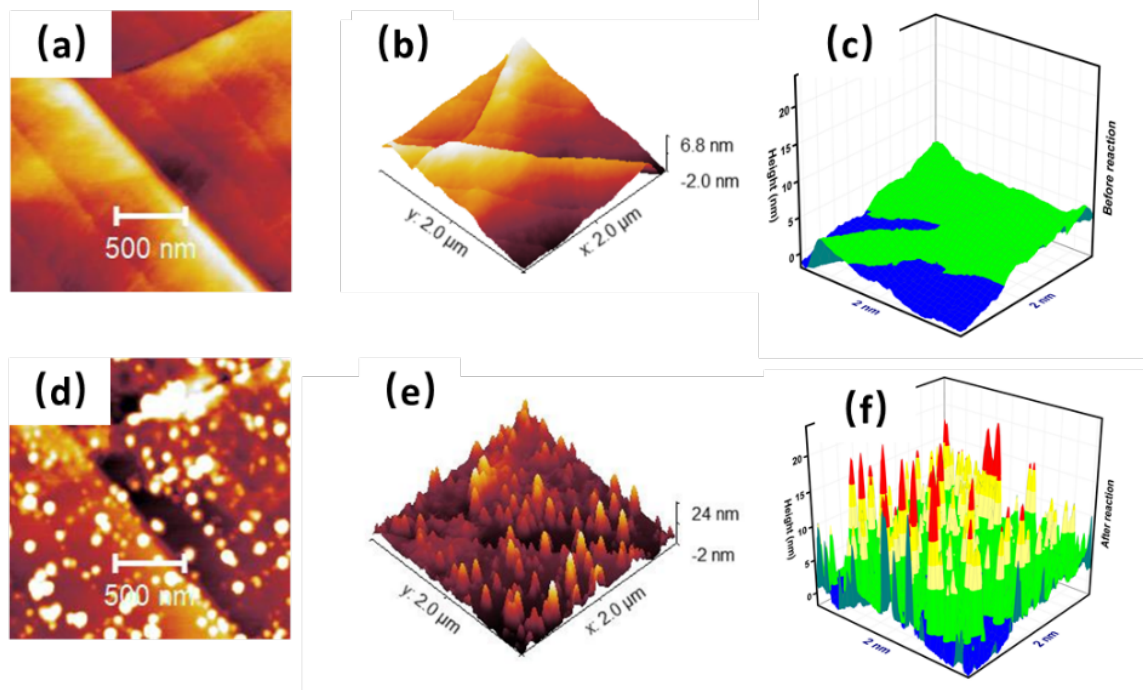


**Figure 5-1:** Illustration of the method used to quantify the excess volume in this work. AFM images of a SrTiO<sub>3</sub> surface before reaction are shown in (a) and (b), as 2D and 3D versions, respectively. The same surface is plotted again in (c), using Originlab and the xyz data extracted from AFM image. AFM images of the same surface after photochemical reaction are shown in (d) and (e), as 2D and 3D versions, respectively. The surface is plotted again in (f), using Originlab and the xyz data extracted from AFM image. The difference of the integral value between (f) and (c) represents the excess value that was used to quantify the silver product volume and reactivity.

### 5.3 Results

A topographic AFM image of the surface of a SrTiO<sub>3</sub> (100) single crystal after annealing at 1100 °C in air for 6 h is shown in Figure 5-2(a). After annealing, the surface is made up of a terrace and step structure, with most steps orientated in the <100> direction. Note that the details of the surface structure depend on the specific surface treatment.<sup>46</sup> The roughness (root-mean-square average of the height profile) of each terrace is less than 1 Å, indicating that they are atomically flat. Topographic AFM images at approximately the same location, after Ag<sup>+</sup> photoreduction at seven different pHs, are shown in Figure 5-2(b)-(h). After these reactions, new contrast appeared on the surface, corresponding to reduced metallic silver. Note that the sample was cleaned to remove the silver between each reaction. At pH 3, 4, and 5, the maximum heights of the silver deposits in Figure 1(b-d) are 5 to 15 nm. At pH 6, the maximum heights of the silver deposits in Figure 5-2(e) are 30 to 40 nm, and at pH 7, 8, and 9, in Figure 5-2(f-h), they are 5 to

10 nm. Note that the vertical scales of the topographic images in Fig. 5-2 were selected to maximize contrast and vary by a factor of 40. The excess volume of photo-deposited silver from pH 3 and pH 9 is illustrated in Figure 5-3. The mean (circle) and standard deviation (bars) were determined from three measurements on clean surfaces without reactions. The combined uncertainties based on three different tips and three different sampling areas are estimated to be 8 %. Both the changes in the heights of the silver deposits and the excess volume show that the amount of reduced silver increases from pH 3 to pH 6, and then decreases at higher pH. When control experiments were conducted with no light exposure, no silver was found on the surface, verifying that the silver was photoreduced and did not simply precipitate from the solution.

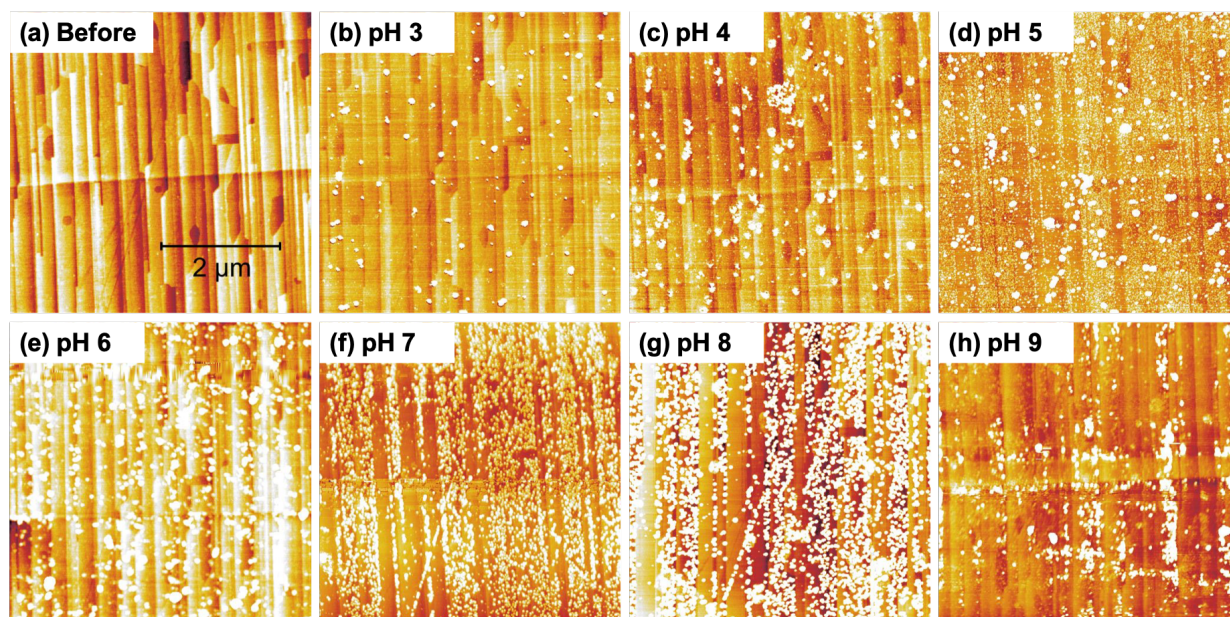


**Figure 5-2:** Topographic AFM images of the same location on a (100) SrTiO<sub>3</sub> single crystal surface (a) before and (b)–(h) after photochemical reaction with an aqueous silver nitrate solution having pH values between pH 3-9, as indicated. The dark to light vertical contrast is (a) 1 nm (b) 20 nm (c) 20 nm (d) 20 nm (e) 40 nm (f) 10 nm (g) 5 nm, and (h) 5 nm.

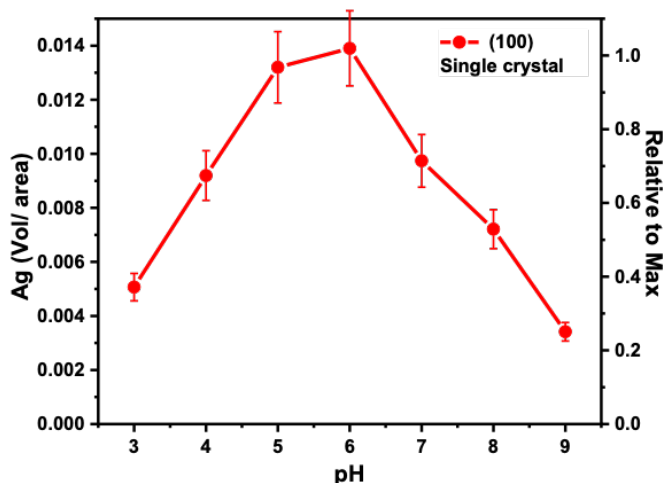


**Figure 5-3:** Excess volume of reduced Ag on the SrTiO<sub>3</sub>(100) surface as a function of pH. Units are  $\mu\text{m}$ , computed by dividing the volume ( $\mu\text{m}^3$ ) by the area ( $\mu\text{m}^2$ ). The point is the mean and the bars represent the standard deviation from three measurements. The uncertainty in the silver volume is estimated to be 8 %. The right-hand vertical axis quantifies the value relative to the maximum value at pH 6.

Figures 5-2(e-g) show that in the pH range of 6 to 8, the silver deposits in a spatially selective fashion, preferring some terraces over others. This selectivity, not obvious at higher or lower pH, may be related to the fact that SrTiO<sub>3</sub>(100) surfaces can be terminated by a TiO<sub>2</sub> or SrO plane.<sup>47</sup> In a more limited study of silver reduction on SrTiO<sub>3</sub>(100) at uncontrolled pH, this selectivity was not observed.<sup>15</sup> However, terrace dependent spatial selectivity of reactions on the SrTiO<sub>3</sub> (110) and (111) surfaces, and their correlation to the sign of the charge associated with the chemical termination, is well documented.<sup>15,16,32</sup> On the SrTiO<sub>3</sub> (110) and (111) surfaces, the differently charged terraces separately promote the photocathodic and photoanodic reactions. To see if this occurs in the same way for the (100) surface, we compared the photocathodic and photoanodic reaction on the same area and the results are illustrated in Figure 5-4. Note that different conditions were used for the two reactions because the photoanodic reaction is much slower than the photocathodic reaction. The image in Figure 5-4(a) illustrates that silver is reduced on only some terraces. Compared to Figure 5-2, these terraces have a different orientation and step spacing, but the reduced silver is clearly localized to certain areas. However, the image in Figure 5-4(b) shows a more homogeneous distribution of small Pb-containing particles on the surface. Therefore, all terraces are somewhat photoanodic, but only some are photocathodic at unadjusted pH (pH 6). The bifunctionality of the (100) is consistent with previous findings.<sup>39</sup>

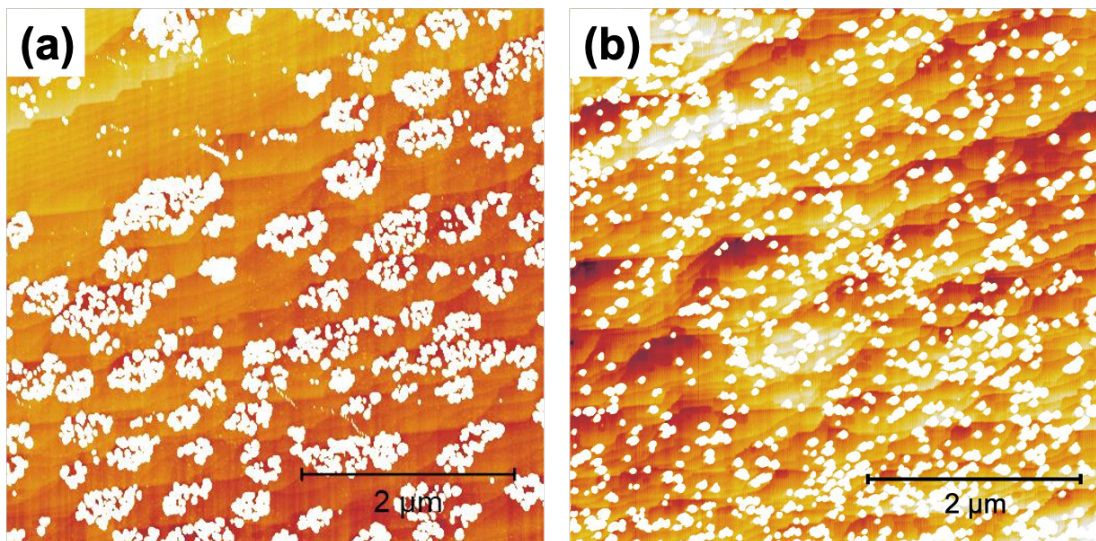


**Figure 5-4:** (a) and (b) show topographic AFM images of the same location of a SrTiO<sub>3</sub> (100) crystal after the reduction of silver the oxidation of lead. (a) has been immersed in neutral 10<sup>-4</sup> M AgNO<sub>3</sub> solution and illuminated under 40 W UV light for 15 min and (b) has been immersed in neutral 10<sup>-3</sup> M Pb(CH<sub>3</sub>COO)<sub>2</sub> solution and illuminated under 100 W UV light for 30 min.

An experiment parallel to the one described above was conducted on the SrTiO<sub>3</sub> (110) single crystal surface and the results are shown in Figure 5-5. The topographic AFM images show the same area (a) before reaction, and (b)-(h) after reaction in aqueous AgNO<sub>3</sub> solutions with pH 3 to 9. The (110) surface consists of (110) terraces with straight step edges; the long step edges have the [001] orientation. As in Figure 5-2, the bright contrast corresponds to silver deposits, and at some values of pH, silver accumulates mainly along the [001] steps. A qualitative comparison of the topographic images suggests that both the number of silver particles and their heights increase with the pH value from pH 3 to 7, and then decrease at pH 8 and 9. The measurements of the excess volume shown in Figure 5-6 are consistent with the qualitative interpretation of the images. The observation that the reactivity maximizes at an intermediate pH is consistent with the findings for the (100) surface. However, note that the absolute photocathodic reactivity on the (110) surface is five times less than on the reactivity of the (100) surface.

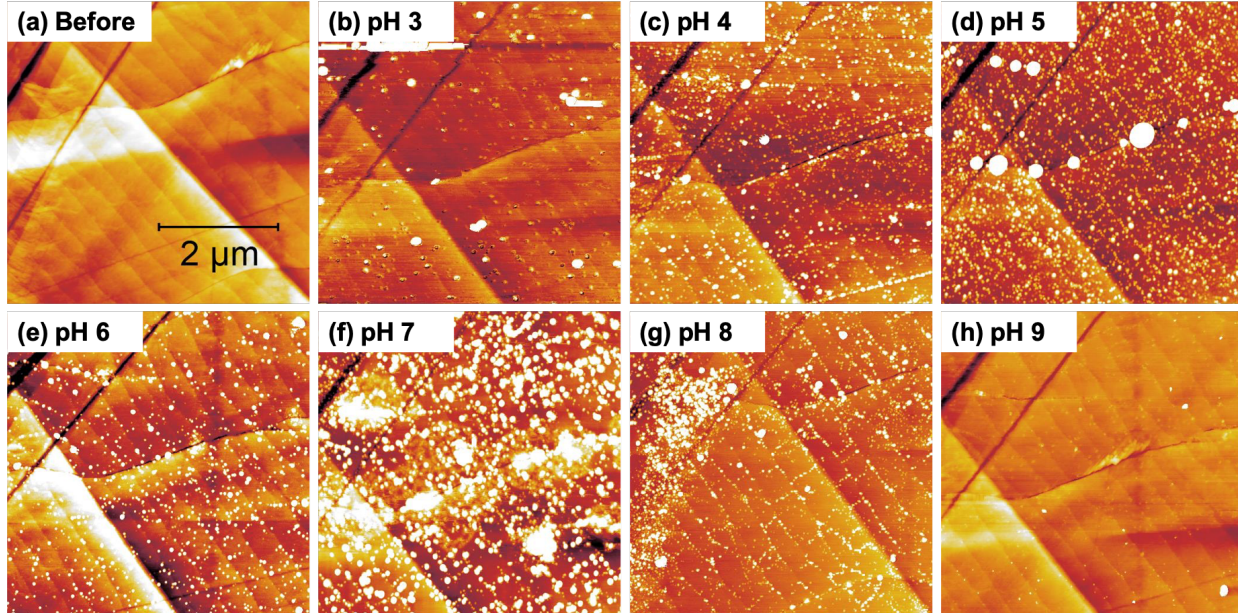


**Figure 5-5:** Topographic AFM images of the same location on a SrTiO<sub>3</sub> (110) single crystal surface (a) before and (b)–(h) after photochemical reaction in aqueous silver nitrate solution having pH values between pH 3-9, as indicated. The dark-to-white contrast shown is 5 nm for (a), (b), and (h), 10 nm for (c), (e), and (g) and 15 nm for (d) and (f).

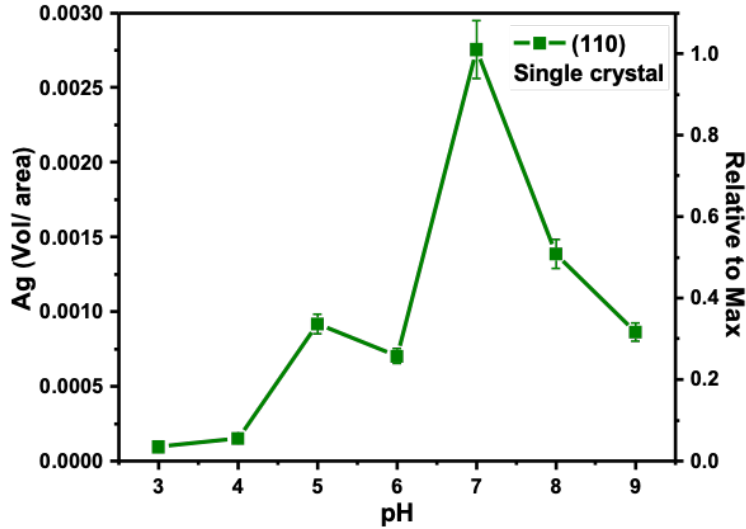


**Figure 5-6:** Excess volume of reduced Ag on the SrTiO<sub>3</sub>(110) surface as a function of pH. Units are  $\mu\text{m}$ , computed by dividing the volume ( $\mu\text{m}^3$ ) by the area ( $\mu\text{m}^2$ ). The uncertainty in the silver volume is estimated to be 6%. The point is the mean and the bars represent the standard deviation from three measurements. The right-hand vertical axis quantifies the value relative to the maximum value at pH 7.

The experiments carried out on the (100) and (110) surfaces were repeated on the (111) surface and the results are shown in Figures 5-7 and 5-8. After annealing, adjacent (111) terraces are separated by a combination of straight and curved steps; the curved step edges are smaller in height

than the straight ones and thus have weaker contrast in the topographic image. The formation of the reduced silver is spatially non-uniform, as reported in previous studies of the reactivity of the (111) surface.<sup>15,32</sup> This is related to the different chemical terminations; one of the terraces is relatively photocathodic (reduces silver) and the other is relatively photoanodic (silver is not reduced). This spatial selectivity is most obvious at pH 3 and is most clearly evident in the upper right corner of Figure 5-7(b). A higher resolution image illustrating the non-uniform reactivity is shown in Figure 5-9. Note that at pH 4, where the most silver is reduced, the surface appears to be the most uniformly reactive. The excess volume as a function of pH is illustrated Figure 5-8. Here, the photocathodic reactivity reaches a maximum at pH 4 and then decreases as pH increases. The absolute reactivity on the (111) surface is close to 90 % of the reactivity of the (100) surface.

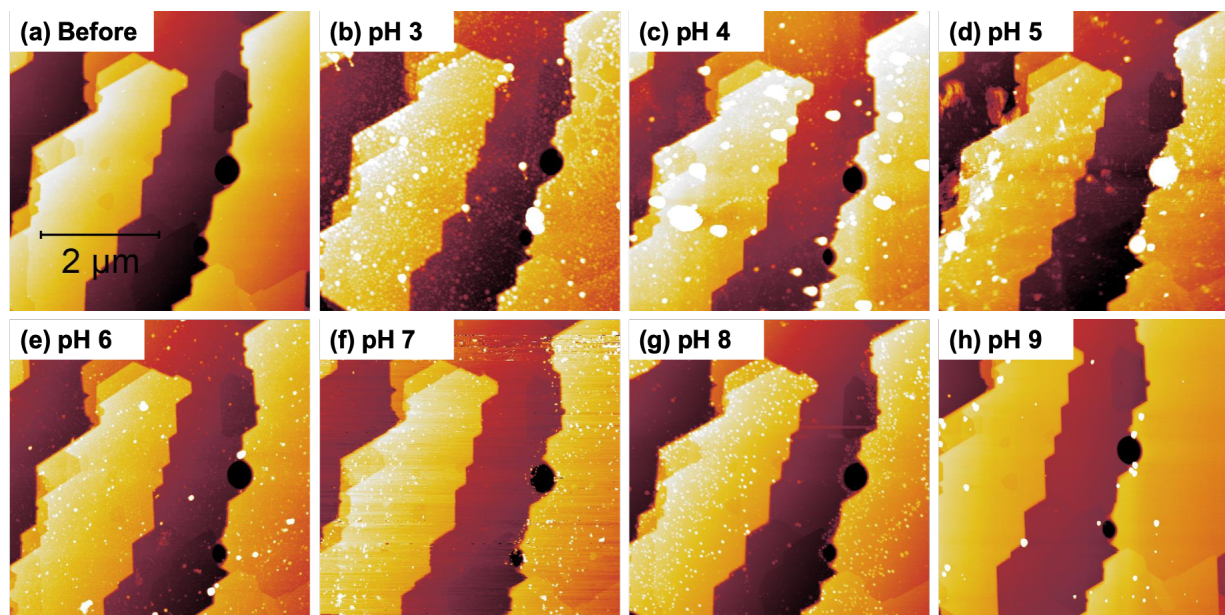


**Figure 5-7:** Topographic AFM images of the same location on a (111) SrTiO<sub>3</sub> single crystal surface (a) before and (b)–(h) after photochemical reaction in an aqueous silver nitrate solution having pH values between pH 3-9, as indicated. The dark-to-white contrast is 18 nm for (a), (g), and (h), and 30 nm for (b), (c), and (d) and 25 nm for (e) and (f).

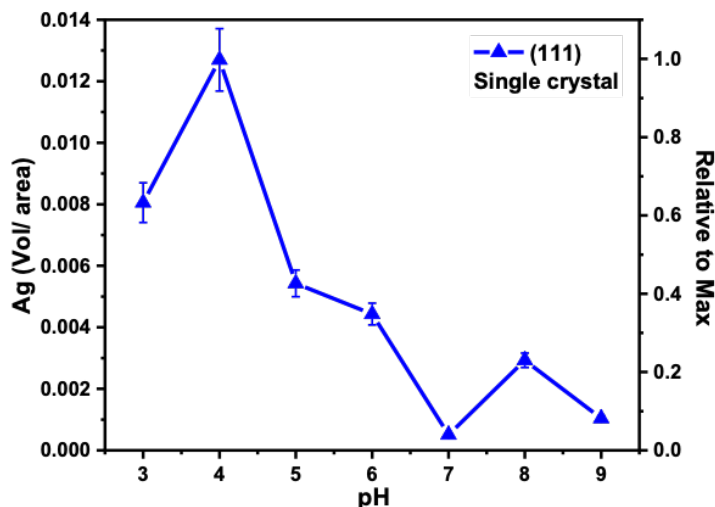


**Figure 5-8:** Excess volume of reduced Ag on the SrTiO<sub>3</sub>(111) surface as a function of pH. Units are  $\mu\text{m}$ , computed by dividing the volume ( $\mu\text{m}^3$ ) by the area ( $\mu\text{m}^2$ ). The point is the mean and the bars represent the standard deviation from three measurements. The uncertainty in the silver volume is estimated to be 9 %. The right-hand vertical axis quantifies the value relative to the maximum value at pH 4.

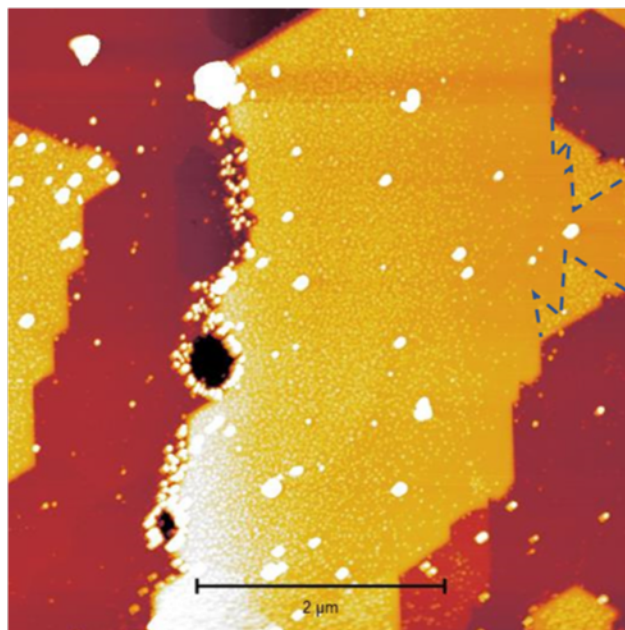


**Figure 5-9:** AFM image of a SrTiO<sub>3</sub>(111) crystal after immersing in  $10^{-5}$  M AgNO<sub>3</sub> solution with a neutral pH (pH  $\approx$  6) and illuminated under 300 W UV light for 30min. The blue dash line marks the boundary of cathodic and anodic surfaces.

Parallel experiments were carried out on crystals at the surface of polycrystals. First, an orientation map was generated by EBSD (see Figure 5-10). Using the orientation map, it was possible to identify grains that were close to (100), (110), and (111) orientations and these grains are labeled in Figure 5-10. The measured deviations from the ideal orientations were  $3.0^\circ$ ,  $2.8^\circ$ , and  $7.6^\circ$  from

(100), (110), and (111), respectively. As before, the surfaces were imaged after the photoreduction of silver in solutions from pH 3 to pH 9. The results for the near (100) surface are illustrated in Figure 5-11 and the results for the near (110) and (111) surface are presented in Figures 5-12 and 5-13. The darkest contrast in Figure 5-11 corresponds to valleys at grain boundaries and residual scratches. The area on the left side of the image is near the (100) orientation. While the near (100) surface has flat (100) terraces (see Figure 5-11a), the surfaces near (110) and (111) have terraces that are too closely spaced to be resolved in any detail. When silver is photoreduced on the near (100) surface, it is preferentially reduced on the terraces close to an upward step. The near (110) and near (111) surfaces are so rough that it is not possible to determine if the deposits are correlated to the underlying surface structure.

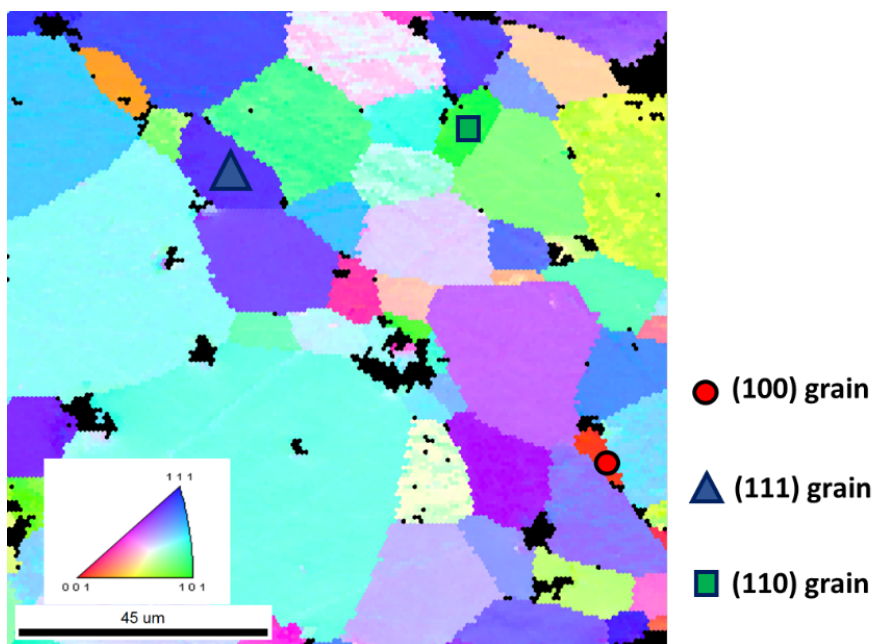


**Figure 5-10:** An orientation map of the polycrystalline SrTiO<sub>3</sub> sample. Selected grains near low index orientations are marked with a red circle (100), a blue triangle (111), and a green box (110).

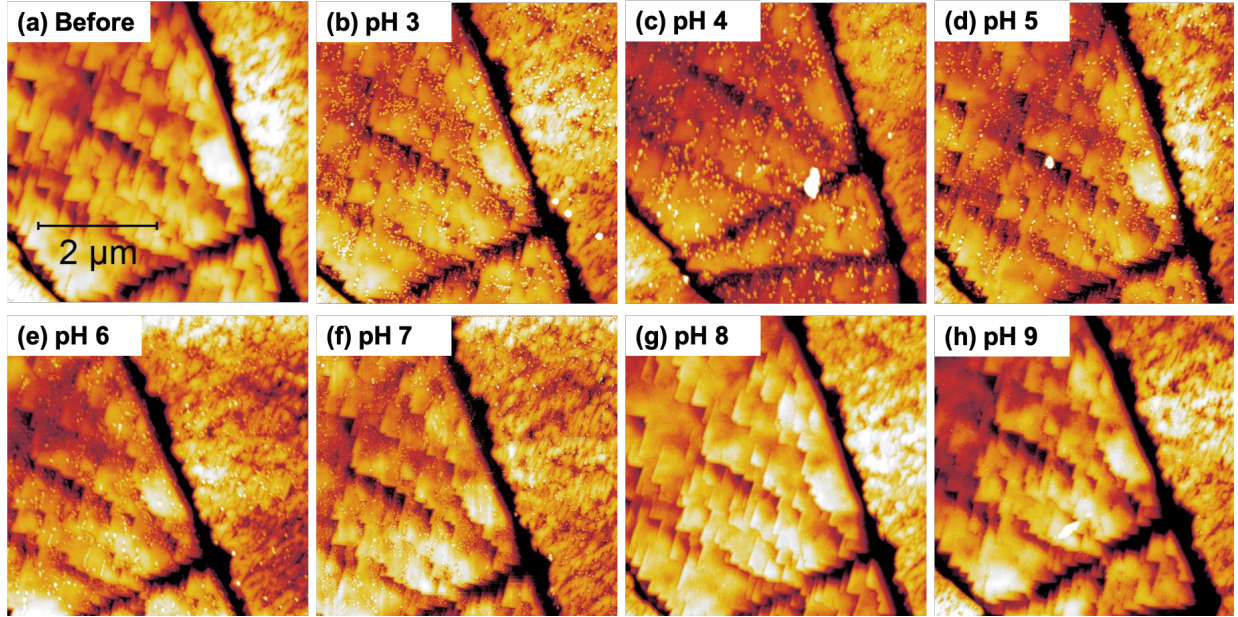


**Figure 5-11:** Topographic AFM images of the same area on a near (100) orientated grain shown in (a) before and (b)-(h) after photochemical reaction in an aqueous silver nitrate solution having pH values between pH 3-9, as indicated. The dark-to-white contrast in all images is 30 nm.

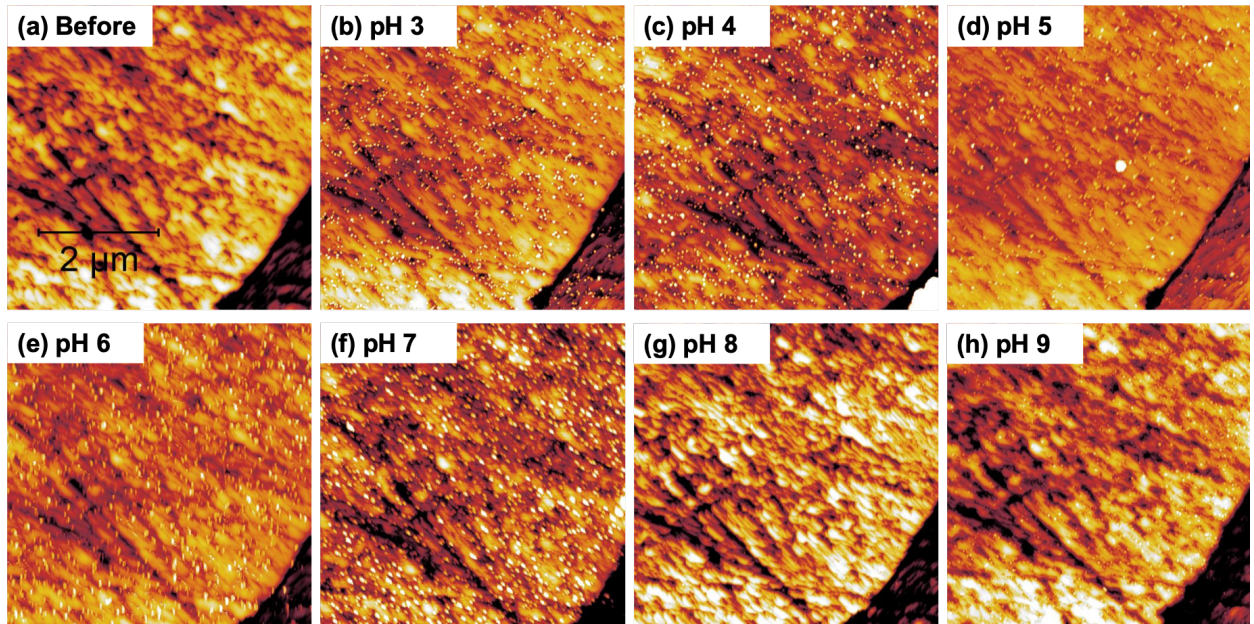


**Figure 5-12:** Topographic AFM images of the same area on a (110) grain shown in (a) before and after photochemical reaction in aqueous silver nitrate solutions with pH values of 3-9 (as indicated). The vertical range from dark to bright is 35 nm in all images.

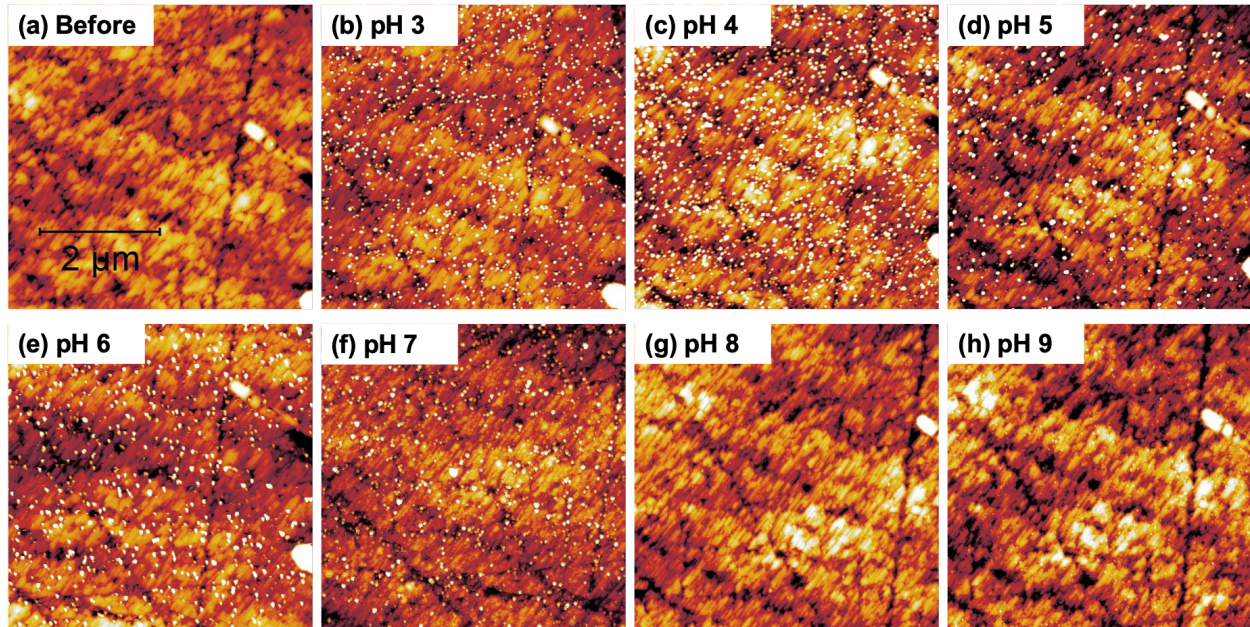


**Figure 5-13:** Topographic AFM images of the same area on a (111) grain shown in (a) before and after photochemical in aqueous silver nitrate solutions with pH values of 3-9 (as indicated). The vertical range from dark to bright is 15 nm in all images.

A visual inspection of the images in Figure 5-11 indicates that there is little reactivity for the lowest and highest pH, and that the reactivity is greatest somewhere between these limits. The maximum of the height of the silver deposits is in the range of (b-d) 3-5 nm (pH 3-5), (e) 5-10 nm (pH 6), and (f-h) 1-3 nm (pH 7-9). The excess volume measurements for the (100), (110), and (111) orientations are summarized in Figure 5-14. For the near (100) surface, the reactivity reaches a maximum at pH 6, for the near (110) surface, the reactivity reaches a maximum at pH 7, and for the near (111) surface, the reactivity reaches a maximum at pH 4. As before, the bars represent the standard deviation of the measurements. The maxima for the reactivity of grains in polycrystals occur at the same pH as the maxima for similarly oriented single crystals. However, there is a wider range of uncertainty for the grains in the polycrystal. The increased uncertainty probably arises from the rougher surfaces, which provide steps with a variety of orientations and makes the determination of a constant background plane more uncertain. The steps also provide surfaces with different orientations that likely affect the overall reactivity.

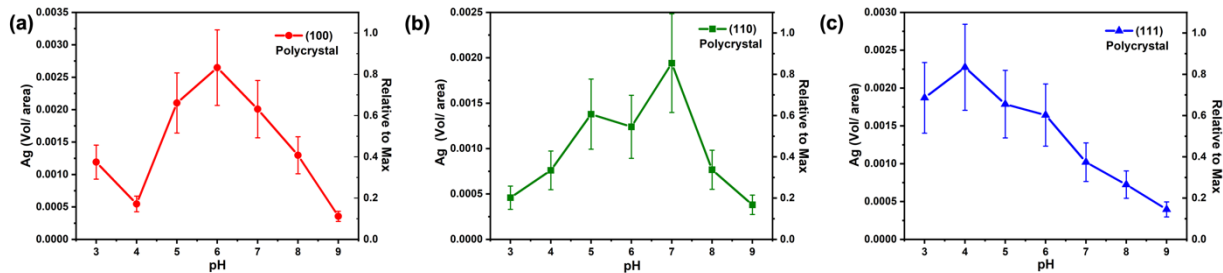


**Figure 5-14:** Excess volume as a function of pH on the polycrystalline sample for (a) the near (100) surface, (b) the near (110) surface, and (c) the near (111) surface. Units are  $\mu\text{m}$ , computed by dividing the volume ( $\mu\text{m}^3$ ) by the area ( $\mu\text{m}^2$ ). Note that the vertical scales vary in each. In each case, the point is the mean and the bars represent the standard deviation. The right-hand vertical axis quantifies the value relative to the maximum average value in each plot.

## 5.4 Discussion

The spatially selective reduction of Ag on certain terraces of the  $\text{SrTiO}_3(100)$  surface has not been reported previously. However, it is not too surprising. The (100) surface can be terminated by a  $\text{TiO}_2$  or  $\text{SrO}$  layer and Paradinas et al.<sup>48</sup> measured a 45 mV difference between the potentials of these terraces by Kelvin probe force microscopy. Similar differences in potentials of the terraces on the (110)<sup>16</sup> and (111)<sup>32</sup> surfaces also lead to the spatially selective reduction of Ag. However, as illustrated in Figure 5-4b, the surface oxidizes lead with no apparent preference for a particular terrace. Therefore, the (100) surface can be considered bi-functional.

Previous observations of silver reduction on  $\text{SrTiO}_3$  (at uncontrolled pH) led to the conclusion that the (100) surface is the most reactive, the (110) surface is the least reactive, and the (111) surface has an intermediate reactivity.<sup>37</sup> The results presented here for the single crystals are consistent with this observation (the data in Figures 5-3, 5-6, and 5-8 are compared on the same scale in Figure 5-15) for most of the pH values. However, because the pH was uncontrolled, and it is doubtful that all three surfaces have the same point of zero charge, the previous measurements were not necessarily made at the same pH. Furthermore, the photocathodic reactivity depends on the surface preparation conditions, which alters the relative coverage of photocathodic terraces.<sup>16,32,49</sup>

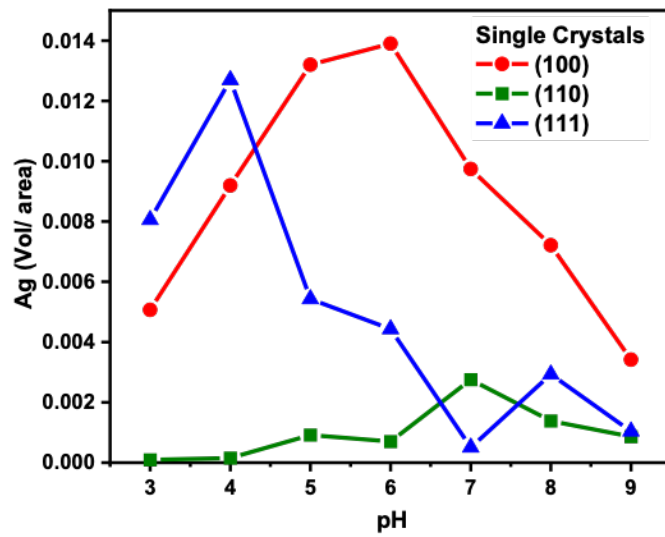


**Figure 5-15:** Comparison of the volume of reduced silver as a function of pH on the (100), (110), and (111) single crystal surfaces. Units are  $\mu\text{m}$ , computed by dividing the volume ( $\mu\text{m}^3$ ) by the area ( $\mu\text{m}^2$ ).

The existence of a maximum in the reactivity can be understood in terms of the surface charge.  $\text{SrTiO}_3$  is an n-type semiconductor; thus, when immersed in a neutral aqueous solution, we expect a negative surface charge to develop that results in a small amount of upward band bending, as illustrated in Figure 5-16b. In this condition, there is a barrier for photogenerated electrons to reach the surface, while the negative surface charge will attract photogenerated holes to the surface. As established decades ago,<sup>50</sup> the pH of the solution alters the charge on the surface and therefore bends the bands. For example, an increase in pH makes more hydroxyl groups interact with the surface, rendering it more negative, increasing upward band bending (see Figure 5-16c). This will make it more difficult for electrons to get to the surface but will more strongly attract holes to the surface. If the pH decreases and more protons interact with the surface, then the surface becomes less negative (see Figure 5-16a). In this case, the barrier for electrons to reach the surface decreases, but holes will not be as strongly attracted to the surface (if the bands bend downward, holes will be repelled). The change in pH from 3 to 9 will lead to a change in the surface potential of 0.35 V, depicted as a change in the band edge positions from Figure 5-16a to 5-16c. With this simple picture in mind, it is easy to see how a maximum reactivity occurs at an intermediate pH. The photocathodic and photoanodic reactions are constrained by charge conservation to occur at the same rate and the overall reaction rate will therefore be limited by the slower of the two reactions.

At the limit of high pH, electrons are strongly repelled from the surface, so the photocathodic reaction will limit the overall reaction rate. At the limit of low pH, holes are not as easily transported to the surface, so the photoanodic reaction will limit the overall reaction rate. It is at some intermediate pH that the maximum rate is achieved where neither reaction limits the other.

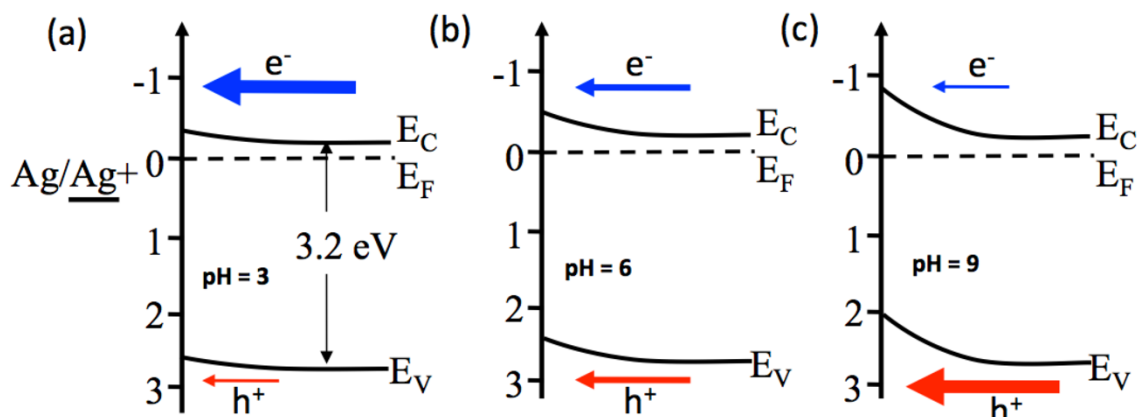


**Figure 5-16:** Schematic electronic energy levels for the bands in SrTiO<sub>3</sub>. The conduction band ( $E_C$ ), valence band ( $E_V$ ), Fermi level ( $E_F$ ), and the silver reduction potential ( $\text{Ag}/\text{Ag}^+$ ) are marked. The upward band bending increase with pH. (c) At high pH, holes are more easily transported to the surface than electrons (indicated by the thickness and length of the arrows). (b) As the pH is reduced and band bending decreases, the barrier for electron transport to the surface remains, but the much higher concentration of electrons in the n-type semiconductor results in comparable electron and hole currents. (a) At the lowest pH, the overall reaction is limited by the transport of holes (minority carriers) to the surface. The energy scale is estimated based on known values for the band gap and silver reduction levels using the method outlined by Morrison.<sup>50</sup>

It is interesting to note that the maximum reactivity for the different surfaces is found at different values of pH. This suggests that the surfaces have different potentials. Considering the fact that the solution potential changes by  $\approx 59$  mV for each pH unit, this implies that the difference in the potential between the (111) and (110) surfaces is 0.177 V. That the different orientations of SrTiO<sub>3</sub> have different potentials is not surprising, considering the anisotropic dispersion of the valence and conduction bands.<sup>51</sup> Evidence for different potentials on different surface orientations of TiO<sub>2</sub> can be found in the work of by Bullard and Cima,<sup>52</sup> who found that the isoelectric points the (100), (110), and (001) surfaces vary over a range of 2.6 pH units (0.153 V). It would be interesting to compare the pH of maximum reactivity with the isoelectric point of SrTiO<sub>3</sub>. Unfortunately, there is little consensus in the literature about the isoelectric point of SrTiO<sub>3</sub>.<sup>53,54</sup> It has been reported to be pH 2.4,<sup>55</sup> pH 3.5,<sup>56</sup> pH 7.8,<sup>57</sup> pH 8.5,<sup>58</sup> pH 9.3,<sup>59</sup> and pH 9.5.<sup>60</sup> Note that we do not expect the maximum reactivity to be at the isoelectric point. Because the electrons are the majority

carriers, we assume that they are abundant at the surface under most conditions. If so, it is likely that the maximum reactivity occurs under conditions where the holes are promoted to the surface by upward band bending and there is still a small barrier for the promotion of electrons to the surface.

It is important to keep in mind that the pH of maximum reactivity identified in these studies is an average behavior found on a heterogeneous surface. All of the surfaces have terraces that are relatively more photocathodic or photoanodic, depending on the termination. Evidence for this can be seen in the spatial selectivity of the silver reduction. Furthermore, depending on the surface preparation, the ratio of photocathodic to photoanodic terraces will vary.<sup>16,32</sup> This will likely influence the isoelectric point of the surface and the pH of maximum reactivity. It is interesting to note that at pH 4, where the (111) surface has maximum reactivity, the spatial selectivity disappears, and all terraces appear equally reactive. On the contrary, at pH 6 where the (100) surface has its maximum reactivity, there are clearly terraces that prefer reduction more than others.

The interpretation presented above is relatively simple and ignores other effects that can occur in solution. For example, in the lowest pH environments, there might be a competition between  $\text{Ag}^+$  ions and protons for surface sites. However, the observation that the pH is the same before and after the reduction reaction suggests that the reaction is still dominated by  $\text{Ag}^+$ . To test for concentration effects, some experiments have been repeated in higher concentrations of  $\text{Ag}^+$  (0.115 M), and the reactivity trend is the same as the low concentration conditions from pH 3 to pH 6.

The results reported here have implications for the design of catalyst particles and reactor conditions. First, because a single pH must be selected for the solution, it would make sense to operate in the pH 6-7 range with particles terminated by (100) or a combination of (100) and (110) facets. In this pH range, the reactivity of the (111) surface is very low, so these facets should be avoided. On the other hand, if it were favorable to operate at pH 4, then an octahedral particle bounded by (111) surfaces only would be best. While the stability of the  $\text{SrTiO}_3$  surface at such a low pH is questionable, it has been shown that the photochemical properties of the  $\text{SrTiO}_3$  surface were not changed by thin protective coatings of  $\text{TiO}_2$ .<sup>61</sup> Consistent with the results presented here, it is known that the (110) surface is relatively photoanodic compared to the (100) surface.<sup>15,39</sup> These two surfaces are part of the equilibrium shape of  $\text{SrTiO}_3$ ,<sup>40,49</sup> and it is known how to produce polyhedral particles bounded by different ratios of (100) and (110) facets.<sup>62</sup> Therefore, one would

hypothesize that crystals with both (100) and (110) facets would have higher reactivity than a particle with only one type of facet. Our observation that, under the same reaction conditions, the polycrystal surfaces with a mixture of facets are much more reactive than the single crystals, is consistent with this idea. Additional support for this idea has been reported by Hsieh et al.,<sup>63</sup> and Mu et al.<sup>39</sup> who showed that SrTiO<sub>3</sub> terminated by (100) and (110) facets produced hydrogen at a greater rate than cube shaped crystals terminated only by (100) facets. The rate of hydrogen production might further be improved by controlling the pH in the range of 6 to 7.

## 5.5 Conclusion

In the pH range of 3 to 9, the (100), (110), and (111) surfaces of SrTiO<sub>3</sub> show a maximum photochemical reactivity for the reduction of silver from an aqueous AgNO<sub>3</sub> solution. For the (100), (110), and (111) surface, the reactivity maxima are at pH 6, 7, and 4, respectively. The same maxima were found on nearly ideal single crystal surfaces and on the surfaces of grains within a polycrystal that are vicinal to the ideal orientations. The relative reactivities at the pH of maximum reactivity for the (100), (110), and (111) surfaces are 1 : 0.2 : 0.9, respectively. The change in the reactivity versus pH can be understood in relation to the surface charge created by the solution. At the lowest (highest) pH, electrons (holes) are drawn to the positively (negatively) charged surface and the overall reaction is limited by the transfer of holes (electrons) to the surface. The maximum reactivity occurs at an intermediate pH where similar concentrations of electrons and holes are at the surface so the photoanodic and photocathodic reactions can proceed at the same rate. The results can be used to optimize the photochemical reactivity of SrTiO<sub>3</sub> for H<sub>2</sub> production or pollutant degradation by designing particles bound by specific combinations of facets and controlling the pH in the reactor.

## 5.6 References

- (1) Fujishima, A.; Honda, K. Electrochemical Photolysis of Water at a Semiconductor Electrode. *Nature* 1972, 238 (5358), 37–38. <https://doi.org/10.1038/238037a0>.
- (2) Han, F.; Kambala, V. S. R.; Srinivasan, M.; Rajarathnam, D.; Naidu, R. Tailored Titanium Dioxide Photocatalysts for the Degradation of Organic Dyes in Wastewater Treatment: A Review. *Appl. Catal. A Gen.* 2009, 359 (1), 25–40. <https://doi.org/10.1016/j.apcata.2009.02.043>.

- (3) Hisatomi, T.; Kubota, J.; Domen, K. Recent Advances in Semiconductors for Photocatalytic and Photoelectrochemical Water Splitting. *Chem. Soc. Rev.* 2014, 43 (22), 7520–7535. <https://doi.org/10.1039/C3CS60378D>.
- (4) McKone, J. R.; Lewis, N. S.; Gray, H. B. Will Solar-Driven Water-Splitting Devices See the Light of Day? *Chem. Mater.* 2014, 26 (1), 407–414. <https://doi.org/10.1021/cm4021518>.
- (5) Wang, Z.; Li, C.; Domen, K. Recent Developments in Heterogeneous Photocatalysts for Solar-Driven Overall Water Splitting. *Chem. Soc. Rev.* 2019, 48 (7), 2109–2125. <https://doi.org/10.1039/C8CS00542G>.
- (6) Maeda, K.; Domen, K. Photocatalytic Water Splitting: Recent Progress and Future Challenges. *J. Phys. Chem. Lett.* 2010, 1 (18), 2655–2661. <https://doi.org/10.1021/jz1007966>.
- (7) Qu, Y.; Duan, X. Progress, Challenge and Perspective of Heterogeneous Photocatalysts. *Chem. Soc. Rev.* 2013, 42 (7), 2568–2580. <https://doi.org/10.1039/C2CS35355E>.
- (8) Spanhel, L.; Haase, M.; Weller, H.; Henglein, A. Photochemistry of Colloidal Semiconductors. 20. Surface Modification and Stability of Strong Luminescing CdS Particles. *J. Am. Chem. Soc.* 1987, 109 (19), 5649–5655. <https://doi.org/10.1021/ja00253a015>.
- (9) Sato, S.; White, J. M. Photodecomposition of Water over Pt/TiO<sub>2</sub> Catalysts. *Chem. Phys. Lett.* 1980, 72 (1), 83–86. [https://doi.org/10.1016/0009-2614\(80\)80246-6](https://doi.org/10.1016/0009-2614(80)80246-6).
- (10) Li, L.; Salvador, P. A.; Rohrer, G. S. Photocatalysts with Internal Electric Fields. *Nanoscale* 2014, 6 (1), 24–42. <https://doi.org/10.1039/c3nr03998f>.
- (11) Wang, X.; Xu, Q.; Li, M.; Shen, S.; Wang, X.; Wang, Y.; Feng, Z.; Shi, J.; Han, H.; Li, C. Photocatalytic Overall Water Splitting Promoted by an  $\alpha$ - $\beta$  Phase Junction on Ga<sub>2</sub>O<sub>3</sub>. *Angew. Chemie Int. Ed.* 2012, 51 (52), 13089–13092. <https://doi.org/10.1002/anie.201207554>.
- (12) Yang, D.; Liu, H.; Zheng, Z.; Yuan, Y.; Zhao, J.; Waclawik, E. R.; Ke, X.; Zhu, H. An Efficient Photocatalyst Structure: TiO<sub>2</sub>(B) Nanofibers with a Shell of Anatase Nanocrystals. *J. Am. Chem. Soc.* 2009, 131 (49), 17885–17893. <https://doi.org/10.1021/ja906774k>.

- (13) Dunn, S.; Jones, P. M.; Gallardo, D. E. Photochemical Growth of Silver Nanoparticles on C- and C+ Domains on Lead Zirconate Titanate Thin Films. *J. Am. Chem. Soc.* 2007, *129* (28), 8724–8728. <https://doi.org/10.1021/ja071451n>.
- (14) Giocondi, J. L.; Rohrer, G. S. Spatially Selective Photochemical Reduction of Silver on the Surface of Ferroelectric Barium Titanate. *Chem. Mater.* 2001, *13* (2), 241–242. <https://doi.org/10.1021/cm000890h>.
- (15) Giocondi, J. L.; Rohrer, G. S. Structure Sensitivity of Photochemical Oxidation and Reduction Reactions on SrTiO<sub>3</sub> Surfaces. *J. Am. Ceram. Soc.* 2003, *86* (7), 1182–1189. <https://doi.org/10.1111/j.1151-2916.2003.tb03445.x>.
- (16) Zhu, Y.; Salvador, P. A.; Rohrer, G. S. Controlling the Termination and Photochemical Reactivity of the SrTiO<sub>3</sub>(110) Surface. *Phys. Chem. Chem. Phys.* 2017, *19* (11), 7910–7918. <https://doi.org/10.1039/C6CP08608J>.
- (17) Chen, F.; Huang, H.; Guo, L.; Zhang, Y.; Ma, T. The Role of Polarization in Photocatalysis. *Angew. Chemie Int. Ed.* 2019, *58* (30), 10061–10073. <https://doi.org/10.1002/anie.201901361>.
- (18) Inoue, Y.; Sato, K.; Sato, K.; Miyama, H. Photoassisted Water Decomposition by Ferroelectric Lead Zirconate Titanate Ceramics with Anomalous Photovoltaic Effects. *J. Phys. Chem.* 1986, *90* (13), 2809–2810. <https://doi.org/10.1021/j100404a006>.
- (19) Kakekhani, A.; Ismail-Beigi, S.; Altman, E. I. Ferroelectrics: A Pathway to Switchable Surface Chemistry and Catalysis. *Surf. Sci.* 2016, *650*, 302–316. <https://doi.org/10.1016/j.susc.2015.10.055>.
- (20) Khan, M. A.; Nadeem, M. A.; Idriss, H. Ferroelectric Polarization Effect on Surface Chemistry and Photo-Catalytic Activity: A Review. *Surf. Sci. Rep.* 2016, *71* (1), 1–31. <https://doi.org/10.1016/j.surfrep.2016.01.001>.
- (21) Li, L.; Rohrer, G. S.; Salvador, P. A. Heterostructured Ceramic Powders for Photocatalytic Hydrogen Production: Nanostructured TiO<sub>2</sub> Shells Surrounding Microcrystalline (Ba,Sr)TiO<sub>3</sub> Cores. *J. Am. Ceram. Soc.* 2012, *95* (4), 1414–1420. <https://doi.org/10.1111/j.1551-2916.2012.05076.x>.

- (22) Munprom, R.; Salvador, P. A.; Rohrer, G. S. Ferroelastic Domains Improve Photochemical Reactivity: A Comparative Study of Monoclinic and Tetragonal  $(\text{Bi}_{1-0.5x}\text{Na}_{0.5x})(\text{V}_{1-x}\text{Mo}_x)\text{O}_4$  Ceramics. *J. Mater. Chem. A* 2016, 4 (8), 2951–2959. <https://doi.org/10.1039/c5ta05551b>.
- (23) Zhong, Y.; Ueno, K.; Mori, Y.; Shi, X.; Oshikiri, T.; Murakoshi, K.; Inoue, H.; Misawa, H. Plasmon-Assisted Water Splitting Using Two Sides of the Same  $\text{SrTiO}_3$  Single-Crystal Substrate: Conversion of Visible Light to Chemical Energy. *Angew. Chemie Int. Ed.* 2014, 53 (39), 10350–10354. <https://doi.org/10.1002/anie.201404926>.
- (24) Ohtani, B.; Okugawa, Y.; Nishimoto, S.; Kagiya, T. Photocatalytic Activity of Titania Powders Suspended in Aqueous Silver Nitrate Solution: Correlation with pH-Dependent Surface Structures. *J. Phys. Chem.* 1987, 91 (13), 3550–3555. <https://doi.org/10.1021/j100297a017>.
- (25) Prairie, M. R.; Evans, L. R.; Stange, B. M.; Martinez, S. L. An Investigation of Titanium Dioxide Photocatalysis for the Treatment of Water Contaminated with Metals and Organic Chemicals. *Environ. Sci. Technol.* 1993, 27 (9), 1776–1782. <https://doi.org/10.1021/es00046a003>.
- (26) Oosawa, Y.; Grätzel, M. Enhancement of Photocatalytic Oxygen Evolution in Aqueous  $\text{TiO}_2$  Suspensions by Removal of Surface-OH Groups. *J. Chem. Soc. Chem. Commun.* 1984, No. 24, 1629–1630. <https://doi.org/10.1039/C39840001629>.
- (27) Guo, Y.; Siretanu, I.; Zhang, Y.; Mei, B.; Li, X.; Mugele, F.; Huang, H.; Mul, G. PH-Dependence in Facet-Selective Photo-Deposition of Metals and Metal Oxides on Semiconductor Particles. *J. Mater. Chem. A* 2018, 6 (17), 7500–7508. <https://doi.org/10.1039/C8TA00781K>.
- (28) Goto, Y.; Hisatomi, T.; Wang, Q.; Higashi, T.; Ishikiriyama, K.; Maeda, T.; Sakata, Y.; Okunaka, S.; Tokudome, H.; Katayama, M.; et al. A Particulate Photocatalyst Water-Splitting Panel for Large-Scale Solar Hydrogen Generation. *Joule* 2018, 2 (3), 509–520. <https://doi.org/10.1016/j.joule.2017.12.009>.
- (29) Luo, J.; Maggard, P. A. Hydrothermal Synthesis and Photocatalytic Activities of  $\text{SrTiO}_3$ -Coated  $\text{Fe}_2\text{O}_3$  and  $\text{BiFeO}_3$ . *Adv. Mater.* 2006, 18 (4), 514–517. <https://doi.org/10.1002/adma.200500109>.

- (30) Zhao, Z.; Goncalves, R. V.; Barman, S. K.; Willard, E. J.; Byle, E.; Perry, R.; Wu, Z.; Huda, M. N.; Moulé, A. J.; Osterloh, F. E. Electronic Structure Basis for Enhanced Overall Water Splitting Photocatalysis with Aluminum Doped SrTiO<sub>3</sub> in Natural Sunlight. *Energy Environ. Sci.* 2019, 12 (4), 1385–1395. <https://doi.org/10.1039/C9EE00310J>.
- (31) Ocal, C.; Bachelet, R.; Garzón, L.; Stengel, M.; Sánchez, F.; Fontcuberta, J. Nanoscale Laterally Modulated Properties of Oxide Ultrathin Films by Substrate Termination Replica through Layer-by-Layer Growth. *Chem. Mater.* 2012, 24 (21), 4177–4184. <https://doi.org/10.1021/cm302444s>.
- (32) Zhu, Y.; Salvador, P. A.; Rohrer, G. S. Controlling the Relative Areas of Photocathodic and Photoanodic Terraces on the SrTiO<sub>3</sub>(111) Surface. *Chem. Mater.* 2016, 28 (14), 5155–5162. <https://doi.org/10.1021/acs.chemmater.6b02205>.
- (33) Song, W.; Salvador, P. A.; Rohrer, G. S. The Effect of pH on the Photochemical Reactivity of BaTiO<sub>3</sub>. *Surf. Sci.* 2018, 675, 83–90. <https://doi.org/10.1016/j.susc.2018.04.021>.
- (34) Song, W.; Lopato, E. M.; Bernhard, S.; Salvador, P. A.; Rohrer, G. S. High-Throughput Measurement of the Influence of pH on Hydrogen Production from BaTiO<sub>3</sub>/TiO<sub>2</sub> Core/Shell Photocatalysts. *Appl. Catal. B Environ.* 2020, 269, 118750. <https://doi.org/https://doi.org/10.1016/j.apcatb.2020.118750>.
- (35) Glickstein, J. J.; Salvador, P. A.; Rohrer, G. S. Computational Model of Domain-Specific Reactivity on Coated Ferroelectric Photocatalysts. *J. Phys. Chem. C* 2016, 120 (23), 12673–12684. <https://doi.org/10.1021/acs.jpcc.6b03875>.
- (36) Chen, P.; Sun, Y.; Liu, H.; Zhou, Y.; Jiang, G.; Lee, S. C.; Zhang, Y.; Dong, F. Facet-Dependent Photocatalytic NO Conversion Pathways Predetermined by Adsorption Activation Patterns. *Nanoscale* 2019, 11 (5), 2366–2373. <https://doi.org/10.1039/C8NR09147A>.
- (37) Giocondi, J. L.; Salvador, P. A.; Rohrer, G. S. The Origin of Photochemical Anisotropy in SrTiO<sub>3</sub>. *Top. Catal.* 2007, 44 (4), 529–533. <https://doi.org/10.1007/s11244-006-0101-y>.

- (38) Li, J.; Dong, X.; Sun, Y.; Cen, W.; Dong, F. Facet-Dependent Interfacial Charge Separation and Transfer in Plasmonic Photocatalysts. *Appl. Catal. B Environ.* 2018, 226, 269–277. <https://doi.org/10.1016/j.apcatb.2017.12.057>.
- (39) Mu, L.; Zhao, Y.; Li, A.; Wang, S.; Wang, Z.; Yang, J.; Wang, Y.; Liu, T.; Chen, R.; Zhu, J.; et al. Enhancing Charge Separation on High Symmetry SrTiO<sub>3</sub> Exposed with Anisotropic Facets for Photocatalytic Water Splitting. *Energy Environ. Sci.* 2016, 9 (7), 2463–2469. <https://doi.org/10.1039/c6ee00526h>.
- (40) Rheinheimer, W.; Baeurer, M.; Chien, H.; Rohrer, G. S.; Handwerker, C. A.; Blendell, J. E.; Hoffmann, M. J. The Equilibrium Crystal Shape of Strontium Titanate and Its Relationship to the Grain Boundary Plane Distribution. *ACTA Mater.* 2015, 82, 32–40. <https://doi.org/10.1016/j.actamat.2014.08.065>.
- (41) Burbure, N. V.; Salvador, P. A.; Rohrer, G. S. Photochemical Reactivity of Titania Films on BaTiO<sub>3</sub> Substrates: Origin of Spatial Selectivity. *Chem. Mater.* 2010, 22 (21), 5823–5830. <https://doi.org/10.1021/cm1018025>.
- (42) Kalinin, S. V.; Bonnell, D. A.; Alvarez, T.; Lei, X.; Hu, Z.; Ferris, J. H.; Zhang, Q.; Dunn, S. Atomic Polarization and Local Reactivity on Ferroelectric Surfaces: A New Route toward Complex Nanostructures. *Nano Lett.* 2002, 2 (6), 589–593. <https://doi.org/10.1021/nl025556u>.
- (43) Wenderich, K.; Mul, G. Methods, Mechanism, and Applications of Photodeposition in Photocatalysis: A Review. *Chem. Rev.* 2016, 116 (23), 14587–14619. <https://doi.org/10.1021/acs.chemrev.6b00327>.
- (44) Delahay, P.; Pourbaix, M.; Rysselberghe, P. Van. Potential-pH Diagram of Silver Construction of the Diagram-Its Applications to the Study of the Properties of the Metal, Its Compounds, and Its Corrosion. *J. Electrochem. Soc.* 1951, 98 (2), 65. <https://doi.org/10.1149/1.2778107>.
- (45) David, N.; Petr, K. Gwyddion: An Open-Source Software for SPM Data Analysis. *Open Physics*. 2012, p 181. <https://doi.org/10.2478/s11534-011-0096-2>.

- (46) Yan, H.; Zhang, Z.; Li, M.; Wang, S.; Ren, L.; Jin, K. Photoresponsive Properties at (0 0 1), (1 1 1) and (1 1 0) LaAlO<sub>3</sub>/SrTiO<sub>3</sub> Interfaces. *J. Phys. Condens. Matter* 2019, 32 (13), 135002. <https://doi.org/10.1088/1361-648x/ab5ebf>.
- (47) Koster, G.; Kropman, B. L.; Rijnders, G. J. H. M.; Blank, D. H. A.; Rogalla, H. Quasi-Ideal Strontium Titanate Crystal Surfaces through Formation of Strontium Hydroxide. *Appl. Phys. Lett.* 1998, 73 (20), 2920–2922. <https://doi.org/10.1063/1.122630>.
- (48) Paradinas, M.; Garzón, L.; Sánchez, F.; Bachelet, R.; Amabilino, D. B.; Fontcuberta, J.; Ocal, C. Tuning the Local Frictional and Electrostatic Responses of Nanostructured SrTiO<sub>3</sub>—Surfaces by Self-Assembled Molecular Monolayers. *Phys. Chem. Chem. Phys.* 2010, 12 (17), 4452–4458. <https://doi.org/10.1039/B924227A>.
- (49) Pisat, A. S.; Salvador, P. A.; Rohrer, G. S. The Facet Structure and Photochemical Reactivity of Arbitrarily Oriented Strontium Titanate Surfaces. *Adv. Mater. Interfaces* 2019, 6 (16), 1900731. <https://doi.org/10.1002/admi.201900731>.
- (50) Morrison, S. R. *Electrochemistry at Semiconductor and Oxidized Metal Electrodes*. 1980.
- (51) Van Benthem, K.; Elsässer, C.; French, R. H. Bulk Electronic Structure of SrTiO<sub>3</sub>: Experiment and Theory. *J. Appl. Phys.* 2001, 90 (12), 6156–6164. <https://doi.org/10.1063/1.1415766>.
- (52) Bullard, J. W.; Cima, M. J. Orientation Dependence of the Isoelectric Point of TiO<sub>2</sub> (Rutile) Surfaces. *Langmuir* 2006, 22 (24), 10264–10271. <https://doi.org/10.1021/la061900h>.
- (53) Kosmulski, M. pH-Dependent Surface Charging and Points of Zero Charge. IV. Update and New Approach. *J. Colloid Interface Sci.* 2009, 337 (2), 439–448. <https://doi.org/10.1016/j.jcis.2009.04.072>.
- (54) Kosmulski, M. The pH Dependent Surface Charging and Points of Zero Charge. VII. Update. *Adv. Colloid Interface Sci.* 2018, 251, 115–138. <https://doi.org/10.1016/j.cis.2017.10.005>.
- (55) Polli, A. D.; Wagner, T.; Rühle, M. Effect of Ca Impurities and Wet Chemical Etching on the Surface Morphology of SrTiO<sub>3</sub> Substrates. *Surf. Sci.* 1999, 429 (1), 237–245. [https://doi.org/10.1016/S0039-6028\(99\)00383-0](https://doi.org/10.1016/S0039-6028(99)00383-0).

- (56) García-López, E.; Marci, G.; Megna, B.; Parisi, F.; Armelao, L.; Trovarelli, A.; Boaro, M.; Palmisano, L. SrTiO<sub>3</sub>-Based Perovskites: Preparation, Characterization and Photocatalytic Activity in Gas–Solid Regime under Simulated Solar Irradiation. *J. Catal.* 2015, 321, 13–22. <https://doi.org/10.1016/j.jcat.2014.10.014>.
- (57) Diamant, Y.; Chen, S. G.; Melamed, O.; Zaban, A. Core–Shell Nanoporous Electrode for Dye Sensitized Solar Cells: The Effect of the SrTiO<sub>3</sub> Shell on the Electronic Properties of the TiO<sub>2</sub> Core. *J. Phys. Chem. B* 2003, 107 (9), 1977–1981. <https://doi.org/10.1021/jp027827v>.
- (58) Ortiz-Oliveros, H. B.; Ordoñez-Regil, E.; Fernández-Valverde, S. M. Sorption of Uranium(VI) onto Strontium Titanate in KNO<sub>3</sub> Medium. *J. Radioanal. Nucl. Chem.* 2009, 279 (2), 601–610. <https://doi.org/10.1007/s10967-007-7142-y>.
- (59) Konstas, P.-S.; Konstantinou, I.; Petrakis, D.; Albanis, T. Development of SrTiO<sub>3</sub> Photocatalysts with Visible Light Response Using Amino Acids as Dopant Sources for the Degradation of Organic Pollutants in Aqueous Systems. *Catalysts* 2018, 8 (11). <https://doi.org/10.3390/catal8110528>.
- (60) Garcia-Rosales, G.; Drot, R.; Mercier-Bion, F.; Lagarde, G.; Simoni, E. Interaction between U(VI) and SrTiO<sub>3</sub> Surfaces versus Temperature. *J. Colloid Interface Sci.* 2009, 333 (1), 104–113. <https://doi.org/10.1016/j.jcis.2009.01.049>.
- (61) Zhu, Y.; Salvador, P. A.; Rohrer, G. S. Buried Charge at the TiO<sub>2</sub>/SrTiO<sub>3</sub> (111) Interface and Its Effect on Photochemical Reactivity. *ACS Appl. Mater. Interfaces* 2017, 9 (8), 7843–7851. <https://doi.org/10.1021/acsami.6b16443>.
- (62) Dong, L.; Shi, H.; Cheng, K.; Wang, Q.; Weng, W.; Han, W. Shape-Controlled Growth of SrTiO<sub>3</sub> Polyhedral Submicro/Nanocrystals. *Nano Res.* 2014, 7 (9), 1311–1318. <https://doi.org/10.1007/s12274-014-0495-y>.
- (63) Hsieh, P.-L.; Naresh, G.; Huang, Y.-S.; Tsao, C.-W.; Hsu, Y.-J.; Chen, L.-J.; Huang, M. H. Shape-Tunable SrTiO<sub>3</sub> Crystals Revealing Facet-Dependent Optical and Photocatalytic Properties. *J. Phys. Chem. C* 2019, 123 (22), 13664–13671. <https://doi.org/10.1021/acs.jpcc.9b02081>.

# Chapter 6: Influence of Particle Size and Shape on the Rate of Hydrogen Produced by Al-doped SrTiO<sub>3</sub> Photocatalysts

*It is known that the photochemical reactivity is anisotropic on the surface of SrTiO<sub>3</sub>. Here, we prepared faceted Al-doped SrTiO<sub>3</sub> particles exposing (100) and (110) facets and studied how a surface area ratio affects the photocatalytic hydrogen generation rate. The experiment is inspired by the idea that the maximum reactivity occurs when the rates of the two half reactions are optimally balanced. It is generally agreed that smaller particles are more reactive since they have higher surface areas, and therefore more reaction sites. However, is this always true? In this study, we found that the reactivity increases with particle size from 200 nm to 500 nm, which is counter intuition. To explain this, we need to consider the interplay of particle size, space charge length and light penetration depth.*

## 6.1 Introduction

Photocatalytic water splitting is a promising technology to reduce humanity's dependence on fossil fuels by converting solar energy to clean and sustainable H<sub>2</sub> fuel. Since the discovery of photoelectrochemical water oxidation using a TiO<sub>2</sub> photoanode by Fujishima and Honda,<sup>1</sup> thousands of semiconductor materials have been reported to be able to split water.<sup>2-4</sup> Among them, SrTiO<sub>3</sub> is one of the promising materials that can split water under UV illumination and has been widely studied. Many researchers focus on doping aliovalent metal cations into SrTiO<sub>3</sub> to control the defect structure and improve photocatalytic reactivity.<sup>5,6</sup> In recent studies, it was found that a flux treatment in SrCl<sub>2</sub> – together with Al doping - can significantly increase the reactivity of SrTiO<sub>3</sub> for water splitting.<sup>7-9</sup> Previous experiments have shown that modifying the band bending in the space charge region either by internal or external electric fields influences the photochemical reactivity.<sup>10-12</sup> The current study was undertaken to understand how crystal shape, crystal size, pH, and added Al, all of which influence band bending, influence the photochemical reactivity of Al-doped SrTiO<sub>3</sub>. To investigate four independent parameters on hydrogen evolution, a time consuming task when each catalyst is measured separately, we leverage the capabilities of a newly

developed parallelized and automated photochemical reactor (PAPCR),<sup>13</sup> which can be used to measure the H<sub>2</sub> generation rate of up to 108 samples simultaneously in one experiment.

It is known that particle shapes, because of the facets exposed, influence photocatalytic performance.<sup>14–16</sup> It is thought that the spatial separation of charge to different exposed facets leads to increased reactivity. For example, Li et al.<sup>17,18</sup> found the spatial separation of photogenerated electrons and holes among {110} and {010} facets in BiVO<sub>4</sub> contributed to an enhancement of photocatalytic water oxidation reactivity. In SrTiO<sub>3</sub>, previous studies have shown that {100} surfaces are photocathodic and {110} surfaces are photoanodic,<sup>19–21</sup> and SrTiO<sub>3</sub> nanocrystals with both {100} and {110} facets exposed are much more reactive than SrTiO<sub>3</sub> nanocubes (exposing only {100} facets) for photocatalytic water splitting.<sup>21,22</sup> Takata et al.<sup>9</sup> demonstrated a quantum efficiency for overall water splitting up to 96 % at 350 nm to 360 nm using faceted Al-doped SrTiO<sub>3</sub> particles with different cocatalysts selectively photodeposited on {100} and {110} facets. A more recent paper<sup>23</sup> reports that SrTiO<sub>3</sub> particles with {100} and {110} surfaces have reactivities that are inferior to those with only {100} surfaces, but the catalyst particles were significantly smaller than in the previous work.<sup>9,21,22</sup> One of the goals of this paper is to determine the optimal shape for Al-doped SrTiO<sub>3</sub>. For example, it has been shown that, for anatase TiO<sub>2</sub>, particles exposing {001} and {101} facets at a ratio of 1.25 are optimal for the photocatalytic reduction of CO<sub>2</sub> to CH<sub>4</sub>.<sup>24</sup> In this work, we will compare catalyst particles with only photocathodic {100} surfaces to particles that have increasing relative areas of photoanodic {110} surfaces.

Particle sizes are also important to photochemical reactions. In general, smaller particles usually have higher surface area and more reaction sites at constant mass, and this potentially increases the photochemical reaction rate. However, smaller particles are not always better. If the particle size is less than twice the width of the space charge, band bending will be reduced, lowering the potential to separate electrons and holes.<sup>25</sup> Quantum confinement can increase the bandgap of smaller particles,<sup>26,27</sup> leading to decreased light absorption and reactivity. Finally, the smallest particles are usually produced at relatively low temperature and may have a higher concentration of structural defects, which typically promote recombination and reduce reactivity. On the other hand, there is clearly an upper limit for particle size. If the particle is too large, charge carriers generated in the flat band region at the center of the crystal are more likely to recombine than to

migrate to the surface. The existence of an optimal particle size has been demonstrated for  $\text{TiO}_2$ ,<sup>28</sup>  $\text{PbTiO}_3$ ,<sup>29</sup> and  $\text{WO}_3$ .<sup>30</sup> One of the goals of this work is to determine if there is an optimal size for Al-doped  $\text{SrTiO}_3$  and whether this optimum is a function of particle shape.

Solution pH is another factor that influences the rate of water splitting by transition metal oxide catalysts because it alters the surface potential and band bending.<sup>31</sup> At room temperature, the surface potential changes by  $\approx 59$  mV for each pH unit. By increasing pH, more hydroxyl groups will adsorb on the surface and bend the bands upward, increasing the barrier for electrons to migrate to the surface. By decreasing pH, more protons will bend the bands downward and holes will be repelled. A previous study indicates that the maximum photocathodic reactivity of  $\text{SrTiO}_3$  occurs at an intermediate pH where the two half reactions proceed at the same rate.<sup>32</sup> However, that work was carried out on single orientations and for only the photocathodic reaction, so it is not obvious that it will apply to overall water splitting by particles with multiple surfaces.

The reactivity of Al-doped  $\text{SrTiO}_3$  is also reported to vary with Al concentration. Zhao et al. prepared Al doped  $\text{SrTiO}_3$  with a hydrothermal route and found that for specimens with Al concentrations in the range of 0 to 7.8 atom % (measured by X-Ray Fluorescence), samples with 7.8 atom % had the highest reactivity.<sup>33</sup> For Al-doped  $\text{SrTiO}_3$  doped in a  $\text{SrCl}_2$  flux, inductively coupled plasma analysis found 0.12, 1.01, and 1.36 % Al in  $\text{SrTiO}_3$  for fluxes containing 0.1, 1.0, and 10 % Al, suggesting that, at this temperature, the solubility is not significantly greater than 1 %.<sup>7</sup> It has been proposed that the dissolution of  $\text{Al}^{3+}$  ions suppresses the formation of a  $\text{Ti}^{3+}$  recombination center and extends charge carrier lifetime.<sup>5,34,35</sup> Here, we also consider how the concentration of Al in a  $\text{SrCl}_2$  flux influences the reactivity.

The purpose of this work is to understand the combined influence of crystal shape, crystal size, solution pH, and Al doping via flux processing on the rate of  $\text{H}_2$  generation by Al-doped  $\text{SrTiO}_3$ . Catalyst particles with  $\{110\}/\{100\}$  surface area ratios from 0 to 2.5 have been tested, with particle diameters of  $\approx 250$  nm, 350 nm, and 450 nm. All catalysts were treated in a  $\text{SrCl}_2$  flux at 1150 °C for 10 h containing 1, 2, 3, or 5 mol % added  $\text{Al}_2\text{O}_3$  and were afterward loaded with a  $\text{RhCrO}_x$  cocatalyst. A smaller number of materials were doped during the synthesis step. High-throughput photocatalytic water splitting experiments have been carried out using the PAPCR with particles either in DI water whose pH has been adjusted from pH 2 to pH 12 or in 10 % aqueous methanol solutions. Altogether, the hydrogen generation rates were measured from more than 500 different

combinations of parameters. All four parameters (shape, size, pH, and the Al doping method) do influence the rate of hydrogen generation, which can vary from 1 to 150  $\mu\text{mol m}^{-2}\text{h}^{-1}$ , depending on the choice of parameters. Additional experiments indicated that Al doping and the  $\text{SrCl}_2$  flux treatments are independent parameters and the  $\text{SrCl}_2$  flux treatment is a necessary condition for achieving high reactivity. The variation in the reactivity with these parameters can be understood by their effects on band bending within the catalyst particle.

## 6.2 Experimental Methods

**Synthesis of catalysts.**  $\text{SrTiO}_3$  crystals were prepared hydrothermally following a procedure reported by Dong et al.<sup>36</sup> Four types of crystals, denoted A, B, C, and D, were prepared in identical fashion with the exception of the surfactant used. In all cases, 0.2 mL of  $\text{TiCl}_4$  (Sigma-Aldrich, 99 %) was dropped into a solution in an ice bath containing 25 mL of deionized water and the surfactant. These types and amounts of surfactants were used to generate large crystals with an average diameter of 450 nm: A- 2 g of ethanol (PHARMCO, 200 Proof), B- 1 g of 1,2-propanediol (Sigma-Aldrich, 99.5%), C- 1 g of ethylene glycol (Alfa Aesar, 99+%), and D- 0.1 g of pentaerythritol (Sigma-Aldrich, 99%). After magnetic stirring for 5 min, 10 mL of  $\text{SrCl}_2$  solution containing 0.42 g  $\text{SrCl}_2$  (Sigma-Aldrich, 99.99%) and 30 ml of LiOH solution containing 2.26 g LiOH (Sigma-Aldrich, 98%) was added. After stirring for another 30 min, the resulting solution was transferred to a 100 ml Teflon-lined hydrothermal autoclave (Techinstro). The autoclave was then heated at 180 °C for 36 h in a furnace. After heat treatment, the solution was removed and the resulting precipitate was centrifuged four times at 4000 rpm for 12 min with deionized water and ethanol, respectively. Finally, the resulting precipitate was dried in an oven at 80 °C overnight. Additionally,  $\text{SrTiO}_3$  crystals of type A (type B) were also prepared in two smaller sizes, with average diameters of 350 nm and 250 nm, referred to as medium and small, following the same procedure but increasing the amount of surfactant to 10 g (6 g) for medium and 20 g (12 g) for small. All samples' abbreviations and corresponding synthesis conditions are summarized in Table 6-1.

Note that during the hydrothermal synthesis, an excess of  $\text{SrCl}_2$ , greater than the stoichiometric ratio for  $\text{SrTiO}_3$ , was employed. In initial experiments where the stoichiometric ratio was used, the product was a mixture of anatase, rutile, and  $\text{SrTiO}_3$ . These small  $\text{TiO}_2$  particles adhere to the

larger SrTiO<sub>3</sub> crystals and blocked the illumination. By adding an excess amount of SrCl<sub>2</sub> in the hydrothermal synthesis, the formation of TiO<sub>2</sub> was inhibited, and clean SrTiO<sub>3</sub> crystals with reproducible morphologies were obtained. It is also noted that the crystals synthesized in our lab have a larger size compared to what is reported by Dong et al.,<sup>36</sup> even though the same amounts of surfactants are added.

**Table 6-1:** Summary of synthesis route and conditions for all samples.

Shape	Type of surfactant	Amount of surfactant	Average size
(100) facet only	Ethanol	2 g	450 nm
(110)/(100) = 1.3	1,2-propanediol	1 g	450 nm
(110)/(100) = 1.8	Ethylene glycol	1 g	450 nm
(110)/(100) = 2.5	Pentaerythritol	0.1 g	450 nm
(100) facet only	Ethanol	10 g	350 nm
(100) facet only	Ethanol	20 g	250 nm
(110)/(100) = 1.3	1,2-propanediol	6 g	350 nm
(110)/(100) = 1.3	1,2-propanediol	12 g	250 nm

SrTiO<sub>3</sub> nanocrystals of type A, B, C, and D were doped with Al in a SrCl<sub>2</sub> flux, as described by Domen and co-workers.<sup>8,9</sup> The hydrothermally grown SrTiO<sub>3</sub>, Al<sub>2</sub>O<sub>3</sub> nanopowders (Sigma-Aldrich, < 50 nm particle size), and SrCl<sub>2</sub> (Alfa Aesar, 99.5%) were mixed at a molar ratio of 1:0.01:10, 1:0.02:10, 1:0.03:10, or 1:0.05:10 with a mortar and pestle. The mixture was then heated at 1150 °C for 10 h in an alumina crucible, a temperature at which the SrCl<sub>2</sub> liquifies. To remove the SrCl<sub>2</sub> thoroughly after the process, the resulting mixture was centrifuged four times at 4000 rpm for 18 min, first with deionized water and then with ethanol. The resulting Al-doped SrTiO<sub>3</sub> powders were then dried in an oven at 80 °C over night.

RhCrO<sub>x</sub> cocatalysts were loaded (0.1 wt% Rh and 0.1 wt% Cr) on all crystals with an impregnation method described elsewhere.<sup>37</sup> 50 mg of as prepared Al-doped SrTiO<sub>3</sub> crystals were dispersed into 0.5 ml of deionized water containing appropriate amounts of Na<sub>3</sub>RhCl<sub>6</sub> (Sigma-Aldrich) and Cr(NO<sub>3</sub>)<sub>3</sub>·6H<sub>2</sub>O (Sigma-Aldrich, 99%) to yield 0.1 wt% Rh and Cr. Note that, in some experiments, this amount was adjusted to study the effect of the amount of cocatalysts loaded on the reactivity. The suspension was evaporated in a water bath under constant manually stirring. The resulting powders were collected and heated at 350 °C for 1 h. A schematic illustration of the catalyst synthesis route is presented in Figure 6-1.

P25 TiO<sub>2</sub> was used as a reference catalyst and included in all panels, so that results could be compared from panel to panel. P25 powders were loaded with 1 wt% Pt by the impregnation method.<sup>38,39</sup> P25 powders (Degussa) were immersed in H<sub>2</sub>PtCl<sub>6</sub> solution (Sigma-Aldrich) for 2 h with magnetic stirring. Then, the powders were reduced using a 5-fold excess of NaOH (Fisher Scientific) and NaBH<sub>4</sub> (Acros) for 2 h with stirring. The powders were then collected and rinsed in DI water by centrifugation and dried overnight.

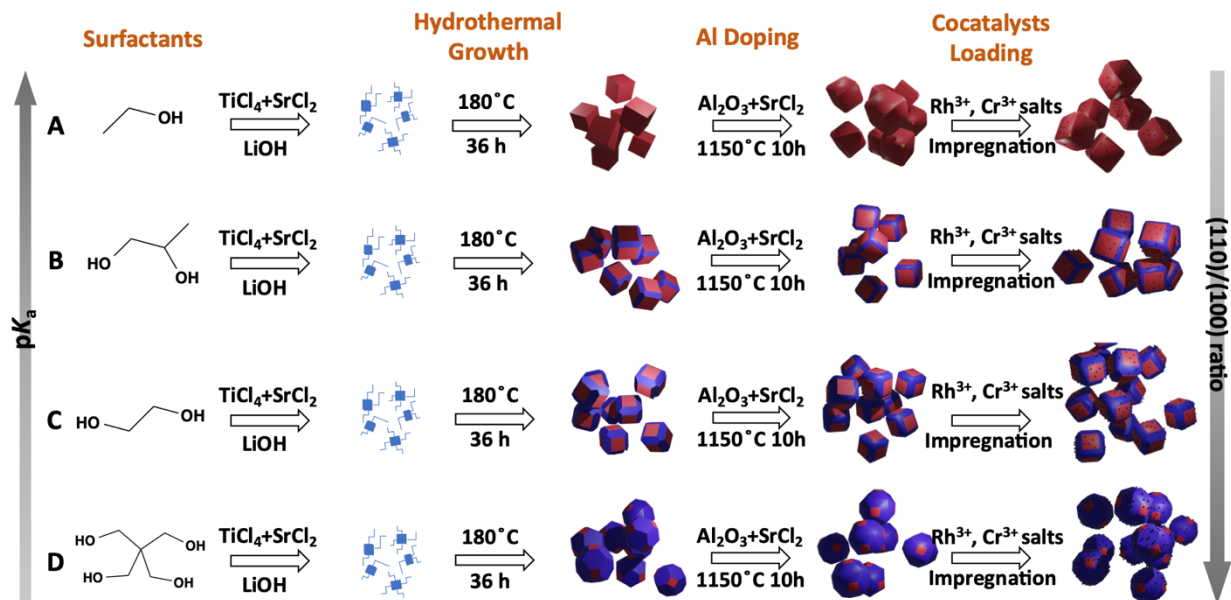


**Figure 6-1:** Schematic diagram illustrating the route of the formation of Al-doped SrTiO<sub>3</sub> catalysts in the presence of different surfactants.

**Characterization.** Powder X-ray diffraction (XRD) was used to determine the phase of each sample with an X'Pert Pro MPD x-ray diffractometer (PANalytical, Philips, Netherlands). A scan rate of 5°-min<sup>-1</sup> was applied in the range of 20–90° at a step size of 0.02°. Scanning Electron Microscopy (SEM) images were obtained to determine the morphologies of all samples using FEI Quanta 600 with a 20 kV beam with a spot size of 3. N<sub>2</sub> adsorption–desorption measurements (Nova 2200e, Quanta-chrome, FL), used to determine the specific surface areas of powders through a Brunauer–Emmett–Teller (BET) approach, was performed at 77 K using a multi-point method. The pore size distribution was obtained using the Barrett-Joyner-Halenda (BJH) model. Pore volume was measured from desorption measurements at the P/P<sub>0</sub> = 0.99 point. The sample was degassed at 110 °C for 24 h prior to measurement.

***Photocatalytic water splitting experiment.*** The photocatalytic reactivity for hydrogen evolution was measured with a high-throughput parallelized and automated photochemical reactor (PAPCR), illustrated schematically in Fig. 6-2.<sup>13</sup> Two 100 W UV LED chips (Chanzon, 380 nm) at the bottom of the reactor were fixed on an aluminum plate to provide constant illumination for the reaction. The LEDs were cooled by a fan and circulating chilled water. At the mid part of the reactor, 108 1 mL shell vials sit on an aluminum plate with small holes drilled at the bottom, through which illumination from the LEDs can transmit into the vials. The vials were covered with a layer of hydrogen sensitive film (DetecTape, Midsun Specialty Products) whose color changes from light to dark with an increase in the local hydrogen concentration. Next, a flexible silicone layer and a rigid plexiglass plate were placed on the top of the FEP film to seal and cover the whole reactor array. At the top of the reactor, a Pi camera (Raspberry Pi Camera Board v2 -8 Megapixels) was fixed. Every six minutes, the LEDs are switched off and the camera takes a picture of the hydrogen sensitive film. After the picture was taken, the LEDs were switched on for another 6-minute cycle. Two rows of white LED strips (JUNWEN, 16 W) were used to illuminate the hydrogen sensitive tape from above while the image was captured. For each image, the RGB values were extracted for an area of 54 pixels in the center of each vial to determine the darkness of the film. These values were then subtracted from the darkness value from the first image. The response of the hydrogen sensitive film was calibrated in the range of 4% to 31% of H<sub>2</sub> by adding known amounts of hydrogen to the vials and recording the response. Based on the calibrated relationship between local hydrogen concentration and the appearance of the film, it is possible to calculate the amount of H<sub>2</sub> production every 6 min as well as the reaction rate.

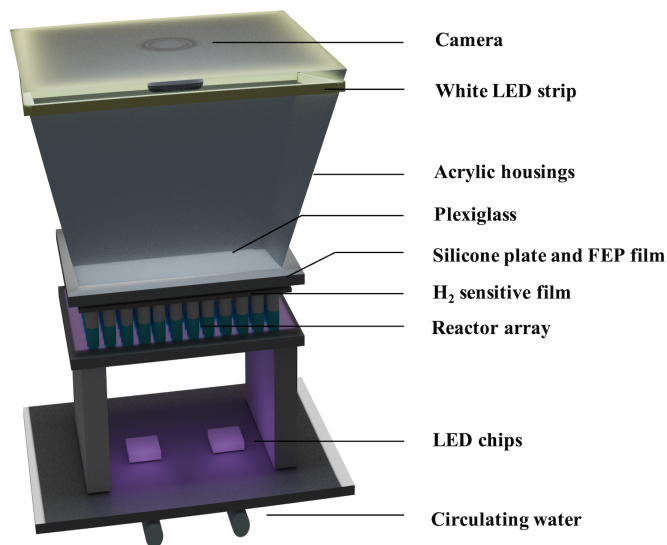


**Figure 6-2:** Schematic illustration of the parallelized and automated photochemical reactor (PAPCR).

By varying the amount of Al-doped SrTiO<sub>3</sub> added to each vial, we found that the absolute rate ( $\mu\text{mol h}^{-1}$ ) of H<sub>2</sub> evolution reached a maximum at 10 mg. Therefore, in all further experiments, 10 mg of Al-doped SrTiO<sub>3</sub> was added to each shell vial with 0.6 ml of DI water whose pH was adjusted from pH 2 to pH 12 by adding acetic acid (Fisher Chemical) or NaOH (Fisher Scientific). The reactor was illuminated for 18 h, during which a total of 180 images were taken, with each image quantifying the hydrogen concentration within each vial. We verified that the acid anion group did not significantly influence reactivity by comparing reaction rates of the same sample in DI water whose pH was adjusted using acetic acid, nitric acid, or hydrochloric acid and confirm the type of acid does not influence reactivity. To determine the effect of adding a hole scavenger, a parallel set of experiments was conducted with solutions containing 10 % methanol and 5 mg of catalyst. Each experiment included three vials with 3.2 mg of the P25 reference catalyst in 6 ml of a 1 % methanol solution. The standard deviation was calculated from the H<sub>2</sub> production rates of the three reference catalysts.

## 6.3 Results

SEM images of Al-doped SrTiO<sub>3</sub> particles are given in Figure 6-3, as a function of type (shape), given in rows, and Al doping concentration, given in columns. Focusing on the undoped crystals in the leftmost column, crystals of type A (top row) are cubes, exposing only six {100} facets.

Crystals of type B, C, and D, shown in descending order, are edge truncated cubes, exposing both  $\{100\}$  and  $\{110\}$  facets, where the ratios of the  $\{110\}$  areas to the  $\{100\}$  areas are 1.3, 1.8, and 2.5 for B, C, and D, respectively. SEM images of crystals after Al doping in the  $\text{SrCl}_2$  flux are shown in the four left most columns in Figure 6-3. Note that we refer to these samples by their initial shape (the capital letter) and the percentage of Al added to the flux (the number). It is clear that exposure to melts with more than 1 % Al significantly impacts crystal morphology. Crystals of type A transform from cubes to corner-truncated cubes, exposing  $\{100\}$  and  $\{111\}$  facets. For crystals of type B, C, and D, the treatment truncates the corners and reduces the areas of  $\{110\}$  facets. The resulting crystals expose all three facets ( $\{100\}$ ,  $\{110\}$  and  $\{111\}$ ). Crystals treated in melts with 5 % Al all have similar cubic shapes exposing primarily  $\{100\}$  facets with a small fraction of  $\{111\}$  facets and  $\{110\}$  facets, as shown in the fifth column in Figure 6-3. This shape is similar to particles in Domen's work.<sup>7,34</sup> All crystals have similar sizes with an average diameter of 450 nm, and the Al doping treatment did not have an obvious influence on the particle size. XRD patterns of the 16 types of Al-doped  $\text{SrTiO}_3$  samples are given in Figure 6-4, showing only peaks attributable to  $\text{SrTiO}_3$ .

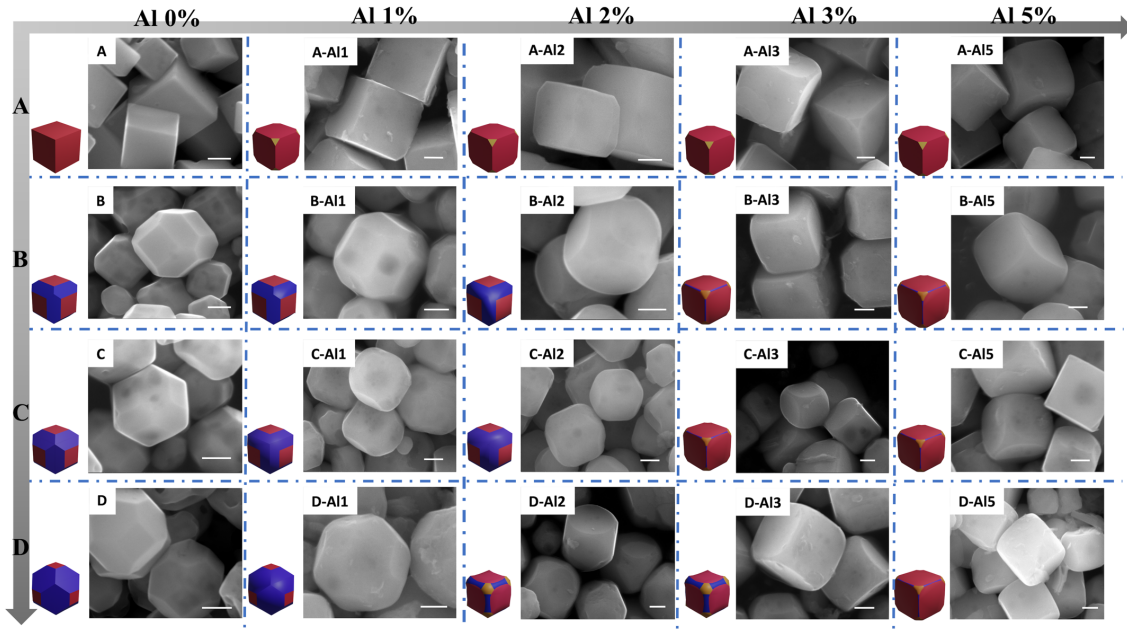


**Figure 6-3:** SEM images as well as schematic diagrams for  $\text{SrTiO}_3$  nanocrystals with different shape and treated in melts with different Al concentrations. Scale bar is 200 nm.

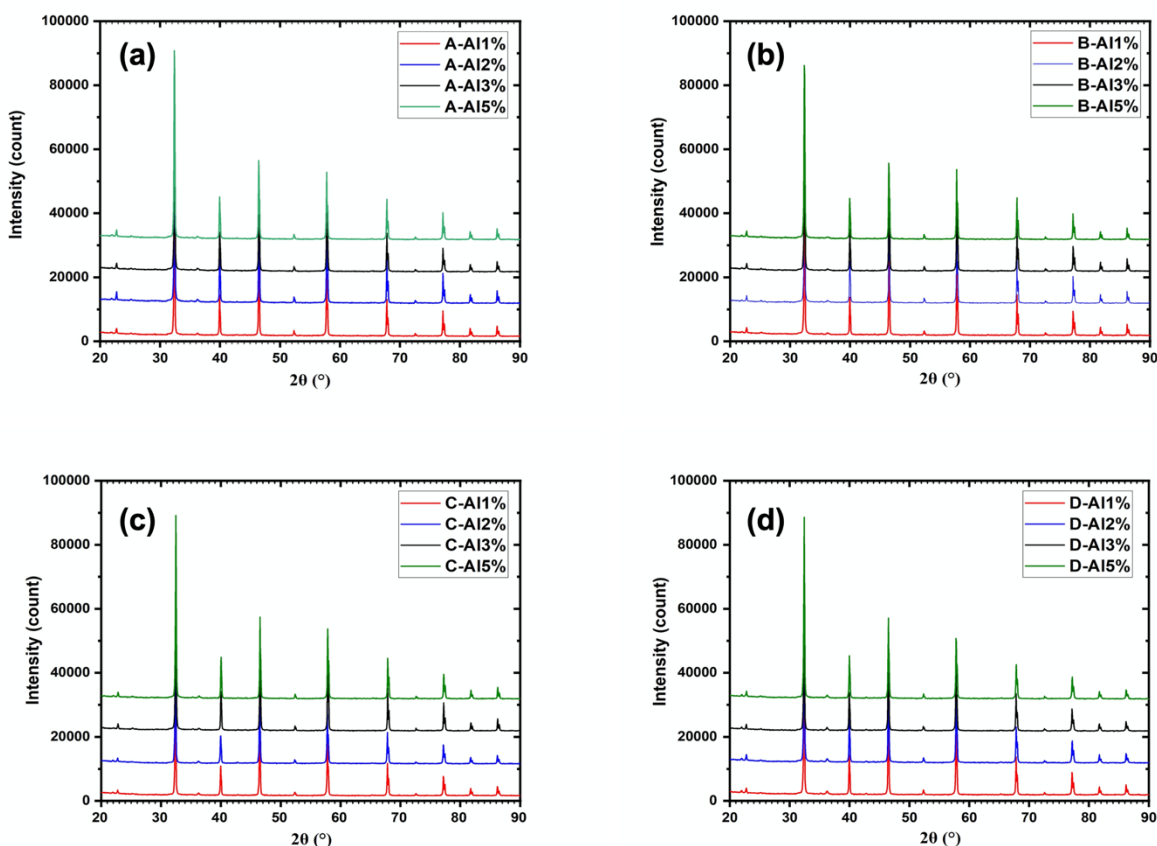


**Figure 6-4:** XRD patterns of type A, B, C and D crystals treated in  $\text{SrCl}_2$  flux with (a) 1%, (b) 2%, (c) 3% and (d) 5% aluminum added.

The mass specific rates ( $\mu\text{mol h}^{-1} \text{g}^{-1}$ ) of  $\text{H}_2$  evolution from the Al-doped  $\text{SrTiO}_3$  crystals shown in Figure 6-3 were measured under UV illumination at 380 nm using the PAPCR and the results are shown in Figure 6-5. The standard deviation is about 12% (11%) for shapes A and B (C and D). As shown in Figure 6-6, the band gap energies of the crystals are also essentially the same (3.28 eV, 3.27 eV, 3.26 eV and 3.27 eV for Type A, B, C and D, respectively), so differences in absorption are not expected to influence the reactivity. Several trends are apparent from Figure 6-5. First, crystals of types of B, C and D produce  $\text{H}_2$  at a greater rate than A. This was also true when the reaction was carried out in 10% methanol solutions. Second, for all four shapes, samples with 1% added Al had the maximum reactivity. The addition of more Al decreased the reactivity, consistent with previous work by Ham et al.<sup>7</sup> Note that the crystals with 5% added Al in the flux all have similar reactivities, consistent with the observation that they have similar shapes (see Figure 6-3). Third, for all types of crystals, the reactivity first increases with pH to a maximum at around pH 7, then decreases at pH 10 and pH 11. At pH 12, there is usually an increase in reactivity.

The initial increase in reactivity with pH is consistent with observations reported for undoped SrTiO<sub>3</sub> single crystals, discussed in Chapter 5.<sup>32</sup> This is likely due to an increase in the absorption of negative charge with increasing pH that bends the bands further upward and promotes the conduction of holes to the surface. While this increase of the upward band bending will increase the energy barrier for electrons to migrate to the surface, the overall photocatalytic reaction rate depends on the slower of the two half reactions. Therefore, the reaction rate will be first limited by the photoanodic reaction at low pH and then the photocathodic reaction at a higher pH. The maximum reactivity should appear at an intermediate pH where neither the photocathodic nor the photoanodic reaction limit the overall reaction rate. Crystals without deliberate Al additions and not treated in the SrCl<sub>2</sub> flux did not generate enough H<sub>2</sub> to exceed the lower calibrated limit of the PAPCR either in pure water or methanol solutions (and are not shown here).

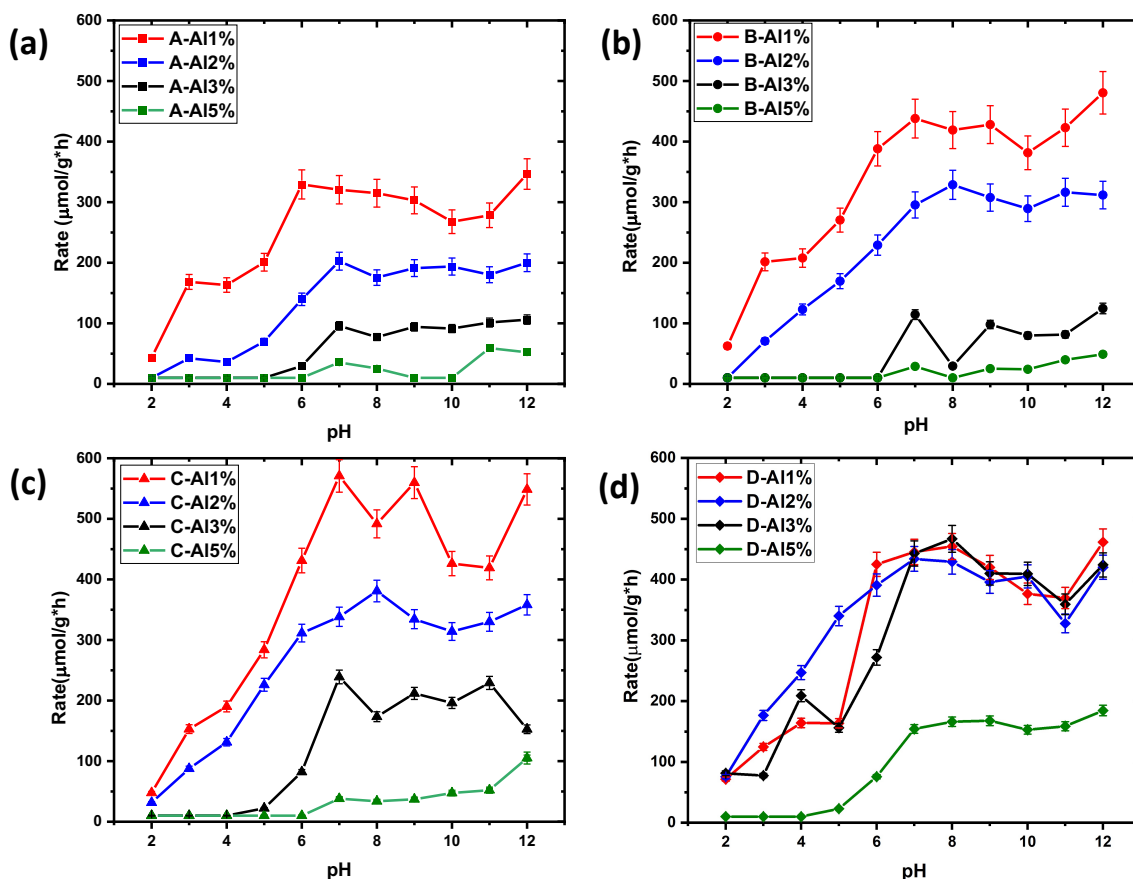


**Figure 6-5:** Mass specific rate of hydrogen generation from suspensions with 16 types of powders in DI water whose pH is in range of pH 2 to pH 12. All powders are of the type designated as Large (450 nm). The bars represent standard deviations.

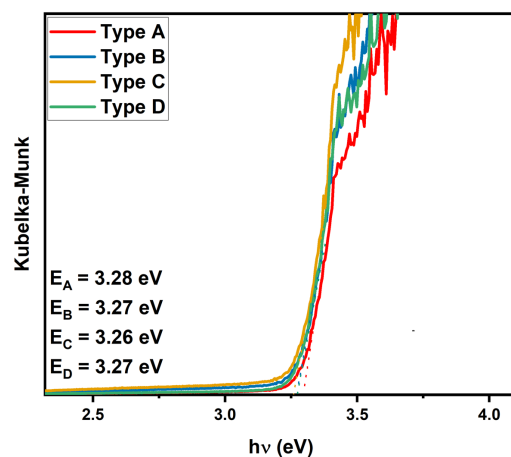


**Figure 6-6:** UV-vis diffuse reflectance spectra of four types of Al-doped SrTiO<sub>3</sub> with 1% Al doped.

To investigate the influence of particle size on the photocatalytic reactivity, 1% and 2% Al-doped SrTiO<sub>3</sub> of shape A and B were prepared with different sizes, by increasing the amount of surfactant in the hydrothermal synthesis. SEM images of the 18 kinds of crystals are shown in Figure 6-7. Large ( $\approx 450$  nm), medium ( $\approx 350$  nm) and small crystals ( $\approx 250$  nm) of shapes A and B are labeled A-L (B-L), A-M (B-M) and A-S (B-S), respectively, given in 6 columns. The L, M, and S particles had size distributions of  $\pm 50$  nm. Each of the three sizes of the two crystal shapes were doped with Al by adding 1 % (Al1) and 2 % Al (Al2) to the SrCl<sub>2</sub> flux treatment, and the SEM images of crystals with increasing Al concentrations are given in descending rows of Fig. 6-7. Note that all crystals in Figure 6-3 are the large size. Consistent with the prior experiments, Al doping rounded the edges of the type B crystals and introduced small {111} facets on the type A crystals. The Al-doped B-S type crystals changed to a near cube shape, as for type A.

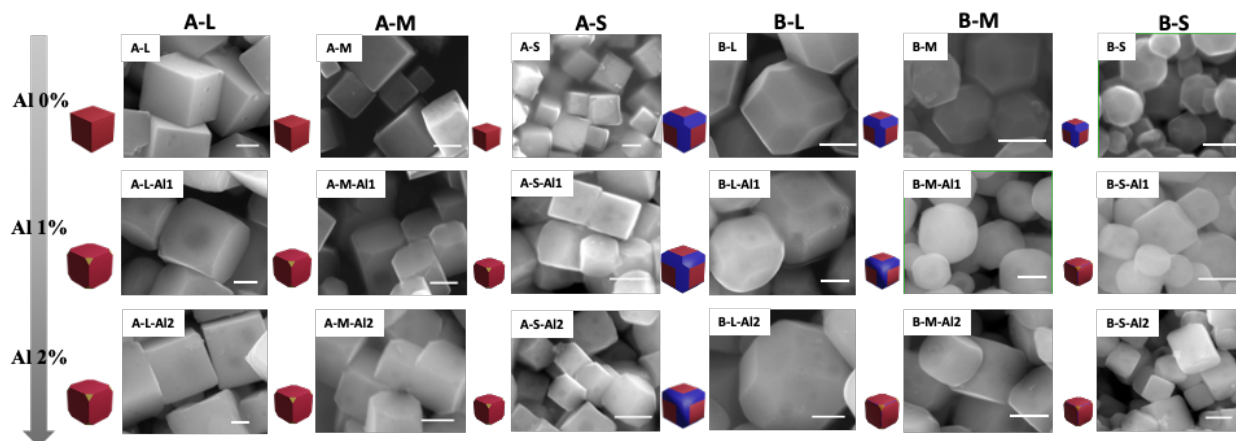


**Figure 6-7:** SEM images as well as schematic diagrams for type A and B SrTiO<sub>3</sub> crystals with large, medium, and small size. Scale bar = 200 nm.

The mass specific hydrogen evolution rates of the six types of Al-doped samples are shown in Figure 6-8. We found that, for both crystal shapes, in the range of 250 nm to 450 nm, the photocatalytic reactivity increased with size and the largest crystals were the most reactive. The trends with solution pH were consistent with the results described in Fig. 6-5. Note that, while the A-L and B-L crystals in this experiment were from a different batch than the crystals in Figure 6-5, their reactivities were similar, illustrating that the results are reproducible. For type B crystals, the crystal shape changed with Al doping, so the results are influenced by both the particle shape and size. The crystals of type A provide the most convincing evidence of the size effect because their shapes are nearly the same in all conditions. Using solutions with 10 % methanol did not change the trend in the relative amounts of hydrogen.

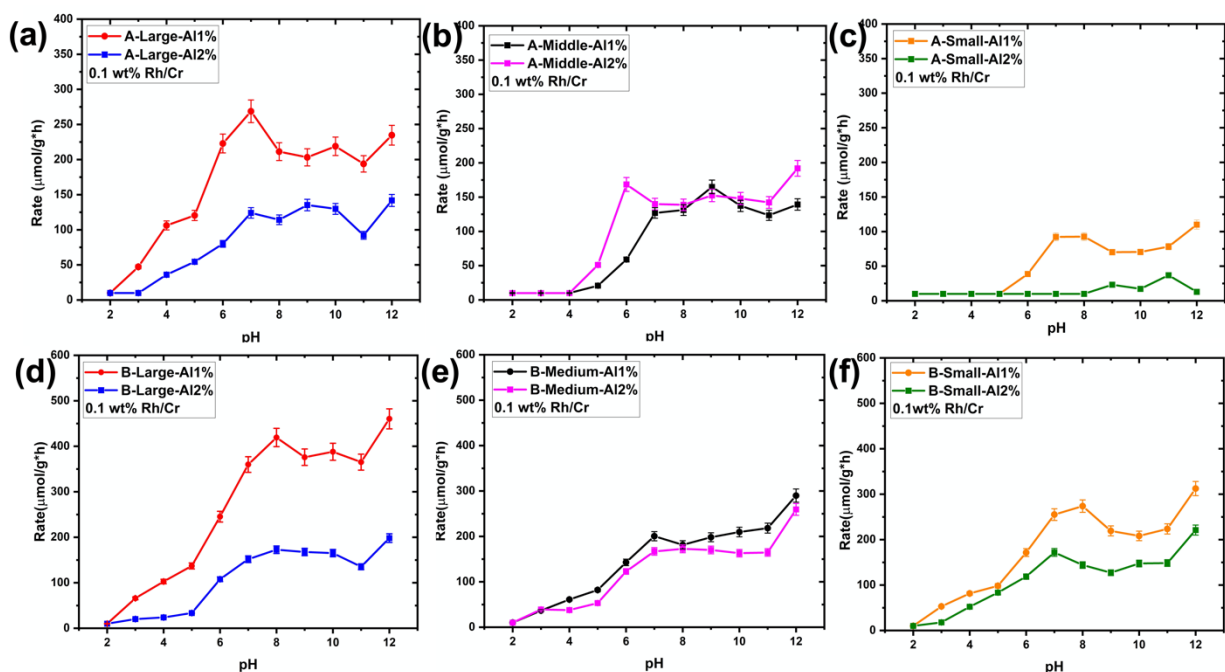


**Figure 6-8:** Mass specific rate of hydrogen production ( $\mu\text{mol g}^{-1}\text{h}^{-1}$ ) from suspensions with crystal type A-L, A-M and A-S under different pH are shown in (a), (b) and (c), respectively. Mass specific rate of hydrogen production ( $\mu\text{mol g}^{-1}\text{h}^{-1}$ ) from suspensions with crystal type B-L, B-M and B-S under different pH are shown in (d), (e) and (f), respectively. The bars represent standard deviation.

Although we have found that the hydrogen evolution rate decreased with decreasing particle size for both type A and type B Al-doped SrTiO<sub>3</sub>, we loaded the same amount of RhCrO<sub>x</sub> cocatalyst

on these crystals. Considering the fact that crystals with the medium size and small size have larger surface areas, as shown in Table 6-2, one might argue that these smaller crystals should have more cocatalyst loaded to maintain a constant amount of cocatalyst per area. Therefore, using shape type B crystals, we changed the cocatalyst loading on the three sizes to maintain a constant coverage per surface area. Based on BET data, the surface areas for B-L, B-M, B-S nanocrystals were 3.2 m<sup>2</sup>/g, 6.7 m<sup>2</sup>/g, 10 m<sup>2</sup>/g, which was roughly in the proportion of 1 : 2 : 3. Therefore, we loaded 0.1 wt%, 0.2 wt% and 0.3 wt% RhCrO<sub>x</sub> (metal ratio) on B-L, B-M and B-S nanocrystals, respectively, and measured their H<sub>2</sub> generation rates. As shown in Figure 6-9, B-L type crystals still had the highest H<sub>2</sub> generation rate. It is found that increasing the amount of cocatalyst did not increase, but rather decreased, the photocatalytic reactivity for B-M and B-S crystals. As a result, we believe that the relatively lower reactivity of the smaller crystals was not because they had a smaller cocatalyst coverage. On the contrary, loading more cocatalyst further decreased the reactivity. It would be interesting to test even larger crystals, because we expect that at some point the reactivity should decrease with the increased size, but we have not been able to synthesize larger crystals with controlled shapes.

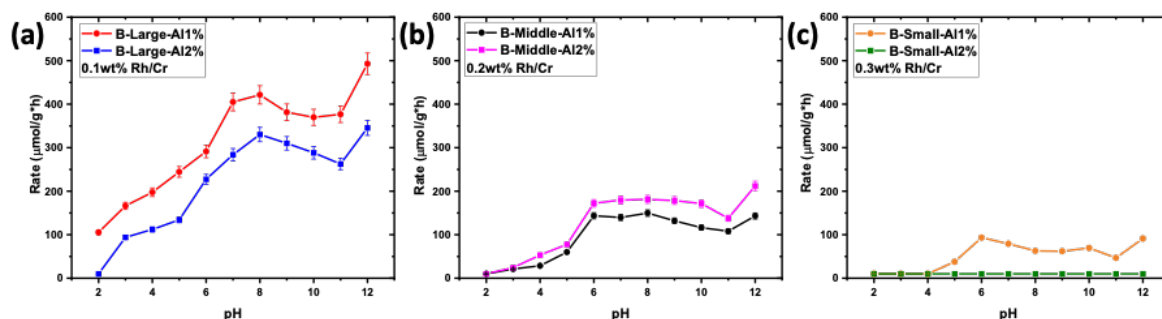


**Figure 6-9:** Absolute rate ( $\mu\text{mol m}^{-2}\text{h}^{-1}$ ) of (a) type B-L crystals loaded with 0.1 wt% Rh and Cr cocatalysts, (b) type B-M crystals loaded with 0.2 wt% Rh and Cr cocatalysts and (c) type B-S crystals loaded with 0.3 wt% Rh and Cr cocatalysts as a function of pH.

**Table 6-2:** BET data of undoped SrTiO<sub>3</sub> crystals.

Type	Crystal size (nm)	Surface area (m <sup>2</sup> /g)
A-L	450	4.33
B-L	450	3.17
C-L	450	4.02
D-L	450	3.35
A-M	350	5.00
A-S	250	11.5
B-M	350	6.67
B-S	250	10.1

## 6.4 Discussion

**Effect of particle shape.** The results described here show that the rate of hydrogen production from Al-doped SrTiO<sub>3</sub> is influenced by crystal shape. The results show that type C crystals had the highest mass specific rate ( $\mu\text{mol h}^{-1} \text{g}^{-1}$ ) with the {110} to {100} surface area ratio equal to 1.8. Increases or decreases in this ratio lower the reactivity. This can be understood by the schematic diagrams in Fig. 6-10 and the fact that the {110} surface is photoanodic in comparison to {100}, which is relatively photocathodic.<sup>20,21</sup> The finding that electrons (holes) migrate to {100} ({110}) surfaces of these particles is validated by the data in Fig. 6-10 which shows that Ag<sup>+</sup> (Mn<sup>2+</sup>) is reduced (oxidized) on the {100} ({110}) surfaces. For the shape with the ideal reactivity, an optimal ratio of electrons and holes migrate to the {100} and {110} surfaces, respectively, where they can contribute to the reaction. However, if there are no {110} facets (see Fig. 6-11 a), then holes must also migrate to the {100} surfaces, where they are likely to recombine with electrons, lowering reactivity; this is the case for the A-type crystals. The opposite case, where there is insufficient photocathodic {100} area to support the reduction reaction, is shown in Fig. 6-11 (c) and represents the D-type crystals. In this case, the reduction in the rate of the cathodic reaction and the likely increased rate of recombination will limit the rate of the overall reaction. It is noted that, after normalizing by surface area, type C crystals still have the best surface area specific rates ( $\mu\text{mol h}^{-1} \text{m}^{-2}$ ) at pH 7, but type B crystals show a higher reactivity at pH 12. This

implies that if we could synthesize particles with a  $\{110\}$  to  $\{100\}$  surface area ratio between 1.3 and 1.8, the photocatalytic reactivity might be further optimized.

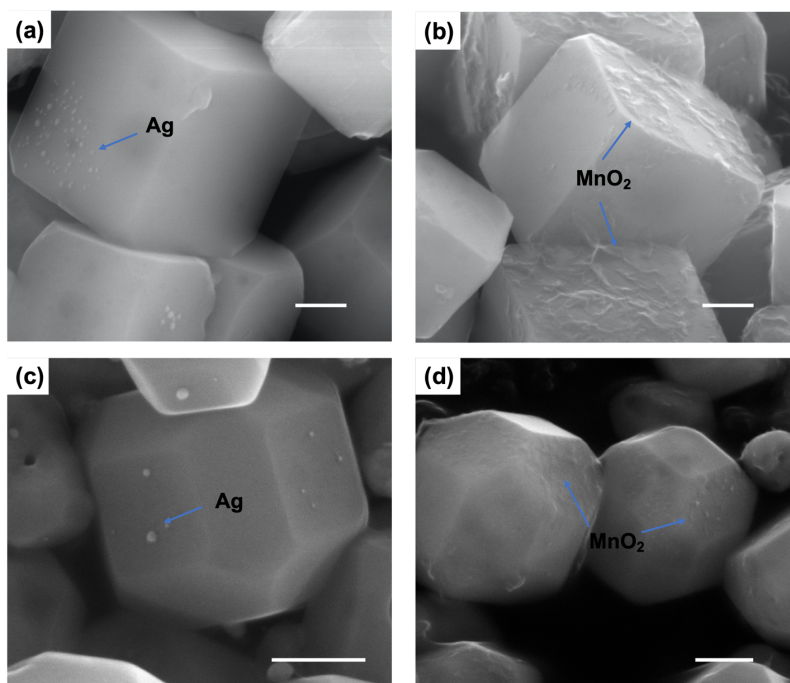


**Figure 6-10:** SEM images of the type A-L-Al ((a) and (b)) and B-L ((c) and (d)) SrTiO<sub>3</sub> nanocrystals with photo-deposition of Ag and MnO<sub>2</sub>. Scale bar represents 200 nm. The purpose of using A-L-Al instead of A-L is to show that, for type A crystals,  $\{100\}$  facets serve as both reduction sites and oxidation sites while  $\{111\}$  facets do not participate into reactions.

**Effect of particle size.** The measurements of the rate of hydrogen evolution from crystals of different sizes indicated that the reactivity increases with crystal size, from 250 nm to 450 nm. This is counter intuitive, considering that the mass specific surface area decreases as the particle size increases. Changes in the reactivity with size are sometimes ascribed to the quantum size effect.<sup>40,41</sup> However, quantum size effects are expected only in crystals much smaller than those considered here. We note that Hsieh et al.<sup>22</sup> reported that the band gap of 290 nm SrTiO<sub>3</sub> was 31 meV smaller than 160 nm SrTiO<sub>3</sub>, but this difference would not increase the absorption enough to account for the increased reactivity.

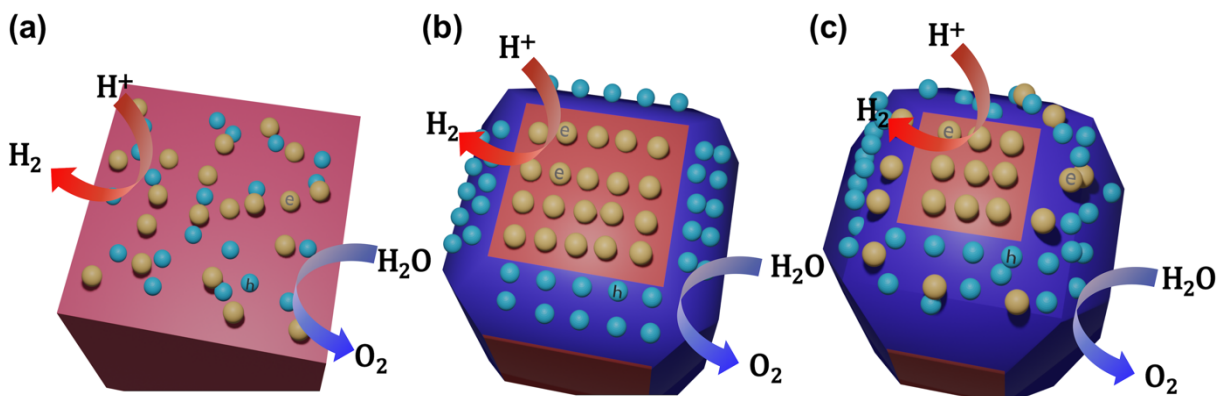


**Figure 6-11:** Schematic illustration of the spatial distribution of photogenerated electrons and holes on (a) {100} facets dominated, (b) optimal ratio of {100} to {110} facets, (c) {110} facet dominated conditions. Red surface and blue surface represent {100} and {110} facets. Yellow balls and blue balls represent to electrons and holes.

There are two plausible explanations for the increase in reactivity of the larger crystals. One possible explanation for the observed size effect is that the reaction is limited by the back reaction of neutral H and hydroxyl radicals on or near the surface. As the particle size decreases, these species are produced in closer proximity, so they do not have to diffuse as far to recombine, and this might limit the reaction rate. However, according to Turchi and Ollis,<sup>42</sup> the diffusion of hydroxyl radicals is fast compared to the rate of reaction with the semiconductor surface and the with other species in solution, so the effect of increasing the particle size on the rate of the back reaction is not expected to be significant.

Another explanation is that the space charge layer beneath the surface is large compared to the particle size. One of the parameters influencing the depth of the space charge in SrTiO<sub>3</sub> is the carrier concentration. Past studies agree that SrTiO<sub>3</sub> with no intentionally added impurities is an acceptor doped n-type semiconductor.<sup>43,44</sup> The n-type electronic properties result from electrons ionized from oxygen vacancies ( $V_O^{\bullet\bullet}$ ) and measurements indicate that the concentration of oxygen vacancies is much greater than the concentration of acceptor impurities. Therefore, the electroneutrality condition is  $2[V_O^{\bullet\bullet}] \approx n$  where n is the concentration of ionized electrons and  $n \approx 10^{19} \text{ cm}^{-3}$ .<sup>44</sup> However, the added Al acts as an acceptor dopant ( $Al_{Ti}'$ ) that can compensate the oxygen vacancies and reduce the electron concentration. Calculations based on data in the literature<sup>45</sup> show that when SrTiO<sub>3</sub> is fully compensated by a small amount of dissolved Al, the carrier concentration is reduced to as low as  $n \approx 10^{16} \text{ cm}^{-3}$  at the temperature of the SrCl<sub>2</sub> flux. At

room temperature, where the catalyst is used, the carrier concentration of ideally compensated SrTiO<sub>3</sub> falls to  $n \approx 10^{12} \text{ cm}^{-3}$ .<sup>46</sup> This reduction in the carrier concentration would expand the width of the space charge layer (the Debye length) from  $\approx 3 \text{ nm}$  (in the undoped condition where  $n = 10^{19} \text{ cm}^{-1}$ ) to  $\approx 9 \times 10^3 \text{ nm}$  (at the point of compensation where  $n = 10^{12} \text{ cm}^{-1}$ ). Not knowing the Al concentration in the samples, we cannot estimate the degree of compensation. However, it is clear that added Al will decrease the carrier concentration and increase the Debye length. Note that a similar mechanism has been proposed to explain the reactivity enhancement that results from Mg doping of SrTiO<sub>3</sub>.<sup>47</sup> At the wavelength of light used here, the absorption coefficient is on the order of  $100 \text{ cm}^{-1}$ ,<sup>48</sup> which implies an absorption depth of  $10^4 \text{ nm}$ . Because of the large absorption depth, increases in the space charge region result in an increase in the number of photogenerated carriers that can be separated by the field.

As discussed above, the Debye length might be on the order of  $10^3 \text{ nm}$ . In this case, for particles smaller than this length, the space charges overlap in the center of the crystal. This reduces the difference between the surface and bulk electric potentials and leads to reduced charge separation.<sup>25</sup> In the larger crystals, the space charge is more fully developed and there is a larger potential to separate charge. This idea is supported by simulations of the reactivity of BaTiO<sub>3</sub> showing that the difference in electric potential (under illumination) at the surface between positive and negative domains is only 0.17 V for a small 10 nm domain, while this difference of potential is 0.60 V for a large 250 nm domain.<sup>49</sup> The increased space charge depth, together with relatively large absorption depth discussed above, should result in increased reactivity. In other words, the larger space charge regions in the larger crystals are more likely to be the cause of their increased reactivity than the suppression of the back reaction by the physical separation of the cathodic and anodic sites.

## 6.5 Conclusion

The influence of particle shape and size on the photocatalytic generation of hydrogen by Al-doped SrTiO<sub>3</sub> has been measured. The most suitable shape was determined to be an edge-truncated cube with a  $\{110\}$  to  $\{100\}$  surface area ratio between 1.3 and 1.8. With this geometry, electrons (holes) move to  $\{100\}$  ( $\{110\}$ ) facets and promote the photoreduction (photooxidation) half reaction, a situation that likely reduces the rate of recombination or back reaction. Crystals with diameters

around 450 nm are more reactive than smaller ones, consistent with the presence of wide space charge regions that result from the Al acceptors that reduce the n-type carrier concentration.

## 6.6 References

- (1) Fujishima, A.; Honda, K. Electrochemical Photolysis of Water at a Semiconductor Electrode. *Nature* **1972**, *238* (5358), 37+. <https://doi.org/10.1038/238037a0>.
- (2) Osterloh, F. E. Inorganic Materials as Catalysts for Photochemical Splitting of Water. *Chem. Mater.* **2008**, *20* (1), 35–54. <https://doi.org/10.1021/cm7024203>.
- (3) Hisatomi, T.; Domen, K. Reaction Systems for Solar Hydrogen Production via Water Splitting with Particulate Semiconductor Photocatalysts. *Nat. Catal.* **2019**, *2* (5), 387–399. <https://doi.org/10.1038/s41929-019-0242-6>.
- (4) Wang, Q.; Domen, K. Particulate Photocatalysts for Light-Driven Water Splitting: Mechanisms, Challenges, and Design Strategies. *Chem. Rev.* **2020**, *120* (2), 919–985. <https://doi.org/10.1021/acs.chemrev.9b00201>.
- (5) Takata, T.; Domen, K. Defect Engineering of Photocatalysts by Doping of Aliovalent Metal Cations for Efficient Water Splitting. *J. Phys. Chem. C* **2009**, *113* (45), 19386–19388. <https://doi.org/10.1021/jp908621e>.
- (6) Jiang, J.; Kato, K.; Fujimori, H.; Yamakata, A.; Sakata, Y. Investigation on the Highly Active SrTiO<sub>3</sub> Photocatalyst toward Overall H<sub>2</sub>O Splitting by Doping Na Ion. *J. Catal.* **2020**, *390*, 81–89. <https://doi.org/10.1016/j.jcat.2020.07.025>.
- (7) Ham, Y.; Hisatomi, T.; Goto, Y.; Moriya, Y.; Sakata, Y.; Yamakata, A.; Kubota, J.; Domen, K. Flux-Mediated Doping of SrTiO<sub>3</sub> Photocatalysts for Efficient Overall Water Splitting. *J. Mater. Chem. A* **2016**, *4* (8), 3027–3033. <https://doi.org/10.1039/C5TA04843E>.
- (8) Goto, Y.; Hisatomi, T.; Wang, Q.; Higashi, T.; Ishikiriyama, K.; Maeda, T.; Sakata, Y.; Okunaka, S.; Tokudome, H.; Katayama, M.; et al. A Particulate Photocatalyst Water-Splitting Panel for Large-Scale Solar Hydrogen Generation. *Joule* **2018**, *2* (3), 509–520. <https://doi.org/10.1016/j.joule.2017.12.009>.

- (9) Takata, T.; Jiang, J.; Sakata, Y.; Nakabayashi, M.; Shibata, N.; Nandal, V.; Seki, K.; Hisatomi, T.; Domen, K. Photocatalytic Water Splitting with a Quantum Efficiency of almost Unity. *Nature* **2020**, *581* (7809), 411–414. <https://doi.org/10.1038/s41586-020-2278-9>.
- (10) Li, L.; Salvador, P. A.; Rohrer, G. S. Photocatalysts with Internal Electric Fields. *Nanoscale* **2014**, *6* (1), 24–42. <https://doi.org/10.1039/c3nr03998f>.
- (11) Chen, F.; Huang, H.; Guo, L.; Zhang, Y.; Ma, T. The Role of Polarization in Photocatalysis. *Angew. Chemie Int. Ed.* **2019**, *58* (30), 10061–10073. <https://doi.org/10.1002/anie.201901361>.
- (12) Marschall, R. Semiconductor Composites: Strategies for Enhancing Charge Carrier Separation to Improve Photocatalytic Activity. *Adv. Funct. Mater.* **2014**, *24* (17), 2421–2440. <https://doi.org/10.1002/adfm.201303214>.
- (13) Lopato, E. M.; Eikey, E. A.; Simon, Z. C.; Back, S.; Tran, K.; Lewis, J.; Kowalewski, J. F.; Yazdi, S.; Kitchin, J. R.; Ulissi, Z. W.; et al. Parallelized Screening of Characterized and DFT-Modeled Bimetallic Colloidal Cocatalysts for Photocatalytic Hydrogen Evolution. *ACS Catal.* **2020**, *10* (7), 4244–4252. <https://doi.org/10.1021/acscatal.9b05404>.
- (14) Liu, G.; Yu, J. C.; Lu, G. Q.; Cheng, H.-M. Crystal Facet Engineering of Semiconductor Photocatalysts: Motivations, Advances and Unique Properties. *Chem. Commun.* **2011**, *47* (24), 6763–6783. <https://doi.org/10.1039/C1CC10665A>.
- (15) Huang, M. H. Facet-Dependent Optical Properties of Semiconductor Nanocrystals. *Small* **2019**, *15* (7), 1804726. <https://doi.org/10.1002/smll.201804726>.
- (16) Bai, S.; Wang, L.; Li, Z.; Xiong, Y. Facet-Engineered Surface and Interface Design of Photocatalytic Materials. *Adv. Sci.* **2017**, *4* (1), 1600216. <https://doi.org/10.1002/advs.201600216>.
- (17) Li, R.; Zhang, F.; Wang, D.; Yang, J.; Li, M.; Zhu, J.; Zhou, X.; Han, H.; Li, C. Spatial Separation of Photogenerated Electrons and Holes among {010} and {110} Crystal Facets of BiVO<sub>4</sub>. *Nat. Commun.* **2013**, *4* (1), 1432. <https://doi.org/10.1038/ncomms2401>.

- (18) Li, R.; Han, H.; Zhang, F.; Wang, D.; Li, C. Highly Efficient Photocatalysts Constructed by Rational Assembly of Dual-Cocatalysts Separately on Different Facets of BiVO<sub>4</sub>. *Energy Environ. Sci.* **2014**, *7* (4), 1369–1376. <https://doi.org/10.1039/C3EE43304H>.
- (19) Giocondi, J. L.; Salvador, P. A.; Rohrer, G. S. The Origin of Photochemical Anisotropy in SrTiO<sub>3</sub>. *Top. Catal.* **2007**, *44* (4), 529–533. <https://doi.org/10.1007/s11244-006-0101-y>.
- (20) Pisat, A. S.; Salvador, P. A.; Rohrer, G. S. The Facet Structure and Photochemical Reactivity of Arbitrarily Oriented Strontium Titanate Surfaces. *Adv. Mater. Interfaces* **2019**, *6* (16), 1900731. <https://doi.org/10.1002/admi.201900731>.
- (21) Mu, L.; Zhao, Y.; Li, A.; Wang, S.; Wang, Z.; Yang, J.; Wang, Y.; Liu, T.; Chen, R.; Zhu, J.; et al. Enhancing Charge Separation on High Symmetry SrTiO<sub>3</sub> Exposed with Anisotropic Facets for Photocatalytic Water Splitting. *Energy Environ. Sci.* **2016**, *9* (7), 2463–2469. <https://doi.org/10.1039/C6EE00526H>.
- (22) Hsieh, P.-L.; Naresh, G.; Huang, Y.-S.; Tsao, C.-W.; Hsu, Y.-J.; Chen, L.-J.; Huang, M. H. Shape-tunable SrTiO<sub>3</sub> Crystals Revealing Facet-Dependent Optical and Photocatalytic Properties. *J. Phys. Chem. C* **2019**, *123* (22), 13664–13671. <https://doi.org/10.1021/acs.jpcc.9b02081>.
- (23) Vijay, A.; Vaidya, S. Tuning the Morphology and Exposed Facets of SrTiO<sub>3</sub> Nanostructures for Photocatalytic Dye Degradation and Hydrogen Evolution. *ACS Appl. Nano Mater.* **2021**. <https://doi.org/10.1021/acsanm.0c03160>.
- (24) Yu, J.; Low, J.; Xiao, W.; Zhou, P.; Jaroniec, M. Enhanced Photocatalytic CO<sub>2</sub>-Reduction Activity of Anatase TiO<sub>2</sub> by Coexposed {001} and {101} Facets. *J. Am. Chem. Soc.* **2014**, *136* (25), 8839–8842. <https://doi.org/10.1021/ja5044787>.
- (25) Albery, W. J.; Bartlett, P. N. The Transport and Kinetics of Photogenerated Carriers in Colloidal Semiconductor Electrode Particles. *J. Electrochem. Soc.* **1984**, *131* (2), 315–325. <https://doi.org/10.1149/1.2115568>.
- (26) Banin, U.; Cao, Y.; Katz, D.; Millo, O. Identification of Atomic-like Electronic States in Indium Arsenide Nanocrystal Quantum Dots. *Nature* **1999**, *400* (6744), 542–544.

<https://doi.org/10.1038/22979>.

- (27) Peng, X.; Manna, L.; Yang, W.; Wickham, J.; Scher, E.; Kadavanich, A.; Alivisatos, A. P. Shape Control of CdSe Nanocrystals. *Nature* **2000**, *404* (6773), 59–61. <https://doi.org/10.1038/35003535>.
- (28) Zhang, Z.; Wang, C.-C.; Zakaria, R.; Ying, J. Y. Role of Particle Size in Nanocrystalline TiO<sub>2</sub>-based Photocatalysts. *J. Phys. Chem. B* **1998**, *102* (52), 10871–10878. <https://doi.org/10.1021/jp982948+>.
- (29) Arney, D.; Watkins, T.; Maggard, P. A. Effects of Particle Surface Areas and Microstructures on Photocatalytic H<sub>2</sub> and O<sub>2</sub> Production over PbTiO<sub>3</sub>. *J. Am. Ceram. Soc.* **2011**, *94* (5), 1483–1489. <https://doi.org/10.1111/j.1551-2916.2010.04262.x>.
- (30) Amano, F.; Ishinaga, E.; Yamakata, A. Effect of Particle Size on the Photocatalytic Activity of WO<sub>3</sub> Particles for Water Oxidation. *J. Phys. Chem. C* **2013**, *117* (44), 22584–22590. <https://doi.org/10.1021/jp408446u>.
- (31) Morrison, S. R. Electrochemistry at semiconductor and oxidized metal electrodes. **1980**.
- (32) Zhang, M.; Salvador, P. A.; Rohrer, G. S. Influence of pH and Surface Orientation on the Photochemical Reactivity of SrTiO<sub>3</sub>. *ACS Appl. Mater. Interfaces* **2020**. <https://doi.org/10.1021/acsami.0c04351>.
- (33) Zhao, Z.; Willard, E. J.; Li, H.; Wu, Z.; Castro, R. H. R.; Osterloh, F. E. Aluminum enhances Photochemical Charge Separation in Strontium Titanate Nanocrystal Photocatalysts for Overall Water Splitting. *J. Mater. Chem. A* **2018**, *6* (33), 16170–16176. <https://doi.org/10.1039/C8TA05885G>.
- (34) Yamakata, A.; Yeilin, H.; Kawaguchi, M.; Hisatomi, T.; Kubota, J.; Sakata, Y.; Domen, K. Morphology-sensitive Trapping States of Photogenerated Charge Carriers on SrTiO<sub>3</sub> Particles Studied by Time-Resolved Visible to Mid-IR Absorption Spectroscopy: The Effects of Molten Salt Flux Treatments. *J. Photochem. Photobiol. A Chem.* **2015**, *313*, 168–175. <https://doi.org/10.1016/j.jphotochem.2015.05.016>.
- (35) Zhao, Z.; Goncalves, R. V.; Barman, S. K.; Willard, E. J.; Byle, E.; Perry, R.; Wu, Z.; Huda,

- M. N.; Moulé, A. J.; Osterloh, F. E. Electronic Structure Basis for Enhanced Overall Water Splitting Photocatalysis with Aluminum Doped SrTiO<sub>3</sub> in Natural Sunlight. *Energy Environ. Sci.* **2019**, *12* (4), 1385–1395. <https://doi.org/10.1039/C9EE00310J>.
- (36) Dong, L.; Shi, H.; Cheng, K.; Wang, Q.; Weng, W.; Han, W. Shape-controlled Growth of SrTiO<sub>3</sub> Polyhedral Submicro/Nanocrystals. *Nano Res.* **2014**, *7* (9), 1311–1318. <https://doi.org/10.1007/s12274-014-0495-y>.
- (37) Maeda, K.; Teramura, K.; Masuda, H.; Takata, T.; Saito, N.; Inoue, Y.; Domen, K. Efficient Overall Water Splitting under Visible-Light Irradiation on (Ga<sub>1-x</sub>Zn<sub>x</sub>)(N<sub>1-x</sub>O<sub>x</sub>) dispersed with Rh–Cr Mixed-Oxide Nanoparticles: Effect of Reaction Conditions on Photocatalytic Activity. *J. Phys. Chem. B* **2006**, *110* (26), 13107–13112. <https://doi.org/10.1021/jp0616563>.
- (38) He, Z.; Xie, L.; Tu, J.; Song, S.; Liu, W.; Liu, Z.; Fan, J.; Liu, Q.; Chen, J. Visible Light-Induced Degradation of Phenol over Iodine-Doped Titanium Dioxide Modified with Platinum: Role of Platinum and the Reaction Mechanism. *J. Phys. Chem. C* **2010**, *114* (1), 526–532. <https://doi.org/10.1021/jp908946c>.
- (39) Li, L.; Liu, X.; Zhang, Y.; Salvador, P. A.; Rohrer, G. S. Heterostructured (Ba,Sr)TiO<sub>3</sub>/TiO<sub>2</sub> Core/Shell Photocatalysts: Influence of Processing and Structure on Hydrogen Production. *Int. J. Hydrogen Energy* **2013**, *38* (17), 6948–6959. <https://doi.org/10.1016/j.ijhydene.2013.03.130>.
- (40) Norris, D. J.; Bawendi, M. G. Measurement and Assignment of the Size-Dependent Optical Spectrum in CdSe Quantum Dots. *Phys. Rev. B* **1996**, *53* (24), 16338–16346. <https://doi.org/10.1103/PhysRevB.53.16338>.
- (41) Mora-Seró, I.; Giménez, S.; Moehl, T.; Fabregat-Santiago, F.; Lana-Villareal, T.; Gómez, R.; Bisquert, J. Factors Determining the Photovoltaic Performance of a CdSe Quantum Dot Sensitized Solar Cell: The Role of the Linker Molecule and of the Counter Electrode. *Nanotechnology* **2008**, *19* (42), 424007. <https://doi.org/10.1088/0957-4484/19/42/424007>.
- (42) Turchi, C. S.; Ollis, D. F. Photocatalytic Degradation of Organic Water Contaminants: Mechanisms Involving Hydroxyl Radical Attack. *J. Catal.* **1990**, *122* (1), 178–192.

[https://doi.org/10.1016/0021-9517\(90\)90269-P](https://doi.org/10.1016/0021-9517(90)90269-P).

- (43) Shi, T.; Chen, Y.; Guo, X. Defect Chemistry of Alkaline Earth Metal (Sr/Ba) Titanates. *Prog. Mater. Sci.* **2016**, *80*, 77–132. <https://doi.org/10.1016/j.pmatsci.2015.10.002>.
- (44) Chan, N.-H.; Sharma, R. K.; Smyth, D. M. Nonstoichiometry in SrTiO<sub>3</sub>. *J. Electrochem. Soc.* **1981**, *128* (8), 1762–1769. <https://doi.org/10.1149/1.2127727>.
- (45) Shin, C.-J.; Yoo, H.-I.; Lee, C.-E. Al-Doped SrTiO<sub>3</sub>: Part I, Anomalous oxygen nonstoichiometry. *Solid State Ionics* **2007**, *178* (15), 1081–1087. <https://doi.org/10.1016/j.ssi.2007.05.007>.
- (46) Waser, R. Bulk Conductivity and Defect Chemistry of Acceptor-Doped Strontium Titanate in the Quenched State. *J. Am. Ceram. Soc.* **1991**, *74* (8), 1934–1940. <https://doi.org/10.1111/j.1151-2916.1991.tb07812.x>.
- (47) Han, K.; Lin, Y.-C.; Yang, C.-M.; Jong, R.; Mul, G.; Mei, B. Promoting Photocatalytic Overall Water Splitting by Controlled Magnesium Incorporation in SrTiO<sub>3</sub> photocatalysts. *ChemSusChem* **2017**, *10* (22), 4510–4516. <https://doi.org/10.1002/cssc.201701794>.
- (48) Noland, J. A. Optical Absorption of Single-Crystal Strontium Titanate. *Phys. Rev.* **1954**, *94* (3), 724. <https://doi.org/10.1103/PhysRev.94.724>.
- (49) Glickstein, J. J.; Salvador, P. A.; Rohrer, G. S. Multidomain Simulations of Coated Ferroelectrics Exhibiting Spatially Selective Photocatalytic Activity with High Internal Quantum Efficiencies. *J. Mater. Chem. A* **2016**, *4* (41), 16085–16093. <https://doi.org/10.1039/C6TA07083C>.

## Chapter 7: Influence of the Molten SrCl<sub>2</sub> Flux Treatment on the Surface Structure and Photochemical Reactivities of SrTiO<sub>3</sub>

*From the experiments in the previous chapter, the molten SrCl<sub>2</sub> flux treatment is of use to prepare highly efficient Al-doped SrTiO<sub>3</sub> photocatalysts. In fact, nearly all the high-performance Al-doped SrTiO<sub>3</sub> catalysts were prepared with this method, but its mechanism is still not clear. It was thought that SrTiO<sub>3</sub> dissolves and recrystallizes in the melt so that the crystallinity improves. But this is inconsistent with the observation that our faceted particles generally maintain the shape after the flux treatment. In this chapter, we explore the effect of this “magic” flux treatment by heating large single crystal substrates in the melt, so that we can use AFM to determine how the flux treatment affects the surface structure.*

### 7.1 Introduction

SrCl<sub>2</sub> flux treated Al-doped SrTiO<sub>3</sub> is one of the most efficient photocatalysts for water splitting that have been developed so far. In 2013, Kato et al. heated SrTiO<sub>3</sub> powders prepared with a polymerized complex method in different molten salts, such as NaCl, KCl, LiCl and SrCl<sub>2</sub>.<sup>1</sup> All salts will change the particle morphology but KCl will give a higher reactivity. Later, Domen and coworkers found that the photocatalytic reactivity of SrTiO<sub>3</sub> could be significantly improved by the SrCl<sub>2</sub> flux treatment, and this is attributed mainly to the doping of Al from the Al<sub>2</sub>O<sub>3</sub> crucibles.<sup>2,3</sup> Since that, they reported a couple of works improving the performance of this material, such as loading anodic cocatalysts<sup>4,5</sup> and photodepositing cocatalysts on different facets.<sup>6</sup> It is understood that Al<sup>3+</sup> can reduce the Ti<sup>3+</sup> deep recombination sites and increase charge carrier lifetime, and this has been confirmed by Zhao et al. using XPS and DFT methods.<sup>7</sup> Recently, there is research showing that co-doped SrTiO<sub>3</sub> by incorporating Al<sup>3+</sup> along with Zr(IV)<sup>8</sup> or La(III)<sup>9</sup> can further improve the reactivity.

While Al doping has been confirmed to be beneficial to the photocatalytic reactivity of SrTiO<sub>3</sub>, the role of the flux treatment is still not clear. This flux treatment is a very simple method, by heating SrTiO<sub>3</sub> in an excess amount of SrCl<sub>2</sub> at a temperature between the melting point and boiling

point of SrCl<sub>2</sub> in an alumina crucible, we will get a highly reactive SrTiO<sub>3</sub> photocatalyst. It is noted that all the studies described previously have employed the SrCl<sub>2</sub> flux treatment for ion doping. Previous studies show that Al-doped SrTiO<sub>3</sub> synthesized via solid state method<sup>3</sup> or hydrothermal method<sup>10</sup> are less reactive than those prepared by the flux method, implying the criticality of the SrCl<sub>2</sub> flux treatment. Ham et al. proposed that part of the SrTiO<sub>3</sub> particles dissolve and recrystallize in the presence of SrCl<sub>2</sub> flux so that the crystallinity is improved.<sup>3</sup> Motivated by these results, we desire to understand how the SrCl<sub>2</sub> flux treatment influences the chemical composition and structure of the SrTiO<sub>3</sub> surface.

Since it is difficult to characterize particle surface directly, in this study, we reproduced the molten SrCl<sub>2</sub> flux treatment on the surface of SrTiO<sub>3</sub> single crystal substrates and investigated how it influences the photochemical reactivities. Air annealed substrates and KCl flux treated substrates were prepared and used for comparison. The surface potential was measured by Kelvin probe force microscopy (KFM) and correlated to the relative reactivities measured by photochemical marker reactions and atomic force microscopy (AFM). Along with X-ray photoelectron spectra (XPS), we found that the concentration of surface OH groups, the surface potential and the photochemical properties were all correlated. The SrCl<sub>2</sub> flux treatment significantly enriches the concentration of surface -OH groups and decreases the surface potential. Meanwhile, the surface potential difference between (100) and (110) surfaces increases from 0.07 V to 0.21 V after the flux treatment, leading to an enhanced charge separation between the two surfaces and improved photocatalytic reactivity.

## 7.2 Experimental Methods

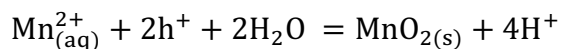
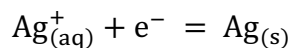
**Sample preparation.** Chemical-mechanical polished (100) and (110) oriented SrTiO<sub>3</sub> single crystals were purchased from MSE Supplies with a size of 5 × 5 × 0.5 mm. The crystals were ultrasonically washed in methanol for 10 min and then annealed at 1100 °C in air for 6 h in a covered alumina crucible. Some crystals were treated in either a SrCl<sub>2</sub> flux or a KCl flux to study the role of the flux treatment. In a typical flux treatment, the air annealed crystal was placed in a 20 ml covered alumina crucible (Sigma-Aldrich) with the polished side facing up, and then 10 times SrCl<sub>2</sub> (Alfa Aesar, 99.5%) or 20 times KCl (Alfa Aesar, 99%) powders in molar ratio was placed on the top of the crystal. The crucible was then transferred to a furnace and annealed at

1150 °C in air for 10 h. After annealing, the crystal was ultrasonically washed in DI water for 1 h and then washed in methanol and acetone each for 10 min.

Al-doped SrTiO<sub>3</sub> particulate catalysts were prepared in a hydrothermal approach reported by Dong et al.<sup>11</sup> In the synthesis, 0.2 mL of TiCl<sub>4</sub> (Sigma-Aldrich, 99 %) was dropped into a solution in an ice bath containing 25 mL of deionized water and the 1 g of ethylene glycol surfactant (Alfa Aesar, 99+%) with 1 mol % (Hydro1%) or 2 mol % (Hydro2%) of AlCl<sub>3</sub>·6H<sub>2</sub>O (Fisher Scientific) mixed with the precursors. After magnetic stirring for 5 min, 10 mL of SrCl<sub>2</sub> solution containing 0.42 g SrCl<sub>2</sub> (Sigma-Aldrich, 99.99%) and 30 ml of LiOH solution containing 2.26 g LiOH (Sigma-Aldrich, 98%) was added. After stirring for another 30 min, the resulting solution was transferred to a 100 ml Teflon-lined hydrothermal autoclave (Techinstro). The autoclave was then heated at 180 °C for 36 h in a furnace. After the heat treatment, the solution was removed and the resulting precipitate was centrifugated four times at 4000 rpm for 12 min with deionized water and ethanol, respectively. Finally, the resulting precipitate was dried in an oven at 80 °C overnight. As for the SrCl<sub>2</sub> flux treatment, 0.3 g powders as prepared was mixed with SrCl<sub>2</sub> (Alfa Aesar, 99.5%) in a ratio of 1:10 and annealed at 1150 °C in air for 10 h in an alumina crucible. The resulting mixture was centrifugated at 4000 rpm for 18 min, four times with deionized water and then four times with ethanol, and finally dried in an oven overnight.

***Photochemical marker reaction.*** This method employs the photoreduction of Ag<sup>+</sup> or the photo-oxidation of Mn<sup>2+</sup> that leaves insoluble photochemical products on the surface at the sites of the reactions.<sup>12,13</sup> An O-ring was placed on the top of the single crystal sample and its interior volume was filled with 0.115 M AgNO<sub>3</sub> solution or 0.115 M MnSO<sub>4</sub> solution with unadjusted pH. A quartz coverslip was then placed on the top of the O-ring to seal the solution without bubbles. The entire setup was then illuminated under a 150 W Xe lamp (Newport, Irvine, CA). For Ag<sup>+</sup> reduction, the sample was illuminated for 20 seconds for (110) crystals and 5 seconds for (100) crystals. For Mn<sup>2+</sup> oxidation, the sample was illuminated for 90 seconds for (110) crystals and 60 seconds for (100) crystals. Reaction conditions were adjusted so that the surface was only partially covered with the products owing to the facts that the (100) surface is much more reactive than the (110) surface,<sup>13,14</sup> and Mn<sup>2+</sup> oxidation is a relatively slow reaction compared with Ag<sup>+</sup> reduction.<sup>15</sup> After the illumination, the sample was rinsed in DI water and dried with a stream of argon. Before carrying out another experiment, the crystal surface would be cleaned with cotton swabs and

ultrasonically cleaned in acetone and methanol, respectively. The two reactions can be expressed in the following way:



Before and after the reaction, the surface topography was imaged by atomic force microscopy (AFM) with a Solver Next AFM (NT-MDT) or an NTEGRA AFM (NT-MDT) operated in semi-contact mode using a standard AFM probe (NCHR, NanoWorld). The local surface potential was measured by Kelvin Probe Force Microscope (KFM) using a silicon AFM probe coated with Pt/Ir (NCHPt, NanoWorld). Before the measurement, the probes were calibrated using an Au (111) thin film sample. The Gwyddion software package was employed to analyze the data.<sup>16</sup>

***Photocatalytic water splitting experiment.*** Photocatalytic water splitting reaction was carried out using a high-throughput parallelized and automated photochemical reactor (PAPCR).<sup>17</sup> The reactor employs a hydrogen sensitive film whose color will change from light to dark when exposed to hydrogen. The relationship between the local hydrogen concentration and film darkness has been calibrated and reported in detail in our previous work (see Chapter 6 and Appendix 4). The image of the film was captured by a camera fixed on the top of the reactor. To measure the H<sub>2</sub> production rate, 10 mg of powder as prepared were placed into a glass vial with 0.4 ml of DI water whose pH was adjusted to pH 5, pH 7, pH 9 and pH 12 by adding nitric acid (Fisher Chemical) or NaOH (Fisher Scientific). The illumination was provided by two 380 nm UV LEDs (Chanzon). The whole illumination lasted for 16 h, during which a total of 160 images were taken, with each image quantifying the hydrogen concentration within each vial.

## 7.3 Results

In a conventional molten salt process, the salt liquifies above the melting point and then solidifies on cooling. At the end of the process, the solid salt is the same phase as it was at the start of the process, but likely containing some impurities. This is a good description of the molten KCl treatment (or other alkali metal chlorides). However, the SrCl<sub>2</sub> process is not like this – at the process temperature, the salt reacts with both the Al<sub>2</sub>O<sub>3</sub> crucible and, to some extent, the SrTiO<sub>3</sub>.

By the end of the process, there is no (or very little)  $\text{SrCl}_2$  left in the crucible. When  $\text{SrCl}_2$  is melted in an alumina crucible (even without any  $\text{SrTiO}_3$  present), it wets and reacts with the crucible, forming yellow reaction products on the outer crucible sidewall. The resulting products were collected by centrifugation and characterized by XRD in Fig. 7-10(a), and it is found that a large percentage of the salts have reacted with the crucible to form  $\text{Sr}_3\text{Al}_2\text{O}_6$  and then  $\text{Sr}_3\text{Al}_2(\text{OH})_{12}$  after rinsing in water. Based on the phase diagram of  $\text{SrO-SrCl}_2$  system in Figure 7-11,  $\text{SrO}$  is likely to form in the melt and react with  $\text{Al}_2\text{O}_3$ . Because of this, the actual time that the  $\text{SrTiO}_3$  is in contact with molten  $\text{SrCl}_2$  is much shorter than 10 hours, as the melt composition changes, and the liquid disappears.

$\text{SrTiO}_3$  particles were prepared via a hydrothermal method<sup>11</sup> with a specific amount of  $\text{AlCl}_3$  added along with the precursors. SEM images of  $\text{SrTiO}_3$  particles with 1% and 2%  $\text{Al}^{3+}$  added are given in the first column of Figure 7-1(a), denoted as Hydro1% and Hydro2%. It is assumed that Al atoms were uniformly distributed within these crystals. After loading  $\text{RhCrO}_x$  cocatalysts (0.1 wt% Rh and Cr), photocatalytic water splitting experiments have been carried out on Hydro1% and Hydro2% crystals. However, no  $\text{H}_2$  evolution was detected by the PAPCR either in methanol solution or in pure water. Next, Hydro1% and Hydro2% crystals were modified by the  $\text{SrCl}_2$  flux treatment in an  $\text{Al}_2\text{O}_3$  crucible. The resulting crystals were referred to as Hydro1%-sA and Hydro2%-sA shown in Figure 7-1(a) and they have morphologies similar to Hydro1% and Hydro2%, but their sharp edges become rounded. Again, the  $\text{RhCrO}_x$  (0.1 wt% Rh and Cr) cocatalyst was loaded. These crystals had significantly enhanced reactivities compared to those crystals that have not heated in the  $\text{SrCl}_2$  flux. As shown in Figure 7-1 (b) and (c), the water splitting reactivities of these crystals reached  $650 \mu\text{mol g}^{-1}\text{h}^{-1}$  in pure water. Note that we have even tried much higher Al concentrations, but they still cannot produce  $\text{H}_2$  in the absence of the  $\text{SrCl}_2$  treatment. The experiment above was inspired by the idea that Al-doping during the hydrothermal synthesis and during the  $\text{SrCl}_2$  flux treatment might lead to a different material. The results confirmed that, to prepare highly reactive  $\text{SrTiO}_3$  photocatalysts, both the incorporation of  $\text{Al}^{3+}$  and the  $\text{SrCl}_2$  flux treatment are necessary. However, the particles are small, and it is difficult to directly characterize their surfaces after the flux treatment. Therefore, we reproduced this experiment by heating  $\text{SrTiO}_3$  single crystal substrates in the flux and compared the surface properties before and after the flux treatment.

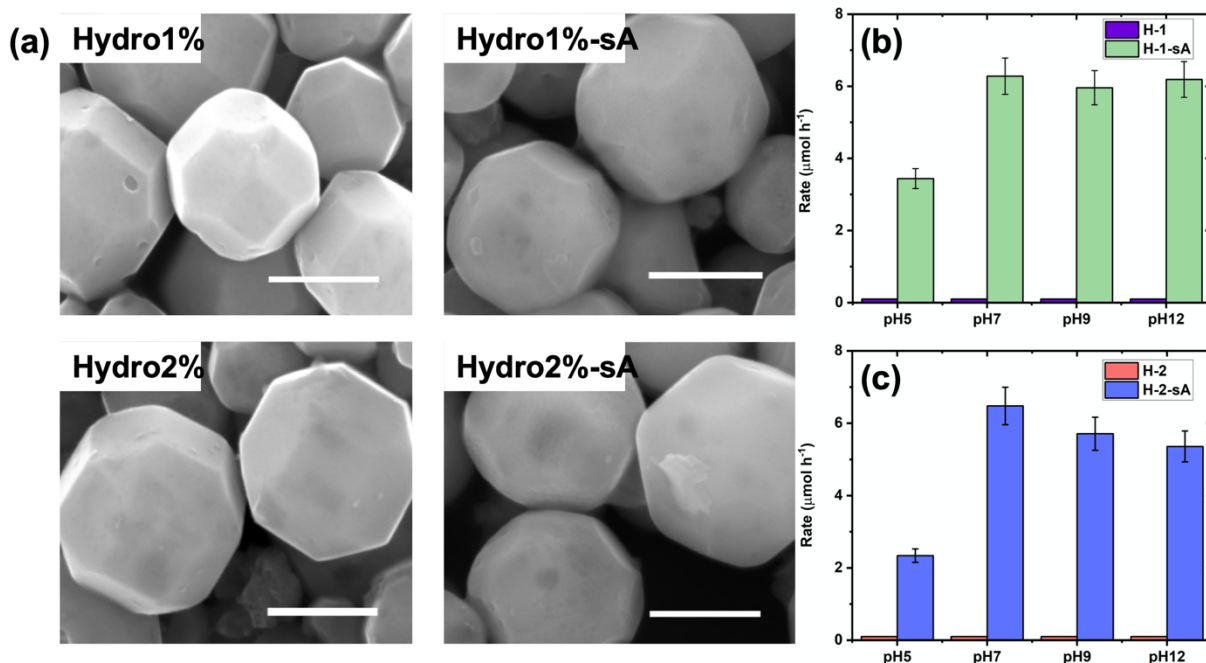


**Figure 7-1:** (a) SEM images of Hydro1% and Hydro2% crystals and the resulting crystals after modifying by SrCl<sub>2</sub> flux in an aluminum crucible. The scale bar represents 400 nm. (b) and (c) show mass specific rates (μmol g<sup>-1</sup>h<sup>-1</sup>) of H<sub>2</sub> generation for Hydro1% and Hydro2% crystals before and after SrCl<sub>2</sub> treatment, respectively. The bars represent the standard deviation.

A SrTiO<sub>3</sub> (110) single crystal purchased from MSE Supplies was annealed in air at 1100 °C for 6 h and a topographic AFM image of its surface is shown in Figure 7-2(a). The surface is made up of large flat (110) terrace and (100) long step edges.<sup>13</sup> The surface potential image, measured with KFM on the same sample but a different location, is shown in Fig. 7-2(a) and the average surface potential is determined to be 0.11 V. After the sample was immersed in a AgNO<sub>3</sub> (MnSO<sub>4</sub>) solution and illuminated, new bright contrast appeared on the surface as shown in Fig. 7-2(c) and (d), corresponding to reduced metallic silver (Mn oxides). It is observed that the photochemical reaction is anisotropic that Ag reduction prefers to occur on the (100) edges and Mn oxidation mainly occurs on the (110) terraces, which is consistent with a previous report.<sup>13</sup>

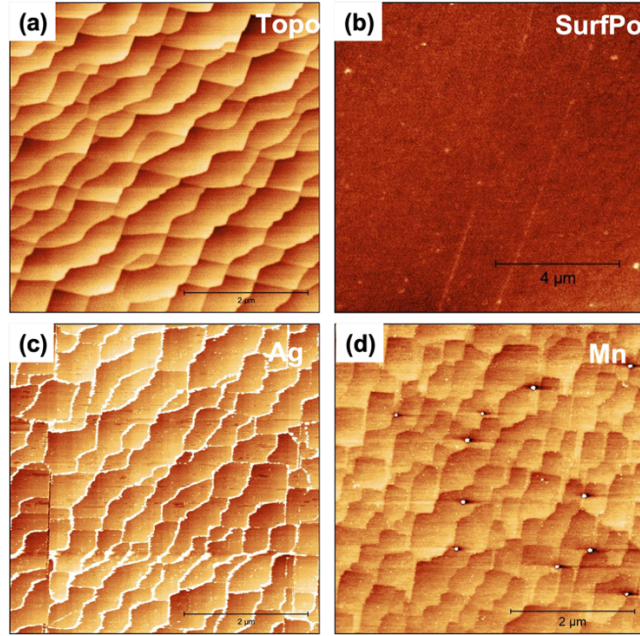


**Figure 7-2:** Topographic AFM image and KFM surface potential image of an air annealed SrTiO<sub>3</sub> (110) surface are given in (a) and (b). The average potential is 0.11 V. Images of the surface after photoreduction of Ag<sup>+</sup> and photooxidation of Mn<sup>2+</sup> are shown in (c) and (d). The dark-to-light vertical contrast is (a): 0 to 3.8 nm, (b): 0.091V to 0.164V, (c): 0 to 5.7 nm, (d): 0 to 8 nm.

Another two air annealed SrTiO<sub>3</sub> (110) single crystals were treated in molten SrCl<sub>2</sub> flux and KCl flux, respectively, and the topographic AFM images of the surfaces are presented in Figure 7-3 (a) and (e). The surface restructures in both fluxes. For the sample treated in the SrCl<sub>2</sub> flux, the large terraces were replaced by very fine terraces as large as a few tens of nanometers with long curved edges. At the same time, it seems that dislocations were etched in the flux as multiple etch pits are observed on the surface. We measured the mass of the sample before and after the SrCl<sub>2</sub> flux treatment and found that the mass was reduced from 0.0653 g to 0.0630 g (~3.5% loss), indicating that some of the crystal dissolves in the flux, revealing a new surface. For the sample treated in the KCl flux, the large (110) terraces remain, but are no longer flat, and many fine rectangular facets appear on the original terrace. The newly appearing facet is about 200 nm long and 20 nm wide. Unlike the SrCl<sub>2</sub> flux, there is no obvious change of mass during the KCl flux treatment. The surface potential was measured on the two samples (on a different location) with KFM, and the corresponding potential images are shown in Figure 7-3(b) and (f). It is found that both flux treatments decrease the surface potential: the SrCl<sub>2</sub> treated (110) surface has a mean potential of -0.27 V, and the KCl treated (110) surface has a mean potential of -0.032 V. The photochemical reactivities of the flux treated surfaces were studied with marker reactions. After the SrCl<sub>2</sub> flux

treatment, the photoreduction of  $\text{Ag}^+$  and photooxidation of  $\text{Mn}^{2+}$  were both enhanced, as shown in Figure 7-3(c) and (d). Under the same illumination conditions, small Ag or  $\text{MnO}_2$  particles uniformly deposit all over the surface. Larger and more widely separated particles are also found. However, the reactivity seems to be isotropic, and no spatial selectivity was resolved. After the KCl flux treatment, shown in Fig. 7-3(g) and (h), the cathodic reactivity seems to increase slightly, but the anodic reactivity remains low.

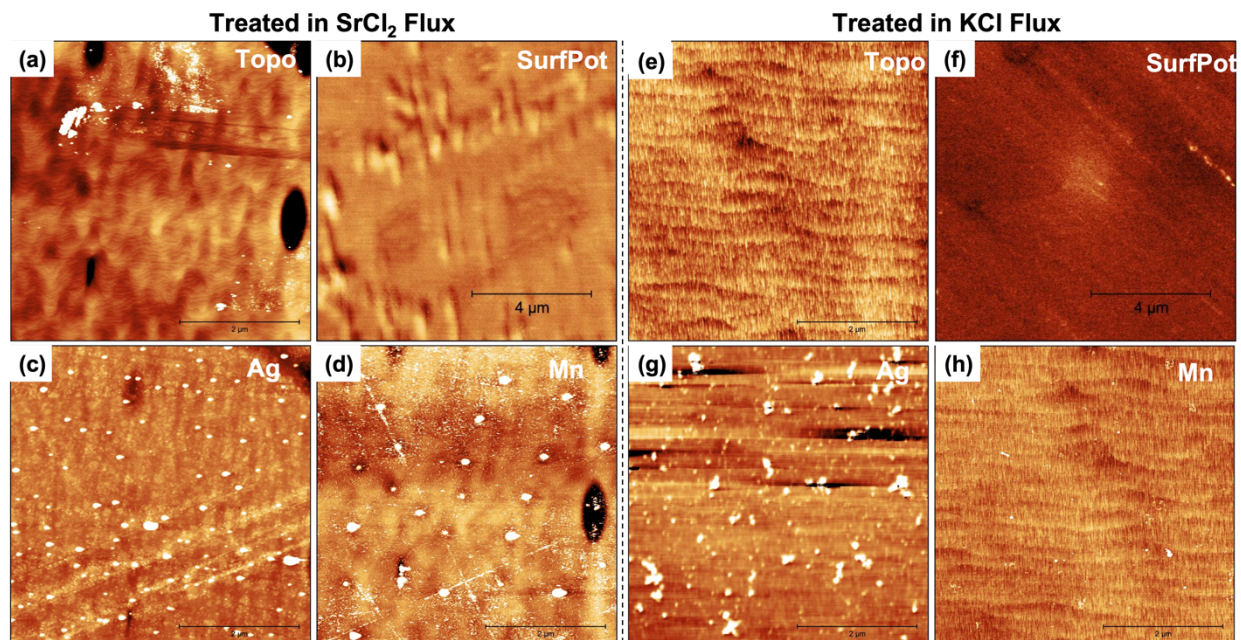


**Figure 7-3:** Topographic AFM images of air annealed  $\text{SrTiO}_3$  (110) single crystal surfaces after treating in molten (a)  $\text{SrCl}_2$  flux and (e) KCl flux. Surface potential images were recorded on the same sample, but different locations are shown in (b) and (f). The average potential is determined to be (b):  $-0.27$  V and (f):  $-0.032$  V. Panel (c) and (d) show AFM images of the  $\text{SrCl}_2$  treated (110) surface after  $\text{Ag}^+$  photoreduction and  $\text{Mn}^{2+}$  photo-oxidation. Panel (g) and (h) show AFM images of the KCl treated (110) surface after  $\text{Ag}^+$  photoreduction and  $\text{Mn}^{2+}$  photo-oxidation. The dark-to-light vertical contrast is (a): 0 to 4 nm, (b):  $-0.33$  to  $-0.22$  V, (c): 0 to 15 nm, (d): 0 to 5.4 nm, (e): 0 to 4.7 nm, (f):  $-0.055$  to  $0.024$  V, (g): 0 to 9 nm, (h): 0 to 7 nm.

The same experiments have been carried out on  $\text{SrTiO}_3$  (100) single crystal surface as well. Topographic AFM images of the surface of  $\text{SrTiO}_3$  (100) single crystal that was annealed in air at  $1100$  °C for 6 h is shown in Figure 7-4(a). The annealing leads to the formation of (100) terraces and steps mostly oriented in the  $\langle 100 \rangle$  direction. A KFM image is given in Fig. 7-4(b) and the average surface potential is determined to be  $0.18$  V. The (100) surface was reported to be bifunctional and here we found that the surface is highly reactive for both the photoreduction of  $\text{Ag}^+$  and the photo-oxidation of  $\text{Mn}^{2+}$ , as shown in Figure 7-4 (c) and (d). It is found that metallic

Ag deposits prefer to accumulate near the step edges and MnO<sub>2</sub> deposits nucleated all over the terrace. It is noted that the (100) surface can be terminated by a TiO<sub>2</sub> or SrO plane,<sup>18</sup> and Paradinas measured a potential difference of the two terminations to be  $45 \pm 10$  mV.<sup>19</sup> A more recent study by Sharma et al. found that water splitting reaction can proceed on (100) surface only when the two terminations coexist, and SrO surface provides the reaction sites and TiO<sub>2</sub> surface affects the electronic band alignment.<sup>20</sup> This might explain the spatial distribution of the photochemical products observed in our experiment.

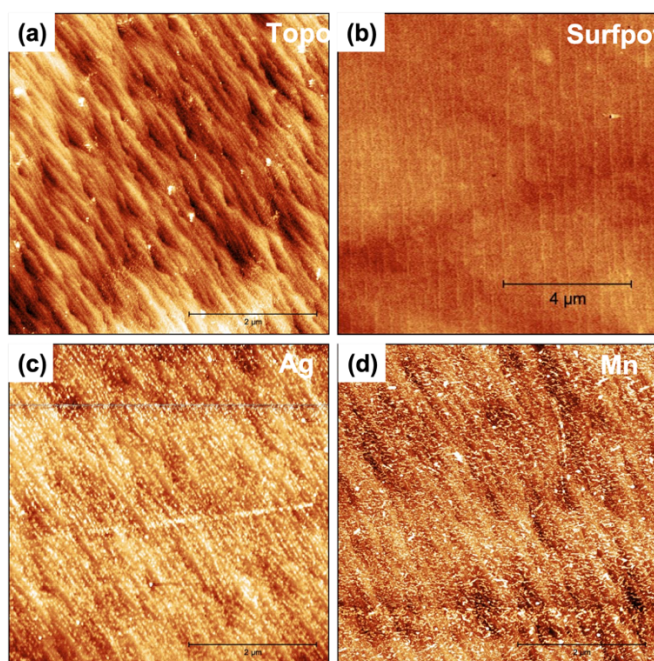


**Figure 7-4:** Topographic AFM image and KFM surface potential image of an air annealed SrTiO<sub>3</sub> (100) surface are given in (a) and (b). The average potential is 0.18 V. Images of the surface after photoreduction of Ag<sup>+</sup> and photooxidation of Mn<sup>2+</sup> are shown in (c) and (d). The dark-to-light vertical contrast is (a): 0 to 2.3 nm, (b): 0.15 V to 0.219 V, (c): 0 to 7 nm, (d): 0 to 4.5 nm.

The SrCl<sub>2</sub> and KCl flux treatments were carried out on air annealed SrTiO<sub>3</sub> (100) single crystals and the topographic AFM images of the surfaces are shown in Figure 7-5 (a) and (e). Like the results on the (110) surface, both flux treatments led to a change of the surface structure of the (100) surface. After the sample was treated in the SrCl<sub>2</sub> flux, as shown in Fig. 7-5(a), the original terraces merged and formed new terraces as wide as 100 nm with long wavy edges. After the sample was treated in the KCl flux, the original terraces remain but new long straight steps appear that cross the surface. The KFM images are given in Fig. 7-5(b) and 5(f) and the averaged surface potential of the (100) surface after treating in the SrCl<sub>2</sub> flux or the KCl flux was determined to be

-0.063 V and 0.12 V, respectively. Again, the crystal slightly dissolved in the SrCl<sub>2</sub> flux in which the mass was reduced from 0.0635 g to 0.0602 g (~5.2% loss), but the crystal mass remains unchanged after the KCl flux treatment. Photochemical properties of the two samples were explored via marker reactions. It is found that, after the SrCl<sub>2</sub> flux treatment, as shown in Fig. 7-5(c) and (d), the photoanodic reactivity is almost terminated and the photocathodic reactivity is also reduced significantly. Furthermore, the spatial distribution of the reaction products disappears as Ag particles uniformly deposit over the surface. As for the KCl flux treated sample, Ag deposits only accumulate near the newly formed steps as shown in Fig. 7-5(g), but MnO<sub>2</sub> only nucleate along the original terraces (see 7-5(h)). Photochemical reactivities of the six samples are grouped into three categories by counting the number of deposits in a 1 μm<sup>2</sup> squared region and shown in Table 7-1 and Figure 7-6, along with the surface potentials measured via KFM. Photochemical reactivities are grouped into three categories by counting averaged deposits in a 1 μm<sup>2</sup> box region: High reactivity (>10 deposits), Mid reactivity (5~10 deposits) and Low reactivity (<5 deposits).

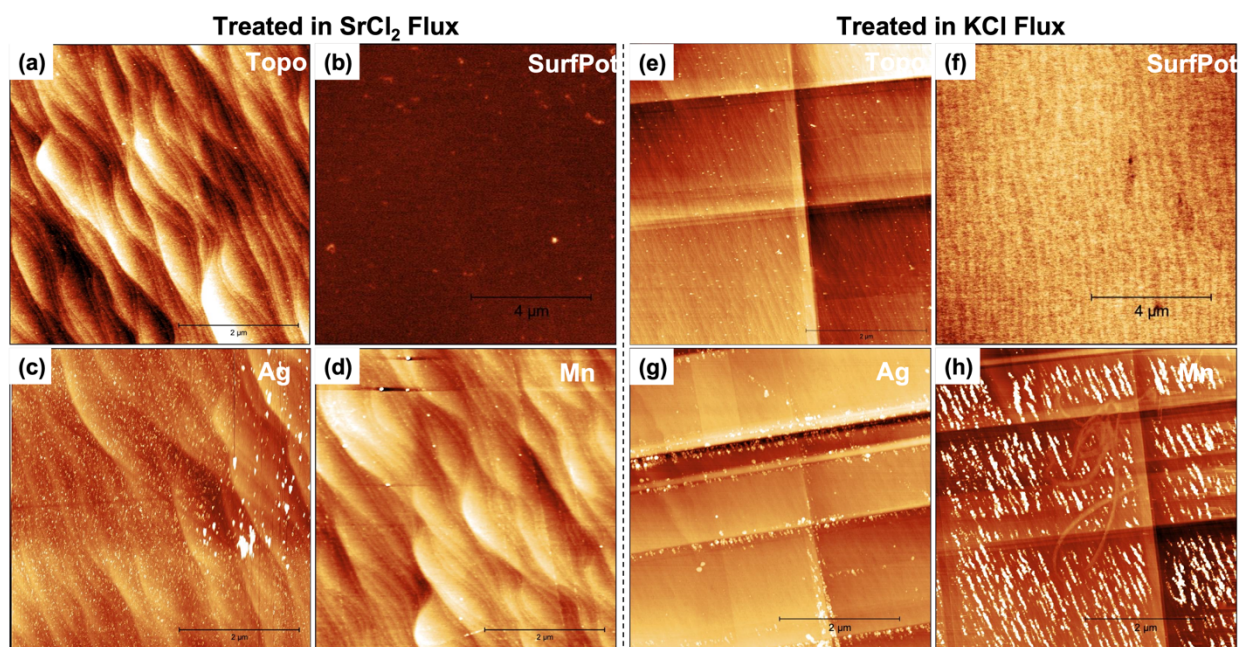


**Figure 7-5:** Topographic AFM images of air annealed SrTiO<sub>3</sub> (100) single crystal surfaces after treating in molten (a) SrCl<sub>2</sub> flux and (e) KCl flux. Surface potential images were recorded on the same sample, but different locations are shown in (b) and (f). The average potential is determined to be (b): -0.063 V and (f): 0.12 V. Panel (c) and (d) show AFM images of the SrCl<sub>2</sub> treated (100) surface after Ag<sup>+</sup> photoreduction and Mn<sup>2+</sup> photo-oxidation. Panel (g) and (h) show AFM images of the KCl treated (100) surface after Ag<sup>+</sup> photoreduction and Mn<sup>2+</sup> photo-oxidation. The dark-to-light vertical contrast is (a): 0 to 2.3 nm, (b): -0.078 to 0.005 V, (c): 0 to 7.2 nm, (d): 0 to 4.7 nm, (e): 0 to 7.4 nm, (f): 0.099 to 0.13 V, (g): 0 to 16.6 nm, (h): 0 to 11 nm.

**Table 7-1:** Photochemical reactivities and surface potential of the six SrTiO<sub>3</sub> single crystal surfaces.

Sample	Air annealed		SrCl <sub>2</sub> treated		KCl treated	
	cathodic	anodic	cathodic	anodic	cathodic	anodic
STO(100)	High	High	Mid	Low	Low	High
	181 mV		-62.9 mV		117 mV	
STO(110)	Low	Mid	High	High	Low	Low
	110 mV		-271 mV		-32.3 mV	

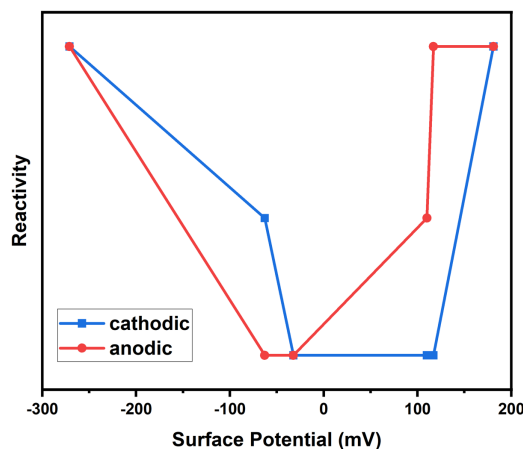


**Figure 7-6:** Summaries of the photochemical reactivities and surface potentials of the six samples in Table 7-1.

XPS spectra were recorded on the surfaces of the six samples to study the surface compositions and chemical states. Figure 7-7 shows the high-resolution O 1s spectra. The O 1s spectrum can be deconvoluted into two peaks, a primary peak is attributed to Ti-O bonding at 531.2 eV and a second peak is attributed to surface hydroxyl groups (-OH) at 533.7 eV,<sup>21,22</sup> shown in Fig. 7-7(a) and (d). The percentage of oxygen bonded in an -OH state is determined to be 24.9% and 28.3% for (100) and (110) air annealed crystals, respectively. After treating the crystals in the flux, the peaks shift about 1.6 eV to a lower binding energy, and this might imply a change of electrical conductivity on the surface. It is found that the surface hydroxyl group density increases after both flux treatments. After the SrCl<sub>2</sub> flux treatment, shown in Fig. 7-7(b) and (e), the hydroxyl group density increases to 39.3% and 52.3% for (100) and (110) oriented crystals. After the KCl flux treatment, shown in Fig. 7-7(c) and (f), the hydroxyl group density increases slightly to 29.6% and 36.2% for (100) and (110) oriented crystals.

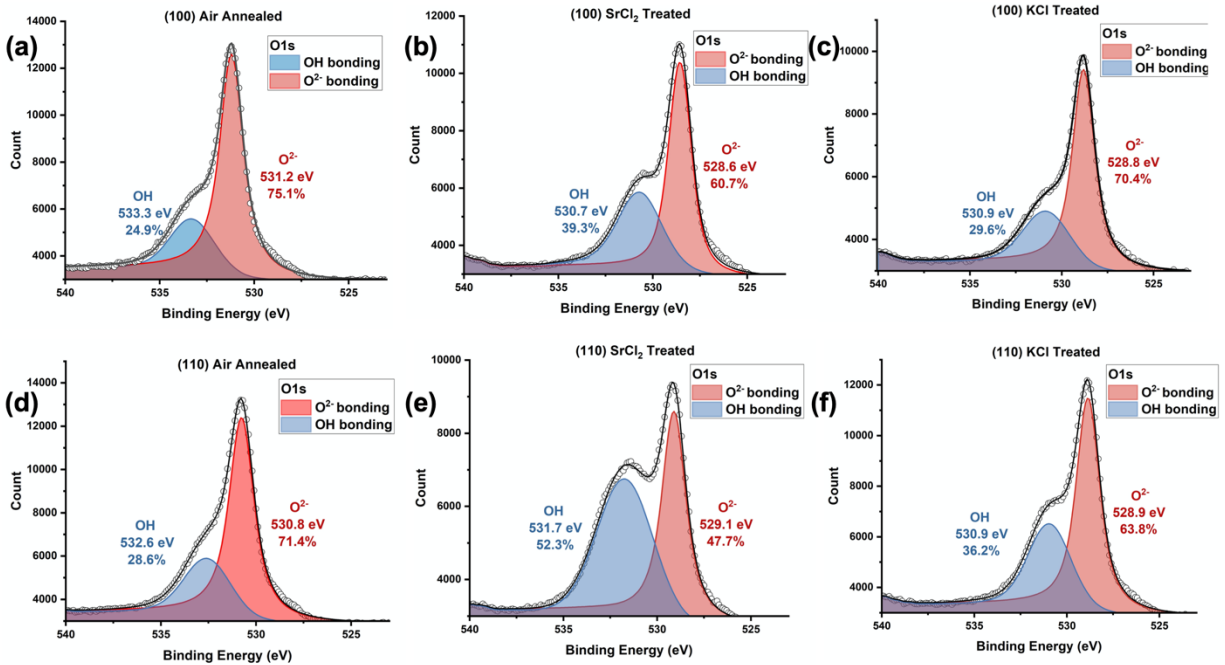


**Figure 7-7:** High resolution O 1s XPS spectra of air annealed (a) (100) and (d) (110) single crystal surfaces, SrCl<sub>2</sub> flux treated (b) (100) and (e) (110) single crystal surfaces and KCl flux treated (c) (100) and (f) (110) single crystal surfaces. The peaks for oxygen atoms bonded in Ti-O and -OH are filled in red and blue, respectively.

High resolution Sr 3d and Ti 2p XPS spectra are given in Figure 7-8 and Figure 7-9. The Sr spectrum is composed of two doublets located at 134.6 eV and 136.3 eV, corresponding to 3d<sub>5/2</sub> and 3d<sub>3/2</sub>. The doublets in the Ti spectrum located near 460.1 eV and 466 eV can be assigned to 2p<sub>3/2</sub> and 2p<sub>1/2</sub> of Ti<sup>4+</sup>. Note that, unlike powdered SrTiO<sub>3</sub> samples,<sup>7</sup> there is no detectable Ti<sup>3+</sup> species in our single crystal samples, implying it is more stoichiometric. The Sr/Ti atomic ratios were determined from the ratio of the integrated intensities of the Sr 3d and Ti 2p spectra. The ratio is determined to be 0.876 and 0.861 for air annealed (100) and (110) single crystals, respectively, meaning a Ti-rich (Sr-depleted) surface. This can be understood since the vapor pressure of SrO is significantly higher than TiO<sub>2</sub> at the annealing temperature,<sup>23,24</sup> so that part of the SrO may escape from the crystal surface during annealing. The two flux treatments change the surface composition in an opposite way. The Sr/Ti ratio is measured to be 0.877 and 0.928 for the SrCl<sub>2</sub> flux treated (100) and (110) single crystal surfaces, respectively, suggesting that the SrO surface is stable in this flux and the Sr concentration might be slightly increased. However, the KCl flux treatment will further remove Sr species from the surface, during which the Sr/Ti ratio is reduced to 0.697 and 0.735 for (100) and (110) surfaces, respectively. A summary of the XPS

data of the three samples is given in Table 7-2. Note that we have also tried to measure Al, K and Cl but cannot detect their signals via XPS, indicating the concentrations of these elements are very low on the surface.

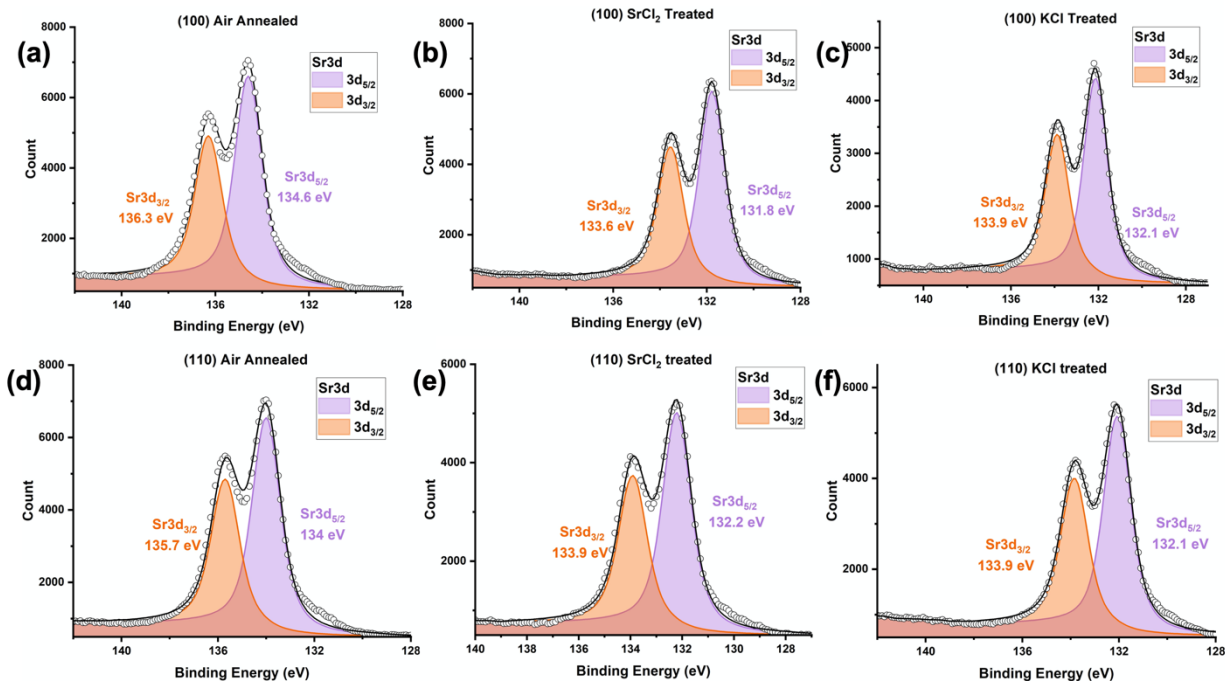


**Figure 7-8:** High resolution Sr 3d XPS spectra of air annealed (a) (100) and (d) (110) single crystal surfaces,  $\text{SrCl}_2$  flux treated (b) (100) and (e) (110) single crystal surfaces and KCl flux treated (c) (100) and (f) (110) single crystal surfaces. The peaks for strontium atoms bonded in  $3d_{5/2}$  and  $-3d_{3/2}$  are filled in purple and orange, respectively.

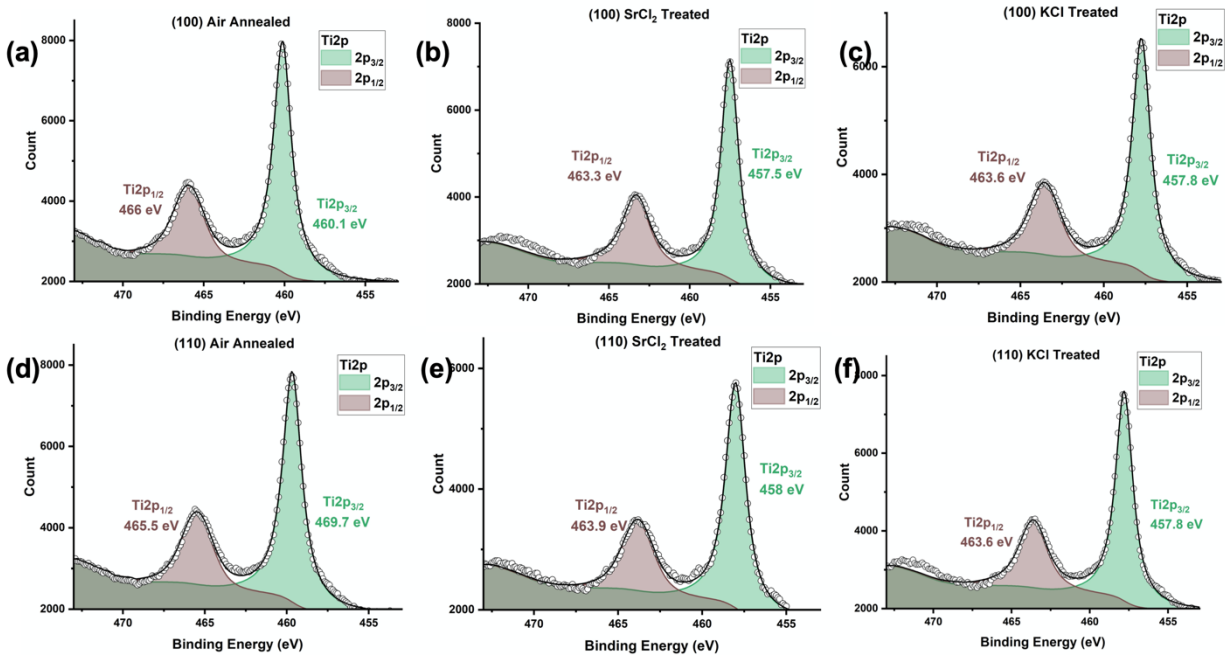


**Figure 7-9:** High resolution Ti 2p XPS spectra of air annealed (a) (100) and (d) (110) single crystal surfaces, SrCl<sub>2</sub> flux treated (b) (100) and (e) (110) single crystal surfaces and KCl flux treated (c) (100) and (f) (110) single crystal surfaces. The peaks for oxygen atoms bonded in 2p<sub>3/2</sub> and 2p<sub>1/2</sub> are filled in green and brown, respectively.

**Table 7-2:** Sr/Ti ratios and surface hydroxyl groups concentrations of the six samples determined with the XPS spectra.

Treatments	Sr/Ti		-OH%	
	(100)	(110)	(100)	(110)
Air annealed	0.876	0.861	24.9%	28.3%
SrCl <sub>2</sub> treated	0.877	0.928	39.3%	52.3%
KCl treated	0.697	0.735	29.6%	36.2%

To further explore the SrCl<sub>2</sub> flux treatment, an in-situ experiment has been performed using a high temperature confocal laser scanning microscope (CLSM). A small piece of (100) SrTiO<sub>3</sub> crystal was cut from the substrate and transferred to a small platinum crucible together with SrCl<sub>2</sub> salt. The crucible was first heated to 900 °C to liquify the salt, shown in Figure 7-10 (a), and then held at 1125 °C for observation in an argon atmosphere. After 5 min, a new phase with brighter contrast appeared near the SrTiO<sub>3</sub> crystal edge, labeled with an arrow in Fig. 7-10 (b). In the following 10 minutes, this new phase grew rapidly, exhibiting well defined facets, shown in (c) to (g), and almost covered the entire crystal surface. Later, the new phase shrinks in seconds, and the SrTiO<sub>3</sub> crystal surface is visible again. The whole experiment is about 1 hour. After cooling the crucible,

we found that the crystal color changed from semi-transparent light yellow to black, suggesting a much higher oxygen vacancy donor concentration. I tentatively assume the appearing phase to be SrO. From the SrCl<sub>2</sub>-SrO phase diagram by Neumann et al,<sup>25</sup> see Figure 7-12, SrO is soluble in the SrCl<sub>2</sub> melt, explaining why the appearing phase dissolves soon afterwards. Recall that there is no or very little amount of O<sub>2</sub> in the atmosphere, the oxygen atoms should come from the crystals. This implies that the SrCl<sub>2</sub> flux treatment would induce a much higher oxygen vacancy concentration, consistent with the blackening of the crystal. But note that the  $P_{O_2}$  is so different in this experiment, it does not really fit in with the experiments described in the earlier sections.

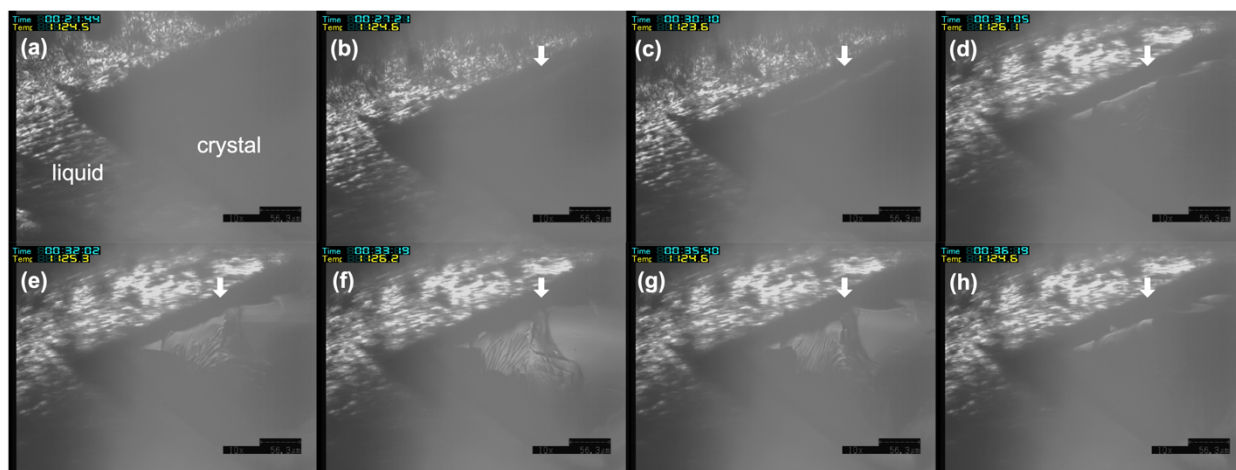


**Figure 7-10:** Images of a (100) SrTiO<sub>3</sub> crystal in molten SrCl<sub>2</sub> flux in a Pt crucible captured with a confocal laser scanning microscope.

## 7.4 Discussion

The results here clearly illustrates that the SrCl<sub>2</sub> flux has a significant influence on the surface structure and chemical compositions of SrTiO<sub>3</sub>. The first apparent difference between SrCl<sub>2</sub> and KCl is that the SrTiO<sub>3</sub> surface slightly dissolves in the molten SrCl<sub>2</sub> flux with a consistent 3% ~ 5% mass loss. There is no detectable loss of mass in the KCl flux. Yamakata et al. proposed that SrTiO<sub>3</sub> dissolves and recrystallizes in the SrCl<sub>2</sub> flux, so that the crystal morphology changes, and the crystallinity is improved.<sup>2</sup> However, considering that particle shape and size is not significantly changed by the flux treatment, as shown in Figure 7-1(a), it is not feasible that the particle completely dissolves and recrystallizes. Based on the results here, a small amount of material dissolves in the flux, and likely diffuses between crystals in the liquid media. At the same time, the mean particle size will increase as the total energy will decrease with the total surface

area, which is known as particle coarsening and Ostwald ripening.<sup>26</sup> Therefore, after the flux treatment, the total number of small particles will decrease and the average particle size will increase.

To eliminate the complication of the reaction with the alumina crucible, we also treated a SrTiO<sub>3</sub> single crystal substrate in molten SrCl<sub>2</sub> in a platinum crucible. In this case, the SrCl<sub>2</sub> remained in the crucible and, as shown in XRD (see Fig.7-10(b)), was still SrCl<sub>2</sub> at the end of the experiment. However, in this case, the crystal dissolved almost completely in the salt. Based on these observations, we reach the following conclusions. First, given sufficient time, SrTiO<sub>3</sub> will dissolve in molten SrCl<sub>2</sub>. However, when SrTiO<sub>3</sub> is heated in the presence of liquid SrCl<sub>2</sub> in an alumina crucible, there is a side reaction with the crucible that depletes the molten salt after dissolving only a small amount of the SrTiO<sub>3</sub>.

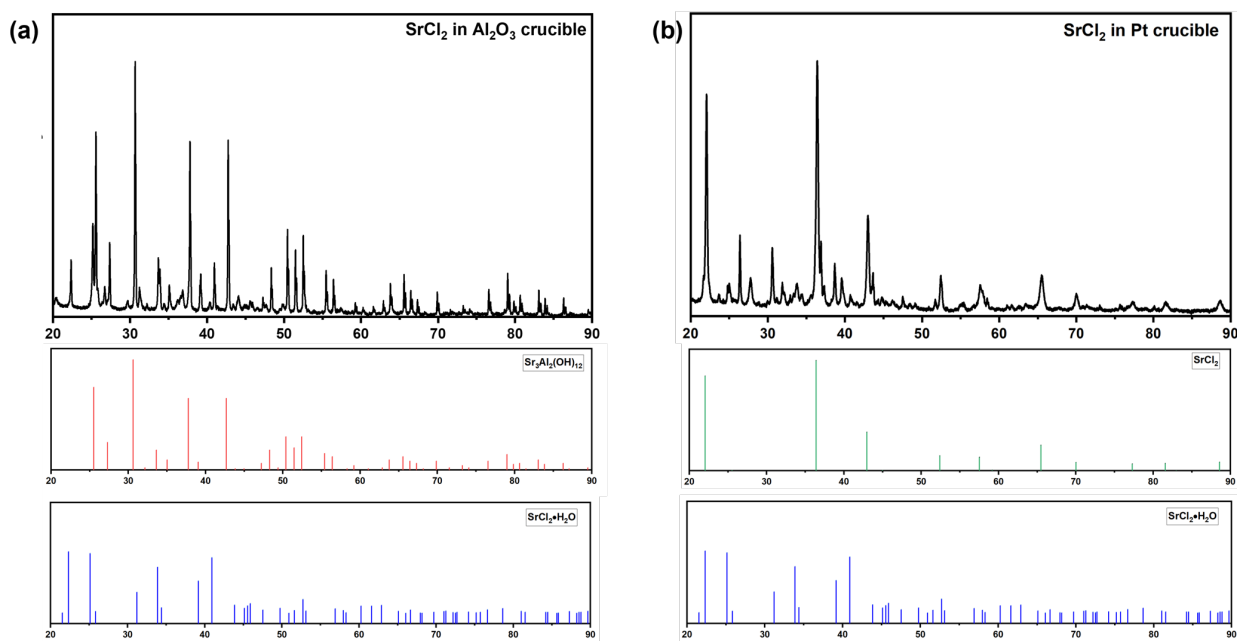


**Figure 7-11:** XRD patterns of the resulting materials by heating SrCl<sub>2</sub> in (a) an alumina crucible and (b) a platinum crucible at 1150 °C for 10 h. The materials were collected by centrifugation using deionized water.

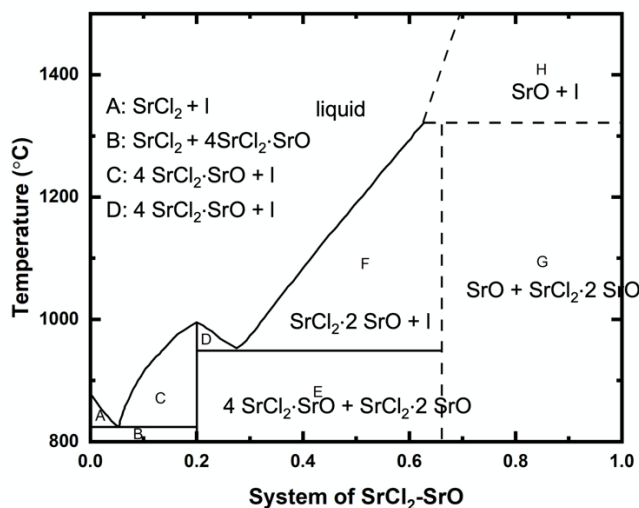


**Figure 7-12:** Phase diagram of SrCl<sub>2</sub>-SrO system. Replotted from ref.<sup>25</sup>

The XPS spectra indicate that the flux treatment leads to a hydroxyl-rich surface, and the KFM studies suggest that the flux treatment decreases the surface potential, and the SrCl<sub>2</sub> flux has a stronger influence than the KCl flux. The hydroxyl concentrations have been correlated to the surface potentials of the six samples, plotted in Figure 7-13(a), indicating that hydroxyl groups induce a negative (anodic) surface, which is consistent with the results by Zhu et al.<sup>22</sup> Past studies agree that surface hydroxyl groups are good hole traps, promoting the anodic reaction and elongating the charge carrier lifetime.<sup>27,28</sup> Secondly, surface hydroxyl groups are determined to be one of the primary water adsorption sites since the protonated lattice oxides easily form hydrogen bonds with water molecules.<sup>20,29</sup> In our case, we only load reduction cocatalysts so that the anodic reaction is supposed to occur on the SrTiO<sub>3</sub> surface. Since the overall reaction rate depends on the slower one of the two half reactions, the promotion of the photoanodic reaction driven by the hydroxyl-rich surface will improve the overall reaction rate. It is also concluded that this effect is orientation dependent; from the KFM data in Fig 7-13(b), the potential of the (110) surface is reduced much more than the potential of the (100) surface. This will increase the potential difference between the two oriented surfaces from 0.07 V to 0.21 V, a situation that enhances the charge separation inside the particle. Su et al. measured surface charge on (100) and (110) facets of SrTiO<sub>3</sub> particles, and the potential difference between the two surfaces is measured to be 40 mV,<sup>30</sup> a little lower than our measurement (70 mV). This is reasonable since we measured the potential in air, and solution species might adsorb to the surface and compensate the charge.

It is plausible to assume a larger potential difference between the two surfaces on a SrCl<sub>2</sub> flux treated SrTiO<sub>3</sub> particle, which is beneficial to photocatalytic reactivity.

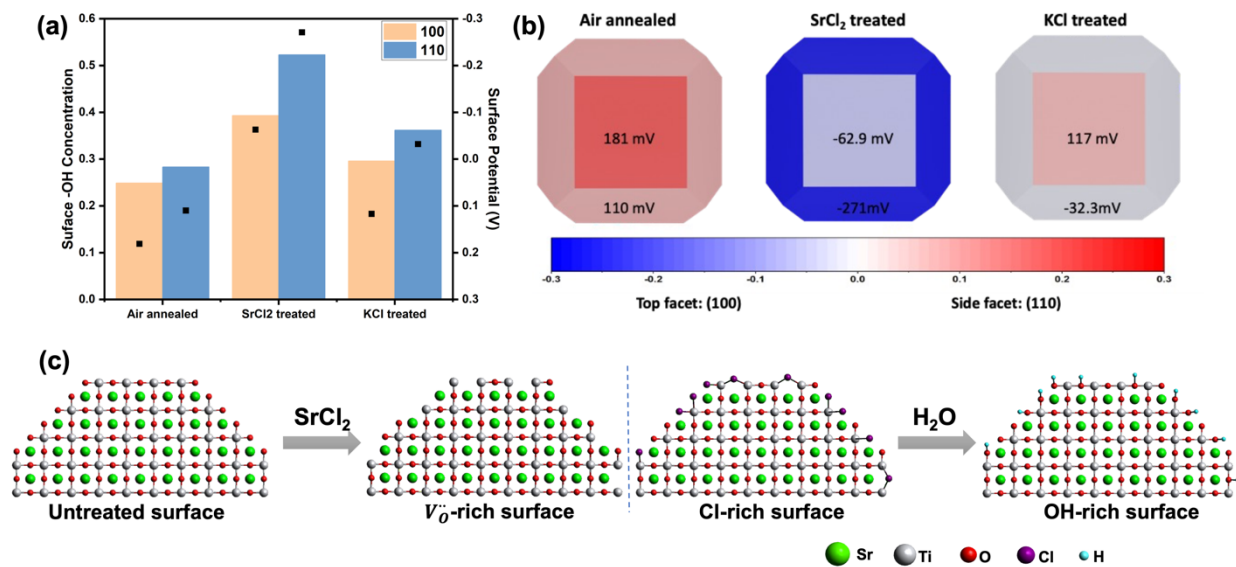


**Figure 7-13:** (a) Surface hydroxyl groups concentrations (shown in bars) and surface potential (shown in dots) of the six samples. (b) Schematic illustration of the change of surface potential induced by the molten SrCl<sub>2</sub> and KCl flux treatment. (c) Schematic illustration of the two possible mechanisms of the hydroxyl group-rich surface.

It is interesting to speculate about how the SrCl<sub>2</sub> flux produces a surface with a high density of hydroxyl groups. When water adsorbs and dissociates on SrTiO<sub>3</sub> surface, a hydroxyl group can bond to a strontium site (Sr-OH), a titanium site (Ti-OH) or directly occupy at an oxygen site (O-H).<sup>29</sup> Several works point out that Sr-rich surfaces are more easily hydroxylated compared with Ti-rich surfaces, so that increasing Sr/Ti atomic ratio on the surface might contribute to the increased hydroxyl concentration. However, based on the XPS data in Table 7-2, the changes of surface hydroxyl concentration and Sr/Ti are not proportional, implying another factor influences the system. Herein, we provide a possible explanation for the change of surface chemistry. Because of the mismatch between the Sr/Ti composition variation and the increase of hydroxyl group concentration, we assume these newly appearing hydroxyl groups should directly occupy an oxygen site. One possibility is that the SrCl<sub>2</sub> flux treatment removes oxygen atoms and leaves oxygen vacancies on the surface, and then hydroxyl groups directly occupy the vacancies during rinsing in water. This is supported by the finding from Fig. 7-10 that the flux might extract oxygen from the crystal to form SrO. In this case, molecular water can serve as an oxidizing agent, filling

the vacancy and transferring a proton to an adjacent oxygen atom, forming a pair of hydroxyl groups.<sup>31,32</sup> This effect has also been observed on the BaTiO<sub>3</sub> surface.<sup>33</sup> Another hypothesis is that the surface oxygen atoms are firstly replaced by Cl, and then replaced by hydroxyl groups, leading to the same result. And the Cl replacement hypothesis appears to depend on the cation of the salt, as SrCl<sub>2</sub> leads to greater OH% than KCl. A schematic of these two possible routes is shown in Figure 7-13 (c).

## 7.5 Conclusion

The influence of the molten SrCl<sub>2</sub> flux treatment on the surface of SrTiO<sub>3</sub> has been studied. It is found that, in Al<sub>2</sub>O<sub>3</sub> crucibles, a small amount of the crystal dissolves in the flux, reducing the mass of the crystal by 3% to 5%. KFM studies indicate that the treatment reduces the surface potential, and the potential drop depends on crystallographic orientation. Therefore, the potential difference between (100) and (110) surfaces increases from 0.07 V to 0.21 V, building a much stronger electric field inside the particle and promoting charge separation. Besides, the decrease of surface potential is proportional to the increase of surface hydroxyl group concentration. Because hydroxyl groups serve as hole traps and contribute to the photoanodic half reaction, the rate limiting step for SrTiO<sub>3</sub>, the overall reactivity is improved.

## 7.6 References

- (1) Kato, H.; Kobayashi, M.; Hara, M.; Kakihana, M. Fabrication of SrTiO<sub>3</sub> Exposing Characteristic Facets Using Molten Salt Flux and Improvement of Photocatalytic Activity for Water Splitting. *Catal. Sci. Technol.* **2013**, *3* (7), 1733–1738. <https://doi.org/10.1039/C3CY00014A>.
- (2) Yamakata, A.; Yeilin, H.; Kawaguchi, M.; Hisatomi, T.; Kubota, J.; Sakata, Y.; Domen, K. Morphology-Sensitive Trapping States of Photogenerated Charge Carriers on SrTiO<sub>3</sub> Particles Studied by Time-Resolved Visible to Mid-IR Absorption Spectroscopy: The Effects of Molten Salt Flux Treatments. *J. Photochem. Photobiol. A Chem.* **2015**, *313*, 168–175. <https://doi.org/10.1016/j.jphotochem.2015.05.016>.
- (3) Ham, Y.; Hisatomi, T.; Goto, Y.; Moriya, Y.; Sakata, Y.; Yamakata, A.; Kubota, J.; Domen,

- K. Flux-Mediated Doping of SrTiO<sub>3</sub> Photocatalysts for Efficient Overall Water Splitting. *J. Mater. Chem. A* **2016**, *4* (8), 3027–3033. <https://doi.org/10.1039/C5TA04843E>.
- (4) Chiang, T. H.; Lyu, H.; Hisatomi, T.; Goto, Y.; Takata, T.; Katayama, M.; Minegishi, T.; Domen, K. Efficient Photocatalytic Water Splitting Using Al-Doped SrTiO<sub>3</sub> Coloaded with Molybdenum Oxide and Rhodium–Chromium Oxide. *ACS Catal.* **2018**, *8* (4), 2782–2788. <https://doi.org/10.1021/acscatal.7b04264>.
- (5) Lyu, H.; Hisatomi, T.; Goto, Y.; Yoshida, M.; Higashi, T.; Katayama, M.; Takata, T.; Minegishi, T.; Nishiyama, H.; Yamada, T.; et al. An Al-Doped SrTiO<sub>3</sub> Photocatalyst Maintaining Sunlight-Driven Overall Water Splitting Activity for over 1000 h of Constant Illumination. *Chem. Sci.* **2019**, *10* (11), 3196–3201. <https://doi.org/10.1039/C8SC05757E>.
- (6) Takata, T.; Jiang, J.; Sakata, Y.; Nakabayashi, M.; Shibata, N.; Nandal, V.; Seki, K.; Hisatomi, T.; Domen, K. Photocatalytic Water Splitting with a Quantum Efficiency of Almost Unity. *Nature* **2020**, *581* (7809), 411–414. <https://doi.org/10.1038/s41586-020-2278-9>.
- (7) Zhao, Z.; Goncalves, R. V.; Barman, S. K.; Willard, E. J.; Byle, E.; Perry, R.; Wu, Z.; Huda, M. N.; Moulé, A. J.; Osterloh, F. E. Electronic Structure Basis for Enhanced Overall Water Splitting Photocatalysis with Aluminum Doped SrTiO<sub>3</sub> in Natural Sunlight. *Energy Environ. Sci.* **2019**, *12* (4), 1385–1395. <https://doi.org/10.1039/C9EE00310J>.
- (8) Cui, J.; Yang, X.; Yang, Z.; Sun, Y.; Chen, X.; Liu, X.; Wang, D.; Jiang, S.; Liu, L.; Ye, J. Zr–Al Co-Doped SrTiO<sub>3</sub> with Suppressed Charge Recombination for Efficient Photocatalytic Overall Water Splitting. *Chem. Commun.* **2021**, *57* (81), 10640–10643. <https://doi.org/10.1039/D1CC04514H>.
- (9) Qin, Y.; Fang, F.; Xie, Z.; Lin, H.; Zhang, K.; Yu, X.; Chang, K. La,Al-Codoped SrTiO<sub>3</sub> as a Photocatalyst in Overall Water Splitting: Significant Surface Engineering Effects on Defect Engineering. *ACS Catal.* **2021**, *11* (18), 11429–11439. <https://doi.org/10.1021/acscatal.1c02874>.
- (10) Zhao, Z.; Willard, E. J.; Li, H.; Wu, Z.; Castro, R. H. R.; Osterloh, F. E. Aluminum Enhances Photochemical Charge Separation in Strontium Titanate Nanocrystal

- Photocatalysts for Overall Water Splitting. *J. Mater. Chem. A* **2018**, *6* (33), 16170–16176. <https://doi.org/10.1039/C8TA05885G>.
- (11) Dong, L.; Shi, H.; Cheng, K.; Wang, Q.; Weng, W.; Han, W. Shape-Controlled Growth of SrTiO<sub>3</sub> Polyhedral Submicro/Nanocrystals. *Nano Res.* **2014**, *7* (9), 1311–1318. <https://doi.org/10.1007/s12274-014-0495-y>.
- (12) Giocondi, J. L.; Rohrer, G. S. Spatially Selective Photochemical Reduction of Silver on the Surface of Ferroelectric Barium Titanate. *Chem. Mater.* **2001**, *13* (2), 241–242. <https://doi.org/10.1021/cm000890h>.
- (13) Giocondi, J. L.; Rohrer, G. S. Structure Sensitivity of Photochemical Oxidation and Reduction Reactions on SrTiO<sub>3</sub> Surfaces. *J. Am. Ceram. Soc.* **2003**, *86* (7), 1182–1189. <https://doi.org/10.1111/j.1151-2916.2003.tb03445.x>.
- (14) Zhang, M.; Salvador, P. A.; Rohrer, G. S. Influence of pH and Surface Orientation on the Photochemical Reactivity of SrTiO<sub>3</sub>. *ACS Appl. Mater. Interfaces* **2020**. <https://doi.org/10.1021/acsmi.0c04351>.
- (15) Pisat, A. S.; Salvador, P. A.; Rohrer, G. S. The Facet Structure and Photochemical Reactivity of Arbitrarily Oriented Strontium Titanate Surfaces. *Adv. Mater. Interfaces* **2019**, *6* (16), 1900731. <https://doi.org/10.1002/admi.201900731>.
- (16) David, N.; Petr, K. Gwyddion: An Open-Source Software for SPM Data Analysis. *Open Physics*. 2012, p 181. <https://doi.org/10.2478/s11534-011-0096-2>.
- (17) Lopato, E. M.; Eikey, E. A.; Simon, Z. C.; Back, S.; Tran, K.; Lewis, J.; Kowalewski, J. F.; Yazdi, S.; Kitchin, J. R.; Ulissi, Z. W.; et al. Parallelized Screening of Characterized and DFT-Modeled Bimetallic Colloidal Cocatalysts for Photocatalytic Hydrogen Evolution. *ACS Catal.* **2020**, *10* (7), 4244–4252. <https://doi.org/10.1021/acscatal.9b05404>.
- (18) Koster, G.; Kropman, B. L.; Rijnders, G. J. H. M.; Blank, D. H. A.; Rogalla, H. Quasi-Ideal Strontium Titanate Crystal Surfaces through Formation of Strontium Hydroxide. *Appl. Phys. Lett.* **1998**, *73* (20), 2920–2922. <https://doi.org/10.1063/1.122630>.
- (19) Paradinas, M.; Garzón, L.; Sánchez, F.; Bachelet, R.; Amabilino, D. B.; Fontcuberta, J.;

- Ocal, C. Tuning the Local Frictional and Electrostatic Responses of Nanostructured SrTiO<sub>3</sub>—Surfaces by Self-Assembled Molecular Monolayers. *Phys. Chem. Chem. Phys.* **2010**, *12* (17), 4452–4458. <https://doi.org/10.1039/B924227A>.
- (20) Sharma, V.; Bein, B.; Lai, A.; Pamuk, B.; Dreyer, C. E.; Fernández-Serra, M.; Dawber, M. Photocatalytic Water Oxidation on SrTiO<sub>3</sub> [001] Surfaces. *arXiv Prepr. arXiv2201.13443* **2022**.
- (21) Vovk, G.; Chen, X.; Mims, C. A. In Situ XPS Studies of Perovskite Oxide Surfaces under Electrochemical Polarization. *J. Phys. Chem. B* **2005**, *109* (6), 2445–2454. <https://doi.org/10.1021/jp0486494>.
- (22) Zhu, Y.; Salvador, P. A.; Rohrer, G. S. Controlling the Relative Areas of Photocathodic and Photoanodic Terraces on the SrTiO<sub>3</sub>(111) Surface. *Chem. Mater.* **2016**, *28* (14), 5155–5162. <https://doi.org/10.1021/acs.chemmater.6b02205>.
- (23) Lamoreaux, R. H.; Hildenbrand, D. L.; Brewer, L. High-Temperature Vaporization Behavior of Oxides II. Oxides of Be, Mg, Ca, Sr, Ba, B, Al, Ga, In, Tl, Si, Ge, Sn, Pb, Zn, Cd, and Hg. *J. Phys. Chem. Ref. Data* **1987**, *16* (3), 419–443. <https://doi.org/10.1063/1.555799>.
- (24) Wang, Z.; Yang, F.; Zhang, Z.; Tang, Y.; Feng, J.; Wu, K.; Guo, Q.; Guo, J. Evolution of the Surface Structures on SrTiO<sub>3</sub>(110) Tuned by Ti or Sr Concentration. *Phys. Rev. B* **2011**, *83* (15), 155453. <https://doi.org/10.1103/PhysRevB.83.155453>.
- (25) Neumann, B.; Kröger, C.; Jüttner, H. Die Systeme Erdalkalichlorid-Erdalkalioxyd Und Die Zersetzung Der Erdalkalichloride Durch Wasserdampf. *Zeitschrift für Elektrochemie und Angew. Phys. Chemie* **1935**, *41* (10), 725–736. <https://doi.org/10.1002/bbpc.19350411005>.
- (26) Day, R. V; Barford, J. Particle Coarsening in the Solid State. *Nature* **1968**, *217* (5134), 1145–1146. <https://doi.org/10.1038/2171145a0>.
- (27) Shirai, K.; Fazio, G.; Sugimoto, T.; Selli, D.; Ferraro, L.; Watanabe, K.; Haruta, M.; Ohtani, B.; Kurata, H.; Di Valentin, C.; et al. Water-Assisted Hole Trapping at the Highly Curved Surface of Nano-TiO<sub>2</sub> Photocatalyst. *J. Am. Chem. Soc.* **2018**, *140* (4), 1415–1422.

<https://doi.org/10.1021/jacs.7b11061>.

- (28) Lawless, D.; Serpone, N.; Meisel, D. Role of Hydroxyl Radicals and Trapped Holes in Photocatalysis. A Pulse Radiolysis Study. *J. Phys. Chem.* **1991**, *95* (13), 5166–5170. <https://doi.org/10.1021/j100166a047>.
- (29) Domingo, N.; Pach, E.; Cordero-Edwards, K.; Pérez-Dieste, V.; Escudero, C.; Verdaguer, A. Water Adsorption, Dissociation and Oxidation on SrTiO<sub>3</sub> and Ferroelectric Surfaces Revealed by Ambient Pressure X-Ray Photoelectron Spectroscopy. *Phys. Chem. Chem. Phys.* **2019**, *21* (9), 4920–4930. <https://doi.org/10.1039/C8CP07632D>.
- (30) Su, S.; Siretanu, I.; van den Ende, D.; Mei, B.; Mul, G.; Mugele, F. Facet-Dependent Surface Charge and Hydration of Semiconducting Nanoparticles at Variable pH. *Adv. Mater.* **2021**, *33* (52), 2106229. <https://doi.org/10.1002/adma.202106229>.
- (31) Ketteler, G.; Yamamoto, S.; Bluhm, H.; Andersson, K.; Starr, D. E.; Ogletree, D. F.; Ogasawara, H.; Nilsson, A.; Salmeron, M. The Nature of Water Nucleation Sites on TiO<sub>2</sub>(110) Surfaces Revealed by Ambient Pressure X-Ray Photoelectron Spectroscopy. *J. Phys. Chem. C* **2007**, *111* (23), 8278–8282. <https://doi.org/10.1021/jp068606i>.
- (32) Li, W.; Liu, S.; Wang, S.; Guo, Q.; Guo, J. The Roles of Reduced Ti Cations and Oxygen Vacancies in Water Adsorption and Dissociation on SrTiO<sub>3</sub>(110). *J. Phys. Chem. C* **2014**, *118* (5), 2469–2474. <https://doi.org/10.1021/jp409076y>.
- (33) Wang, J. L.; Gaillard, F.; Pancotti, A.; Gautier, B.; Niu, G.; Vilquin, B.; Pillard, V.; Rodrigues, G. L. M. P.; Barrett, N. Chemistry and Atomic Distortion at the Surface of an Epitaxial BaTiO<sub>3</sub> Thin Film after Dissociative Adsorption of Water. *J. Phys. Chem. C* **2012**, *116* (41), 21802–21809. <https://doi.org/10.1021/jp305826e>.

# Chapter 8: Space Charge Engineering via Defect Compensation for Enhanced Photocatalytic Reactivity

*Following Al-doped SrTiO<sub>3</sub>, we have discussed the role of the molten SrCl<sub>2</sub> flux in Chapter 7, in this chapter, we are moving to the dopant effect. One question that we are going to answer is that if Al<sup>3+</sup> is truly special or if we could employ other elements to get a similar reactivity. Herein, we compare Al<sup>3+</sup> with Mg<sup>2+</sup> and Ga<sup>3+</sup>. Mg<sup>2+</sup> and Al<sup>3+</sup> have a similar ion's radius, and Ga<sup>3+</sup> has the same valence as Al<sup>3+</sup>. It is found that all three elements contribute to the reactivity and the result is strongly influenced by doping concentration. At the end of this chapter, we provide a compensation model to explain the doping effect from the perspective of defect chemistry.*

## 8.1 Introduction

The introduction of foreign ions to a host material, referred to here as doping, is a widely employed method to improve the performance of semiconductor based photocatalysts.<sup>1,2</sup> For example, doping can modify the crystal defect structure, reduce the concentration of recombination centers and increase the charge carrier lifetime.<sup>3-5</sup> Takata et al. demonstrated that doping SrTiO<sub>3</sub> with a lower valence cation could modify the defect structure and enhance its photocatalytic reactivity.<sup>6</sup> Sakata et al. doped numerous divalent cations into Ga<sub>2</sub>O<sub>3</sub> and found that Zn<sup>2+</sup> gave a remarkable efficiency for water splitting, which is ascribed to the increased hole concentration.<sup>7</sup> Another application of doping foreign elements is to sensitize wide band gap materials for visible light response.<sup>1</sup> For example, co-doping iridium ions and alkaline earth metal ions into NaNbO<sub>3</sub> and NaTaO<sub>3</sub> contributes to their photocatalytic reactivity in the visible light region.<sup>8</sup> Kim et al. found that the substitution of Pb<sup>2+</sup> into layered perovskites is a general strategy for visible light sensitization for these ultraviolet (UV)-active materials.<sup>9</sup> Moreover, a Rh-doped SrTiO<sub>3</sub> photocatalyst loaded with a Pt cocatalyst had a quantum yield of 5.2% at 420 nm for H<sub>2</sub> evolution,<sup>10</sup> and this approach has been confirmed to work for CaTiO<sub>3</sub> as well.<sup>11</sup>

Dopant concentration is also known to affect the photocatalytic reactivity. Sakata et al. examined the effects of Na<sup>+</sup> and found that 2 atomic% Na added to SrTiO<sub>3</sub> has the most favorable reactivity.<sup>12</sup> Zhao et al. observed a volcano-like dependence on Al concentration on the hydrogen production

rate for Al-doped SrTiO<sub>3</sub> prepared with a hydrothermal approach.<sup>13</sup> Hideki et al. have studied NiO loaded NaTaO<sub>3</sub> with a La doping concentration from 0% to 10% and found that 2% La-doped sample shows the highest reactivity for water splitting.<sup>14</sup> The photocatalytic hydrogen production rates of Ba-doped La<sub>2</sub>Ti<sub>2</sub>O<sub>7</sub> also depend on doping concentration, and the highest reactivity is reached when 8% Ba is added.<sup>15</sup> As for Zn-doped Ga<sub>2</sub>O<sub>3</sub>, 1 mol% has been determined to be the optimal doping concentration for water splitting.<sup>7</sup> All the studies here demonstrate that the photo reactivity would first increase with dopant concentration, reach a maximum at an optimal concentration, and decrease at higher concentration. One motivation of this study is to understand the universal physical interpretation of the optimal doping concentration from the perspective of defect chemistry.

In this work, we studied the photocatalytic water splitting reactivities of acceptor doped SrTiO<sub>3</sub>, a well-known material whose defect chemistry has been thoroughly studied in past decades.<sup>16</sup> Al<sup>3+</sup> has been determined to be a suitable dopant to improve the photocatalytic performance of SrTiO<sub>3</sub>, and numerous works have been reported on it.<sup>17-20</sup> In this study, we investigated the effect of Al<sup>3+</sup> along with Mg<sup>2+</sup> and Ga<sup>3+</sup>, as all of them would occupy Ti<sup>4+</sup> sites and serve as acceptor dopants. The catalysts were prepared with a hydrothermal approach, followed by a molten SrCl<sub>2</sub> flux treatment, and the hydrogen production rates were measured with a parallelized and automated photochemical reactor (PAPCR) either in pure water or in aqueous methanol solution. It is found that the three dopants contribute to the reactivity, and the doping effect strongly depends on dopant concentration and crucible materials. Brouwer diagrams were obtained by simulating the concentrations of point defects as a function of oxygen partial pressure. It is suggested that the introduction of Al<sup>3+</sup>, Mg<sup>2+</sup>, and Ga<sup>3+</sup> could reduce the free electron concentration and lower the Fermi level, and the optimal reactivity is close to a situation where the oxygen vacancy donors are fully compensated by acceptors.

## 8.2 Experimental Methods

SrTiO<sub>3</sub> particles were prepared in a hydrothermal method modified from Dong et al.<sup>21</sup> 0.2 ml of pure TiCl<sub>4</sub> (Sigma-Aldrich, 99%) was dropped into a solution in an ice bath containing 25 ml of DI water and ethylene glycol (Alfa Aesar, 99+%) as surfactant. The choice of the surfactant is based on our previous work showing that it yields a suitable crystal shape for charge separation.<sup>22</sup>

After magnetic stirring for 5 min, 10 ml of 0.265 M SrCl<sub>2</sub> solution containing 0.42 g SrCl<sub>2</sub> (Sigma-Aldrich, 99.99%) and 30 ml of 3 M LiOH solution containing 2.16 g LiOH (Sigma-Aldrich, 98%) was added. Specific amounts of AlCl<sub>3</sub>·6H<sub>2</sub>O (Fisher Scientific, 99%), MgCl<sub>2</sub> (Sigma-Aldrich, anhydrous, ≥98%) or GaCl<sub>3</sub> (Alfa Aesar, ultra-dry, 99.999%) was added along with SrCl<sub>2</sub> to yield a concentration of 1%, 2%, 3%, 5%, and 10%. After stirring for another 30 min, the resulting solution was transferred to a 100 ml Teflon-lined hydrothermal autoclave (Techinstro). The autoclave was then heated at 180 °C for 36 h in a furnace. After annealing, the solution was removed and the resulting precipitate was centrifugated four times at 4000 rpm for 12 min with deionized water and ethanol, respectively. Finally, the resulting precipitate was dried in an oven at 80 °C overnight. To conduct the SrCl<sub>2</sub> flux treatment, 0.3 g of as prepared doped SrTiO<sub>3</sub> powders were mixed with SrCl<sub>2</sub> (Alfa Aesar, 99.5%) in a ratio of 1:10 and annealed at 1150 °C in air for 10 h in an alumina crucible (Sigma-Aldrich, Coors™ high-alumina, 50 ml), a platinum crucible (Sigma-Aldrich, 30 ml), or a magnesia crucible (MSE Supplies, 30 ml). The resulting mixture was centrifugated at 4000 rpm for 18 min, four times with deionized water and then four times with ethanol, and finally dried in an oven overnight. The catalysts in this work will be denoted as “Dopant-Dopant addition-s-Crucible materials”. For example, Al3-sP represents Al-doped samples with a 3% Al added that have been heated in the SrCl<sub>2</sub> flux in a platinum crucible.

RhCrO<sub>x</sub> cocatalysts were deposited (0.1 wt% Rh and 0.1 wt% Cr) on all samples with an impregnation method described elsewhere.<sup>23</sup> 50 mg of as prepared powdered samples were dispersed into 0.5 ml of deionized water containing appropriate amounts of Na<sub>3</sub>RhCl<sub>6</sub> (Sigma-Aldrich) and Cr(NO<sub>3</sub>)<sub>3</sub>·6H<sub>2</sub>O (Sigma-Aldrich, 99%) to yield 0.1 wt% Rh and Cr. The suspension was evaporated in a boiling water bath under constant manually stirring. The resulting powders were collected and heated at 350 °C for 1 h.

Scanning Electron Microscopy (SEM) images were obtained to determine the morphologies of all samples using a FEI Quanta 600 with a 30 kV accelerating beam and a spot size of 3. An Oxford full analytical XMAX 80mm SDD EDX detector was equipped on the SEM for chemical composition analysis (EDS). Inductively coupled plasma optical emission spectroscopy (ICP-OES) was carried out at Element Technology to determine the dopant concentration. Photocatalytic hydrogen generation rate was measured with a high-throughput method using a Paralyzed and Automated Photochemical Reactor (PAPCR).<sup>22,24,25</sup> In a typical measurement, 10

mg of as prepared powders were added into a 1 ml glass vial together with 0.4 ml pH 7 DI water or 10% methanol solution with unadjusted pH. The illumination was provided by two high power 380 nm UV LED chips (Chanzon). Brouwer diagrams of Al-doped SrTiO<sub>3</sub> were plotted by simulating the concentration of the point defects using a python script modified from a code on co-doping BaTiO<sub>3</sub> developed Ryu et al.<sup>26,27</sup> The code employs NumPy and SciPy packages on solving the electroneutrality condition equation as a function of oxygen partial pressure. The mass-action-law parameters were taken from Yoo et al.<sup>28</sup>

### 8.3 Results

A SEM image of undoped SrTiO<sub>3</sub> prepared via a hydrothermal method is given in Figure 8-1. Particles exhibit (100) and (110) facets at a suitable ratio that promotes charge separation and a diameter around 500 nm. However, the photocatalytic reactivity of these undoped particles are low and we cannot detect the hydrogen production from these powders with the PAPCR, consistent with previous work.<sup>22</sup> The particles were then heated in the molten SrCl<sub>2</sub> flux in an alumina crucible, a platinum crucible, or a magnesia crucible, denoted as Undoped-sA, Undoped-sP and Undoped-sM. SEM images of the flux treated particles are given in Figure 8-1, and particles that have been flux treated in different crucibles have different morphologies. For particles flux treated in an alumina crucible, they basically retain the original shape. But, the (110) facets became rougher, and the particle edges are less defined. For particles flux treated in a platinum crucible, they grew much larger to several microns. It seems that the large flat (110) no longer exist, and the particles exhibit stacks of (100) layers growing off (100) facets of a central cube. Based on the results in Chapter 7, these crystals (-sP) likely undergo a dissolution-recrystallization process. For particles flux-treated in a magnesia crucible, they adopt shapes like an intermediate between the last two discussed, where the (110) facets compose of large evenly spaced straight steps along <100> direction.

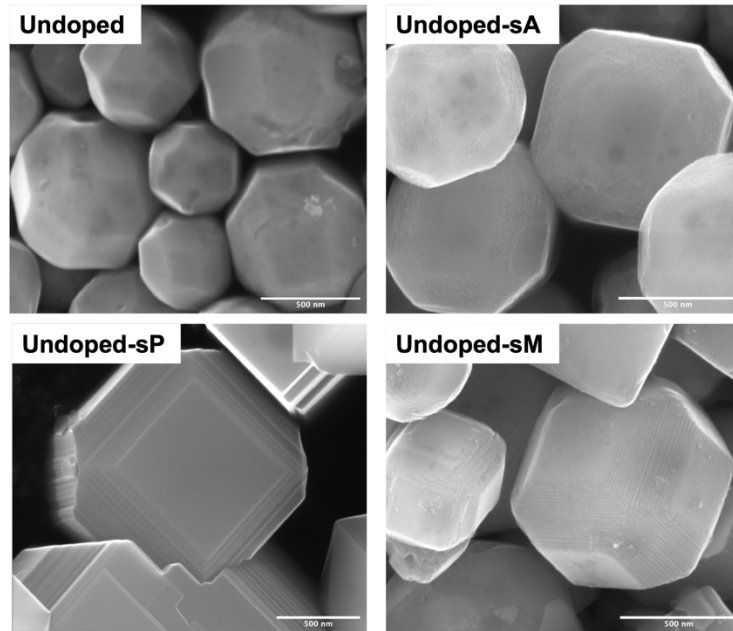


**Figure 8-1:** SEM images of hydrothermally synthesized pure SrTiO<sub>3</sub> particles, denoted as “undoped”. The particles were then treated in a molten SrCl<sub>2</sub> flux in an alumina crucible, a platinum crucible, and a magnesia crucible, denoted as “undoped-sA”, “undoped-sP” and “undoped-sM”. Scale bars represent 500 nm.

Al-doped SrTiO<sub>3</sub> were prepared by introducing specific amounts of AlCl<sub>3</sub> along with the hydrothermal synthesis precursors to yield particles with 1% Al, 2% Al, 3% Al, 5% Al and 10% Al added, denoted as Al1, Al2, Al3, Al5 and Al10, respectively. Although, this does not actually mean that such an amount of Al<sup>3+</sup> was doped into the crystals; the actual doping concentration should increase with the dopant addition until the solubility limit is reached. Next, the crystals were treated in the molten SrCl<sub>2</sub> in an alumina crucible, a platinum crucible, or a magnesia crucible, denoted as -sA, -sP and -sM, and the SEM images of the resulting particles are given in Figure 8-2. The particle morphologies are generally consistent with those in Figure 8-1. SrCl<sub>2</sub> flux treatment in a platinum crucible yields larger particles and a layered feature on the surface. Particles that have been flux treated in an alumina crucible basically keep the original shape. While for those that were flux treated in a magnesia crucible, they are relatively irregular exposing stepped (110) facets. The amount of Al added seems to have little influence on the final shape.

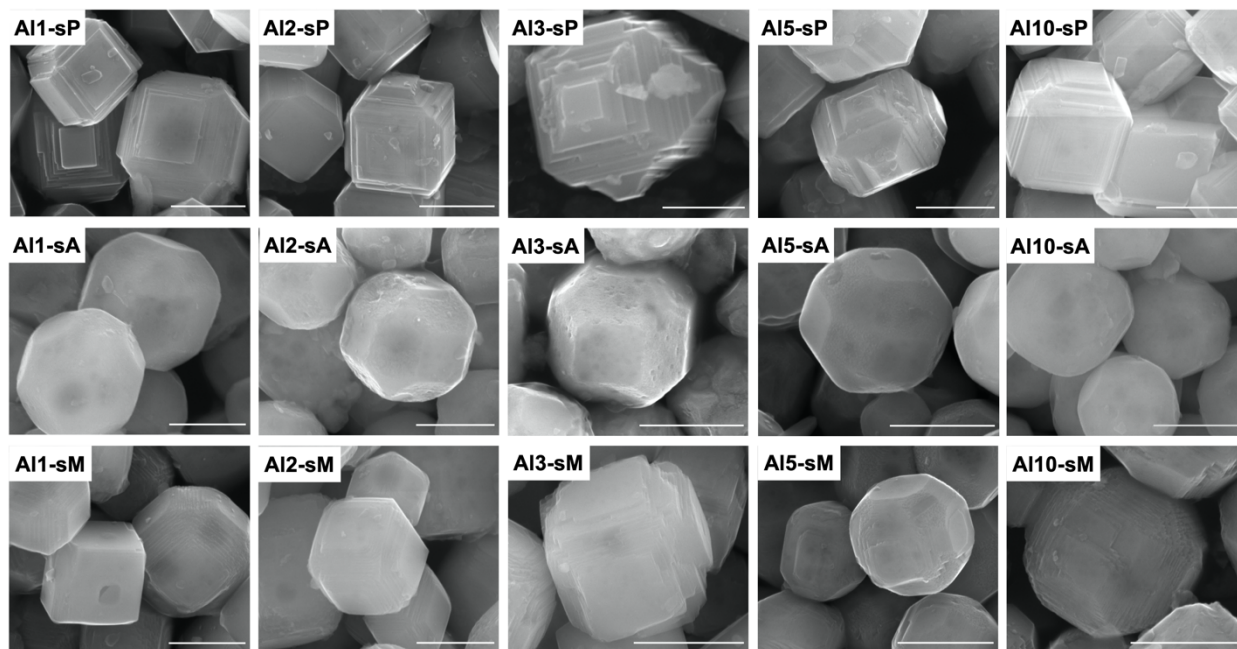


**Figure 8-2:** SEM images of Al-doped particles that have been treated in the  $\text{SrCl}_2$  flux in a platinum crucible (-sP), an alumina crucible (-sA) and a magnesia crucible (-sM). The numbers represent Al dopant additions. The scale bar represents 500 nm.

Photocatalytic hydrogen production rates of the 15  $\text{SrCl}_2$  flux treated Al-doped  $\text{SrTiO}_3$  crystals were measured using the PAPCR in pH 7 deionized water or 10% methanol solution with an unadjusted pH. The maximum production rates were plotted in Figure 8-3 as a function of Al dopant addition (not the actual doping concentration). Particles that have been flux treated in an alumina crucible are much more reactive than those treated in a magnesia crucible or a platinum crucible. However, it seems that the Al addition has a relatively weak effect on the reactivity if the flux treatment was carried out in an alumina crucible. Flux treatment in a platinum crucible yield the lowest reactivity, and we cannot detect the hydrogen production using the PAPCR until 10%  $\text{Al}^{3+}$  was introduced into the precursors. Flux treatment in a magnesia crucible gives the intermediate reactivity, and the reactivity generally increases with the  $\text{Al}^{3+}$  addition. Adding methanol as hole scavenger will contribute to the reactivity for all samples, consistent with previous reports.<sup>29</sup> Recall that the  $\text{SrCl}_2$  flux might dissolve  $\text{Al}^{3+}$  from the alumina crucible, as we have discussed in Chapter 7, and this explains that why the reactivity is almost the same even if  $\text{AlCl}_3$  was not added to the precursors.

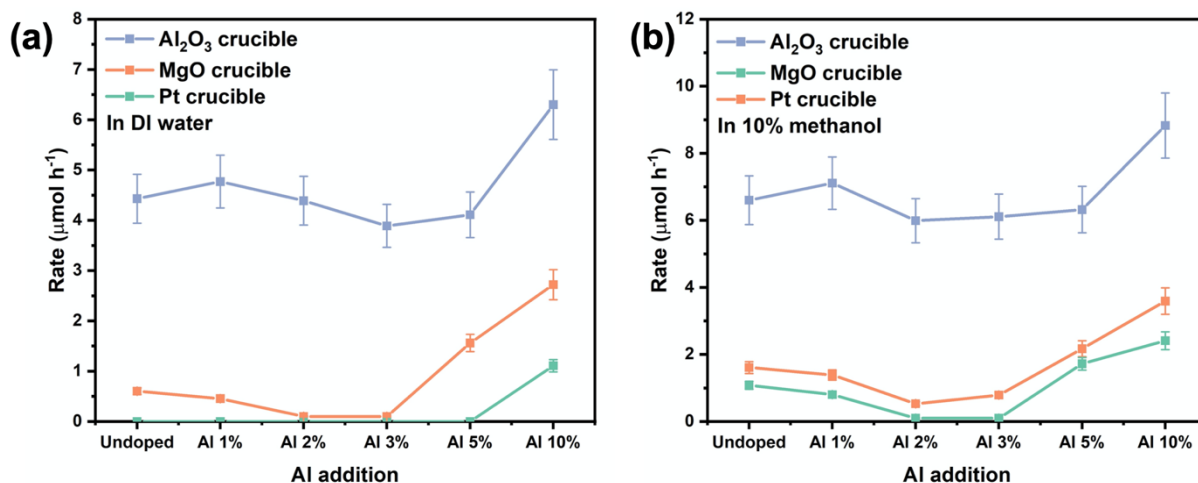


**Figure 8-3:** Photocatalytic maximum hydrogen production rates of Al-doped SrTiO<sub>3</sub> crystals in (a) pH 7 DI water and (b) 10% methanol as a function of Al addition. The crystals have been treated in the molten SrCl<sub>2</sub> flux in an alumina crucible, a magnesia crucible, or a platinum crucible. The bars represent standard deviations.

Mg-doped and Ga-doped SrTiO<sub>3</sub> were prepared by mixing specific amount of MgCl<sub>2</sub> or GaCl<sub>3</sub> into the precursors of the hydrothermal synthesis. Again, the dopant additions were controlled to be 1%, 2%, 3%, 5% and 10%. SEM images of the 15 Mg-doped SrTiO<sub>3</sub> images are shown in Figure 8-4 and the particle morphologies are slightly different from the Al-doped crystals. For example, Mg-doped samples flux treated in a platinum crucible have a layer-stacking feature, but we can still identify hexagonal (110) facets in Mg1-sP and Mg2-sP. Besides, for crystals that have undergone a SrCl<sub>2</sub> flux treatment in a magnesia crucible, the (110) facets in Mg-doped samples have fewer steps compared with Al-doped samples. Again, flux treatment in an alumina crucible maintain the original morphology. Photocatalytic hydrogen production rates of the 15 Mg-doped SrTiO<sub>3</sub> were measured and shown in Figure 8-5, and they are more reactive in general, than their Al-doped counterparts (see Fig 8-3). When the flux treatment was carried out in an alumina crucible, Mg-doped samples basically produce hydrogen at a similar level as Al-doped samples. However, when the flux treatment was carried out in a magnesia crucible and platinum crucible, Mg-doped samples are much more reactive than Al-doped samples flux-treated in those crucibles (though these are still less reactive than samples flux treated in alumina crucibles). Furthermore, a volcano-like trend is observed that the reactivity increases with the Mg<sup>2+</sup> addition, reaching a maximum at 3%, and then decreases at higher Mg<sup>2+</sup> additions when using Pt or MgO crucibles. This is true in both pure water and 10% methanol solutions.

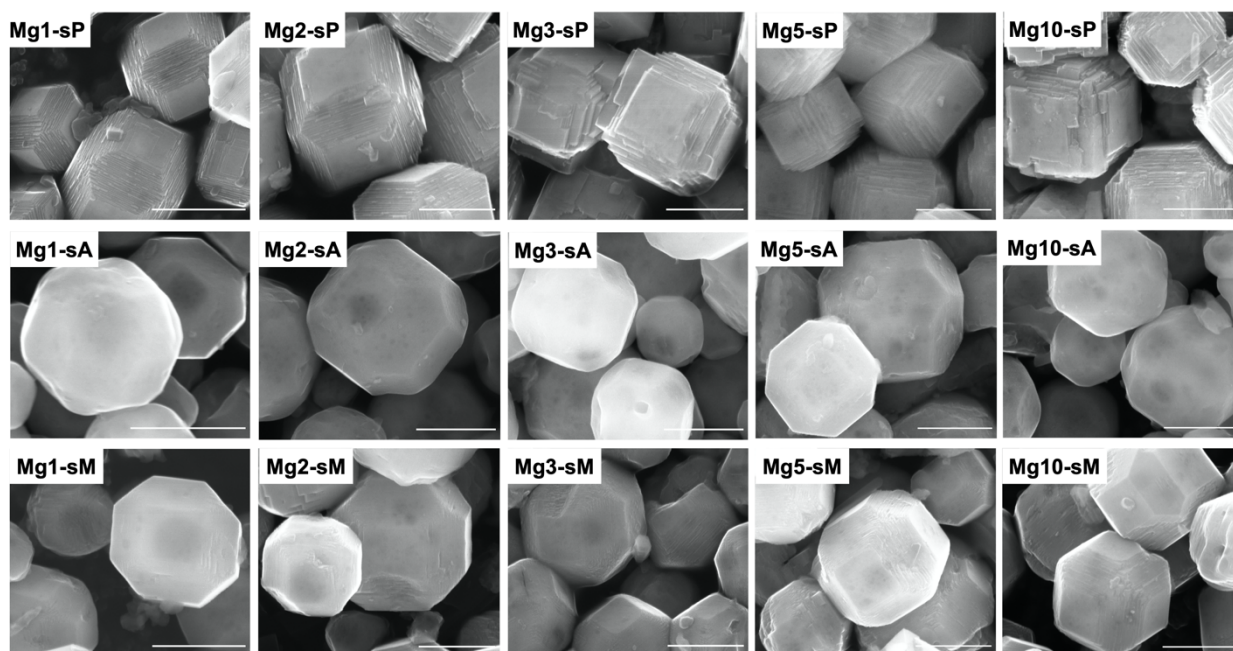


**Figure 8-4:** SEM images of Mg-doped particles that have been treated in the  $\text{SrCl}_2$  flux in a platinum crucible (-sP), an alumina crucible (-sA) and a magnesia crucible (-sM). The numbers represent Mg dopant additions. The scale bar represents 500 nm.

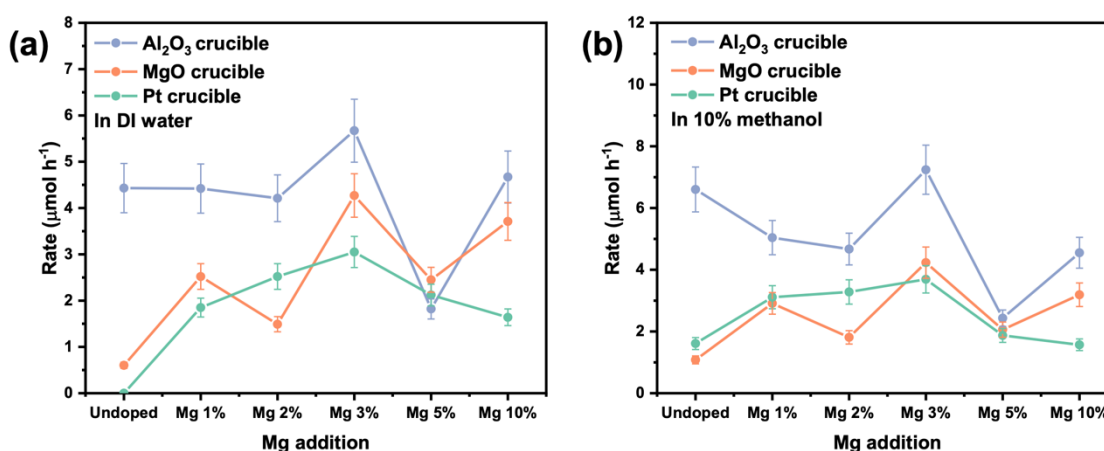


**Figure 8-5:** Photocatalytic maximum hydrogen production rates of Mg-doped  $\text{SrTiO}_3$  crystals in (a) pH 7 DI water and (b) 10% methanol as a function of Mg addition. The crystals have been treated in the molten  $\text{SrCl}_2$  flux in an alumina crucible, a magnesia crucible, or a platinum crucible. The bars represent standard deviations.

SEM images of the 15 flux treated Ga-doped  $\text{SrTiO}_3$  crystals are given in Figure 8-6. Their morphologies are basically the same as Al-doped samples, depending on the type of crucibles for the flux treatment. The photocatalytic hydrogen production rates are plotted in Figure 8-7 as a

function of Ga addition. Consistent with the results in Fig. 8-3 and Fig. 8-5, samples heated in an alumina crucible will give the best reactivity. Unfortunately, the hydrogen productions are very low for Ga-doped samples flux treated in either a platinum crucible or a magnesia crucible. The influence of the doping concentration of  $\text{Ga}^{3+}$  is not obvious in this experiment.

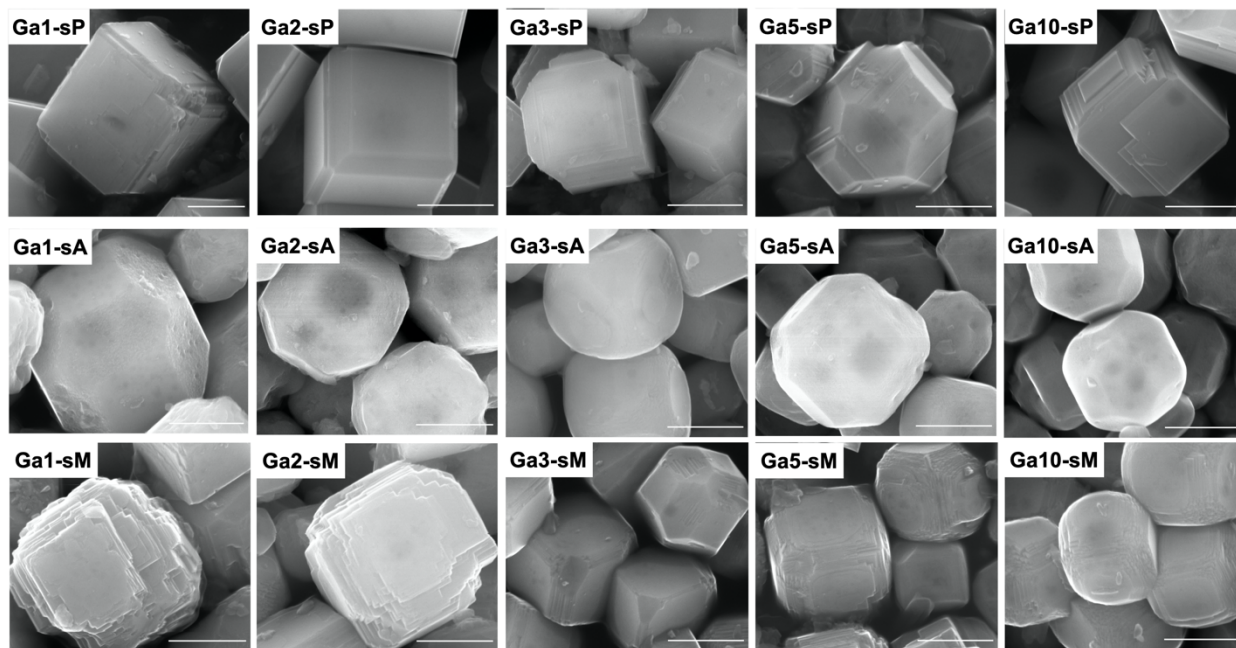


**Figure 8-6:** SEM images of Ga-doped particles that have been treated in the  $\text{SrCl}_2$  flux in a platinum crucible (-sP), an alumina crucible (-sA) and a magnesia crucible (-sM). The numbers represent Ga dopant additions. The scale bar represents 500 nm.

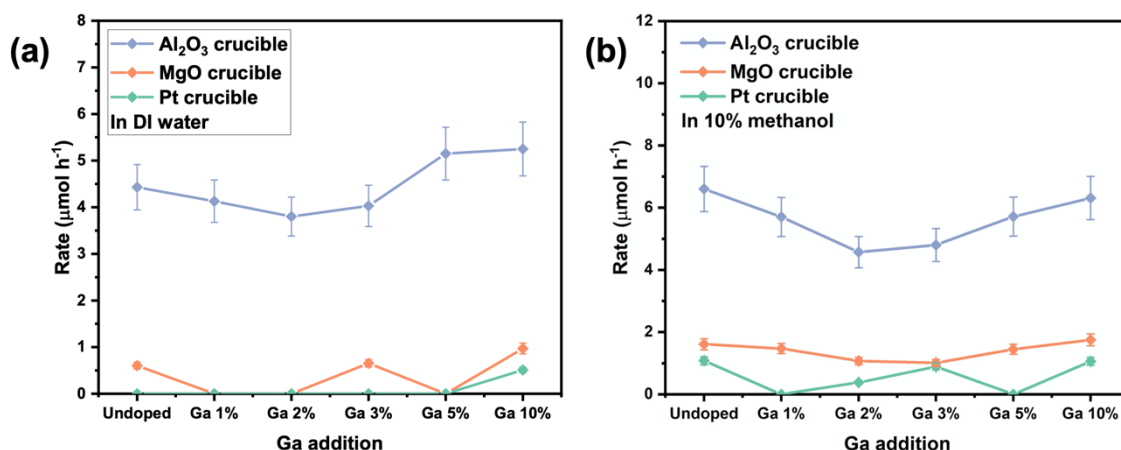


**Figure 8-7:** Photocatalytic maximum hydrogen production rates of Ga-doped SrTiO<sub>3</sub> crystals in (a) pH 7 DI water and (b) 10% methanol as a function of Ga addition. The crystals have been treated in the molten SrCl<sub>2</sub> flux in an alumina crucible, a magnesia crucible, or a platinum crucible. The bars represent standard deviations.

Recall that the numbers describe the amount of dopant added into the precursors. To investigate the actual doping concentration, ICP-OES analysis has been carried out on selected samples. A total of five samples were measured and the corresponding doping concentrations were given in Table 8-1. Al1, Mg1, Mg3 and Ga3 represents hydrothermal doped crystals without the SrCl<sub>2</sub> treatment. The letters represent the type of dopant added, and the number represent the dopant additions: 1%, 1%, 3% and 3%. Undoped-sA corresponds to hydrothermal particles without any dopants introduced that have been treated in the molten SrCl<sub>2</sub> flux in an alumina crucible.

**Table 8-1:** Molar ratios determined by ICP-OES of selected SrTiO<sub>3</sub> crystals.

Sample	M% / (M% + Ti%)
Al1	0.044%
Mg1	0.24%
Mg3	1.01%
Ga3	0.36%
Undoped-sA	2.58%

The dopant concentration of the rest of the samples were estimated with the number in Table 8-1, assuming that the dopant concentration is proportional to dopant addition, and given in Table 8-2:

**Table 8-2:** Molar ratios of the 15 hydrothermally doped SrTiO<sub>3</sub> crystals estimated from the data in Table 8-1. These crystals were not treated in the SrCl<sub>2</sub> flux.

Sample	$\frac{\text{Al}\%}{\text{Al}\% + \text{Ti}\%}$	Sample	$\frac{\text{Mg}\%}{\text{Mg}\% + \text{Ti}\%}$	Sample	$\frac{\text{Ga}\%}{\text{Ga}\% + \text{Ti}\%}$
A11	0.044%	Mg1	0.24%	Ga1	0.12%
A12	0.088%	Mg2	0.63%	Ga2	0.24%
A13	0.13%	Mg3	1.01%	Ga3	0.36%
A15	0.22%	Mg5	1.49%	Ga5	0.60%
A110	0.44%	Mg10	2.98%	Ga10	1.2%

A plausible assumption is that the platinum crucible won't introduce impurities into the samples, therefore we employ the numbers in Table 8-2 as the doping concentration for those samples that have been SrCl<sub>2</sub> flux treated in a platinum crucible (-sP). Their photocatalytic hydrogen production rates were plotted in Figure 8-8 as a function of doping concentrations. The data for undoped-sA, pure SrTiO<sub>3</sub> particles that were flux treated in an alumina crucible, was added to the figure as a hollow square. In this way, it is easier to compare the influence of the dopant elements and doping concentration. If the SrCl<sub>2</sub> flux treatment is carried out in a platinum crucible, Mg<sup>2+</sup> is definitely the best dopant, and Ga<sup>3+</sup> is the worst one. Another important finding is that the three dopants have different optimal doping concentration. As for Al-doped samples, the hydrogen production rate will increase with the doping concentration and the maximum reactivity is achieved at a number greater than 2.5%. However, as for Mg-doped samples, the optimal reactivity is observed at 1%, much lower than Al-doped ones. For Ga-doped samples, it is found that the reactivity increases with doping concentration, but we cannot confirm its optimal concentration using the data here. Note that, we assume concentration is constant before and after the flux treatment in a platinum crucible. But the dopants might dilute or concentrate owing to the dissolution/precipitation in the melt or the change of oxygen vacancies.

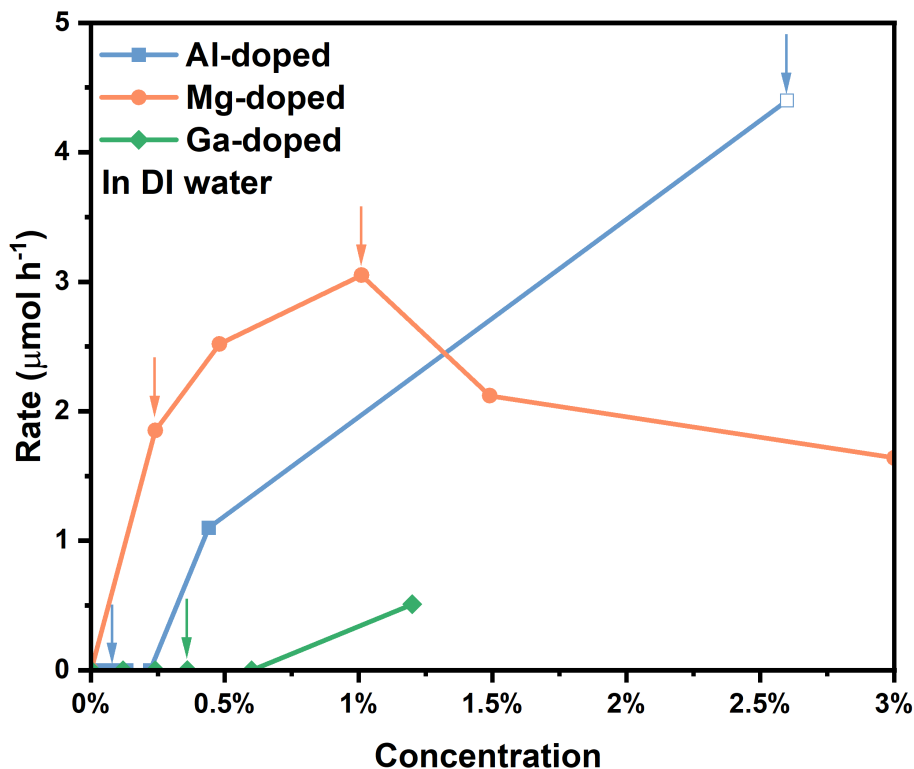


**Figure 8-8:** Photocatalytic maximum hydrogen production rates in DI water of Al-doped, Mg-doped, and Ga-doped SrTiO<sub>3</sub> crystals as a function of doping concentration. The undoped samples flux treated in an alumina crucible is plotted as an empty square. The rest of the samples were flux treated in a platinum crucible. The measured points are labeled with arrows.

## 8.4 Discussion

The experiments in this chapter were inspired by the idea that doping acceptor cations into SrTiO<sub>3</sub> could compensate oxygen vacancy donors and contribute to photocatalytic reactivity. Al<sup>3+</sup> is known to be an efficient dopant for SrTiO<sub>3</sub> since it can reduce the formation of Ti<sup>3+</sup> recombination centers,<sup>19</sup> an important issue limiting the reactivity.<sup>30</sup> Here, Mg<sup>2+</sup> and Ga<sup>3+</sup> are studied along with Al<sup>3+</sup> and they all occupy Ti sites. Mg<sup>2+</sup> has a similar ionic radius as Al<sup>3+</sup>, and Ga<sup>3+</sup> has the same valence state as Al<sup>3+</sup>. In this section, we discuss the doping effect from the perspective of defect chemistry.

SrTiO<sub>3</sub> is generally agreed to be a n-type semiconductor because of intrinsic oxygen vacancies.<sup>16,31</sup> There might be background acceptor impurities from the source materials, such as monovalent

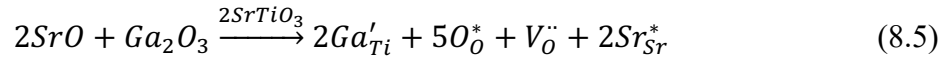
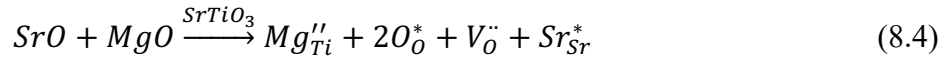
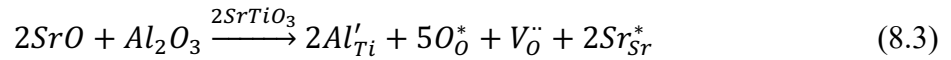
alkali ions (Na(I) and K(I)) on the A-site and trivalent metals (Fe(III) and Al(III)) on the B-site. Since the oxygen vacancy concentration is much higher than the background impurities, especially in this experiment that we employed high purity precursors in the hydrothermal synthesis, the material is overall n-type. The formation of oxygen vacancies can be expressed as:



The free electron is trapped by a  $Ti^{4+}$  site near an oxygen vacancy forming a  $Ti^{3+}$  recombination center:



The defect reactions of Al, Mg, and Ga doped  $SrTiO_3$  can be written assuming ionic compensation as:<sup>6,28,32</sup>



Their ionization reactions can be written as (note that they won't have to be fully ionized and the equilibrium constant varies with dopant):

$$\emptyset(e_{vb}^* + h_{cb}^*) = e_{vb}' + h_{cb} \quad (8.6)$$

$$Al_{Ti}^* = Al_{Ti}' + h \quad (8.7)$$

$$Mg_{Ti}^* = Mg_{Ti}'' + 2h \quad (8.8)$$

$$Ga_{Ti}^* = Ga_{Ti}' + h \quad (8.9)$$

Here, we could see that each Mg acceptor dopant ( $Mg_{Ti}''$ ) can provide two positive charges, while each Al or Ga dopant can only provide one positive charge. This implies the fully compensated point, a doping concentration makes  $n = p$ , should be different for  $Mg^{2+}$  and  $Al^{3+}$  ( $Ga^{3+}$ ). For Mg-

doped SrTiO<sub>3</sub>, it should go to the compensation point at a lower doping concentration compared with Al and Ga. The electroneutrality condition equations can then be written as:

$$n + [Al'_{Ti}] + [Ti'_{Ti}] = p + 2[V_{O}^{\bullet\bullet}] \quad (8.10)$$

$$n + 2[Mg''_{Ti}] + [Ti'_{Ti}] = p + 2[V_{O}^{\bullet\bullet}] \quad (8.11)$$

$$n + [Ga'_{Ti}] + [Ti'_{Ti}] = p + 2[V_{O}^{\bullet\bullet}] \quad (8.12)$$

Note the Schottky reaction is significant in SrTiO<sub>3</sub> when  $T > 1500$  °C.<sup>33</sup> Since the SrCl<sub>2</sub> flux treatment is carried out at 1150 °C, the concentration of strontium vacancies should be negligibly small, thus we did not consider it here. We also ignore eq. 8.2 here as the equilibrium constant has not been reported yet. But the concentration of  $Ti'_{Ti}$  traps should be proportional to the free electron concentration and the oxygen vacancy concentration (based on 8.2). To solve the electroneutrality condition equation, the concentrations of the point defects have been calculated for Al-doped SrTiO<sub>3</sub> using the mass-action-law parameters measured by Yoo et al.<sup>28</sup>

$$\emptyset = e' + h \quad K_i/cm^{-6} = np = 6.01 \times 10^{41} \exp(-2.12 eV/kT) \quad (8.13)$$

$$V_{O}^{\bullet\bullet} + \frac{1}{2}O_2 = O_O^* + 2h \quad K_O/cm^{-3} = p^2/[V_{O}^{\bullet\bullet}]p_{O_2}^{1/2} = 6.57 \times 10^{23} \exp(-2.23 eV/kT) \quad (8.14)$$

$$Al_{Ti}^* = Al'_{Ti} + h \quad K_{Al}/cm^{-3} = [Al'_{Ti}]p/[Al_{Ti}^*] = 2.71 \times 10^{25} \exp(-1.35 eV/kT) \quad (8.15)$$

Brouwer diagrams of undoped SrTiO<sub>3</sub> at 1150 °C and 100 °C have been plotted in Figure 8-9 (a) and (b) as a function of oxygen partial pressure. The high temperature plots describe the situation in the molten SrCl<sub>2</sub> flux and the low temperature plots are close to the materials in the reactor. When oxygen partial pressure is set to 0.21 atm, the free electron concentration and hole concentration are on the order of  $10^{17} \text{ cm}^{-3}$  and  $10^{16} \text{ cm}^{-3}$  at 1150 °C. After cooling the materials, the carriers will not be thermally ionized to the same degree. However, the free electron concentration needs to be basically at the same order of oxygen vacancy concentration to keep charge neutral so it remains on the order of  $10^{17} \text{ cm}^{-3}$ , but the hole concentration will drop to the order of  $10^{-5} \text{ cm}^{-3}$ . This will enhance the n-type characteristic of the materials and shift the Fermi level to a more cathodic region.

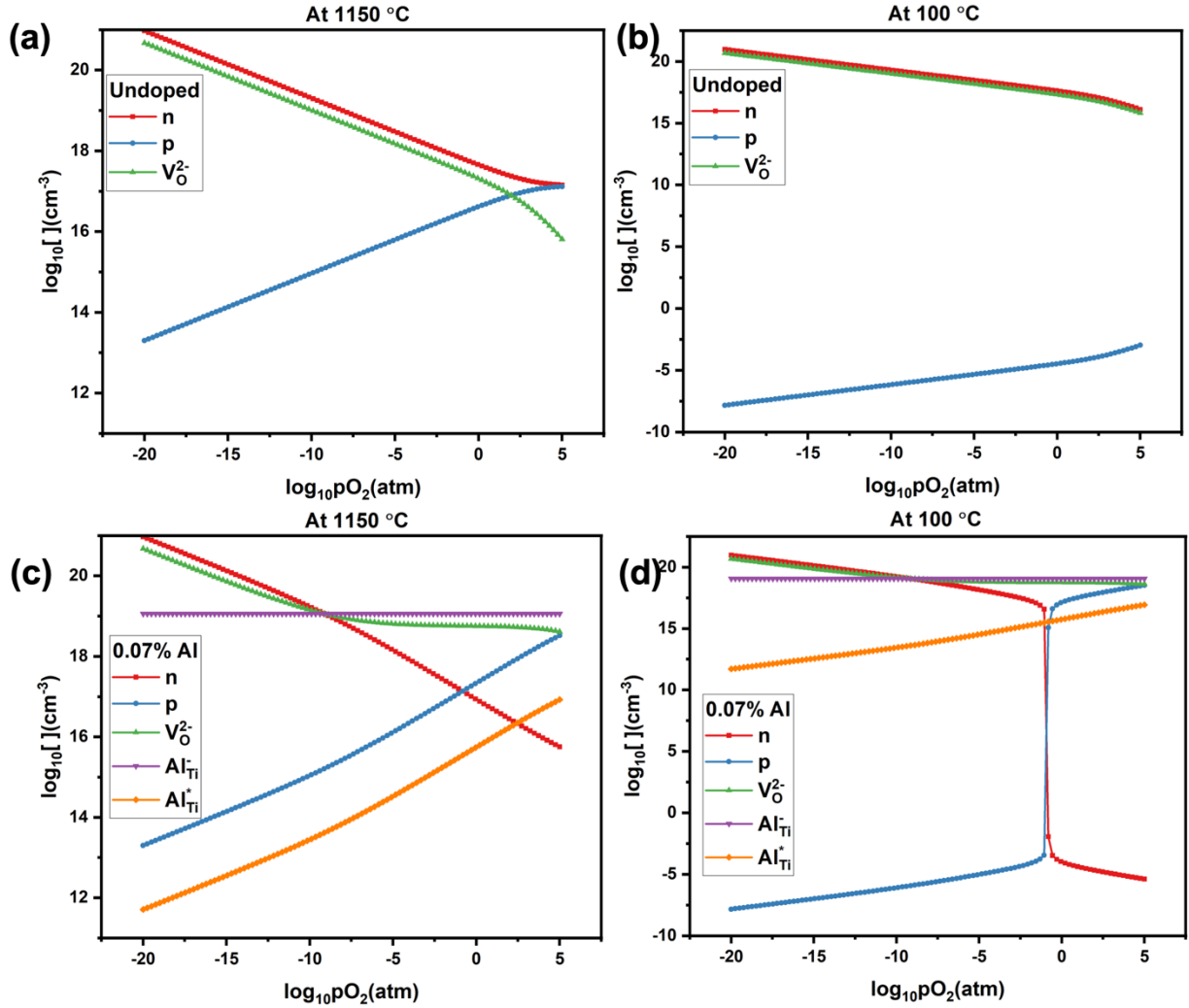


**Figure 8-9:** Brouwer diagrams of undoped SrTiO<sub>3</sub> and 0.07% Al-doped SrTiO<sub>3</sub> at 1150 °C and 100 °C. The calculation employed a python code modified from the code on co-doping BaTiO<sub>3</sub> developed by Ryu et al.<sup>26,27</sup>

Brouwer diagrams of 0.07% Al-doped SrTiO<sub>3</sub> are given in Figure 8-9 (c) and (d), a doping concentration describing  $[V_O^{\cdot\cdot}] \approx 2[Al_{Ti}']$ . At 0.21 atm, the free electron concentration is very close to the hole concentration, meaning that the semiconductor is close to the fully compensation point. After cooling the materials, at the compensation point, there will be a precipitous drop in electron concentration which has been studied by Waser et al.<sup>34</sup> This will significantly reduce the free electron concentration from the order of  $10^{17} \text{ cm}^{-3}$  to the order of  $10^{13} \text{ cm}^{-3}$ . Note that the Debye length of SrTiO<sub>3</sub> was estimated to be 3.2 nm, assuming a carrier concentration of  $3 \times 10^{19} \text{ cm}^{-3}$ .<sup>35</sup> If the dielectric constant is conserved, the six order of magnitude decrease of the free electron concentration will then increase the length of Debye length and the space charge length

roughly 1000 times. The light penetration length is roughly 10  $\mu\text{m}$  at 380 nm illumination, assuming the absorption coefficient is on the order of  $100\text{ cm}^{-1}$ .<sup>36</sup> Therefore, more photogenerated charge carriers will now be generated in the space charge layer instead of the flat band region and they can be separated by the electric field induced by band bending and migrate to the surface to participate in reactions.<sup>37–39</sup> This will lead to a reduced charge recombination and much longer charge carrier lifetime, increasing the photocatalytic reactivity. On the other hand, adding excessive dopants lowers the Fermi level and the potential difference between the semiconductor and the solution, therefore reduces the degree of band bending, the benefit of the compensation will be lost. This explains the existence of the optimal acceptor doping concentrations for photocatalytic reactions.<sup>13,17,22</sup> However, the mass action law parameters of Mg-doped and Ga-doped SrTiO<sub>3</sub> have not yet been reported quantitatively so that we cannot provide their Brouwer diagrams. Based on the ionization reactions (see equation 8.7), each Mg dopant can provide two positive charges, suggesting that it can compensate the oxygen vacancies more efficiently. From the data in Figure 8-8, the optimal concentration for Mg-doped samples is roughly 0.5 times of the Al-doped samples, consistent with this model. A possible reason for the poor reactivity of Ga-doped samples is that the mass law action parameter of eq.8.9 is lower than eq.8.7. A schematic illustration of our defect compensation model is presented in Figure 8-10.

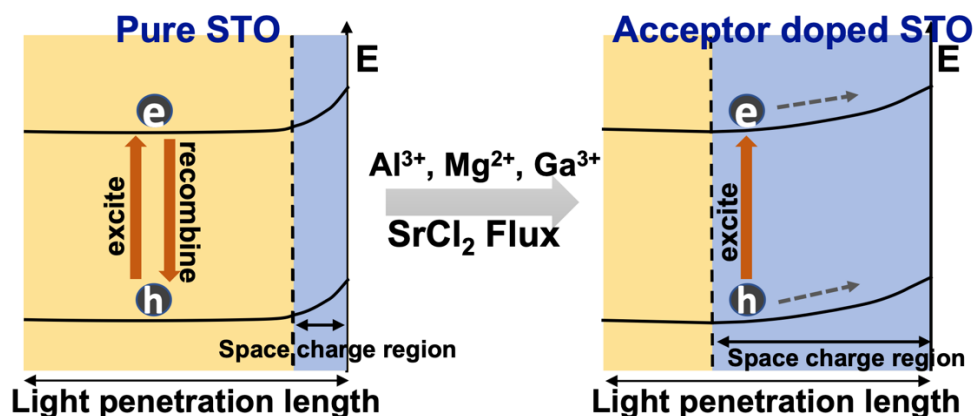


**Figure 8-10:** Schematic illustration of how the incorporation of  $\text{Al}^{3+}$ ,  $\text{Mg}^{2+}$  and  $\text{Ga}^{3+}$  influences the space charge of SrTiO<sub>3</sub>.

There are a couple of studies supporting our model from different perspectives. Zhao et al. studied the electronic structure of Al-doped SrTiO<sub>3</sub> using XPS and DFT and found that the incorporation of  $\text{Al}^{3+}$  might lower the Fermi level and make the material less n-type,<sup>19</sup> which is consistent with

our calculation of the decrease of the free electron concentration. Their simulation also shows the sensitivity of the Al locations, if two Al ions sit next to the oxygen vacancy, the band gap of the material will resemble pure SrTiO<sub>3</sub>, a situation close to the fully compensated (semi-insulated) material. Besides, the decrease of free electron concentration as well as the formation of  $[Al'_{Ti} - V_{\ddot{O}} - Al'_{Ti}]$  will reduce the formation of Ti<sup>3+</sup> traps that can be understood by equation 8.2. Cheng and Long studied Al-doped and Na-doped SrTiO<sub>3</sub> using nonadiabatic molecular dynamics, indicating that when two Ti<sup>4+</sup> ions or two Sr<sup>2+</sup> ions are equally replaced by Al<sup>3+</sup> or Na<sup>+</sup> ions, the in-gap trap state created by oxygen vacancies can be eliminated and the charge carrier lifetime increases significantly.<sup>40</sup> Han et al. have studied solid state prepared Mg-doped SrTiO<sub>3</sub>, suggesting that the incorporation of Mg<sup>2+</sup> would expand the depletion layer and improve the photocatalytic reactivity.<sup>41</sup> Similar results have also been reported on other materials. For example, in n-type Si doped with In, as the concentration of deep acceptor levels increases in a narrow range close to the concentration of shallow donors, the electron and hole lifetimes and the photoconductivity increase by several orders of magnitude.<sup>42</sup>

One issue that needs to be addressed is that the optimal Al concentration measured from the experiment is obviously higher than the calculated compensation point. We believe this distinction is ascribed to the fact that the calculation is based on mass action parameters in air rather than the SrCl<sub>2</sub> flux. Based on the experiments in Chapter 6, Chapter 7, and Chapter 8, the SrCl<sub>2</sub> flux treatment will lead to a different material, and the type of crucible also has a significant influence on this. One possible explanation is that the oxygen pressure is much lower in the SrCl<sub>2</sub> melt, requiring more acceptor dopants to compensate the material. This is supported by the fact that a SrTiO<sub>3</sub> single crystal substrate turned black after heating in the SrCl<sub>2</sub> flux in a platinum crucible.

$$n + 2[V''_{Sr}] + [Al'_{Ti}] + [Ti'_{Ti}] = p + 2[V_{\ddot{O}}] + ([Cl_{\ddot{O}}]) \quad (8.16)$$

Another explanation is that the defect reactions are more complex in the flux compared with air. A more completed electroneutrality condition equation can be written as equation 8.16. Note that we ignored the existence of strontium vacancies in the simulation based on the Schottky reaction parameters.<sup>33</sup> It should be noted that the melt is a Sr-rich environment that can further inhibit the formation of strontium vacancies. And the donor concentration could be higher than our expectation. In particular, the oxygen vacancy concentration could be higher because the melt could be a very reducing experiment. From the CLSM result in Chapter 7, the SrCl<sub>2</sub> melt is likely

to extract oxygen atoms from SrTiO<sub>3</sub> to form SrO, and this might induce a high oxygen vacancy concentration. This is also related to the previous argument on the depleted oxygen environment because the oxygen vacancy concentration is inversely proportional to oxygen partial pressure, as shown in Figure 8-9. It is also likely that other donors exist in the system, such as Cl<sub>O</sub><sup>•</sup>, assuming that chlorine ions from the flux diffuse into the crystal driven by the large concentration gradient and occupy oxygen sites. All the factors described here will contribute to the free electron concentration and the n-type characteristic of SrTiO<sub>3</sub>, implying that a higher acceptor concentration is needed to compensate the donors.

## 8.5 Conclusion

The influences of Al<sup>3+</sup>, Mg<sup>3+</sup>, and Ga<sup>3+</sup> acceptor dopants on the photocatalytic reactivity of SrTiO<sub>3</sub> have been explored in a hybrid approach. The catalysts were doped via a hydrothermal method and treated in the molten SrCl<sub>2</sub> flux, and the photocatalytic hydrogen production rates were measured with a high-throughput parallelized and automated photochemical reactor (PAPCR). The concentrations of various point defects were simulated by solving the electroneutrality condition equation as a function of oxygen partial pressure. It is found that the three dopants all contribute to the reactivity, and the results depend on the type of crucibles employed in the flux treatment. In an alumina crucible, the three dopants behave similarly; but in a platinum crucible, Mg-doped samples yielded the most hydrogen. It is found that the photocatalytic reactivity is strongly influenced by doping concentration, and the optimal concentration is close to the situation where the oxygen vacancy donors are fully compensated with acceptor dopants, which can be simplified as  $[V_{\text{O}}^{\bullet\bullet}] \approx 2[Al'_{\text{Ti}}]$ ,  $[V_{\text{O}}^{\bullet\bullet}] \approx [Mg''_{\text{Ti}}]$  and  $[V_{\text{O}}^{\bullet\bullet}] \approx 2[Ga'_{\text{Ti}}]$  for the three dopants, respectively. At the compensation point, the space charge layer would expand to the order of 1000 times longer, so that more photogenerated charge carriers can be separated by the field and move to the surface. The reduction of the free electron concentration associated with the formation of  $[Al'_{\text{Ti}} - V_{\text{O}}^{\bullet\bullet} - Al'_{\text{Ti}}]$  would also lower the Fermi level and inhibit the formation of Ti<sup>3+</sup> traps. Our work offers a plausible quantitative explanation to the effect of acceptor dopants on the reactivity of SrTiO<sub>3</sub>, and the principle can be used to design and optimize more oxide photocatalysts.

## 8.6 References

- (1) Kudo, A.; Miseki, Y. Heterogeneous Photocatalyst Materials for Water Splitting. *Chem. Soc. Rev.* **2009**, *38* (1), 253–278. <https://doi.org/10.1039/B800489G>.
- (2) Wang, Q.; Domen, K. Particulate Photocatalysts for Light-Driven Water Splitting: Mechanisms, Challenges, and Design Strategies. *Chem. Rev.* **2020**, *120* (2), 919–985. <https://doi.org/10.1021/acs.chemrev.9b00201>.
- (3) Feng, Y.; Wu, J.; Chi, Q.; Li, W.; Yu, Y.; Fei, W. Defects and Aliovalent Doping Engineering in Electroceramics. *Chem. Rev.* **2020**, *120* (3), 1710–1787. <https://doi.org/10.1021/acs.chemrev.9b00507>.
- (4) Bai, S.; Zhang, N.; Gao, C.; Xiong, Y. Defect Engineering in Photocatalytic Materials. *Nano Energy* **2018**, *53*, 296–336. <https://doi.org/10.1016/j.nanoen.2018.08.058>.
- (5) Liu, J.; Wei, Z.; Shanguan, W. Defects Engineering in Photocatalytic Water Splitting Materials. *ChemCatChem* **2019**, *11* (24), 6177–6189. <https://doi.org/10.1002/cctc.201901579>.
- (6) Takata, T.; Domen, K. Defect Engineering of Photocatalysts by Doping of Aliovalent Metal Cations for Efficient Water Splitting. *J. Phys. Chem. C* **2009**, *113* (45), 19386–19388. <https://doi.org/10.1021/jp908621e>.
- (7) Sakata, Y.; Matsuda, Y.; Yanagida, T.; Hirata, K.; Imamura, H.; Teramura, K. Effect of Metal Ion Addition in a Ni Supported Ga<sub>2</sub>O<sub>3</sub> Photocatalyst on the Photocatalytic Overall Splitting of H<sub>2</sub>O. *Catal. Letters* **2008**, *125* (1), 22–26. <https://doi.org/10.1007/s10562-008-9557-7>.
- (8) Iwase, A.; Saito, K.; Kudo, A. Sensitization of NaMO<sub>3</sub> (M: Nb and Ta) Photocatalysts with Wide Band Gaps to Visible Light by Ir Doping. *Bull. Chem. Soc. Jpn.* **2009**, *82* (4), 514–518. <https://doi.org/10.1246/bcsj.82.514>.
- (9) Kim, H. G.; Becker, O. S.; Jang, J. S.; Ji, S. M.; Borse, P. H.; Lee, J. S. A Generic Method of Visible Light Sensitization for Perovskite-Related Layered Oxides: Substitution Effect

- of Lead. *J. Solid State Chem.* **2006**, *179* (4), 1214–1218. <https://doi.org/10.1016/j.jssc.2006.01.024>.
- (10) Konta, R.; Ishii, T.; Kato, H.; Kudo, A. Photocatalytic Activities of Noble Metal Ion Doped SrTiO<sub>3</sub> under Visible Light Irradiation. *J. Phys. Chem. B* **2004**, *108* (26), 8992–8995. <https://doi.org/10.1021/jp049556p>.
- (11) Nishimoto, S.; Matsuda, M.; Miyake, M. Photocatalytic Activities of Rh-Doped CaTiO<sub>3</sub> under Visible Light Irradiation. *Chem. Lett.* **2006**, *35* (3), 308–309. <https://doi.org/10.1246/cl.2006.308>.
- (12) Sakata, Y.; Miyoshi, Y.; Maeda, T.; Ishikiriyama, K.; Yamazaki, Y.; Imamura, H.; Ham, Y.; Hisatomi, T.; Kubota, J.; Yamakata, A.; et al. Photocatalytic Property of Metal Ion Added SrTiO<sub>3</sub> to Overall H<sub>2</sub>O Splitting. *Appl. Catal. A Gen.* **2016**, *521*, 227–232. <https://doi.org/10.1016/j.apcata.2015.12.013>.
- (13) Zhao, Z.; Willard, E. J.; Li, H.; Wu, Z.; Castro, R. H. R.; Osterloh, F. E. Aluminum Enhances Photochemical Charge Separation in Strontium Titanate Nanocrystal Photocatalysts for Overall Water Splitting. *J. Mater. Chem. A* **2018**, *6* (33), 16170–16176. <https://doi.org/10.1039/C8TA05885G>.
- (14) Kato, H.; Asakura, K.; Kudo, A. Highly Efficient Water Splitting into H<sub>2</sub> and O<sub>2</sub> over Lanthanum-Doped NaTaO<sub>3</sub> Photocatalysts with High Crystallinity and Surface Nanostructure. *J. Am. Chem. Soc.* **2003**, *125* (10), 3082–3089. <https://doi.org/10.1021/ja027751g>.
- (15) Kim, J.; Hwang, D. W.; Kim, H. G.; Bae, S. W.; Lee, J. S.; Li, W.; Oh, S. H. Highly Efficient Overall Water Splitting Through Optimization of Preparation and Operation Conditions of Layered Perovskite Photocatalysts. *Top. Catal.* **2005**, *35* (3), 295–303. <https://doi.org/10.1007/s11244-005-3837-x>.
- (16) Shi, T.; Chen, Y.; Guo, X. Defect Chemistry of Alkaline Earth Metal (Sr/Ba) Titanates. *Prog. Mater. Sci.* **2016**, *80*, 77–132. <https://doi.org/10.1016/j.pmatsci.2015.10.002>.
- (17) Ham, Y.; Hisatomi, T.; Goto, Y.; Moriya, Y.; Sakata, Y.; Yamakata, A.; Kubota, J.; Domen,

- K. Flux-Mediated Doping of SrTiO<sub>3</sub> Photocatalysts for Efficient Overall Water Splitting. *J. Mater. Chem. A* **2016**, *4* (8), 3027–3033. <https://doi.org/10.1039/C5TA04843E>.
- (18) Goto, Y.; Hisatomi, T.; Wang, Q.; Higashi, T.; Ishikiriyama, K.; Maeda, T.; Sakata, Y.; Okunaka, S.; Tokudome, H.; Katayama, M.; et al. A Particulate Photocatalyst Water-Splitting Panel for Large-Scale Solar Hydrogen Generation. *Joule* **2018**, *2* (3), 509–520. <https://doi.org/10.1016/j.joule.2017.12.009>.
- (19) Zhao, Z.; Goncalves, R. V.; Barman, S. K.; Willard, E. J.; Byle, E.; Perry, R.; Wu, Z.; Huda, M. N.; Moulé, A. J.; Osterloh, F. E. Electronic Structure Basis for Enhanced Overall Water Splitting Photocatalysis with Aluminum Doped SrTiO<sub>3</sub> in Natural Sunlight. *Energy Environ. Sci.* **2019**, *12* (4), 1385–1395. <https://doi.org/10.1039/C9EE00310J>.
- (20) Takata, T.; Jiang, J.; Sakata, Y.; Nakabayashi, M.; Shibata, N.; Nandal, V.; Seki, K.; Hisatomi, T.; Domen, K. Photocatalytic Water Splitting with a Quantum Efficiency of Almost Unity. *Nature* **2020**, *581* (7809), 411–414. <https://doi.org/10.1038/s41586-020-2278-9>.
- (21) Dong, L.; Shi, H.; Cheng, K.; Wang, Q.; Weng, W.; Han, W. Shape-Controlled Growth of SrTiO<sub>3</sub> Polyhedral Submicro/Nanocrystals. *Nano Res.* **2014**, *7* (9), 1311–1318. <https://doi.org/10.1007/s12274-014-0495-y>.
- (22) Zhang, M.; Salvador, P. A.; Rohrer, G. S. Influence of Particle Size and Shape on the Rate of Hydrogen Produced by Al-Doped SrTiO<sub>3</sub> Photocatalysts. *J. Am. Ceram. Soc.* **2022**, *00*, 1–11. <https://doi.org/10.1111/jace.18488>.
- (23) Maeda, K.; Teramura, K.; Masuda, H.; Takata, T.; Saito, N.; Inoue, Y.; Domen, K. Efficient Overall Water Splitting under Visible-Light Irradiation on (Ga<sub>1-x</sub>Zn<sub>x</sub>)(N<sub>1-x</sub>O<sub>x</sub>) Dispersed with Rh–Cr Mixed-Oxide Nanoparticles: Effect of Reaction Conditions on Photocatalytic Activity. *J. Phys. Chem. B* **2006**, *110* (26), 13107–13112. <https://doi.org/10.1021/jp0616563>.
- (24) Lopato, E. M.; Eikey, E. A.; Simon, Z. C.; Back, S.; Tran, K.; Lewis, J.; Kowalewski, J. F.; Yazdi, S.; Kitchin, J. R.; Ulissi, Z. W.; et al. Parallelized Screening of Characterized and DFT-Modeled Bimetallic Colloidal Cocatalysts for Photocatalytic Hydrogen Evolution.

- ACS Catal.* **2020**, *10* (7), 4244–4252. <https://doi.org/10.1021/acscatal.9b05404>.
- (25) Song, W.; Lopato, E. M.; Bernhard, S.; Salvador, P. A.; Rohrer, G. S. High-Throughput Measurement of the Influence of pH on Hydrogen Production from BaTiO<sub>3</sub>/TiO<sub>2</sub> Core/Shell Photocatalysts. *Appl. Catal. B Environ.* **2020**, *269*, 118750. <https://doi.org/10.1016/j.apcatb.2020.118750>.
- (26) Bowes, P. C.; Ryu, G. H.; Baker, J. N.; Dickey, E. C.; Irving, D. L. Fermi Level Pinning in Co-Doped BaTiO<sub>3</sub>: Part II. Defect Chemistry Models. *J. Am. Ceram. Soc.* **2021**, *104* (11), 5859–5872. <https://doi.org/10.1111/jace.17938>.
- (27) Ryu, G. H.; Bowes, P. C.; McGarrah, J. R.; Irving, D. L.; Dickey, E. C. Fermi Level Pinning in Co-Doped BaTiO<sub>3</sub>: Part I. DC and AC Electrical Conductivities and Degradation Behavior. *J. Am. Ceram. Soc.* **2022**, *105* (1), 292–298. <https://doi.org/10.1111/jace.18042>.
- (28) Shin, C.-J.; Yoo, H.-I.; Lee, C.-E. Al-Doped SrTiO<sub>3</sub>: Part I, Anomalous Oxygen Nonstoichiometry. *Solid State Ionics* **2007**, *178* (15), 1081–1087. <https://doi.org/10.1016/j.ssi.2007.05.007>.
- (29) Puangpetch, T.; Sreethawong, T.; Yoshikawa, S.; Chavadej, S. Hydrogen Production from Photocatalytic Water Splitting over Mesoporous-Assembled SrTiO<sub>3</sub> Nanocrystal-Based Photocatalysts. *J. Mol. Catal. A-CHEMICAL* **2009**, *312* (1–2), 97–106. <https://doi.org/10.1016/j.molcata.2009.07.012>.
- (30) Takata, T.; Domen, K. Defect Engineering of Photocatalysts by Doping of Aliovalent Metal Cations for Efficient Water Splitting. *J. Phys. Chem. C* **2009**, *113* (45), 19386–19388. <https://doi.org/10.1021/jp908621e>.
- (31) Chan, N.-H.; Sharma, R. K.; Smyth, D. M. Nonstoichiometry in SrTiO<sub>3</sub>. *J. Electrochem. Soc.* **1981**, *128* (8), 1762–1769. <https://doi.org/10.1149/1.2127727>.
- (32) Zhou, X.; Toft Sørensen, O.; Xu, Y. Defect Structure and Oxygen Sensing Properties of Mg-Doped SrTiO<sub>3</sub> Thick Film Sensors. *Sensors Actuators B Chem.* **1997**, *41* (1), 177–182. [https://doi.org/10.1016/S0925-4005\(97\)80292-4](https://doi.org/10.1016/S0925-4005(97)80292-4).
- (33) Moos, R.; Hardtl, K. H. Defect Chemistry of Donor-Doped and Undoped Strontium Titanate

- Ceramics between 1000° and 1400°C. *J. Am. Ceram. Soc.* **1997**, *80* (10), 2549–2562. <https://doi.org/10.1111/j.1151-2916.1997.tb03157.x>.
- (34) Waser, R. Bulk Conductivity and Defect Chemistry of Acceptor-Doped Strontium Titanate in the Quenched State. *J. Am. Ceram. Soc.* **1991**, *74* (8), 1934–1940. <https://doi.org/10.1111/j.1151-2916.1991.tb07812.x>.
- (35) Bhardwaj, A.; Burbure, N. V; Rohrer, G. S. Enhanced Photochemical Reactivity at the Ferroelectric Phase Transition in  $\text{Ba}_{1-x}\text{Sr}_x\text{TiO}_3$ . *J. Am. Ceram. Soc.* **2010**, *93* (12), 4129–4134. <https://doi.org/10.1111/j.1551-2916.2010.04002.x>.
- (36) Noland, J. A. Optical Absorption of Single-Crystal Strontium Titanate. *Phys. Rev.* **1954**, *94* (3), 724. <https://doi.org/10.1103/PhysRev.94.724>.
- (37) Albery, W. J.; Bartlett, P. N. The Transport and Kinetics of Photogenerated Carriers in Colloidal Semiconductor Electrode Particles. *J. Electrochem. Soc.* **1984**, *131* (2), 315–325. <https://doi.org/10.1149/1.2115568>.
- (38) Li, L.; Salvador, P. A.; Rohrer, G. S. Photocatalysts with Internal Electric Fields. *Nanoscale* **2014**, *6* (1), 24–42. <https://doi.org/10.1039/c3nr03998f>.
- (39) Liu, M.; Lyons, J. L.; Yan, D.; Hybertsen, M. S. Semiconductor-Based Photoelectrochemical Water Splitting at the Limit of Very Wide Depletion Region. *Adv. Funct. Mater.* **2016**, *26* (2), 219–225. <https://doi.org/10.1002/adfm.201503692>.
- (40) Cheng, C.; Long, R. Charge-Compensated Doping Extends Carrier Lifetimes in  $\text{SrTiO}_3$  by Passivating Oxygen Vacancy Defects. *J. Phys. Chem. Lett.* **2021**, *12* (50), 12040–12047. <https://doi.org/10.1021/acs.jpcclett.1c03775>.
- (41) Han, K.; Lin, Y.-C.; Yang, C.-M.; Jong, R.; Mul, G.; Mei, B. Promoting Photocatalytic Overall Water Splitting by Controlled Magnesium Incorporation in  $\text{SrTiO}_3$  Photocatalysts. *ChemSusChem* **2017**, *10* (22), 4510–4516. <https://doi.org/10.1002/cssc.201701794>.
- (42) Karazhanov, S. Z. Properties of Precisely Compensated Semiconductors. *Semiconductors* **2000**, *34* (8), 872–879. <https://doi.org/10.1134/1.1188091>.

# Chapter 9: Ion Exchange between Perovskite Oxides and Molten Salts: A Potential Strategy to Synthesize Highly Efficient Photocatalysts for Water Splitting

*The motivation of this project is to apply the Al-doping and flux treatments to other materials. Many experiments have been carried out by our lab, like heating BaTiO<sub>3</sub> in molten BaCl<sub>2</sub> and heating PbTiO<sub>3</sub> in molten PbCl<sub>2</sub>. Unfortunately, none of these materials are good catalysts. Later, we tried heating BaTiO<sub>3</sub> in molten SrCl<sub>2</sub> and this produced a very reactive photocatalyst, the best one we have ever synthesized. What's even more surprising is that the XRD study indicated that BaTiO<sub>3</sub> converted to SrTiO<sub>3</sub> in the SrCl<sub>2</sub> flux. In this chapter, I am going to describe my understanding of this special ion exchange and how it helps synthesize good photocatalysts.*

## 9.1 Introduction

Photocatalytic water splitting, a technique that can directly convert water into hydrogen and oxygen under illumination, has attracted significant attention in past decades.<sup>1,2</sup> As a high density and pollutant-free energy source, solar hydrogen is considered to be a potential candidate to reduce humanity's dependence on fossil fuels.<sup>3</sup> At present, two of the major issues that limit its application are the rapid recombination process of photogenerated charge carriers<sup>4</sup> and surface back reactions.<sup>5</sup> Hence, a great amount of research has focused on developing catalysts with enhanced charge separation properties using a variety of strategies, such as defect engineering,<sup>6,7</sup> facet engineering,<sup>8,9</sup> and heterojunction construction.<sup>10-12</sup> Currently, a molten salt flux treatment has been considered as a promising method because of its unique advantages in optimizing the properties of the SrTiO<sub>3</sub> photocatalyst.<sup>13</sup> In a liquid phase media, the mass transfer between precursors is accelerated and the reaction temperature is reduced compared with conventional solid state synthesis.<sup>14,15</sup>

Previous studies show that a molten salt treatment is an excellent approach to synthesize high crystallinity catalysts with enhanced photocatalytic reactivities.<sup>16</sup> By varying the choice of the salt, it is feasible to promote particle crystallization and manipulate particle morphology to expose specific facets with enhanced charge separation properties.<sup>17,18</sup> For example, Al-doped SrTiO<sub>3</sub>

synthesized in a molten SrCl<sub>2</sub> flux is one of the most efficient semiconductor-based photocatalysts that have been developed so far.<sup>19</sup> By selectively photodepositing cocatalysts on (100) and (110) facets, Domen and coworkers demonstrated Al-doped SrTiO<sub>3</sub> catalysts with an external quantum efficiency of up to 96 percent at wavelengths between 350 and 360 nm for overall water splitting.<sup>20</sup> Besides, in the molten SrCl<sub>2</sub> flux, it has been supposed, without experimental evidence, that a high degree of crystalline structure forms which can avoid electron's trapping inside the particles.<sup>21</sup> One of the motivations of this paper is to employ molten salt flux treatments to synthesize new photocatalysts with superior performance.

Another important application of molten salt treatments is to exchange foreign ions into host materials. This method has been proved to be an effective approach to sensitize wide bandgap photocatalysts to visible light. For example, Kudo and coworkers have successfully exchanged alkali ions with Ag(I) and Cu(I) ions in a series of wide-band-gap metal oxides with layered or tunneling structures and improved the photocatalytic reactivity in visible light region.<sup>22,23</sup> Ladasiu et al. exchanged potassium cations with protons in Dion–Jacobson type layered perovskite niobium oxides and improved the photocatalytic reactivity significantly.<sup>24</sup> Maggard's group reported on molten SnCl<sub>2</sub>/SnF<sub>2</sub> fluxes and successfully prepared visible light responsive photocatalysts with metastable structures such as Sn<sub>2</sub>TiO<sub>4</sub>,<sup>25</sup> (Ba<sub>1-x</sub>Sn<sub>x</sub>)Nb<sub>4</sub>O<sub>15</sub>,<sup>26</sup> and (Ba<sub>1-x</sub>Sn<sub>x</sub>)(Zr<sub>1-y</sub>Ti<sub>y</sub>)O<sub>3</sub>.<sup>27</sup> While most of the host materials for ion exchange have relatively large interstitial spaces, in this study, we focus on densely structured ABO<sub>3</sub>-based perovskite oxide, an excellent photocatalyst candidate for water splitting.

Herein, we demonstrate a direct ion exchange reaction between perovskite titanate oxides and alkali earth molten salts. Through this reaction, we have successfully prepared a series of new SrTiO<sub>3</sub> photocatalysts with improved efficiency with respect to conventional SrTiO<sub>3</sub> for overall water splitting using BaTiO<sub>3</sub>, PbTiO<sub>3</sub>, CaTiO<sub>3</sub>, and rutile or anatase TiO<sub>2</sub> as precursors in one step synthesis. Among them, BaTiO<sub>3</sub>-derived SrTiO<sub>3</sub>, following a probable reaction route BaTiO<sub>3(s)</sub> + SrCl<sub>2(l)</sub> → SrTiO<sub>3(s)</sub> + BaCl<sub>2(l)</sub>, exhibits a remarkable performance for overall water splitting with an apparent quantum yield (AQY) over 11.37% at 380 nm. The mechanism appears to be that Sr<sup>2+</sup> cations exchange with Ba<sup>2+</sup> cations and Sr<sup>2+</sup> diffuse inward, while Ba<sup>2+</sup> diffuse outward. The ion exchanged material is observed to have SrO planar faults near the surface, and therefore appears to be Sr-excess, a condition that reduces the defect states that trap electron. At the same time, Cl<sup>-</sup>

is nonuniformly doped into the crystals, creating an internal electric field, and this might also contribute to charge separation and enhanced photocatalytic reactivity. Furthermore, we have found that this ion exchange reaction is broadly applicable and that the A-site cations in perovskite oxides can be exchange with cations in molten salts, suggesting a promising strategy to synthesize highly efficient photocatalysts for water splitting.

## 9.2 Experimental Methods

**Photocatalysts synthesis.** All catalysts were prepared using a flux method. In a typical reaction, 0.3 g titanate precursor, such as SrTiO<sub>3</sub> (Sigma-Aldrich, 99.9%), BaTiO<sub>3</sub> (CERAC, 99.9%), CaTiO<sub>3</sub> (CERAC, 99.9%), PbTiO<sub>3</sub> (Alfa Aesar, 99.9%), anatase TiO<sub>2</sub> (CERAC, 99%), and rutile TiO<sub>2</sub> (Sigma-Aldrich, 99.9%), was mixed with SrCl<sub>2</sub> (Alfa Aesar, 99.5%), at a molar ratio of 1:10 with an agate mortar. The mixture was then transferred to either a covered alumina crucible (Sigma-Aldrich, Coors™ high-alumina, 50 ml) or a covered platinum crucible (Sigma-Aldrich, 30 ml) and annealed at 1150 °C for 10 h in air with a ramp rate of 10 °C/min. Next, the mixture was centrifuged four times in deionized water and four times in ethanol to remove any residue of the SrCl<sub>2</sub> flux. The powders collected through the centrifugation was dried in an oven at 80 °C overnight. In this paper, samples treated in alumina and platinum crucibles will be referred to as “precursor-sA” and “precursor-sP” respectively to highlight the materials of the precursors before the flux treatment and the crucibles.

RhCrO<sub>x</sub> cocatalysts were deposited (0.1 wt% Rh and 0.1 wt% Cr) on all samples with an impregnation method described elsewhere.<sup>28</sup> 50 mg of as prepared powdered samples were dispersed into 0.5 ml of deionized water containing appropriate amounts of Na<sub>3</sub>RhCl<sub>6</sub> (Sigma-Aldrich) and Cr(NO<sub>3</sub>)<sub>3</sub>·6H<sub>2</sub>O (Sigma-Aldrich, 99%) to yield 0.1 wt% Rh and Cr. The suspension was evaporated in a boiling water bath under constant manually stirring. The resulting powders were collected and heated at 350 °C for 1 h.

**Characterization.** The crystal phase was analyzed with an Empyrean X'pert PRO X-ray Diffractometer (PANalytical, Philips, Netherlands) in the range of 20–90° using a step size of 0.01°, equipped with a high-intensity (45 kV, 40 mA) Cu K $\alpha$  radiation source (K $\alpha$ 1 = 1.5406 Å, K $\alpha$ 2 = 1.5444 Å). Scanning Electron Microscopy (SEM) images were obtained to determine the

morphologies of all samples using a FEI Quanta 600 with a 30 kV accelerating beam and a spot size of 3. An Oxford full analytical XMAX 80mm SDD EDX detector was equipped on the SEM for chemical composition analysis (EDS). The particle cross-section samples were prepared using a focused ion beam (FIB) milling process with a gallium source on an FEI NOVA 600. Transmission electron microscopy (TEM) images were recorded with a Thermal Fisher Themis 200 at 200 kV. XPS spectra were recorded using a SPECS System with a PHOIBOS 150 Analyzer. N<sub>2</sub> adsorption–desorption measurements (Nova 2200e, Quanta- chrome, FL), used to determine the specific surface areas of powders through a Brunauer–Emmett–Teller (BET) approach, was performed at 77 K using a multi-point method. The sample was degassed at 120 °C for 24 h prior to measurement. UV-vis diffuse reflectance spectra were recorded on an OL 770 Multi-Channel Spectroradiometer (Optronic Laboratories). Inductively coupled plasma optical emission spectroscopy (ICP-OES) was carried out at Element Technology to determine the Al<sup>3+</sup> concentration. X-ray fluorescence spectroscopy (XRF) was used to measure the concentration of Cl<sup>-</sup> in samples using an Oxford X-supreme 8000.

***High-throughput screening of photocatalysts.*** Photocatalytic hydrogen generation was measured with a high-throughput method using a paralyzed and automated photochemical reactor (PAPCR) which enables us to study up to 108 samples simultaneously.<sup>29–31</sup> The reactor array consists of 108 1 ml glass vials with 10 mg catalyst powders added, and the illumination is provided by two high power LED chips (Chanzon). The illumination wavelength of the LEDs is 380 nm. To explore the solution effect on the photocatalysts, 0.4 mL of DI water whose pH was adjusted to pH 2, pH 7, and pH 12 or 10% methanol solution with a natural pH was injected into each vial. The headspace of the vials was covered by a layer of H<sub>2</sub> sensitive film (DetecTape, Tape-Midsun Specialty Products) whose color will change from light to dark when exposed to H<sub>2</sub>. The calibration between the film darkness and local H<sub>2</sub> concentration has been extensively reported in our previous publication (and Appendix 4).<sup>31</sup> During a 16 h illumination, the H<sub>2</sub> sensitive film is captured by a camera every 6 minutes and the pictures were used to calculate the rate of hydrogen production.

***Apparent quantum yield measurement.*** To measure the apparent quantum yield (AQY), a gas-chromatography based reactor setup is employed. In a measurement, 200 mg degassed catalyst powders, together with 20 ml DI water, is added into a 50 ml EPA glass vial with argon atmosphere

inside. The vial is illuminated for 3 hours by two LEDs with a peak wavelength at 380 nm. After illumination, the amount of hydrogen in the vial headspace is analyzed with a gas chromatography. The light intensity of the LEDs is measured with a photodiode. The resulting photon fluxes are integrated over the bottom area of the vial (4.9 cm<sup>2</sup>), with the irradiation of the photocatalyst estimated to be  $5.6 \times 10^{16}$  photons s<sup>-1</sup>. The AQY is calculated according to the following equation:

$$\text{AQY}(\%) = \frac{\text{number of H}_2 \text{ molecules produced} \times 2}{\text{number of incident photons}} \times 100\%$$

### 9.3 Results

SEM images of the six titanate precursors after the molten SrCl<sub>2</sub> treatment in alumina crucibles are shown in Figure 9-1(a). For SrTiO<sub>3</sub> powders treated in the flux (denoted as STO-sA), particles exhibit cube shapes bounded by {100} crystal planes, which is consistent with previous reports.<sup>19,32</sup> Similarly, for BaTiO<sub>3</sub> and PbTiO<sub>3</sub> powders treated in the molten SrCl<sub>2</sub>, denoted as BTO-sA and PTO-sA, respectively, particles exhibit cubic shapes while the particle sizes are slightly different. As for CaTiO<sub>3</sub> powders treated in the molten SrCl<sub>2</sub>, denoted as CTO-sA, the particle shape is relatively irregular, and the edges are less defined. However, for the molten SrCl<sub>2</sub> treated rutile and anatase TiO<sub>2</sub>, denoted as Rutile-sA and Anatase-sA, particles have much larger sizes around several microns. Also, they have truncated edges and corners, exhibiting (110) and (111) facets. Powder X-ray diffraction has been carried out on the six samples and the resulting patterns are given in Fig. 9-1(b). All samples exhibit a cubic symmetry with sharp peaks, and the patterns are close to standard SrTiO<sub>3</sub>, plotted as black droplines in Fig. 9-1(b), suggesting that all titanates became high crystallinity SrTiO<sub>3</sub> after the molten SrCl<sub>2</sub> flux treatment. A magnified image for the (110) reflection is shown in Fig. 9-1(b) in a separated panel. It is found that STO-sA, Rutile-sA and Anatase-sA exhibit symmetric peaks, while for the other three, the peaks are slightly asymmetrical. BTO-sA, as well as PTO-sA, has a small tail at the left side of the peak, indicating that a small portion of the precursors remained in the powders. As for CTO-sA, a small tail is observed at the right side of the (110) peak, and all peaks shift to larger angles with respect to the standard SrTiO<sub>3</sub> pattern. The lattice parameters of all patterns have been refined using HighScore and are given in Table 9-1.

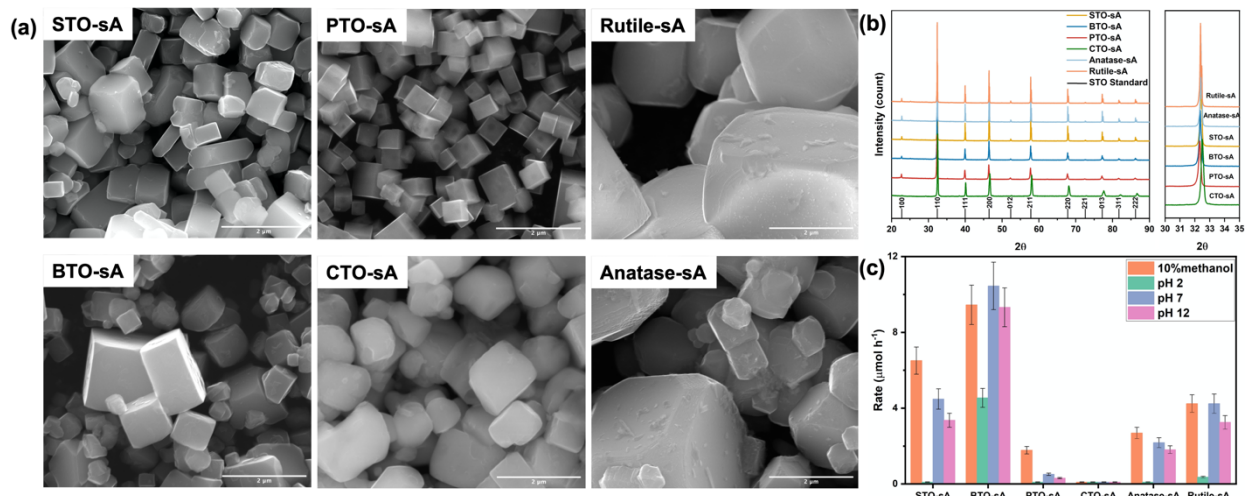


**Figure 9-1:** (a) SEM images of molten  $\text{SrCl}_2$  flux treated  $\text{SrTiO}_3$ ,  $\text{BaTiO}_3$ ,  $\text{PbTiO}_3$ ,  $\text{CaTiO}_3$ , rutile and anatase  $\text{TiO}_2$ . Scale bar: 2  $\mu\text{m}$ . (b) XRD patterns of the six flux treated samples with a standard  $\text{SrTiO}_3$  pattern plotted as black droplines (ICDD: 01-074-1296). (c) Photocatalytic maximum  $\text{H}_2$  production rates from the six samples in 10% methanol solution, pH 2 water, pH 7 water and pH 12 water under 380 nm illumination.

**Table 9-1:** Refined lattice parameters and unit cell volumes (refined with HighScore) of the six samples in Figure 9-1. The reference lattice parameter of  $\text{SrTiO}_3$  (ICDD: 01-073-0661) is 3.9050  $\text{\AA}$ .

Sample	Lattice parameter ( $\text{\AA}$ )	Cell Volume ( $\text{\AA}^3$ )
STO-sA	3.9050(1)	59.55
BTO-sA	3.9054(1)	59.56
PTO-sA	3.9085(9)	59.71
CTO-sA	3.8989(1)	59.23
Rutile-sA	3.9046(6)	59.53
Anatase-sA	3.9047(5)	59.54

Photocatalytic water splitting experiments have been carried out on the six samples using the PAPCR in a variety of solutions illuminated by 380 nm LEDs, and the maximum  $\text{H}_2$  evolution rates are shown in Figure 9-1(c). STO-sA, Anatase-sA and Rutile-sA show photocatalytic reactivities at a similar level that can produce  $\text{H}_2$  at a rate of 4  $\mu\text{mol h}^{-1}$  in pH 7 water. PTO-sA shows a much lower reactivity, and CTO-sA cannot produce enough  $\text{H}_2$  to be measured by our reactor. BTO-sA shows the highest reactivity, producing  $\text{H}_2$  at a rate of 10  $\mu\text{mol h}^{-1}$  in pH 7 water, which is about 2.5 times reactive compared with the regular STO-sA. Adding methanol as hole scavenger will improve the  $\text{H}_2$  production rates except for BTO-sA and Rutile-sA. As for the pH

effect, all catalysts are more reactive at pH 7 and pH 12 than pH 2, which is consistent with our previous work.<sup>31,33</sup> Using our GC-based reactor setup, BTO-sA can produce 57.3  $\mu\text{mol H}_2$  in 3 hours under the same illumination and the apparent quantum yield is determined to be about 11.4% under 380 nm. It is noted that the actual AQY might be even higher because the powders are not dispersed in water but just sitting at the bottom of the vial, and this may block the light coming from the LEDs. Owing to the excellent reactivity of BTO-sA, more studies have been carried out on this material.

The XRD pattern in Fig. 9-1(c) indicates that  $\text{Ba}^{2+}$  exchanges with  $\text{Sr}^{2+}$  during the molten salt treatment, therefore we adjusted the annealing time and temperature to understand the reaction more thoroughly. Figure 9-2(a) shows the XRD patterns of  $\text{BaTiO}_3$  treated in the molten  $\text{SrCl}_2$  flux at different temperature and time. All patterns exhibit cubic symmetry with peaks only attributed to  $\text{SrTiO}_3$ . From the magnified (110) reflections, it is observed that the tail at the left side of the peak shrinks when increasing the annealing temperature and time. Since the tail corresponds to  $\text{Ba}^{2+}$  remaining in the crystals, it is concluded that the exchange rate (what percentage of  $\text{Ba}^{2+}$  was exchanged by  $\text{Sr}^{2+}$ ) will increase with the annealing temperature and time. Lattice parameters have been refined from the patterns, given in Fig. 9-2(b), showing that the cell volume decreases with the increasing annealing temperature and time, which is consistent with the XRD patterns. Photocatalytic water splitting reactions have been carried out on the seven samples and the  $\text{H}_2$  production rates in pH 7 and pH 12 DI water are shown in Fig. 9-2(c) and (d). The  $\text{H}_2$  production rate will increase with the ion exchange, indicating that the diffusion of  $\text{Sr}^{2+}$  ( $\text{Ba}^{2+}$ ) cations into (out of) the crystal contributes to the improvement of the photocatalytic reactivity.

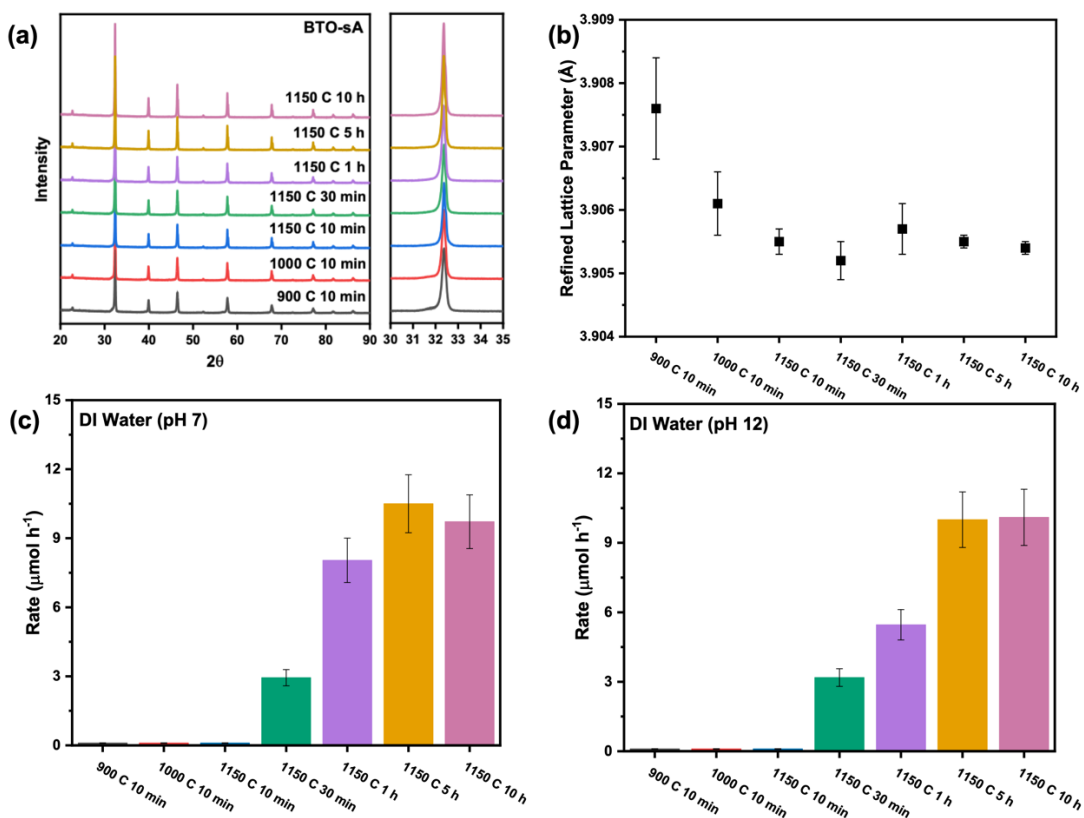


**Figure 9-2:** (a) XRD patterns of BaTiO<sub>3</sub> treated in the molten SrCl<sub>2</sub> flux for a variety of temperature and time combinations. (b) Lattice parameters refined from the XRD patterns. The bars represent standard deviations. (c) Photocatalytic H<sub>2</sub> production rates of the samples in pH 7 DI water. (d) Photocatalytic H<sub>2</sub> production rates of the samples in pH 12 DI water.

Previous studies reported that the SrCl<sub>2</sub> flux treatment in alumina crucibles will incorporate Al<sup>3+</sup> ions into SrTiO<sub>3</sub> lattice, and this will increase the photogenerated charge carrier lifetime by inhibiting the formation of Ti<sup>3+</sup> defects.<sup>21,34</sup> Therefore, it is likely that our SrTiO<sub>3</sub> samples prepared with this ion exchange reactions will have Al<sup>3+</sup> doped as well. To examine this, ICP-OES analysis was carried out on the BTO-sA as well as the benchmark sample STO-sA, and the results are presented in Table 9-2. The results confirm that Al<sup>3+</sup> is incorporated into both samples since alumina crucibles would slightly dissolve in the flux. However, the Al<sup>3+</sup> concentration of BTO-sA is obviously lower than STO-sA. At the same time, Ba<sup>2+</sup> is still measurable in the samples which is consistent with the XRD pattern, indicating that the exchange reaction is not quite completed yet. We also detected Cl<sup>-</sup> in both samples with XRF that BTO-sA has a higher Cl<sup>-</sup> concentration and this might be ascribed to the diffusion of Cl<sup>-</sup> anions into the samples from the flux. Because of the existence of large Ba<sup>2+</sup> cation expanding the lattice, Cl<sup>-</sup> might be much easier

to diffuse into the samples and occupy oxygen sites, forming a donor defect  $\text{Cl}_\text{O}$ . It is noted that, before the XRF measurements, the sample will be washed for half an hour with vacuum filtration to completely remove any  $\text{SrCl}_2$  flux residues. Besides, BET data show that the two samples have similar surface area so this cannot explain their different reactivities.

**Table 9-2:** BET surface areas,  $\text{Al}^{3+}$  and  $\text{Ba}^{2+}$  concentrations determined by ICP-OES,  $\text{Cl}^-$  concentrations determined by XRF of STO-sA and BTO-sA.

Sample	BET Surface Area ( $\text{m}^2/\text{g}$ )	ICP-OES Data			XRF Concentration
		Al	Ba	Ti	Cl
STO-sA	1.6273	0.7%	0%	23.78%	0.47%
BTO-sA	1.7972	0.38%	1.94%	24.68%	0.77%

Another experiment varying the Al concentration has been carried out by heating  $\text{BaTiO}_3$  together with additional  $\text{Al}_2\text{O}_3$  from 0% to 5% (Al metal concentration) during the flux treatment. To further confirm the influence of  $\text{Al}^{3+}$  in this material, we carried out the  $\text{SrCl}_2$  flux treatment in either a Pt crucible or an  $\text{Al}_2\text{O}_3$  crucible, denoted as BTO-sP and BTO-sA, respectively. SEM images of BTO-sA and BTO-sP without additional Al added are given in Figure 9-3(a) and (b). It is found that both crucible materials and Al addition will influence the particle shape and size. When no additional Al added, for alumina crucible samples, particles exhibit a cuboid shape with an average particle size about a half a micrometer; for Pt crucible samples, particles will grow to cubes as large as several micrometers and a step structure is observed on particle edges. Note that these results are similar to what we observed in Chapter 8. The cubed shape is close to its equilibrium shape as reported since (100) surface has the minimum energy.<sup>35,36</sup> The increasing particle size is ascribed to the result of coarsening that atoms transport between particles.<sup>37</sup> As additional Al is added into the flux, as shown in Figure 9-4 and 9-5, particles will become smaller and more irregular. Recall that we have found that  $\text{SrCl}_2$  will react with  $\text{Al}_2\text{O}_3$  at this temperature forming  $\text{Sr}_3\text{Al}_2\text{O}_6$  and change the flux composition in Chapter 7. As more  $\text{Al}_2\text{O}_3$  added, the flux treatment will naturally terminate, and crystals are less likely to convert to their equilibrium shape or coarsen. This also explains why BTO-sP are much larger than BTO-sA since no Al can dissolve from a Pt crucible.

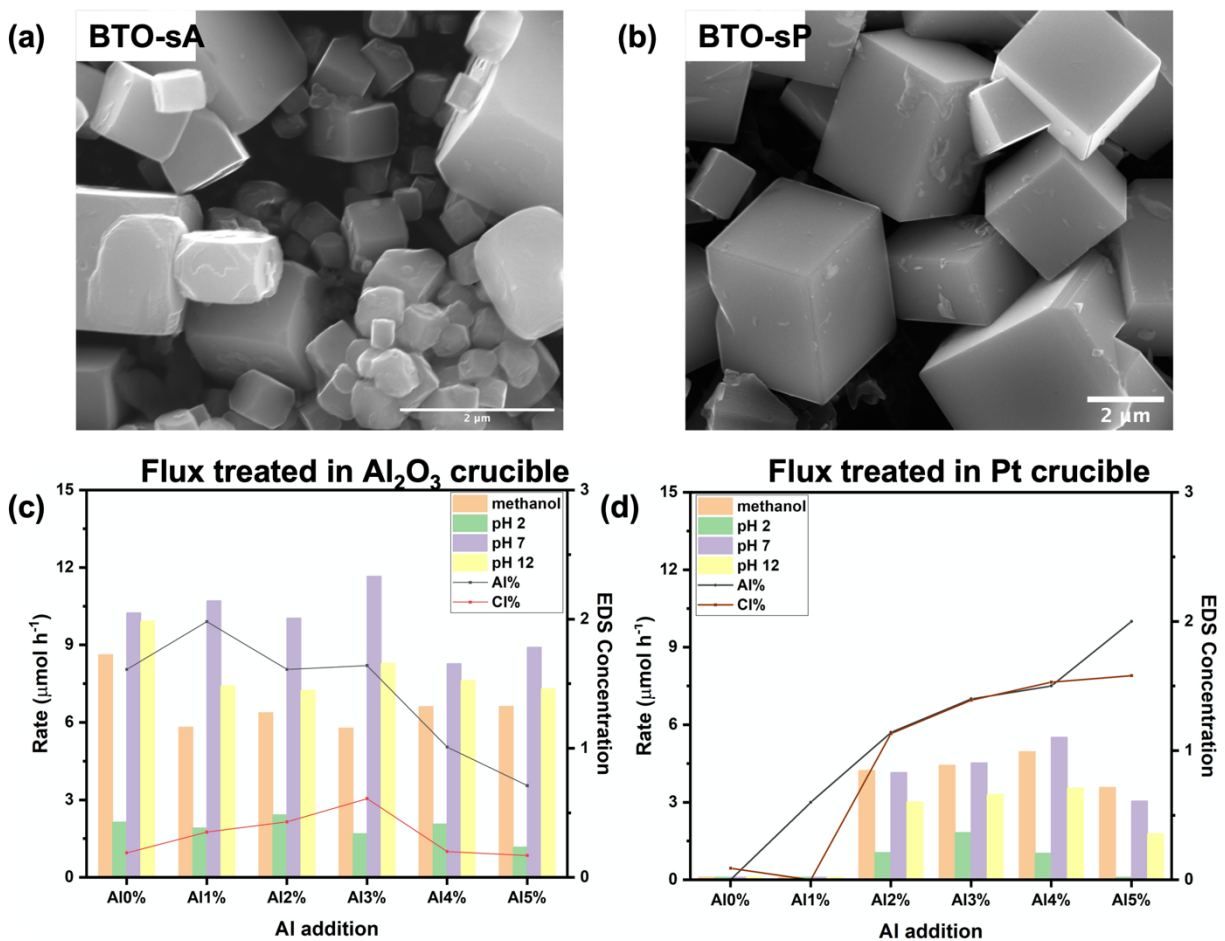


**Figure 9-3:** SEM images of BaTiO<sub>3</sub> treated in molten SrCl<sub>2</sub> flux in an alumina crucible or a platinum crucible are shown in (a) and (b), respectively. Scale bars are shown in the images. Maximum H<sub>2</sub> production rates measured with the PAPCR of BaTiO<sub>3</sub> treated in the molten SrCl<sub>2</sub> flux with different amount of Al added in an alumina crucible or a platinum crucible are shown in (c) and (d). The concentration of Al<sup>3+</sup> and Cl<sup>-</sup> are determined with EDS and shown in the images in a different axis.

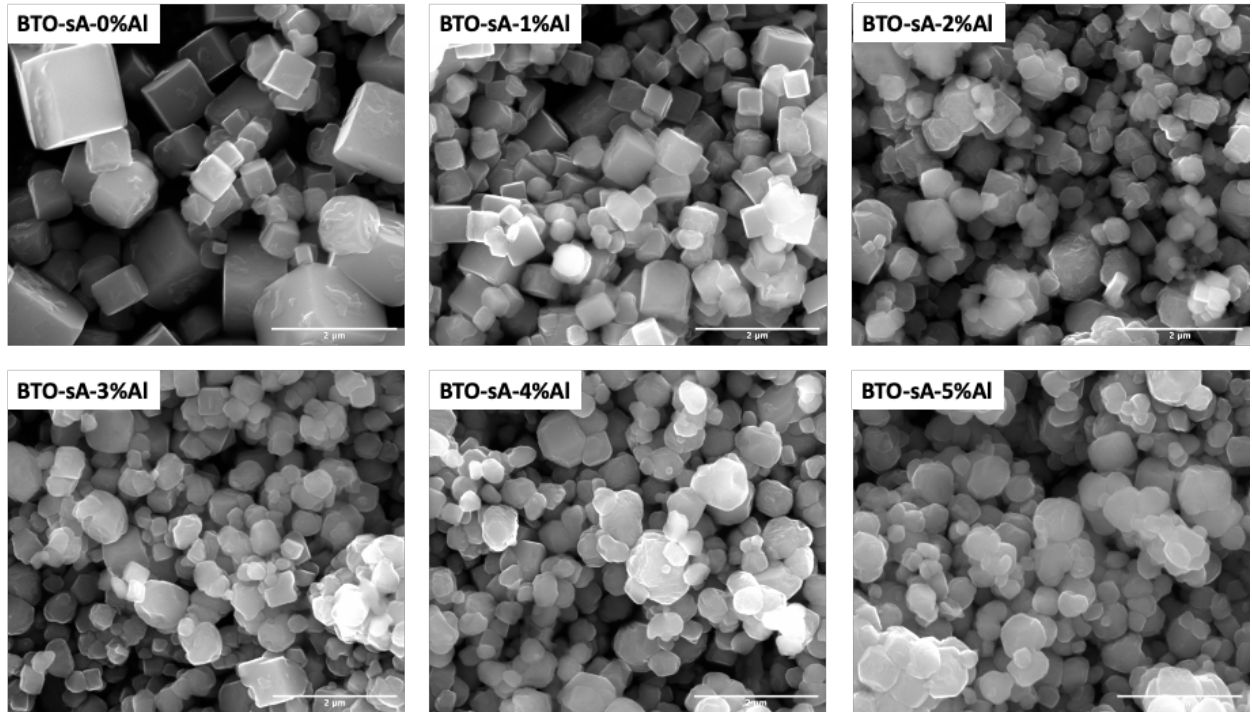


**Figure 9-4:** SEM images of BaTiO<sub>3</sub> treated in the SrCl<sub>2</sub> flux in an alumina crucible with different amount of Al added.

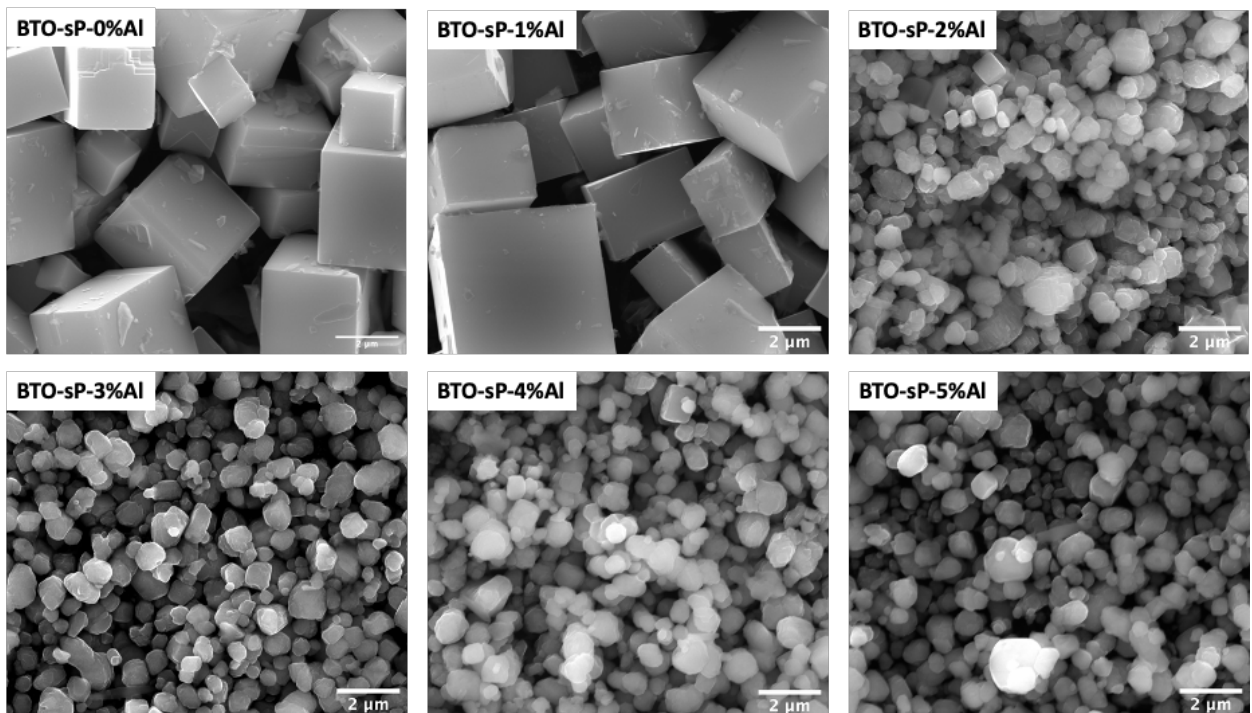


**Figure 9-5:** SEM images of BaTiO<sub>3</sub> treated in the molten SrCl<sub>2</sub> flux in a platinum crucible with different amount of Al added.

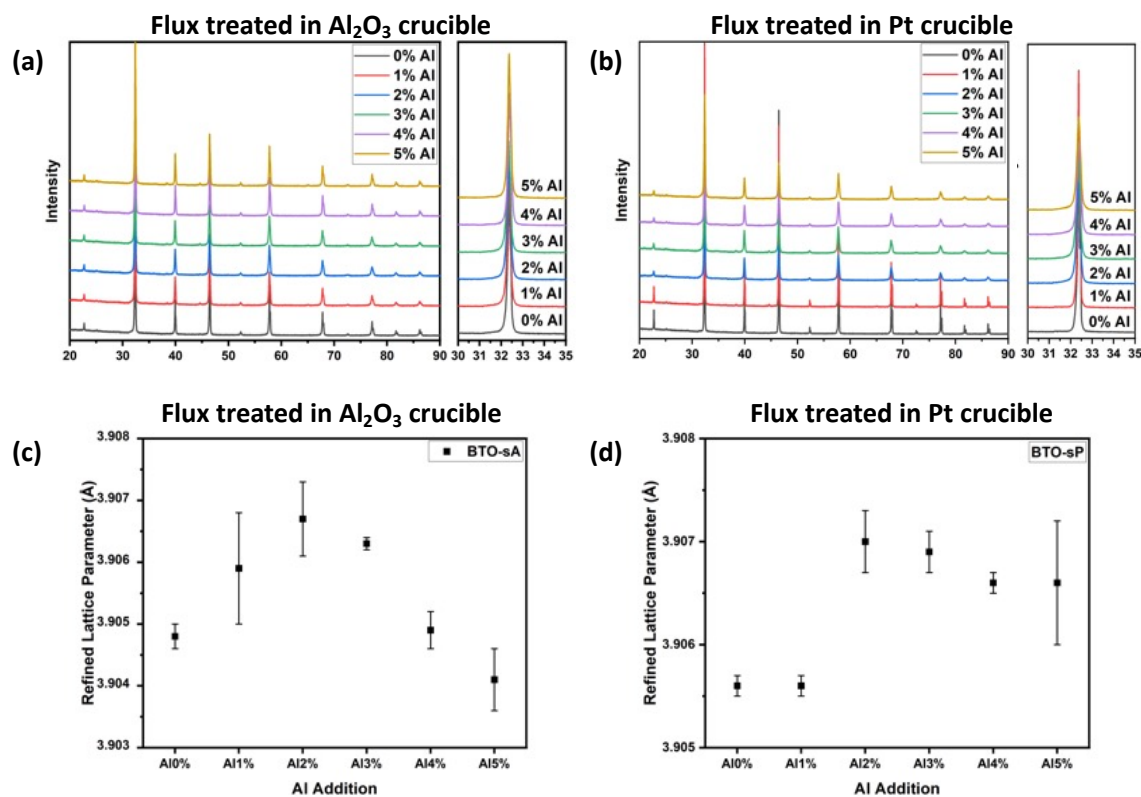


**Figure 9-6:** XRD patterns of BaTiO<sub>3</sub> treated in the molten SrCl<sub>2</sub> flux with different amount of Al<sub>2</sub>O<sub>3</sub> added in an alumina crucible or a platinum crucible are shown in (a) and (b), respectively. A magnified image of the (110) reflection is given in a separated panel in both (a) and (b). Lattice parameters have been refined with HighScore and given in (c) and (d). The bars represent standard deviations. Note that the minor peaks at 38.6°, 44.9° and 65.3° are attribute to the (111), (200) and (220) reflections of the Al sample stage in the diffractometer but not from the samples.

Photocatalytic H<sub>2</sub> production from BTO-sA and BTO-sP with different Al additions was measured with the PAPCR in different solutions and shown in Fig. 9-3(c) and (d). In summary, BaTiO<sub>3</sub> powders treated in an alumina crucible are much more reactive than those treated in a Pt crucible, consistent with the observation in Chapter 8. If the flux treatment is carried out in an alumina crucible, adding additional Al seems to have minor contribution to the photocatalytic reactivity. From the EDS data, Al<sup>3+</sup> concentration decreases with the Al added and this is likely due to the actual reaction time will decrease with the amount of Al added. Cl<sup>-</sup> is detectable in these samples as well. If the flux treatment is carried out in a Pt crucible, adding additional Al will contribute to the reactivity significantly. When 0% or 1% Al is added in the flux, the resulting powders are brown and cannot produce enough H<sub>2</sub> that can be detected by the PAPCR. After 2% or more Al added, the powders become white and start to produce H<sub>2</sub> in a comparable level with STO-sA.

From the EDS data, both  $\text{Al}^{3+}$  and  $\text{Cl}^-$  are related to the photocatalytic reactivity. It is likely a co-doping effect occurs in this  $\text{BaTiO}_3$ -derived  $\text{SrTiO}_3$  catalyst and contributes to the photocatalytic reactivity. XRD patterns and refined lattice parameter of BTO-sA and BTO-sP with different Al added during the flux treatment are presented in Figure 9-6. For samples from alumina crucibles, adding Al into the flux will firstly expand the lattice, increase the cell volume, and then decrease it, which is consistent with the trend of  $\text{Cl}^-$  concentration determined by EDS. For Pt crucible ones, when the Al addition is 0% and 1%, the tail that we observed at the left side of the (110) reflection disappeared, indicating that  $\text{Ba}^{2+}$  was completely exchanged by  $\text{Sr}^{2+}$  and the lattice is close to a standard  $\text{SrTiO}_3$ . Adding more Al will expand the lattice, let more  $\text{Cl}^-$  incorporate into the crystal, and this might contribute to the photocatalytic reactivity.

XPS was employed to study the surface composition and chemical states of pristine  $\text{SrTiO}_3$ , STO-sA and BTO-sA. Figure 9-7 (a) shows the high-resolution Sr 3d spectrum of pristine  $\text{SrTiO}_3$  purchased from Sigma-Aldrich without any treatment.  $\text{Sr}^{2+}$  peaks have been deconvoluted into SrO and  $\text{SrTiO}_3$ , and the doublets located around 134.8 eV and 132.9 eV can be assigned to  $3d_{3/2}$  and  $3d_{5/2}$ .<sup>38,39</sup> Sr 3d spectra of STO-sA and BTO-sA have been recorded and shown in Fig. 9-7 (b) and (c). The relative  $\text{Sr}^{2+}$  species ratios of SrO to  $\text{SrTiO}_3$  are calculated and shown in Table 9-3, showing that the  $\text{SrCl}_2$  flux treatment increased the SrO concentration on the surface slightly. Ti 2p spectrum of pristine  $\text{SrTiO}_3$  is shown in Figure 9-7 (d), and spectrum is divided into Ti  $2p_{1/2}$  and Ti  $2p_{3/2}$  peaks at around 464.7 eV and 458.7 eV, respectively. A second doublet can be deconvoluted from the spectra at 463.1 eV and 457.1 eV, suggesting the existence of  $\text{Ti}^{3+}$  defects. The percentage of  $\text{Ti}^{3+}$  is calculated to be 36.4% in pristine  $\text{SrTiO}_3$  but relatively lower in flux treated samples, which is determined to be 29.6% and 27.7% for STO-sA and BTO-sA, shown in Fig. 9-7 (e) and (f) and Table 9-3. Composition ratios of Sr/Ti have been calculated to be 0.84, 1.42 and 1.35 for pristine  $\text{SrTiO}_3$ , STO-sA and BTO-sA, respectively, suggesting that the  $\text{SrCl}_2$  flux treatment leads to a significantly Sr-rich surface environment. Additionally, O 1s scans of the three samples are presented in Figure 9-7 (g)-(i). The primary peak close to 529.9 eV is attributed to lattice  $\text{O}^{2-}$  ions bonded to metal cations, and the second peak at around 532.3 eV is ascribed to hydroxyl-groups (-OH) on the surface.<sup>40,41</sup> Compared with pristine  $\text{SrTiO}_3$ , the percentage of hydroxyl-group increases from 24.3% to 40.2% and 36.2% for STO-sA and BTO-sA, respectively. High resolution scans of  $\text{Al}^{3+}$ ,  $\text{Cl}^-$  and  $\text{Ba}^{2+}$  in STO-sA and BTO-sA have been conducted, and it is concluded that  $\text{Al}^{3+}$  is detectable on the surface of both samples,  $\text{Cl}^-$  is only

detected on STO-sA surface and Ba<sup>2+</sup> is detected on BTO-sA surface. Note that the XPS data here is quite different from the data for single crystals (see Chapter 7), and this might imply that the powder samples are less stoichiometric.

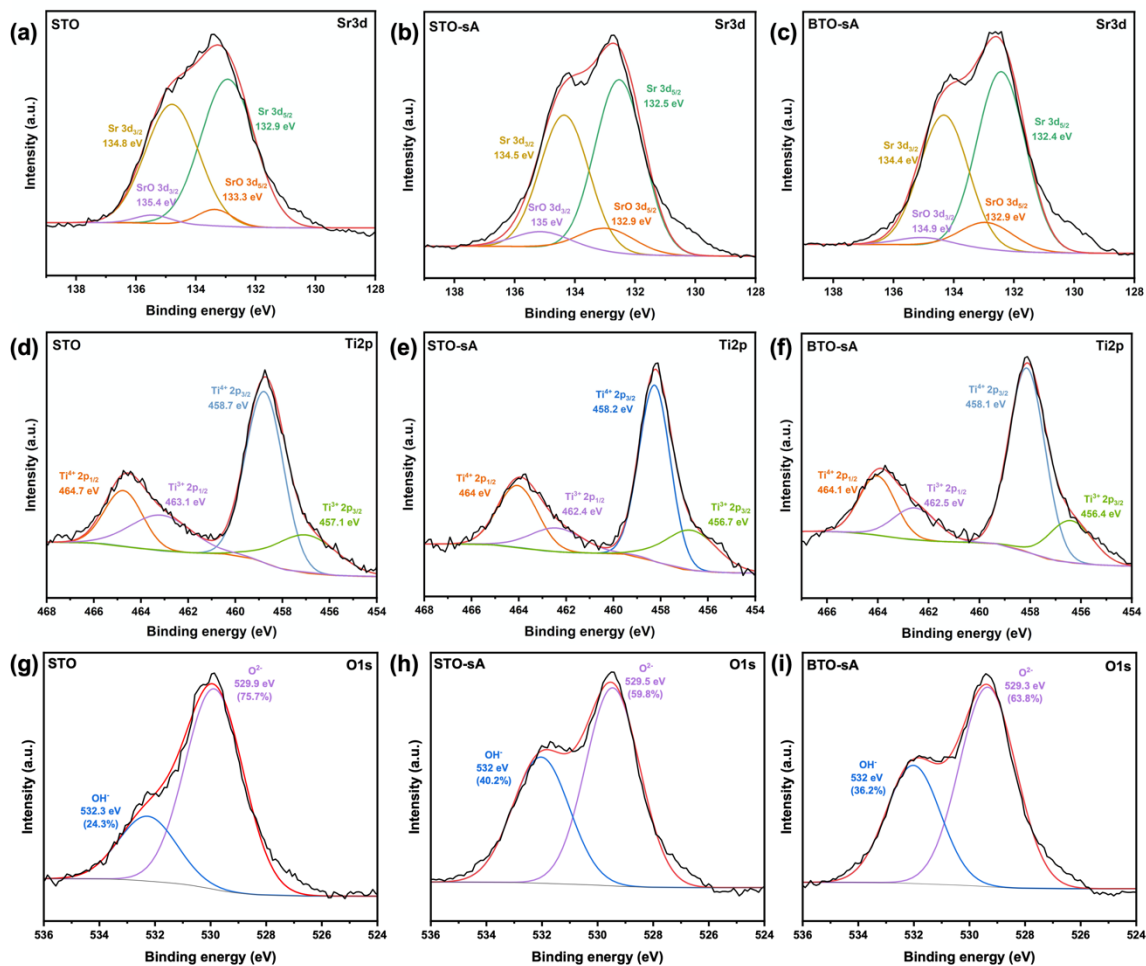


**Figure 9-7:** High resolution XPS spectra of Sr 3d region in (a) pristine SrTiO<sub>3</sub>, (b) STO-sA, (c) BTO-sA; Ti 2p region in (d) pristine SrTiO<sub>3</sub>, (e) STO-sA, (f) BTO-sA; and O 1s scan in (g) pristine SrTiO<sub>3</sub>, (h) STO-sA, (i) BTO-sA.

**Table 9-3:** Surface Compositions and Chemical State of Sr, Ti and O of pristine SrTiO<sub>3</sub>, STO-sA and BTO-sA determined from XPS spectra.

Catalyst	Sr 3d		Ti 2p		O 1s		Sr/Ti
	SrO	SrTiO <sub>3</sub>	Ti <sup>3+</sup>	Ti <sup>4+</sup>	-OH	O <sup>2-</sup>	
Pristine STO	5.7%	94.3%	36.4%	63.6%	24.3%	75.7%	0.84
STO-sA	12.4%	87.6%	29.6%	70.4%	40.2%	59.8%	1.42
BTO-sA	11.9%	88.1%	27.7%	72.3%	36.2%	63.8%	1.35

## 9.4 Discussion

The results indicate that ion exchange can occur between densely structured perovskite titanates and molten salts. In a highly concentrated molten  $\text{SrCl}_2$  flux,  $\text{Ba}^{2+}$ ,  $\text{Ca}^{2+}$ , and  $\text{Pb}^{2+}$  cations can be exchanged by  $\text{Sr}^{2+}$  cations by mass diffusion forming high crystallinity  $\text{SrTiO}_3$ . One might suggest that the oxide dissolves in the flux and then recrystallizes to form  $\text{SrTiO}_3$  due to the thermodynamic stability. To examine this possibility, we prepared particle cross section samples via FIB milling. After cutting several BTO-sA particles, as shown in Figure 9-8 (a), cubic cavities were observed at the center of the particles with a diameter of about 10 nm. We believe that this is attributed to the well-known Kirkendall effect resulting from the difference in diffusivities of the two atoms,<sup>42</sup> which is commonly observed in diffusion couples<sup>43</sup> and hollow nanomaterials synthesis.<sup>44</sup> In our case,  $\text{Ba}^{2+}$  and  $\text{Sr}^{2+}$  ions exchange with the assistance of vacancies at different rates, If Ba diffuses out of the crystal faster than Sr diffuses in, then internal cavities can form. And Ti is supposed to diffuse along with Ba to the surface as well. Hence, this is the evidence that the reaction is controlled by mass diffusion instead of dissolution and recrystallization. Note that Kirkendall pores are observed in PTO-sA and CTO-sA as well, shown in Figure 9-9, indicating that a similar ion exchange reaction is going on. There are a number of studies showing that hollow particles might exhibit a red shift of the absorption edge compared with solid ones and thus have high photocatalytic reactivity.<sup>45,46</sup> However, considering the much smaller volume ratio of the cavity to our particle, it is less likely that the optical properties can be significantly enhanced. UV-vis diffuse reflectance spectrum of the BTO-sA sample has been recorded, and the bandgap is determined to be 3.27 eV (not shown here), similar to the value of standard  $\text{SrTiO}_3$ .<sup>47</sup> This cannot explain the superior photocatalytic reactivity of the sample, especially since PTO-sA and CTO-sA are not improved photocatalysts, but also have voids inside.

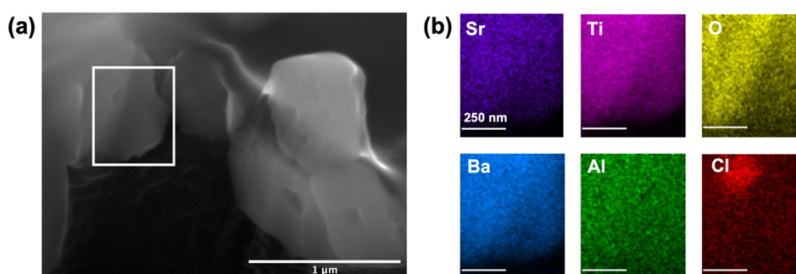


**Figure 9-8:** (a) SEM images of BTO-sA particle cross section samples prepared via FIB milling. (b) EDS element maps of the box region in (a).

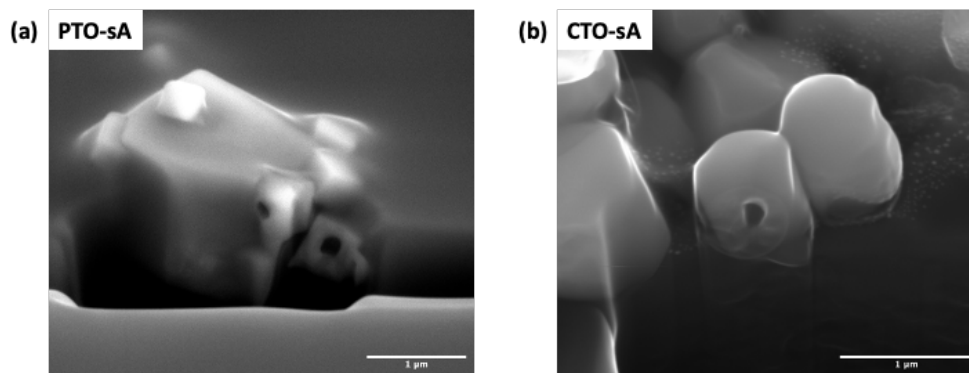


**Figure 9-9:** SEM images of particle cross section samples of (a) PTO-sA and (b) CTO-sA. Kirkendall pores are observed in both samples. Scale bars are shown in the images. Note that the small particles in (b) correspond to redeposition during ion milling.

EDS analysis has been carried out on a BTO-sA particle cross section (the box region in Fig. 9-8(a)) and the element maps are shown in Fig. 9-8(b).  $\text{Ba}^{2+}$ ,  $\text{Al}^{3+}$ , and  $\text{Cl}^-$  are detected inside the particle, which is consistent with the chemical analysis results in Table 9-3. Among them,  $\text{Cl}^-$  shows an obvious uneven distribution and mostly accumulates at the center of the particle, this explains why we can't detect  $\text{Cl}^-$  under XPS since the information depth of XPS is generally below 10 nm. Considering the mass transfer between  $\text{Ba}^{2+}$  and  $\text{Sr}^{2+}$ ,  $\text{Cl}^-$  is likely to incorporate into the crystal because of the concentration gradient and lattice expansion. As a control, we have prepared STO-sA particle cross-section samples but cannot detect  $\text{Cl}^-$  inside the crystal, confirming the correlation between the uneven  $\text{Cl}^-$  distribution and ion exchange. Furthermore, no interior voids were observed. Because the diffusing atoms are compensated by vacancies, and the voids originates from the accumulation of vacancies, the absence of voids is consistent with the idea that the voids form because of the Kirkendall effect. It is likely that  $\text{Ba}^{2+}$  and  $\text{Sr}^{2+}$  ions diffuse through A-site vacancies and meantime  $\text{Cl}^-$  diffuse into the crystal forming  $\text{Cl}_\text{O}^\cdot$  donors. While this is just a likely explanation, further studies are necessary to fully understand the mechanism of this special ion exchange reaction in future. Benefited from the nonuniformly distributed positive charged  $\text{Cl}_\text{O}^\cdot$ , it is thought that the center of the particle is Cl doped and the rest of the particle is vacancy doped, therefore an internal electric field is built inside the particle, driving more photogenerated holes to migrate to the surface and participate in reactions. Since the overall reactivity depends on the slower one of the two half reactions, the promotion of the anodic half reaction should increase the overall reaction rate of  $\text{SrTiO}_3$ .

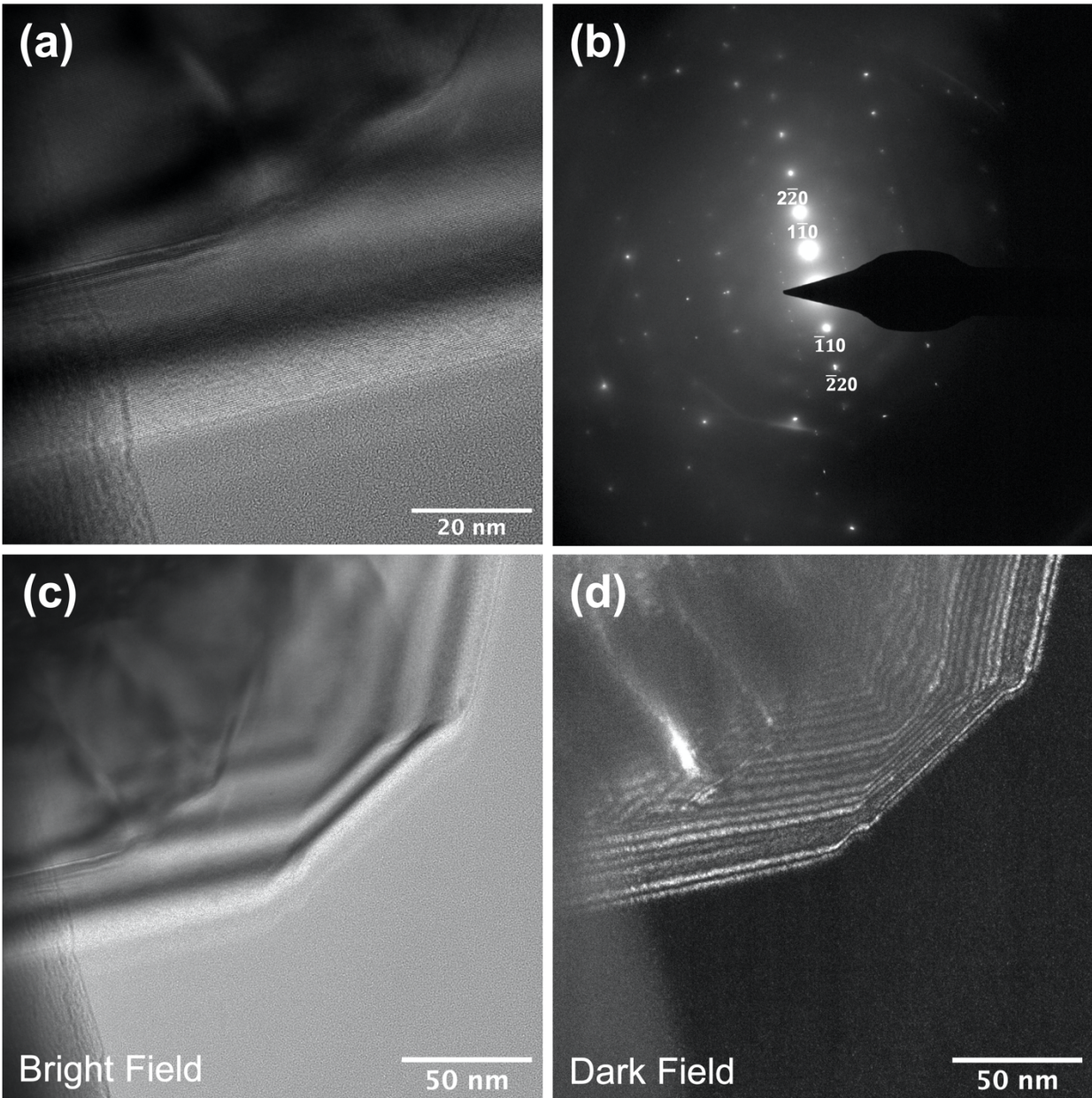


**Figure 9-10:** (a) High resolution TEM image of a particle edge of BTO-sA. (b) SAED pattern recorded on the lattice in (a). Bright field and dark field images on the same particle edge are shown in (c) and (d). Scale bars are given in the images.

TEM studies have been carried out to further understand the structure of BTO-sA. Although the particle surface looks quite uniform under SEM, we observed Morié patterns on particle edges under TEM. A high-resolution image recorded on a particle edge is given in Fig. 9-10(a), the length of each layer is determined to be around 10 nm and the d-spacing is measured to be about 0.28 nm, corresponding to (110) planes of SrTiO<sub>3</sub>. Selected-area electron diffraction (SAED)

pattern recorded on the lattice fringes is shown in Fig. 9-10(b) with brighter spots in the center column corresponding to reflections near SrTiO<sub>3</sub> [110] zone axis. Another two columns of weak split spots are observed on both sides of the SrTiO<sub>3</sub> (110) reflections, corresponding to reflections from a long range superlattice structure with a different stacking period. Bright field and dark field TEM images recorded on the same particle but in a lower magnification are given in Fig 9-10(c) and (d), respectively. The dark field image was recorded by selecting the SrTiO<sub>3</sub> (220) reflection in Fig. 9-10(b). From the dark field image, it is found that the particle is not uniform, composed of SrTiO<sub>3</sub> whose (110) planes have the ideal spacing (bright areas) and other regions that do not have the same spacing (dark areas). FFT and inverse-FFT analysis of the lattice fringes are given in Figure 9-11, suggesting that the split superlattice spots originate from the irregularly spaced planar defects. A plausible explanation for the observations here is that the perovskite particle surface has extra SrO planes in the near surface region, a situation similar to the Sr<sub>n+1</sub>Ti<sub>n</sub>O<sub>3n+1</sub> Ruddlesden-Popper structure,<sup>48</sup> but without the long range order. In this case, the split spots come from the diffraction close to [111] zone of the Ruddlesden-Popper superlattice, and the Morié patterns arise from the interference between the defected lattices on the two sides of the edges. Past studies agreed that a Sr-rich environment reduces the concentration of recombination centers and improves the photocatalytic reactivity.<sup>49,50</sup> Sun et al. suggested that the Ruddlesden-Popper phase has a 2D charge transport character that is beneficial to charge separation.<sup>51</sup> Additional TEM images supporting this argument are presented in Figure 9-12. None of these microstructure defects are found in regular STO-sA, indicating that they might arise from the ion exchange reaction. The formation of SrO<sub>x</sub>·SrTiO<sub>3</sub> in the near surface region attracts Ti toward the surface to relax it to SrTiO<sub>3</sub>, which also serves a role in the formation of the Kirkendall voids.

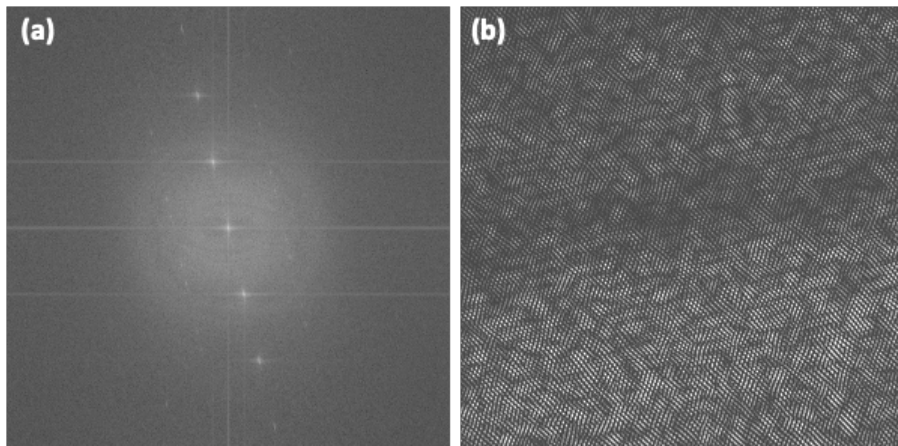


**Figure 9-11:** (a) FFT pattern of the lattice fringes in Fig. 9-10(a). (b) Inverse-FFT pattern by selecting the split spots in (a).

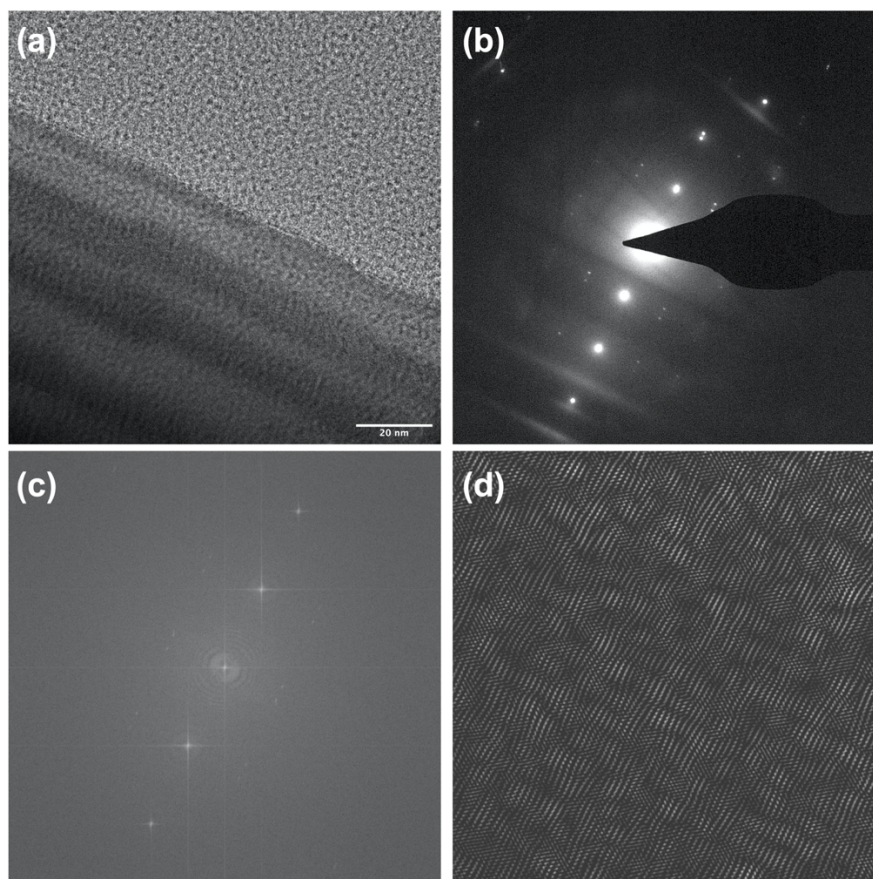


**Figure 9-12:** A high resolution TEM image of a BTO-sA particle edge is given in (a) with its corresponding (b) SAED pattern and (c) FFT pattern. (d) Inverse-FFT pattern by selecting the split spots in (c).

From the Pt crucible experiments, shown in Fig. 9-3(d), the incorporation of  $\text{Al}^{3+}$  into the lattice is necessary to prepare reactive  $\text{SrTiO}_3$  photocatalyst. Extensive studies have been carried out on

Al-doped SrTiO<sub>3</sub> photocatalysts,<sup>19,20,31,32,38,52–54</sup> and it is understood that Al<sup>3+</sup> can eliminate the formation of Ti<sup>3+</sup> recombination centers, increase the lifetime of charge carriers and improve the photocatalytic reactivities.<sup>6,34</sup> Note that this same process decreases the concentration of carriers and increase width of the depletion region (see Chapter 8). Also, the incorporation of Al<sup>3+</sup> has to be along with a molten SrCl<sub>2</sub> flux treatment to reach superior water splitting reactivity. We have found that the SrCl<sub>2</sub> flux treatment can modify the surface chemistry by introducing a much higher surface hydroxide group concentration, increase the potential difference between the (100) and (110) surfaces and enhance the ability of SrTiO<sub>3</sub> to separate charge. These have been thoroughly discussed in Chapter 7 and Chapter 8. However, these observations cannot explain why our ion-exchanged SrTiO<sub>3</sub> samples prepared via treating BaTiO<sub>3</sub> in the molten SrCl<sub>2</sub> flux has a better reactivity compared with the normal SrCl<sub>2</sub> flux treated SrTiO<sub>3</sub> even it has a lower Al<sup>3+</sup> concentration.

We believe that the better photocatalytic reactivity is mainly owing to its nonuniform distribution of Cl<sub>0</sub> donors and the SrO planar defects formed in the near surface region during ion exchange. To supplement this, we have studied why CTO-sA and PTO-sA have relatively low reactivities. From the XRD data of CTO-sA, it is observed that the exchange rate is much lower, suggesting that Ca<sup>2+</sup> is much harder to be replaced by Sr<sup>2+</sup>. After a second SrCl<sub>2</sub> flux treatment, the photocatalytic reactivity of CTO-sA increases and can be detected by the PAPCR. As for PTO-sA, the insoluble PbCl<sub>2</sub> formed during the flux treatment might remain on the particle surface and block the light. By soaking the same sample in acidic solutions for some time, the reactivity will increase significantly. The photocatalytic hydrogen production data of the improved PTO-sA and CTO-sA is given in Figure 9-13.

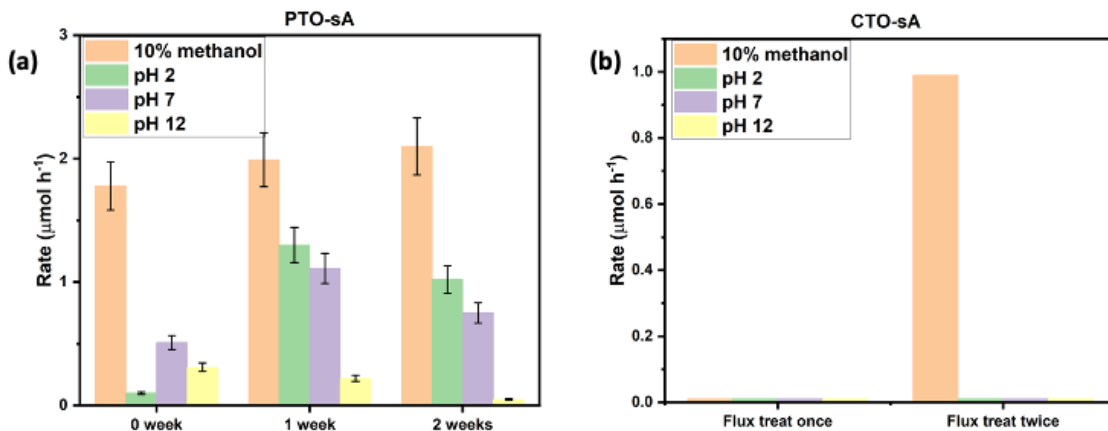


**Figure 9-13:** (a) Photocatalytic maximum H<sub>2</sub> production rates of PTO-sA and the same sample that has been soaked in 10% methanol solution, pH 2 water, pH 7 water and pH 12 water for 1 or 2 weeks. The illumination is provided by 380 nm LEDs. (b) Photocatalytic maximum H<sub>2</sub> production rates of CaTiO<sub>3</sub> that have been treated in the SrCl<sub>2</sub> flux for one or two times. The rates are measured in 10% methanol, pH 2 water, pH 7 water and pH 12 water under 380 nm illumination.

The observation of ion exchange in molten SrCl<sub>2</sub> inspired us to explore more ion exchange reactions between perovskite oxides and molten salts. To explore this, BaTiO<sub>3</sub>, SrTiO<sub>3</sub> and CaTiO<sub>3</sub> are heated in 10 times ratio of molten CaCl<sub>2</sub> and MgCl<sub>2</sub>. It is not surprised that Ca<sup>2+</sup> can replace Sr<sup>2+</sup> or Ba<sup>2+</sup> from SrTiO<sub>3</sub> and BaTiO<sub>3</sub> to form CaTiO<sub>3</sub>. Heating SrTiO<sub>3</sub> in molten BaCl<sub>2</sub> can only form a solid solution with a cubic symmetry indicating a low exchange rate. MgCl<sub>2</sub>, on the other hand, reacts with CaTiO<sub>3</sub> and SrTiO<sub>3</sub> to form Mg<sub>2</sub>TiO<sub>4</sub>. Similarly, titania reacts with molten SrCl<sub>2</sub> to form SrTiO<sub>3</sub>. These reactions are not topotactic and unlikely to proceed by ion exchange. The results are summarized in Table 9-4. Together with the results on the molten SnCl<sub>2</sub>/SnF<sub>2</sub> flux published by Maggard's group,<sup>27</sup> it is thought that this ion exchange reaction can be applied to many perovskite oxide materials. It is concluded that, in a ABO<sub>3</sub> perovskite oxide, the cations in a molten salt can exchange with the A-site cations following a size rule that smaller cations can replace larger cations easily. Meanwhile, we believe this reaction provides a new strategy to synthesis new photocatalysts with enhanced reactivity for overall water splitting.

**Table 9-4:** Summary of ion exchange materials in this work.

Precursor	Flux	Product	Exchange Rate
BaTiO <sub>3</sub>	SrCl <sub>2</sub>	SrTiO <sub>3</sub>	94.5%
PbTiO <sub>3</sub>	SrCl <sub>2</sub>	SrTiO <sub>3</sub>	86.7%
CaTiO <sub>3</sub>	SrCl <sub>2</sub>	SrTiO <sub>3</sub>	68.5%
Sr <sub>2</sub> TiO <sub>4</sub>	SrCl <sub>2</sub>	SrTiO <sub>3</sub>	100%
BaTiO <sub>3</sub>	CaCl <sub>2</sub>	CaTiO <sub>3</sub>	94.6%
SrTiO <sub>3</sub>	CaCl <sub>2</sub>	CaTiO <sub>3</sub>	74.1%
SrTiO <sub>3</sub>	MgCl <sub>2</sub>	Mg <sub>2</sub> TiO <sub>4</sub>	100%
CaTiO <sub>3</sub>	MgCl <sub>2</sub>	Mg <sub>2</sub> TiO <sub>4</sub>	100%
SrTiO <sub>3</sub>	BaCl <sub>2</sub>	Ba <sub>x</sub> Sr <sub>1-x</sub> TiO <sub>3</sub>	31.4%

Note that the exchange rate is calculated by the following equation using the concentration determined by EDS:

$$[\text{exchange rate \%}] = \frac{[\text{Foreign cations from the flux}]}{([\text{Foreign cations from the flux}] + [\text{A-site cations from the precursor}])} \times 100$$

## 9.5 Conclusion

In this work, we demonstrate a special ion exchange reaction between perovskite titanate oxides and alkali earth metal chloride molten salts. By heating BaTiO<sub>3</sub>, PbTiO<sub>3</sub>, CaTiO<sub>3</sub>, rutile and anatase TiO<sub>2</sub> in a molten SrCl<sub>2</sub> flux, we have successfully synthesized a variety of SrTiO<sub>3</sub> photocatalysts in one single step that can split water under UV illuminations. Among them, the BaTiO<sub>3</sub> derived SrTiO<sub>3</sub> photocatalyst exhibits the highest reactivity with an apparent quantum yield over 11.37% at 380 nm. Kirkendal cavities are observed inside the particles, which implies that the reaction is driven by mass diffusion instead of dissolution and recrystallization. Based on FIB-EDS and TEM analysis, it is likely the planar defects in the near surface region might create a Sr enriched region with superior water splitting properties and the accumulation of Cl in the core might favor the transport of holes to the surface. Moreover, it is found that this ion exchange reaction occurs in multiple perovskites where the A-site cation in perovskite oxide can be replaced with smaller cations from molten salts. The results demonstrate that ion exchange for perovskite oxides can be employed as a potential strategy to design and synthesize highly reactive photocatalysts for water splitting.

## 9.6 References

- (1) Fujishima, A.; Honda, K. Electrochemical Photolysis of Water at a Semiconductor Electrode. *Nature* **1972**, 238 (5358), 37+. <https://doi.org/10.1038/238037a0>.

- (2) Wang, Q.; Domen, K. Particulate Photocatalysts for Light-Driven Water Splitting: Mechanisms, Challenges, and Design Strategies. *Chem. Rev.* **2020**, *120* (2), 919–985. <https://doi.org/10.1021/acs.chemrev.9b00201>.
- (3) Mazloomi, K.; Gomes, C. Hydrogen as an Energy Carrier: Prospects and Challenges. *Renew. Sustain. Energy Rev.* **2012**, *16* (5), 3024–3033. <https://doi.org/10.1016/j.rser.2012.02.028>.
- (4) Spanhel, L.; Haase, M.; Weller, H.; Henglein, A. Photochemistry of Colloidal Semiconductors. 20. Surface Modification and Stability of Strong Luminescing CdS Particles. *J. Am. Chem. Soc.* **1987**, *109* (19), 5649–5655. <https://doi.org/10.1021/ja00253a015>.
- (5) Sato, S.; White, J. M. Photodecomposition of Water over Pt/TiO<sub>2</sub> Catalysts. *Chem. Phys. Lett.* **1980**, *72* (1), 83–86. [https://doi.org/10.1016/0009-2614\(80\)80246-6](https://doi.org/10.1016/0009-2614(80)80246-6).
- (6) Takata, T.; Domen, K. Defect Engineering of Photocatalysts by Doping of Aliovalent Metal Cations for Efficient Water Splitting. *J. Phys. Chem. C* **2009**, *113* (45), 19386–19388. <https://doi.org/10.1021/jp908621e>.
- (7) Liu, J.; Wei, Z.; Shanguan, W. Defects Engineering in Photocatalytic Water Splitting Materials. *ChemCatChem* **2019**, *11* (24), 6177–6189. <https://doi.org/10.1002/cctc.201901579>.
- (8) Bai, S.; Wang, L.; Li, Z.; Xiong, Y. Facet-Engineered Surface and Interface Design of Photocatalytic Materials. *Adv. Sci.* **2017**, *4* (1), 1600216. <https://doi.org/10.1002/advs.201600216>.
- (9) Liu, G.; Yu, J. C.; Lu, G. Q.; Cheng, H.-M. Crystal Facet Engineering of Semiconductor Photocatalysts: Motivations, Advances and Unique Properties. *Chem. Commun.* **2011**, *47* (24), 6763–6783. <https://doi.org/10.1039/C1CC10665A>.
- (10) Teranishi, T.; Sakamoto, M. Charge Separation in Type-II Semiconductor Heterodimers. *J. Phys. Chem. Lett.* **2013**, *4* (17), 2867–2873. <https://doi.org/10.1021/jz4013504>.
- (11) Tada, H.; Mitsui, T.; Kiyonaga, T.; Akita, T.; Tanaka, K. All-Solid-State Z-Scheme in CdS–Au–TiO<sub>2</sub> Three-Component Nanojunction System. *Nat. Mater.* **2006**, *5* (10), 782–786.

<https://doi.org/10.1038/nmat1734>.

- (12) Xu, Q.; Zhang, L.; Cheng, B.; Fan, J.; Yu, J. S-Scheme Heterojunction Photocatalyst. *Chem* **2020**, *6* (7), 1543–1559. <https://doi.org/10.1016/j.chempr.2020.06.010>.
- (13) Luo, L.; Wang, S.; Wang, H.; Tian, C.; Jiang, B. Molten-Salt Technology Application for the Synthesis of Photocatalytic Materials. *Energy Technol.* **2021**, *9* (2), 2000945. <https://doi.org/10.1002/ente.202000945>.
- (14) Kerridge, D. H. Recent Advances in Molten Salts as Reaction Media. *Pure Appl. Chem.* **1975**, *41* (3), 355–371. <https://doi.org/10.1351/pac197541030355>.
- (15) Sundermeyer, W. Fused Salts and Their Use as Reaction Media. *Angew. Chemie Int. Ed. English* **1965**, *4* (3), 222–238. <https://doi.org/10.1002/anie.196502221>.
- (16) Xue, P.; Wu, H.; Lu, Y.; Zhu, X. Recent Progress in Molten Salt Synthesis of Low-Dimensional Perovskite Oxide Nanostructures, Structural Characterization, Properties, and Functional Applications: A Review. *J. Mater. Sci. Technol.* **2018**, *34* (6), 914–930. <https://doi.org/10.1016/j.jmst.2017.10.005>.
- (17) Kato, H.; Kobayashi, M.; Hara, M.; Kakihana, M. Fabrication of SrTiO<sub>3</sub> Exposing Characteristic Facets Using Molten Salt Flux and Improvement of Photocatalytic Activity for Water Splitting. *Catal. Sci. Technol.* **2013**, *3* (7), 1733–1738. <https://doi.org/10.1039/C3CY00014A>.
- (18) Ma, S. S. K.; Hisatomi, T.; Maeda, K.; Moriya, Y.; Domen, K. Enhanced Water Oxidation on Ta<sub>3</sub>N<sub>5</sub> Photocatalysts by Modification with Alkaline Metal Salts. *J. Am. Chem. Soc.* **2012**, *134* (49), 19993–19996. <https://doi.org/10.1021/ja3095747>.
- (19) Ham, Y.; Hisatomi, T.; Goto, Y.; Moriya, Y.; Sakata, Y.; Yamakata, A.; Kubota, J.; Domen, K. Flux-Mediated Doping of SrTiO<sub>3</sub> Photocatalysts for Efficient Overall Water Splitting. *J. Mater. Chem. A* **2016**, *4* (8), 3027–3033. <https://doi.org/10.1039/C5TA04843E>.
- (20) Takata, T.; Jiang, J.; Sakata, Y.; Nakabayashi, M.; Shibata, N.; Nandal, V.; Seki, K.; Hisatomi, T.; Domen, K. Photocatalytic Water Splitting with a Quantum Efficiency of Almost Unity. *Nature* **2020**, *581* (7809), 411–414. <https://doi.org/10.1038/s41586-020->

2278-9.

- (21) Yamakata, A.; Yeilin, H.; Kawaguchi, M.; Hisatomi, T.; Kubota, J.; Sakata, Y.; Domen, K. Morphology-Sensitive Trapping States of Photogenerated Charge Carriers on SrTiO<sub>3</sub> Particles Studied by Time-Resolved Visible to Mid-IR Absorption Spectroscopy: The Effects of Molten Salt Flux Treatments. *J. Photochem. Photobiol. A Chem.* **2015**, *313*, 168–175. <https://doi.org/10.1016/j.jphotochem.2015.05.016>.
- (22) Iwashina, K.; Iwase, A.; Kudo, A. Sensitization of Wide Band Gap Photocatalysts to Visible Light by Molten CuCl Treatment. *Chem. Sci.* **2015**, *6* (1), 687–692. <https://doi.org/10.1039/C4SC01829J>.
- (23) Watanabe, K.; Iwashina, K.; Iwase, A.; Nozawa, S.; Adachi, S.; Kudo, A. New Visible-Light-Driven H<sub>2</sub>- and O<sub>2</sub>-Evolving Photocatalysts Developed by Ag(I) and Cu(I) Ion Exchange of Various Layered and Tunneling Metal Oxides Using Molten Salts Treatments. *Chem. Mater.* **2020**, *32* (24), 10524–10537. <https://doi.org/10.1021/acs.chemmater.0c03461>.
- (24) Ladasiu, C.; Kulischow, N.; Marschall, R. Tuning the Photocatalytic Activity of Layered Perovskite Niobates by Controlled Ion Exchange and Hydration. *Catal. Sci. Technol.* **2022**. <https://doi.org/10.1039/D1CY02057A>.
- (25) O'Donnell, S.; Hamilton, A.; Maggard, P. A. Fast Flux Reaction Approach for the Preparation of Sn<sub>2</sub>TiO<sub>4</sub>: Tuning Particle Sizes and Photocatalytic Properties. *J. Electrochem. Soc.* **2019**, *166* (5), H3084–H3090. <https://doi.org/10.1149/2.0141905jes>.
- (26) O'Donnell, S.; Smith, A.; Carbone, A.; Maggard, P. A. Structure, Stability, and Photocatalytic Activity of a Layered Perovskite Niobate after Flux-Mediated Sn(II) Exchange. *Inorg. Chem.* **2022**, *61* (9), 4062–4070. <https://doi.org/10.1021/acs.inorgchem.1c03846>.
- (27) O'Donnell, S.; Chung, C.-C.; Carbone, A.; Broughton, R.; Jones, J. L.; Maggard, P. A. Pushing the Limits of Metastability in Semiconducting Perovskite Oxides for Visible-Light-Driven Water Oxidation. *Chem. Mater.* **2020**, *32* (7), 3054–3064. <https://doi.org/10.1021/acs.chemmater.0c00044>.

- (28) Maeda, K.; Teramura, K.; Masuda, H.; Takata, T.; Saito, N.; Inoue, Y.; Domen, K. Efficient Overall Water Splitting under Visible-Light Irradiation on  $(\text{Ga}_{1-x}\text{Zn}_x)(\text{N}_{1-x}\text{O}_x)$  Dispersed with Rh–Cr Mixed-Oxide Nanoparticles: Effect of Reaction Conditions on Photocatalytic Activity. *J. Phys. Chem. B* **2006**, *110* (26), 13107–13112. <https://doi.org/10.1021/jp0616563>.
- (29) Lopato, E. M.; Eikey, E. A.; Simon, Z. C.; Back, S.; Tran, K.; Lewis, J.; Kowalewski, J. F.; Yazdi, S.; Kitchin, J. R.; Ulissi, Z. W.; et al. Parallelized Screening of Characterized and DFT-Modeled Bimetallic Colloidal Cocatalysts for Photocatalytic Hydrogen Evolution. *ACS Catal.* **2020**, *10* (7), 4244–4252. <https://doi.org/10.1021/acscatal.9b05404>.
- (30) Song, W.; Lopato, E. M.; Bernhard, S.; Salvador, P. A.; Rohrer, G. S. High-Throughput Measurement of the Influence of pH on Hydrogen Production from  $\text{BaTiO}_3/\text{TiO}_2$  Core/Shell Photocatalysts. *Appl. Catal. B Environ.* **2020**, *269*, 118750. <https://doi.org/10.1016/j.apcatb.2020.118750>.
- (31) Zhang, M.; Salvador, P. A.; Rohrer, G. S. Influence of Particle Size and Shape on the Rate of Hydrogen Produced by Al-Doped  $\text{SrTiO}_3$  Photocatalysts. *J. Am. Ceram. Soc.* **2022**, *00*, 1–11. <https://doi.org/10.1111/jace.18488>.
- (32) Zhao, Z.; Willard, E. J.; Li, H.; Wu, Z.; Castro, R. H. R.; Osterloh, F. E. Aluminum Enhances Photochemical Charge Separation in Strontium Titanate Nanocrystal Photocatalysts for Overall Water Splitting. *J. Mater. Chem. A* **2018**, *6* (33), 16170–16176. <https://doi.org/10.1039/C8TA05885G>.
- (33) Zhang, M.; Salvador, P. A.; Rohrer, G. S. Influence of pH and Surface Orientation on the Photochemical Reactivity of  $\text{SrTiO}_3$ . *ACS Appl. Mater. Interfaces* **2020**. <https://doi.org/10.1021/acami.0c04351>.
- (34) Zhao, Z.; Goncalves, R. V.; Barman, S. K.; Willard, E. J.; Byle, E.; Perry, R.; Wu, Z.; Huda, M. N.; Moulé, A. J.; Osterloh, F. E. Electronic Structure Basis for Enhanced Overall Water Splitting Photocatalysis with Aluminum Doped  $\text{SrTiO}_3$  in Natural Sunlight. *Energy Environ. Sci.* **2019**, *12* (4), 1385–1395. <https://doi.org/10.1039/C9EE00310J>.
- (35) Sano, T.; Saylor, D. M.; Rohrer, G. S. Surface Energy Anisotropy of  $\text{SrTiO}_3$  at 1400°C in

- Air. J. Am. Ceram. Soc.* **2003**, *86* (11), 1933–1939. <https://doi.org/10.1111/j.1151-2916.2003.tb03584.x>.
- (36) Rheinheimer, W.; Baeurer, M.; Chien, H.; Rohrer, G. S.; Handwerker, C. A.; Blendell, J. E.; Hoffmann, M. J. The Equilibrium Crystal Shape of Strontium Titanate and Its Relationship to the Grain Boundary Plane Distribution. *ACTA Mater.* **2015**, *82*, 32–40. <https://doi.org/10.1016/j.actamat.2014.08.065>.
- (37) Rohrer, G. S.; Rohrer, C. L.; Mullins, W. W. Coarsening of Faceted Crystals. *J. Am. Ceram. Soc.* **2002**, *85* (3), 675–682. <https://doi.org/10.1111/j.1151-2916.2002.tb00149.x>.
- (38) Qin, Y.; Fang, F.; Xie, Z.; Lin, H.; Zhang, K.; Yu, X.; Chang, K. La,Al-Codoped SrTiO<sub>3</sub> as a Photocatalyst in Overall Water Splitting: Significant Surface Engineering Effects on Defect Engineering. *ACS Catal.* **2021**, *11* (18), 11429–11439. <https://doi.org/10.1021/acscatal.1c02874>.
- (39) Vovk, G.; Chen, X.; Mims, C. A. In Situ XPS Studies of Perovskite Oxide Surfaces under Electrochemical Polarization. *J. Phys. Chem. B* **2005**, *109* (6), 2445–2454. <https://doi.org/10.1021/jp0486494>.
- (40) Zhu, Y.; Salvador, P. A.; Rohrer, G. S. Controlling the Relative Areas of Photocathodic and Photoanodic Terraces on the SrTiO<sub>3</sub>(111) Surface. *Chem. Mater.* **2016**, *28* (14), 5155–5162. <https://doi.org/10.1021/acs.chemmater.6b02205>.
- (41) Nagarkar, P. V.; Searson, P. C.; Gealy, F. D. Effect of Surface Treatment on SrTiO<sub>3</sub>: An X-ray Photoelectron Spectroscopic Study. *J. Appl. Phys.* **1991**, *69* (1), 459–462. <https://doi.org/10.1063/1.347685>.
- (42) Smigelskas, A. D. Zinc Diffusion in Alpha Brass. *Trans. Aime* **1947**, *171*, 130–142.
- (43) Paul, A.; van Dal, M. J. H.; Kodentsov, A. A.; van Loo, F. J. J. The Kirkendall Effect in Multiphase Diffusion. *Acta Mater.* **2004**, *52* (3), 623–630. <https://doi.org/10.1016/j.actamat.2003.10.007>.
- (44) Yin, Y.; Rioux, R. M.; Erdonmez, C. K.; Hughes, S.; Somorjai, G. A.; Alivisatos, A. P. Formation of Hollow Nanocrystals Through the Nanoscale Kirkendall Effect. *Science*

- (80-). **2004**, *304* (5671), 711–714. <https://doi.org/10.1126/science.1096566>.
- (45) Li, G.; Zhu, J.; Tian, W.; Ma, C. Preparation and Optical Property of Anatase Hollow Microsphere with Mesoporosity. *Mater. Res. Bull.* **2009**, *44* (2), 271–275. <https://doi.org/10.1016/j.materresbull.2008.06.012>.
- (46) Liu, J.; Maarroof, A. I.; Wieczorek, L.; Cortie, M. B. Fabrication of Hollow Metal “Nanocaps” and Their Red-Shifted Optical Absorption Spectra. *Adv. Mater.* **2005**, *17* (10), 1276–1281. <https://doi.org/10.1002/adma.200500035>.
- (47) Kumar, A.; Santangelo, P. G.; Lewis, N. S. Electrolysis of Water at SrTiO<sub>3</sub> Photoelectrodes: Distinguishing between the Statistical and Stochastic Formalisms for Electron-Transfer Processes in Fuel-Forming Photoelectrochemical Systems. *J. Phys. Chem.* **1992**, *96* (2), 834–842. <https://doi.org/10.1021/j100181a057>.
- (48) Ruddlesden, S. N.; Popper, P. The Compound Sr<sub>3</sub>Ti<sub>2</sub>O<sub>7</sub> and Its Structure. *Acta Crystallogr.* **1958**, *11* (1), 54–55. <https://doi.org/10.1107/S0365110X58000128>.
- (49) Yamada, K.; Suzuki, H.; Abe, R.; Saeki, A. Complex Photoconductivity Reveals How the Nonstoichiometric Sr/Ti Affects the Charge Dynamics of a SrTiO<sub>3</sub> Photocatalyst. *J. Phys. Chem. Lett.* **2019**, *10* (8), 1986–1991. <https://doi.org/10.1021/acs.jpcclett.9b00880>.
- (50) Kato, H.; Sasaki, Y.; Shirakura, N.; Kudo, A. Synthesis of Highly Active Rhodium-Doped SrTiO<sub>3</sub> Powders in Z-Scheme Systems for Visible-Light-Driven Photocatalytic Overall Water Splitting. *J. Mater. Chem. A* **2013**, *1* (39), 12327–12333. <https://doi.org/10.1039/C3TA12803B>.
- (51) Sun, X.; Mi, Y.; Jiao, F.; Xu, X. Activating Layered Perovskite Compound Sr<sub>2</sub>TiO<sub>4</sub> via La/N Codoping for Visible Light Photocatalytic Water Splitting. *ACS Catal.* **2018**, *8* (4), 3209–3221. <https://doi.org/10.1021/acscatal.8b00369>.
- (52) Goto, Y.; Hisatomi, T.; Wang, Q.; Higashi, T.; Ishikiriyama, K.; Maeda, T.; Sakata, Y.; Okunaka, S.; Tokudome, H.; Katayama, M.; et al. A Particulate Photocatalyst Water-Splitting Panel for Large-Scale Solar Hydrogen Generation. *Joule* **2018**, *2* (3), 509–520. <https://doi.org/10.1016/j.joule.2017.12.009>.

- (53) Lyu, H.; Hisatomi, T.; Goto, Y.; Yoshida, M.; Higashi, T.; Katayama, M.; Takata, T.; Minegishi, T.; Nishiyama, H.; Yamada, T.; et al. An Al-Doped SrTiO<sub>3</sub> Photocatalyst Maintaining Sunlight-Driven Overall Water Splitting Activity for over 1000 h of Constant Illumination. *Chem. Sci.* **2019**, *10* (11), 3196–3201. <https://doi.org/10.1039/C8SC05757E>.
- (54) Chiang, T. H.; Lyu, H.; Hisatomi, T.; Goto, Y.; Takata, T.; Katayama, M.; Minegishi, T.; Domen, K. Efficient Photocatalytic Water Splitting Using Al-Doped SrTiO<sub>3</sub> Coloaded with Molybdenum Oxide and Rhodium–Chromium Oxide. *ACS Catal.* **2018**, *8* (4), 2782–2788. <https://doi.org/10.1021/acscatal.7b04264>.

## Chapter 10: Integrated Discussion and Future Work

A photocatalytic reaction consists of three major processes, light absorption, charge carrier transport and surface reactions. My work focuses on accelerating the charge transport, and the results discussed in previous chapters illustrate the feasibility to improve it by modifying the space charge region, which I call space charge engineering. Space charge engineering could be conducted by many approaches such as adjusting solution pH, building internal dipolar fields, tailoring particle shape and particle size and introducing foreign elements.

In Chapter 4,  $\text{La}_2\text{Ti}_2\text{O}_7$  was studied because there are two internal electric fields inside the crystals. Previous studies show that both ferroelectric polarization and crystal orientation affect the transport of charge carriers, and in this material, they might drive the charge carriers to different directions. The results illustrate that the photochemical reactivity is only influenced by crystal orientation, implying that the band bending induced by the ferroelectricity cannot overcome the intrinsic potential difference at different surfaces. Therefore, ferroelectricity does not always contribute to photocatalytic reactivity, especially for a crystal with a strongly anisotropic structure.

In Chapter 5, the pH effect has been investigated on  $\text{SrTiO}_3$  single crystals. Solution pH could be considered as an external electric field, and there are more negative charges adsorbed to the surface at a higher pH, leading to an increasing upward band bending. This can be easily understood with the Nernst equation. The increasing upward band bending can promote the transport of holes to the surface but limit the transport of electrons. As the overall reaction depends on the slower one of the two half reactions, the highest reactivity appears at an intermediate pH where neither the photocathodic nor the photoanodic reaction limits the reactivity. Note that the idea that balancing the two half reaction rates contributes to overall reactivity is frequently employed in this thesis.

In Chapter 6, we transit from marker reactions to water splitting and explore how particle shape and size affects the reactivity of Al-doped  $\text{SrTiO}_3$ . The shape study focuses on tuning the surface area ratio of (110) facets to (100) facets. (100) and (110) facets serve as cathodic and anodic sites, respectively, and the results suggest that the reactivity is optimized at a surface area ratio where the two half reactions balance with each other. This is fairly similar to the story in the pH effect. As for the size effect, the main point is not just that larger particles are better. What matters is an appropriate particle size relative to the space charge width and light penetration length. The ideal

particle is close to a condition where twice the space charge width  $\leq$  particle size  $\leq$  light penetration length. In a small particle, assuming the potential is constant at the surface, the band cannot completely relax to the bulk level, therefore the particle cannot fully take advantage of band bending. If the particle is too large, this benefit will be reduced due to the formation of long flat band region as well as the low surface area ratio (few reaction sites). Hence, there should be an optimal particle size that balances these factors. Unfortunately, in my study I did not observe this optimum, as I could not prepare even larger crystals. One should note that when measuring the size effect on reactivity, particle size should be the only variable parameter in the system. For example, it is not appropriate to compare large particles prepared via high temperature solid state synthesis and small particles prepared with hydrothermal approach since their chemical compositions and defect chemistry could be quite different.

Chapter 7 and Chapter 8 are two parts of the study on understanding the flux synthesized Al-doped SrTiO<sub>3</sub>. Chapter 7 focuses on the SrCl<sub>2</sub> flux, and the results clearly explain why it is essential for making an active catalyst. To my understanding, this “magical” flux treatment provides a very suitable SrTiO<sub>3</sub> surface for water splitting, including a higher hydroxyl density, a higher Sr/Ti ratio and possibly a higher oxygen vacancy concentration. These changes also lead to a decreased surface potential and an enhanced charge separation property between (100) and (110) surfaces. It is also found that the flux treatment in different crucibles yields catalysts with different properties. Many crucibles have been tested, including magnesia, platinum and quartz, and elsewhere yttria, but the flux treatment in an alumina crucible yields the highest reactivity. This is not because it can provide Al<sup>3+</sup>. It was not possible to produce a catalyst with the same reactivity in a platinum crucible, even when sufficient Al<sup>3+</sup> is added to the flux. It was shown that the flux reacts with the alumina crucible. Therefore, the molten salt in the alumina crucible has a different composition than in the others, and this might be the reason that the catalyst is more reactive.

Chapter 8 focus on the effect of dopants. Al<sup>3+</sup>, Mg<sup>2+</sup> and Ga<sup>3+</sup> dopants all contribute to the reactivity, and the doping concentration has a significant effect. We provide a compensation model to explain how introducing acceptor dopants increases the width of the space charge region, and the optimal doping concentration is close to a situation where the oxygen vacancies are fully compensated by accepters. One question is that what actually happens after the compensation point. From the Brouwer diagram, the semiconductor will become p-type, but very few studies

show that they can really make these titanates p-type at room pressure. There are two explanations I can come up with to illustrate the “over-doped” condition. First, there is a solubility limit for the dopants, meaning that the excess dopants cannot dissolve into the crystal but form some impurity phases. Second, the origin of band bending is the different work functions of the semiconductor and the solution. Decreasing the free electron concentration will lower the Fermi level, narrow the potential difference, and consequently reduce the degree of band bending. If so, this is again an optimization problem that we are tuning the increasing space charge length and decreasing band bending by adjusting doping concentration. To sum up, Al-doping provides a suitable structure in the bulk, and the molten SrCl<sub>2</sub> flux treatment provides a highly reactive surface. I have also tried Fe<sup>3+</sup> doping, and the results are shown in Appendix 2. As a multi-valence transition metal, the effect of Fe<sup>3+</sup> is more complex because of the formation of midgap defect states.

The ion exchange reaction introduced in Chapter 9 provides a promising approach to develop new efficient catalysts. The main point of the chapter is that the A-site cations in a perovskite oxide can be exchanged with smaller cations from the molten salt, through which we synthesized highly efficient SrTiO<sub>3</sub> with BaTiO<sub>3</sub> as a precursor. It is a bit surprising that ion exchange can happen in a closely packed structure. What’s more interesting is the difference between this ion exchanged SrTiO<sub>3</sub> and normal SrTiO<sub>3</sub>. At present, it is thought that the uneven Cl distribution and the planar SrO defects led to the improved reactivity, but more research should be carried out to fully understand this material in the future.

SrTiO<sub>3</sub> might never become an ideal photocatalyst under solar illumination due to the large band gap. Thus, future work should focus on materials with smaller band gaps. As exchanging alkali earth metal cations into titanates cannot narrow the band gap, introducing transition metal ions is worth trying. It is also promising to modify other perovskite system with ion exchange, such as ANbO<sub>3</sub>, ASnO<sub>3</sub>, AGeO<sub>3</sub>. Besides native oxides, we should also attempt to explore other systems, such as oxynitrides, magneli phases, and high-entropy ceramics. Owing to the rapid feedback, the PAPCR provides a new mode of the photocatalyst development. At present, combining DFT and machine learning realizes a powerful approach to predict novel photocatalysts, and the PAPCR accelerates the screening of the newly developed catalysts and the optimization of the synthesis route. Ideally, the knowledge on space charge engineering learned from SrTiO<sub>3</sub> can be employed to optimize these new photocatalysts.

## Appendix I: Determining the Effect of Surface Orientation on Photochemical Reactivity using Photochemical Marker Reactions

In semiconductor-based photocatalysts, the reactivity is always found to be influenced by the surface orientation.<sup>1-4</sup> This orientation effect can be roughly divided into two categories. The first category is that some orientations behave more reactive than others. For example, in anatase  $\text{TiO}_2$ ,  $\{001\}$  surfaces provides much higher reaction rate in photo degradation of methyl orange than  $\{010\}$  and  $\{101\}$  surfaces.<sup>5</sup> Preparing crystals with a higher surface ratio of this highly reactive surface is beneficial to the reactivity. The other category is that when two surfaces (facets) coexist, one orientation is more photocathodic while the other one is more photoanodic. One of the most famous examples is  $\text{BiVO}_4$ , shown in Figure 11-1, whose reduction reactions occur on  $\{010\}$  facets and oxidation reactions occur on  $\{110\}$  facets. The reason for this selectivity is that photogenerated electrons and holes tend to migrate to different facets and participate in different reactions.

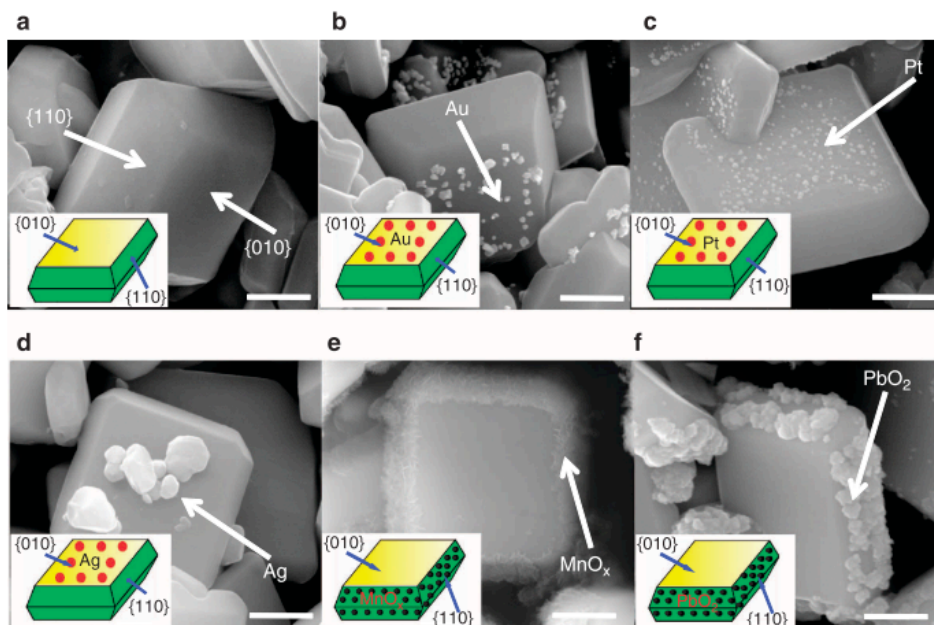


**Figure 11-1:** SEM images of the surface of (a) bare  $\text{BiVO}_4$ , and the surface after photodepositing (b) Au, (c) Pt, (d) Ag, (e)  $\text{MnO}_2$ , (f)  $\text{PbO}_2$ . Scale bar, 500 nm. Reproduced from ref.<sup>6</sup>

There are a lot of theories explaining this orientation effect on semiconductor based photocatalysts, for instance: (1) Surface atomic structure: Surface with different orientations may have different atomic arrangements so that species in solutions will selectively adsorb and desorb on specific surface sites due to the different activation energy. To be specific, one commonly used criterion to predict highly reactive orientation is to measure the density of undercoordinated atoms. In anatase, the (010) surface and the (001) surface have 100%  $Ti_{5c}$  (five-coordinated) site, while the (101) surface has 50%  $Ti_{5c}$  site and 50%  $Ti_{6c}$  (six-coordinated) sites.<sup>7,8</sup> Illustration of the surface structure of the three surfaces are shown in Figure 11-2. These undercoordinated atoms are more likely to serve as adsorption/reaction sites and improve the reactivity. It is found that the (010) surface is more reactive than the (101) surface, but the (001) surface was the least reactive, which is likely owing to its lower conduction band edge and smaller overpotential.<sup>9</sup> In  $Co_3O_4$ , it is known that (001) and (111) surfaces contain only  $Co^{2+}$  cations, while (110) surface contains mostly  $Co^{3+}$  cations. Therefore,  $Co_3O_4$  nanobelts with more (110) surfaces exposed show much higher reactivity than nanocubes exposed only (001) surfaces for photocatalytic CO oxidation.<sup>10</sup>

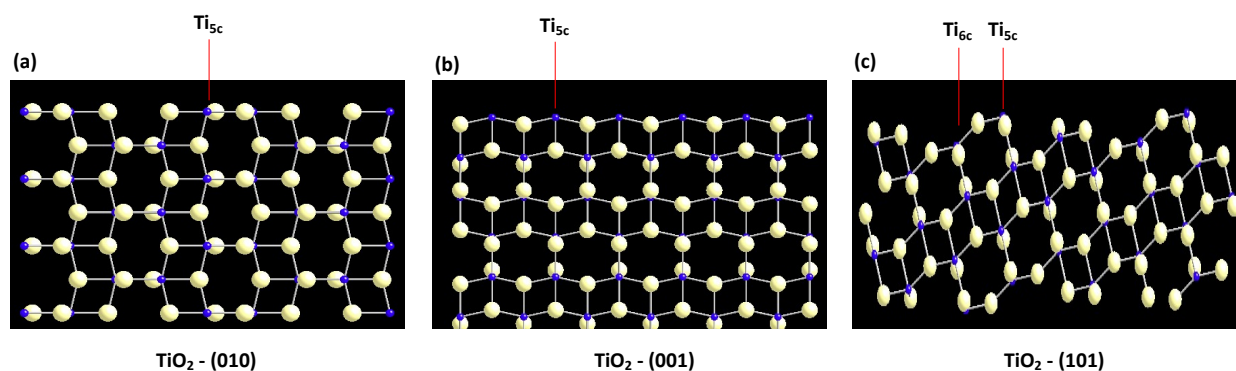


**Figure 11-2:** Surface atomic structure of anatase (a) (010), (b) (001) and (c) (010) surface.

(2) Electronic band structure: From the band theory, it is known that in a periodic lattice of atoms, the electron energy varies from point to point in Brillouin zone. Given the same energy level in the bulk, surfaces with different orientations will have different degrees of band bending and band edge positions. Hence, electrons will move to an orientation with a lower band edge while holes will move to an orientation with a higher band edge. This contributes to a separation of photogenerated charge carriers and arises an orientation dependent photocatalytic reactivity. For example, BiOBr has been well studied by Li and coworkers.<sup>11</sup> Two types of nanosheets were synthesized, one exposes (001) and (110) facets, denoted as BiOBr-(001), and the other one exposes (010) and (102) facets, denoted as BiOBr-(010). The band structure and density of states

were calculated by DFT method, showing that when (001) and (110) facets coexist, both valence band bottom and conduction band top positions of (001) facets are higher than those of (110) facets, respectively. Hence, (110) facet is supposed to be photocathodic and (001) facet is photoanodic. Furthermore, the valence band bottom and conduction band top positions of (010) facets are higher than those of (102) facets, as shown in Figure 11-3, meaning that (102) facet is more photocathodic, and (010) facet is more photoanodic. Photochemical marker reaction was carried out, showing that Pt reductions occurred on (110) and (102) facets, and Mn oxidations occurred on (001) and (010) facets, which is consistent with the calculated band structure. Similar results are found on  $\text{Ag}_2\text{O}$ ,<sup>12</sup>  $\text{BiVO}_4$ ,<sup>13</sup>  $\text{BiOI}$ ,<sup>14</sup>  $\text{La}_2\text{Ti}_2\text{O}_7$ ,<sup>15,16</sup> etc. It is worth noting that, except band edges, detailed band structure also provides information like band gap, effective mass of charge carriers and charge migration rate. All of these factors may influence the photocatalytic reactivities of materials and give rise to orientation effects.

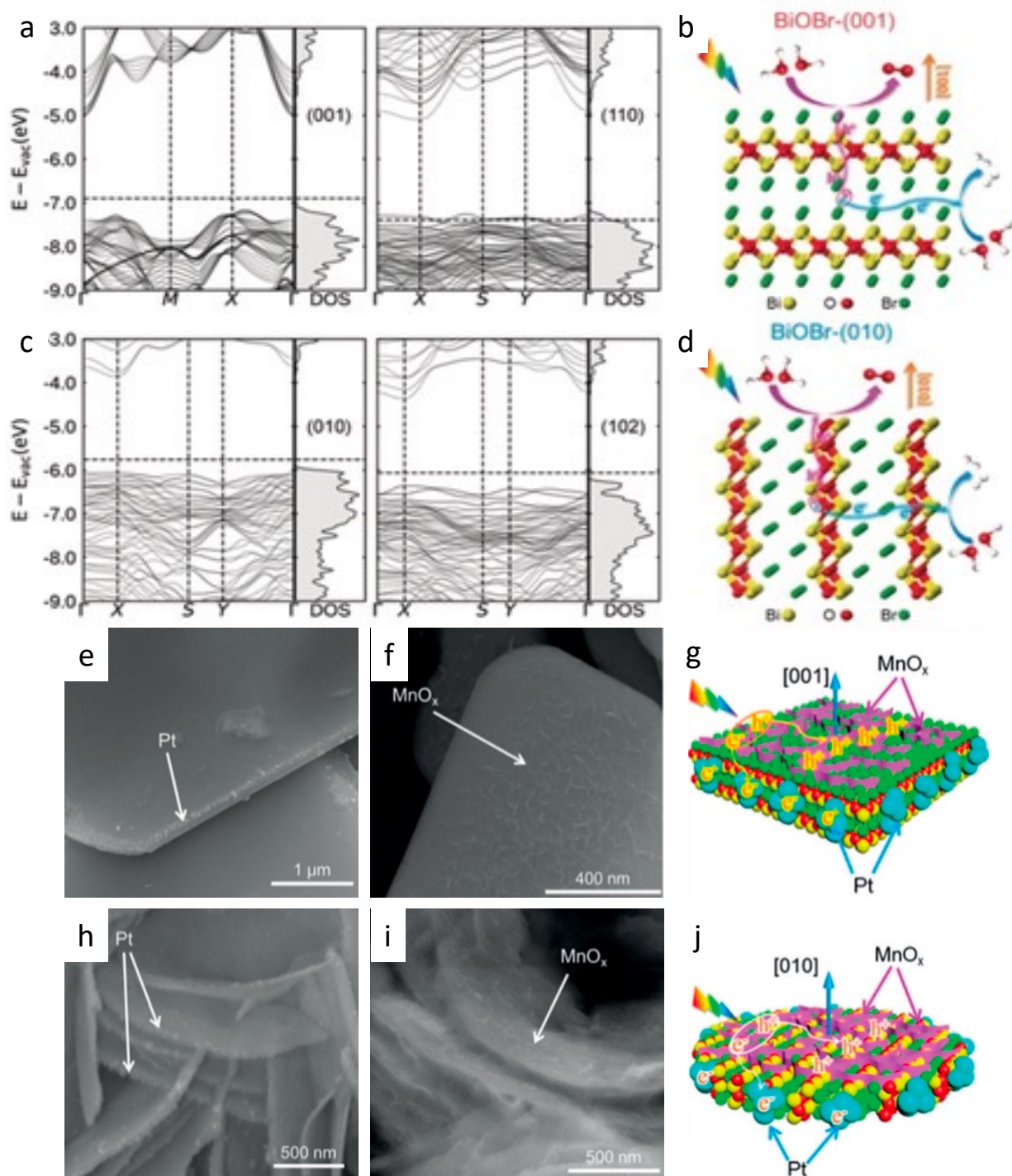


**Figure 11-3:** DFT calculated band structure and density of states (DOS) of BiOBr (a) (001), (110) and (c) (010), (102) facets. Crystal structure of BiOBr (001) and BiOBr (010) are illustrated in (b) and (d). ((e) (f)) SEM images of BiOBr-(001) after in situ photodeposited with Pt and  $MnO_x$ . ((h) (i)) SEM images of BiOBr-(010) after in situ photodeposited with Pt and  $MnO_x$ . Schematic illustration of photoexcited charge distributions on BiOBr-(001) and BiOBr-(010) are shown in (g) and (j). Adapted from Ref.<sup>11</sup>

(3) Surface energy and surface potential: With the help of surface characterization techniques, like KFM, it is possible to measure the potential of surfaces with different orientations. It is found that surface with more positive potential will become more photocathodic, and surface with more negative potential will become more photoanodic. This can be easily understood by considering the electronic attraction between charge carriers and surface. The surface potential has been measured on the grains of an  $\alpha$ -Fe<sub>2</sub>O<sub>3</sub> ceramic surface, and the (1 $\bar{1}$ 02) surface was tested to have the most positive potential, shown in Figure 11-4. Next, the photoreduction of Ag<sup>+</sup> was carried out on the same sample, and grains close to (1 $\bar{1}$ 02) have the largest Ag product coverage. This means that electrons are more likely to move to (1 $\bar{1}$ 02) surface and enhance the photocathodic reactivity. It is noted that the surface potential was usually measured in air by conventional KFM, therefore, it is likely to differ from the actual potential in solutions, due to the charge compensation by solution species. A more recent study has measured the electrostatic and hydration forces of faceted SrTiO<sub>3</sub> nanoparticles in aqueous electrolyte at variable pH.<sup>17</sup> This paper demonstrated that the surface potential of (100) surface is roughly 40 mV higher than (110) surface at pH 6, which is consistent with previous works on the spatial selectivity between the two surfaces.<sup>18-21</sup>

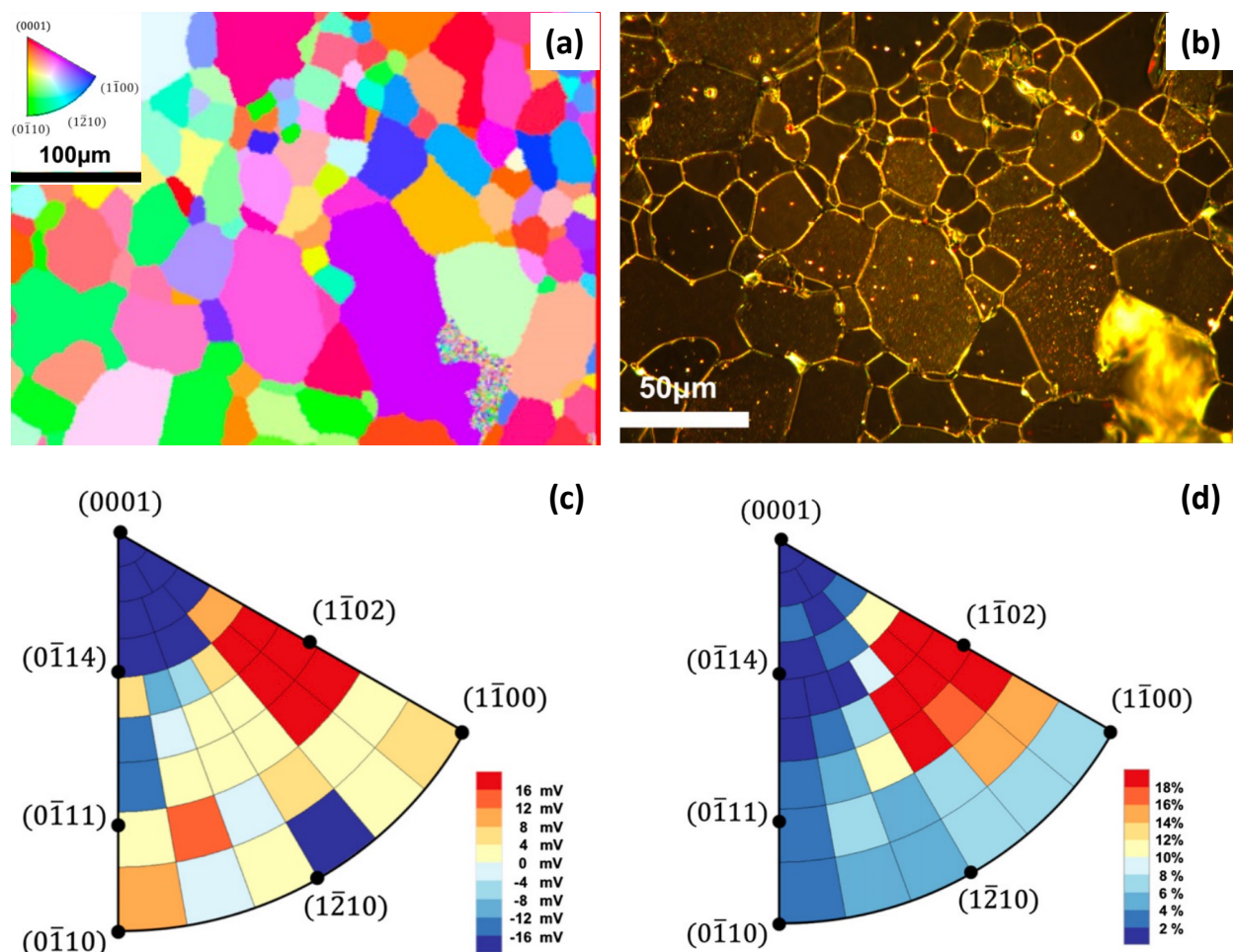


**Figure 11-4:** (a) Orientation map of an  $\alpha$ - $\text{Fe}_2\text{O}_3$  ceramic surface. (b) Dark-field optical microscopy images of the  $\alpha$ - $\text{Fe}_2\text{O}_3$  surface after the photochemical reduction of Ag. The brighter contrasts correspond to silver products. (c) The average relative potential value measured by KFM (for 167 grains from 16 different images) plotted versus orientation on a stereographic projection broken into 39 regions. (d) A similar plot of the average activity measured from DF-OM images. Adapted from ref.<sup>22</sup>

(4) Electrical conductivity: In crystalline materials, the electrical conductivity can vary from highly conductive to nonconductive on different orientations. This will influence the charge migration rate as well as the degree of band bending, giving rise to anisotropic photocatalytic reactivity. Huang's group focus on this field, employing a probe technique that can directly measure the electric conductivity of nano particles.<sup>23</sup> Extensive studies have been carried out on  $\text{Cu}_2\text{O}$  crystals shaped in cubic, octahedral and rhombic dodecahedral. It is found that (111) facets (octahedral) are highly conductive, while the (100) facets (cubes) are moderately conductive and (110) facets (rhombic dodecahedral) are the least conductive. This anisotropic conductivity is understood by an assumption that electrons will meet a larger barrier if the degree of band bending is large. In

this way, the order of the degree of band bending should be  $(110) > (100) > (111)$ .<sup>24</sup> Together with light absorption and emission data, a modified band structure was reported by the same group, shown in Figure 11-5(f). The three orientations not only have different degrees of band bending but also different band gaps because of the different particle size. The rhombic dodecahedron has a smaller band gap and therefore a better reactivity. This is supported by the photocatalytic reactivity on MO degradation that  $\text{Cu}_2\text{O}$ - (110) is the most reactive.<sup>25,26</sup> Similar theories have been proposed to  $\text{Ag}_2\text{O}$ ,<sup>27</sup>  $\text{Ag}_3\text{PO}_4$ ,<sup>28</sup>  $\text{PbS}$ <sup>29</sup> and  $\text{SrTiO}_3$ .<sup>30</sup>

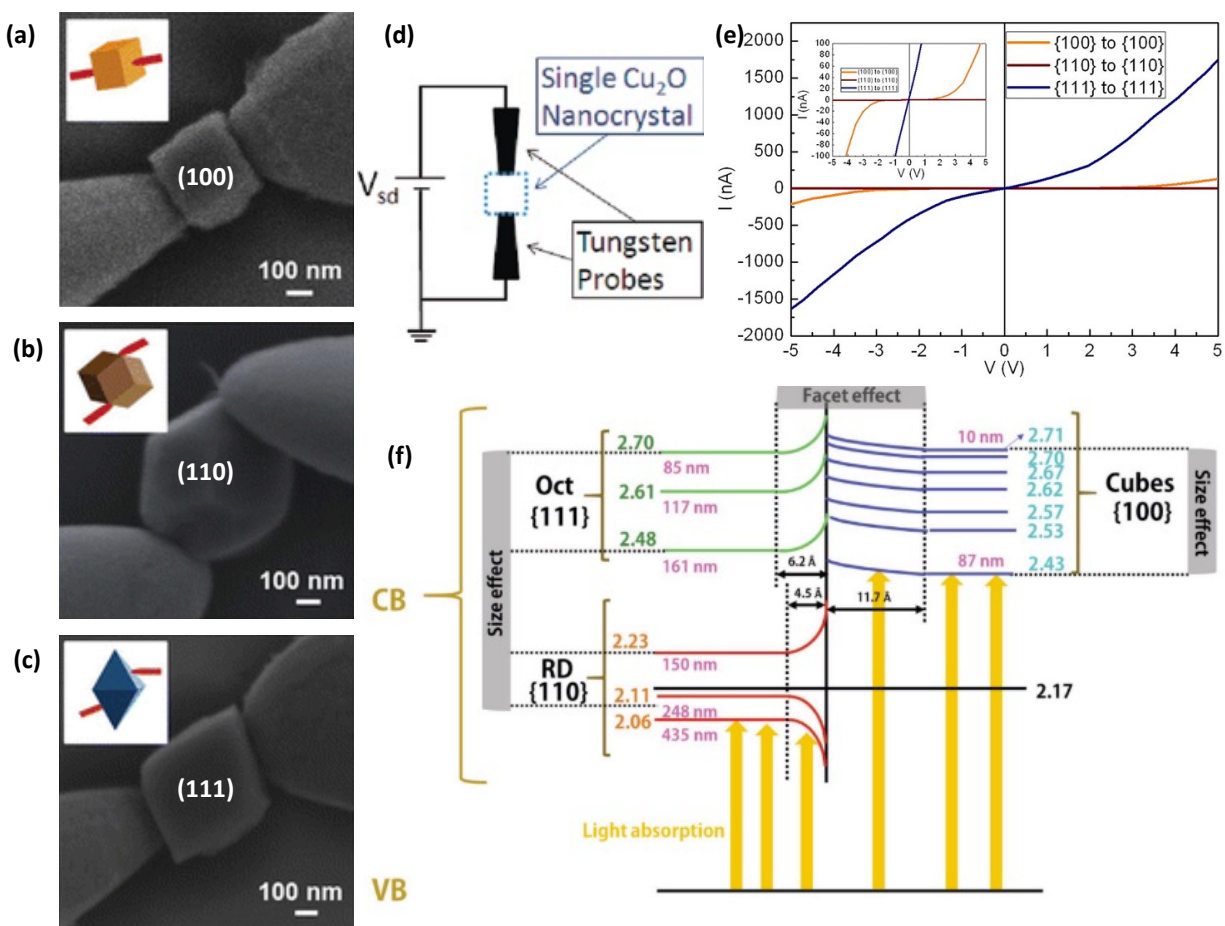


**Figure 11-5:** (a–c) Tungsten probes contacting single  $\text{Cu}_2\text{O}$  crystals for their electrical conductivity measurements. (d) Schematic illustration of the measurement set up. (e) I–V curves for the (100), (110), and (111) faces of  $\text{Cu}_2\text{O}$  crystals. (f) Modified general band diagram of  $\text{Cu}_2\text{O}$  crystals accounting for their observed optical size and facet effects. Adapted from ref.<sup>23,24,26</sup>

(5) Optical property: It is found that nanoparticles exposing different crystal facets might have shifted light absorption bands.<sup>26</sup> For instance, anatase  $\text{TiO}_2$  nano particles with 18% (001) facets show a raised conduction band edge by 0.1 eV and higher photocatalytic reactivity compared with

particles with 72% (001) facets.<sup>31</sup> In  $\text{Ag}_3\text{PO}_4$ , the absorption edge of (110) plane bounded rhombic dodecahedron microcrystals shifted to longer wavelength and absorb more light compared with (100) plane bounded cubed microcrystals,<sup>32,33</sup> shown in Figure 11-6 (b). For  $\text{Cu}_2\text{O}$ , given the same crystal size, cubes will show a more redshifted absorption band than that of octahedra.<sup>34</sup> Similar results are found for  $\text{CeO}_2$  that nanorods with (110) facets dominated showed smaller bandgaps than nanocubes with (100) facets dominated.<sup>35</sup>

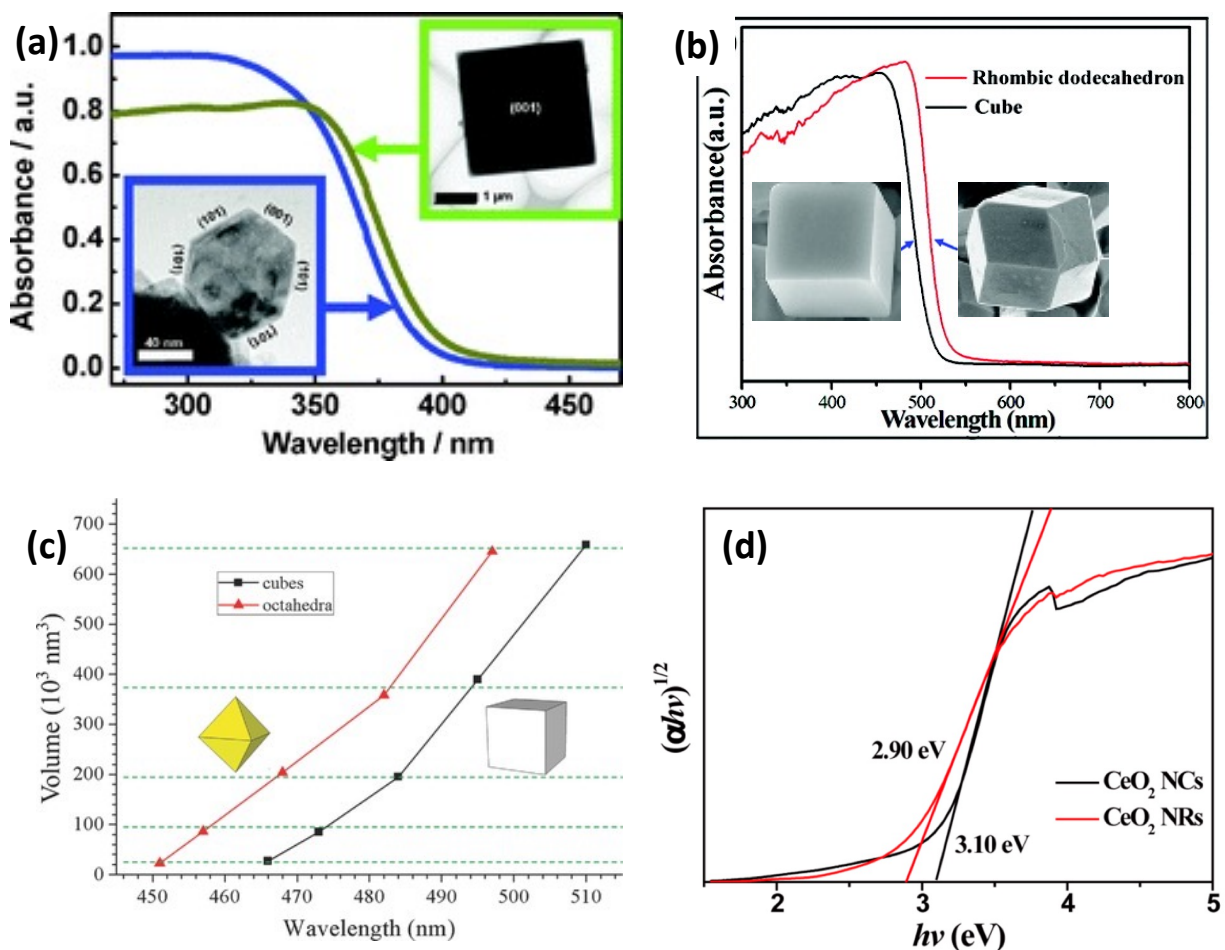


**Figure 11-6:** (a) UV-visible spectra of anatase  $\text{TiO}_2$  particles exposing 18% (001) facets and 72% (001) facets, reproduced from ref.<sup>31</sup> (b) UV-vis diffusive reflectance spectra of  $\text{Ag}_3\text{PO}_4$  nano cubes and rhombic dodecahedrons, adapted from ref.<sup>32</sup> (c) A plot summarizing the volume variation of  $\text{Cu}_2\text{O}$  octahedra and cubes with respect to their UV-vis absorption band positions reproduced from ref.<sup>34</sup> (d) Plots of  $(\alpha h\nu)^{1/2}$  versus photon energy ( $h\nu$ ) of  $\text{CeO}_2$  nanocrystals, reproduced from ref.<sup>35</sup>

It is noted that these explanations are highly correlated to each other but not isolated. In literatures, the orientation effects are usually explained in combined theories. Table 11-1 lists 21 catalysts that have been reported to exhibit orientation dependent photochemical properties.

**Table 11-1:** Summary of photocatalysts with orientation dependent photochemical reactivities.

Materials	Structure	Space group	Photocathodic Orientation	Photoanodic Orientation	Explanation	Ref
Ag <sub>2</sub> O	bcc	<i>Pn3m</i>	{100} most reactive		Surface energy/potential; electric conductivity	12,27,36
Ag <sub>3</sub> PO <sub>4</sub>	bcc	<i>P4̄3n</i>	{110} more reactive than {100}		Surface energy/potential; optical property	28,32,37
BiVO <sub>4</sub>	monoclinic	<i>I2/b</i>	{010}	{110}	Adsorption effect; band structure; electric conductivity	6,13,38-40
BiOBr	tetragonal	<i>P4/nmm</i>	(102), (110)	(010), (001)	Band structure	41
BiOCl	tetragonal	<i>P4/nmm</i>	(001)	(110)	Electric conductivity; surface atomic structure	42,43
BiOI	tetragonal	<i>P4/nmm</i>	(100)	(001)	Electric conductivity; band structure; optical property	14
CaTiO <sub>3</sub>	orthorhombic	<i>Pcmm</i>	(111)	(011)	Surface energy/potential; Band structure	44
Cu <sub>2</sub> WS <sub>4</sub>	Tetragonal	<i>P4̄2m</i>	(001)	(101)	Band structure	45
CeO <sub>2</sub>	bcc	<i>Im3̄m</i>	(111)	(100)	Band structure; optical property	35,46
Co <sub>3</sub> O <sub>4</sub>	fcc	<i>Fm3̄m</i>	(110) > (001) ≈ (110)		Surface atomic structure	10,47
Cu <sub>2</sub> O	bcc	<i>Pn3m</i>	(100)	(111)	Electric conductivity; band structure	23,24,26,48
			(111) highly conductive; (100) moderately conductive; (110) nonconductive.			
α-Fe <sub>2</sub> O <sub>3</sub>	hexagonal	<i>hR30</i>	(11̄02)	(0001)	Surface potential	22
La <sub>2</sub> Ti <sub>2</sub> O <sub>7</sub>	monoclinic	<i>P2<sub>1</sub></i>	(001)	(010)	Surface potential; band structure	15,16
NaNbO <sub>3</sub>	cubic	<i>Pm3̄m</i>	(111) > (110) > (100)		Ferroelectric polarization; band structure	49
PbS	cubic	<i>Fm3̄m</i>	{110} and {100} highly conductive; {111} nonconductive		Electric conductivity	29
SrTiO <sub>3</sub>	cubic	<i>Pm3̄m</i>	(100)	(110)	Band structure; electric conductivity; surface potential	19,20,30,50-52
TiO <sub>2</sub> anatase	tetragonal	<i>I4<sub>1</sub>/amd</i>	{101}	{001}	Surface atomic structure; surface energy/potential	9,53,54
			{010} > {101} > {001}			
TiO <sub>2</sub> Brookite	orthorhombic	<i>Pbca</i>	(210), (101)	(201)	Surface atomic structure	55
TiO <sub>2</sub> rutile	tetragonal	<i>P4<sub>2</sub>/mmm</i>	{101}, {001}, {111} > {100}, {110}; {110} photocathodic and {011} photoanodic		Surface structure; surface chemistry; charge transport	56-58
WO <sub>3</sub>	monoclinic	<i>P2<sub>1</sub>/c</i>	(200), (020)	(002)	Band structure	59
ZnO	tetragonal	<i>P6<sub>3</sub>mc</i>	(110) > (100) > (001)		Surface potential; band bending	60

The first method to determine the orientation effect is to carry out photodeposition reactions on a faceted submicro or nano particles. In usual, the particle is single crystalline exposing specific facets, resulting from anisotropic crystal growth. For instance, in Figure 11-7, a well-grown crystal exposes violet facets, blue facets, and brown facets. The surface orientation could be determined with electron diffraction in TEM. After carrying photochemical reduction of  $\text{Ag}^+$  and  $\text{Pb}^{2+}$ , Ag particles prefer to nucleate on blue facets and  $\text{PbO}_2$  particles prefer to nucleate on brown facets. This will be good evidence that the photochemical reactivity of this material is anisotropic, the blue surface is more photocathodic and the brown surface is more photoanodic. This method is straight forward, but one important task is to synthesize such high crystallinity faceted particles. These particles are usually grown with hydrothermal methods and molten salt methods. Hence, selecting appropriate surfactants and salts will be critical. Another limitation is that only a small number of orientations can be studied in one experiment.

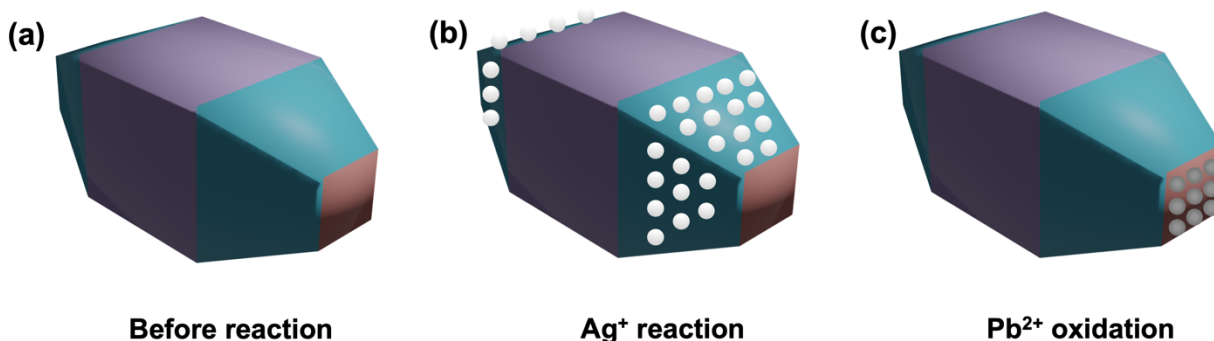


**Figure 11-7:** Schematic of a (a) faceted particle and the same particle after (b) photoreduction of  $\text{Ag}^+$  and (c) photo-oxidation of  $\text{Pb}^{2+}$ .

Another method to determine the orientation effect is to carry out photodeposition on a polycrystalline ceramic surface. Compared with the first method, a ceramic is much easier to prepare, and a larger number of orientations can be studied simultaneously. In a typical experiment, a ceramic sample was prepared and polished. Then a surface region with a large number of grains will be characterized by EBSD to acquire an orientation map. Next, photodeposition reactions will be carried out, and the surface will be characterized by SEM or AFM before and after the reaction. The number of deposits will be counted to identify the photocatalytic reactivity of each grain, and the relationship between photo reactivity and grain orientation will be studied.

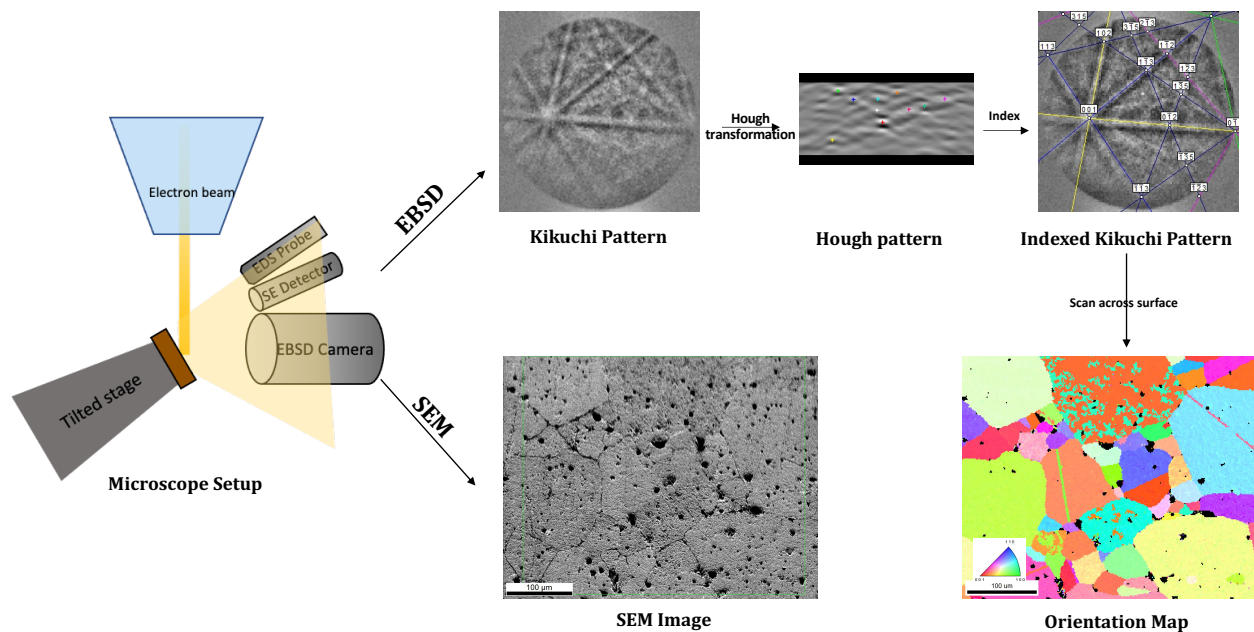


**Figure 11-8:** Illustration of EBSD analysis process of  $\text{Ba}_{0.8}\text{Sr}_{0.2}\text{TiO}_3$  ceramic surface. The pattern was collected and processed through OIM Collection software.

In a EBSD experiment, a well-polished polycrystalline sample was mounted on the SEM stage and tilted to  $70^\circ$  from the horizontal level. The scattered electron will fluoresce a phosphor screen and form a diffraction pattern (Kikuchi pattern). The pattern was then collected by a camera and processed in the EBSD analytical software. In a Kikuchi pattern, the bands and intersections correspond to crystallographic plane and zone axis, respectively. To identify the position of the Kikuchi bands, a Hough transformation will be used, and the Kikuchi bands are seen as peaks in Hough space. Since the detailed crystal information was imported to the software, with the identified Kikuchi band positions and interplanar angles, it is possible to calculate the crystallographic orientation of the pattern. After scanning across a large region of surface, an orientation map will be generated, and this map can be further improved in EBSD software. In Figure 11-8, a large surface region of a  $\text{Ba}_{0.8}\text{Sr}_{0.2}\text{TiO}_3$  ceramic surface was analyzed by the EBSD technique. The SEM image was acquired by a Quanta 200 SEM (FEI Company) with a EBSD analysis system (EDAX) attached. The Kikuchi pattern was collected and processed by OIM Collection software, and the orientation map was processed by OIM Analysis software. Consequently, the surface orientation information of approximately 50 grains is acquired.

Munprom et al. studied the orientation dependent photochemical reactivity of polycrystalline  $\text{BiVO}_4$  ceramic surface, shown in Figure 11-9.<sup>38</sup> Surface orientations of the grains, measured by

EBSD, were correlated to the amounts of reduced and oxidized deposits on each surface. The surface after photochemical  $\text{Ag}^+$  reduction and  $\text{Pb}^{2+}$  oxidation was measured by AFM, shown in Fig 11-9 (a) and (d), with the orientation maps showing in (b) and (e). The bright contrasts in AFM images correspond to photo deposits. All grains are categorized in High reactivity or Low reactivity. It is found that the photochemical reduction of  $\text{Ag}^+$  is strongly favored on (001) surfaces and the oxidation of  $\text{Pb}^{2+}$  is strongly favored on (hk0) surfaces that are perpendicular to (001). This indicates that the photochemical reactivity is strongly dependent on surface orientations, summarizing in (c) and (f). The result is consistent with work on  $\text{BiVO}_4$  particles in Figure 11-1.

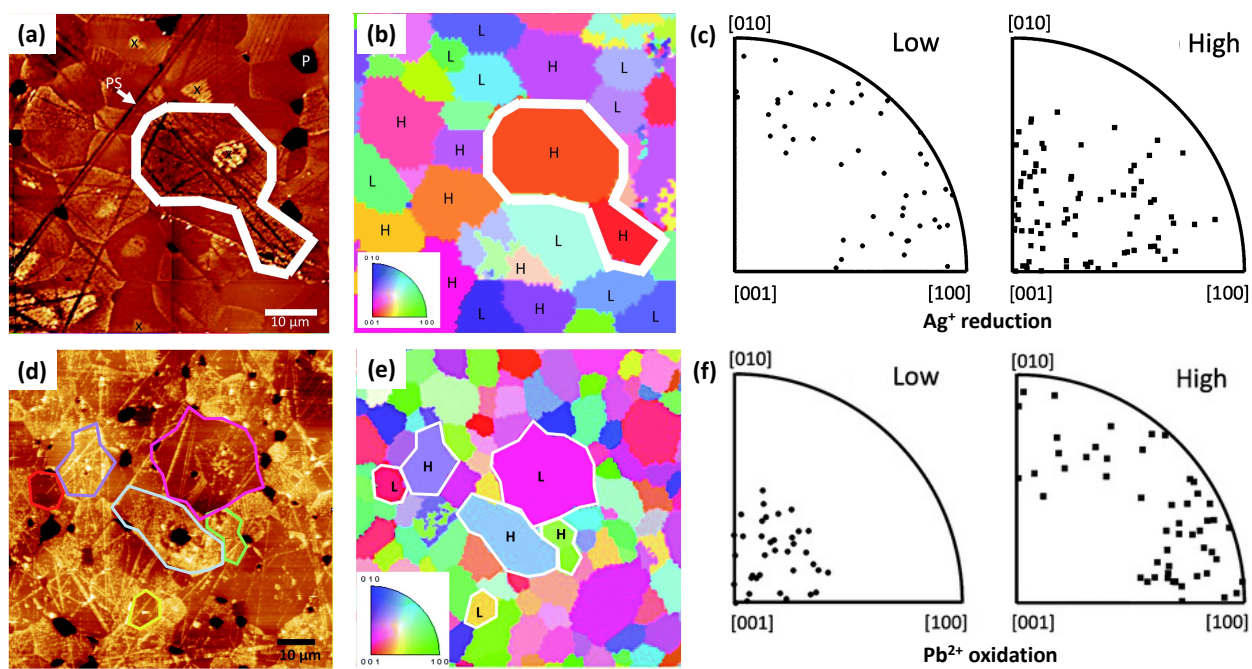


**Figure 11-9:** Topographic AFM image of the  $\text{BiVO}_4$  surface after a photochemical reaction (a) after reduction and (d) after oxidation. The corresponding orientation maps are shown in (b) and (e). Orientations of grains on the  $\text{BiVO}_4$  surface that were classified as low and high reactivity for the photochemical oxidation of (c)  $\text{Ag}^+$  reduction and (f)  $\text{Pb}^{2+}$  oxidation. Each point corresponds to an observed grain and the points are plotted in stereographic projection. Reproduced from Ref.<sup>38</sup>

Both methods discussed here would help people understand the orientation effects and develop more efficient photocatalyst. And materials with such property will be good candidates for photocatalytic water splitting. By photodepositing cocatalyst on (100) and (110) facets separately, the external quantum efficiency of Al-doped  $\text{SrTiO}_3$  can reach 95% under 350 nm to 360 nm illumination, which is one of the efficient catalysts developed so far.<sup>18</sup> It is expected more efficient catalysts could be developed by appropriate facet engineering and morphology controlling.

## References

- (1) Huang, M. H.; Madasu, M. Facet-Dependent and Interfacial Plane-Related Photocatalytic Behaviors of Semiconductor Nanocrystals and Heterostructures. *Nano Today* **2019**, *28*, 100768. <https://doi.org/10.1016/j.nantod.2019.100768>.
- (2) Huang, K.; Yuan, L.; Feng, S. Crystal Facet Tailoring Arts in Perovskite Oxides. *Inorg. Chem. Front.* **2015**, *2* (11), 965–981. <https://doi.org/10.1039/C5QI00168D>.
- (3) Wang, S.; Liu, G.; Wang, L. Crystal Facet Engineering of Photoelectrodes for Photoelectrochemical Water Splitting. *Chem. Rev.* **2019**, *119* (8), 5192–5247. <https://doi.org/10.1021/acs.chemrev.8b00584>.
- (4) Bai, S.; Wang, L.; Li, Z.; Xiong, Y. Facet-Engineered Surface and Interface Design of Photocatalytic Materials. *Adv. Sci.* **2017**, *4* (1), 1600216. <https://doi.org/10.1002/advs.201600216>.
- (5) Li, C.; Koenigsmann, C.; Ding, W.; Rudshiteyn, B.; Yang, K. R.; Regan, K. P.; Konezny, S. J.; Batista, V. S.; Brudvig, G. W.; Schmittenmaer, C. A.; et al. Facet-Dependent Photoelectrochemical Performance of TiO<sub>2</sub> Nanostructures: An Experimental and Computational Study. *J. Am. Chem. Soc.* **2015**, *137* (4), 1520–1529. <https://doi.org/10.1021/ja5111078>.
- (6) Li, R.; Zhang, F.; Wang, D.; Yang, J.; Li, M.; Zhu, J.; Zhou, X.; Han, H.; Li, C. Spatial Separation of Photogenerated Electrons and Holes among {010} and {110} Crystal Facets of BiVO<sub>4</sub>. *Nat. Commun.* **2013**, *4*. <https://doi.org/10.1038/ncomms2401>.
- (7) Annabella, S. Anatase Shows Its Reactive Side. *Nat. Mater.* **2008**, *7* (August), 613–615.
- (8) Gong, X.-Q.; Selloni, A. Reactivity of Anatase TiO<sub>2</sub> Nanoparticles: The Role of the Minority (001) Surface. *J. Phys. Chem. B* **2005**, *109* (42), 19560–19562. <https://doi.org/10.1021/jp055311g>.
- (9) Pan, J.; Liu, G.; Lu, G. Q.; Cheng, H.-M. On the True Photoreactivity Order of {001}, {010}, and {101} Facets of Anatase TiO<sub>2</sub> Crystals. *Angew. Chemie Int. Ed.* **2011**, *50* (9), 2133–

2137. <https://doi.org/10.1002/anie.201006057>.
- (10) Hu, L.; Sun, K.; Peng, Q.; Xu, B.; Li, Y. Surface Active Sites on Co<sub>3</sub>O<sub>4</sub> Nanobelt and Nanocube Model Catalysts for CO Oxidation. *Nano Res.* **2010**, *3* (5), 363–368. <https://doi.org/10.1007/s12274-010-1040-2>.
- (11) Shi, M.; Li, G.; Li, J.; Jin, X.; Tao, X.; Zeng, B.; Pidko, E. A.; Li, R.; Li, C. Intrinsic Facet-Dependent Reactivity of Well-Defined BiOBr Nanosheets on Photocatalytic Water Splitting. *Angew. Chemie Int. Ed.* **2020**, *59* (16), 6590–6595. <https://doi.org/10.1002/anie.201916510>.
- (12) Wang, G.; Ma, X.; Huang, B.; Cheng, H.; Wang, Z.; Zhan, J.; Qin, X.; Zhang, X.; Dai, Y. Controlled Synthesis of Ag<sub>2</sub>O Microcrystals with Facet-Dependent Photocatalytic Activities. *J. Mater. Chem.* **2012**, *22* (39), 21189–21194. <https://doi.org/10.1039/C2JM35010F>.
- (13) Tachikawa, T.; Ochi, T.; Kobori, Y. Crystal-Face-Dependent Charge Dynamics on a BiVO<sub>4</sub> Photocatalyst Revealed by Single-Particle Spectroelectrochemistry. *ACS Catal.* **2016**, *6* (4), 2250–2256. <https://doi.org/10.1021/acscatal.6b00234>.
- (14) Ye, L.; Jin, X.; Ji, X.; Liu, C.; Su, Y.; Xie, H.; Liu, C. Facet-Dependent Photocatalytic Reduction of CO<sub>2</sub> on BiOI Nanosheets. *Chem. Eng. J.* **2016**, *291*, 39–46. <https://doi.org/10.1016/j.cej.2016.01.032>.
- (15) Zhang, M.; Salvador, P. A.; Rohrer, G. S. Influence of Orientation and Ferroelectric Domains on the Photochemical Reactivity of La<sub>2</sub>Ti<sub>2</sub>O<sub>7</sub>. *J. Eur. Ceram. Soc.* **2020**. <https://doi.org/10.1016/j.jeurceramsoc.2020.09.020>.
- (16) Bruyer, E.; Sayede, A. Density Functional Calculations of the Structural, Electronic, and Ferroelectric Properties of High-k Titanate Re<sub>2</sub>Ti<sub>2</sub>O<sub>7</sub> (Re=La and Nd). *J. Appl. Phys.* **2010**, *108* (5), 53705. <https://doi.org/10.1063/1.3459891>.
- (17) Su, S.; Siretanu, I.; van den Ende, D.; Mei, B.; Mul, G.; Mugele, F. Facet-Dependent Surface Charge and Hydration of Semiconducting Nanoparticles at Variable pH. *Adv. Mater.* **2021**, *33* (52), 2106229. <https://doi.org/10.1002/adma.202106229>.

- (18) Takata, T.; Jiang, J.; Sakata, Y.; Nakabayashi, M.; Shibata, N.; Nandal, V.; Seki, K.; Hisatomi, T.; Domen, K. Photocatalytic Water Splitting with a Quantum Efficiency of Almost Unity. *Nature* **2020**, *581* (7809), 411–414. <https://doi.org/10.1038/s41586-020-2278-9>.
- (19) Mu, L.; Zhao, Y.; Li, A.; Wang, S.; Wang, Z.; Yang, J.; Wang, Y.; Liu, T.; Chen, R.; Zhu, J.; et al. Enhancing Charge Separation on High Symmetry SrTiO<sub>3</sub> Exposed with Anisotropic Facets for Photocatalytic Water Splitting. *Energy Environ. Sci.* **2016**, *9* (7), 2463–2469. <https://doi.org/10.1039/C6EE00526H>.
- (20) Hsieh, P.-L.; Naresh, G.; Huang, Y.-S.; Tsao, C.-W.; Hsu, Y.-J.; Chen, L.-J.; Huang, M. H. Shape-Tunable SrTiO<sub>3</sub> Crystals Revealing Facet-Dependent Optical and Photocatalytic Properties. *J. Phys. Chem. C* **2019**, *123* (22), 13664–13671. <https://doi.org/10.1021/acs.jpcc.9b02081>.
- (21) Zhang, M.; Salvador, P. A.; Rohrer, G. S. Influence of Particle Size and Shape on the Rate of Hydrogen Produced by Al-Doped SrTiO<sub>3</sub> Photocatalysts. *J. Am. Ceram. Soc.* **2022**, *00*, 1–11. <https://doi.org/10.1111/jace.18488>.
- (22) Zhu, Y.; Schultz, A. M.; Rohrer, G. S.; Salvador, P. A. The Orientation Dependence of the Photochemical Activity of  $\alpha$ -Fe<sub>2</sub>O<sub>3</sub>. *J. Am. Ceram. Soc.* **2016**, *99* (7), 2428–2435. <https://doi.org/10.1111/jace.14201>.
- (23) Kuo, C.-H.; Yang, Y.-C.; Gwo, S.; Huang, M. H. Facet-Dependent and Au Nanocrystal-Enhanced Electrical and Photocatalytic Properties of Au–Cu<sub>2</sub>O Core–Shell Heterostructures. *J. Am. Chem. Soc.* **2011**, *133* (4), 1052–1057. <https://doi.org/10.1021/ja109182y>.
- (24) Tan, C.-S.; Hsu, S.-C.; Ke, W.-H.; Chen, L.-J.; Huang, M. H. Facet-Dependent Electrical Conductivity Properties of Cu<sub>2</sub>O Crystals. *Nano Lett.* **2015**, *15* (3), 2155–2160. <https://doi.org/10.1021/acs.nanolett.5b00150>.
- (25) Huang, J.-Y.; Madasu, M.; Huang, M. H. Modified Semiconductor Band Diagrams Constructed from Optical Characterization of Size-Tunable Cu<sub>2</sub>O Cubes, Octahedra, and Rhombic Dodecahedra. *J. Phys. Chem. C* **2018**, *122* (24), 13027–13033.

<https://doi.org/10.1021/acs.jpcc.8b02169>.

- (26) Huang, M. H. Facet-Dependent Optical Properties of Semiconductor Nanocrystals. *Small* **2019**, *15* (7), 1804726. <https://doi.org/10.1002/sml.201804726>.
- (27) Tan, C.-S.; Chen, Y.-J.; Hsia, C.-F.; Huang, M. H. Facet-Dependent Electrical Conductivity Properties of Silver Oxide Crystals. *Chem. Asian J.* **2017**, *12* (3), 293–297. <https://doi.org/10.1002/asia.201601520>.
- (28) Hsieh, M.-S.; Su, H.-J.; Hsieh, P.-L.; Chiang, Y.-W.; Huang, M. H. Synthesis of Ag<sub>3</sub>PO<sub>4</sub> Crystals with Tunable Shapes for Facet-Dependent Optical Property, Photocatalytic Activity, and Electrical Conductivity Examinations. *ACS Appl. Mater. Interfaces* **2017**, *9* (44), 39086–39093. <https://doi.org/10.1021/acsami.7b13941>.
- (29) Tan, C.-S.; Chen, H.-S.; Chiu, C.-Y.; Wu, S.-C.; Chen, L.-J.; Huang, M. H. Facet-Dependent Electrical Conductivity Properties of PbS Nanocrystals. *Chem. Mater.* **2016**, *28* (5), 1574–1580. <https://doi.org/10.1021/acs.chemmater.6b00274>.
- (30) Hsieh, P.-L.; Madasu, M.; Hsiao, C.-H.; Peng, Y.-W.; Chen, L.-J.; Huang, M. H. Facet-Dependent and Adjacent Facet-Related Electrical Conductivity Properties of SrTiO<sub>3</sub> Crystals. *J. Phys. Chem. C* **2021**, *125* (18), 10051–10056. <https://doi.org/10.1021/acs.jpcc.1c01047>.
- (31) Liu, G.; Sun, C.; Yang, H. G.; Smith, S. C.; Wang, L.; Lu, G. Q. (Max); Cheng, H.-M. Nanosized Anatase TiO<sub>2</sub> Single Crystals for Enhanced Photocatalytic Activity. *Chem. Commun.* **2010**, *46* (5), 755–757. <https://doi.org/10.1039/B919895D>.
- (32) Bi, Y.; Ouyang, S.; Umezawa, N.; Cao, J.; Ye, J. Facet Effect of Single-Crystalline Ag<sub>3</sub>PO<sub>4</sub> Sub-Microcrystals on Photocatalytic Properties. *J. Am. Chem. Soc.* **2011**, *133* (17), 6490–6492. <https://doi.org/10.1021/ja2002132>.
- (33) Martin, D. J.; Umezawa, N.; Chen, X.; Ye, J.; Tang, J. Facet Engineered Ag<sub>3</sub>PO<sub>4</sub> for Efficient Water Photooxidation. *Energy Environ. Sci.* **2013**, *6* (11), 3380–3386. <https://doi.org/10.1039/C3EE42260G>.
- (34) Ke, W.-H.; Hsia, C.-F.; Chen, Y.-J.; Huang, M. H. Synthesis of Ultrasmall Cu<sub>2</sub>O Nanocubes

- and Octahedra with Tunable Sizes for Facet-Dependent Optical Property Examination. *Small* **2016**, *12* (26), 3530–3534. <https://doi.org/10.1002/sml.201600064>.
- (35) Lei, W.; Zhang, T.; Gu, L.; Liu, P.; Rodriguez, J. A.; Liu, G.; Liu, M. Surface-Structure Sensitivity of CeO<sub>2</sub> Nanocrystals in Photocatalysis and Enhancing the Reactivity with Nanogold. *ACS Catal.* **2015**, *5* (7), 4385–4393. <https://doi.org/10.1021/acscatal.5b00620>.
- (36) Lyu, L.-M.; Huang, M. H. Investigation of Relative Stability of Different Facets of Ag<sub>2</sub>O Nanocrystals through Face-Selective Etching. *J. Phys. Chem. C* **2011**, *115* (36), 17768–17773. <https://doi.org/10.1021/jp2059479>.
- (37) Yi, Z.; Ye, J.; Kikugawa, N.; Kako, T.; Ouyang, S.; Stuart-Williams, H.; Yang, H.; Cao, J.; Luo, W.; Li, Z.; et al. An Orthophosphate Semiconductor with Photooxidation Properties under Visible-Light Irradiation. *Nat. Mater.* **2010**, *9* (7), 559–564. <https://doi.org/10.1038/nmat2780>.
- (38) Munprom, R.; Salvador, P. A.; Rohrer, G. S. The Orientation Dependence of the Photochemical Reactivity of BiVO<sub>4</sub>. *J. Mater. Chem. A* **2015**, *3* (5), 2370–2377. <https://doi.org/10.1039/c4ta06045h>.
- (39) Tan, H. L.; Wen, X.; Amal, R.; Ng, Y. H. BiVO<sub>4</sub> {010} and {110} Relative Exposure Extent: Governing Factor of Surface Charge Population and Photocatalytic Activity. *J. Phys. Chem. Lett.* **2016**, *7* (7), 1400–1405. <https://doi.org/10.1021/acs.jpcclett.6b00428>.
- (40) Wang, D.; Jiang, H.; Zong, X.; Xu, Q.; Ma, Y.; Li, G.; Li, C. Crystal Facet Dependence of Water Oxidation on BiVO<sub>4</sub> Sheets under Visible Light Irradiation. *Chem. Eur. J.* **2011**, *17* (4), 1275–1282. <https://doi.org/10.1002/chem.201001636>.
- (41) Shi, M.; Li, G.; Li, J.; Jin, X.; Tao, X.; Zeng, B.; Pidko, E. A.; Li, R.; Li, C. Intrinsic Facet-Dependent Reactivity of Well-Defined BiOBr Nanosheets on Photocatalytic Water Splitting. *Angew. Chemie Int. Ed.* **2020**, *59* (16), 6590–6595. <https://doi.org/10.1002/anie.201916510>.
- (42) Zhang, L.; Wang, W.; Sun, S.; Jiang, D.; Gao, E. Selective Transport of Electron and Hole among {001} and {110} Facets of BiOCl for Pure Water Splitting. *Appl. Catal. B Environ.*

- 2015**, *162*, 470–474. <https://doi.org/10.1016/j.apcatb.2014.07.024>.
- (43) Zhao, K.; Zhang, L.; Wang, J.; Li, Q.; He, W.; Yin, J. J. Surface Structure-Dependent Molecular Oxygen Activation of BiOCl Single-Crystalline Nanosheets. *J. Am. Chem. Soc.* **2013**, *135* (42), 15750–15753. <https://doi.org/10.1021/ja4092903>.
- (44) Zitello, K. E.; Salvador, P. A.; Rohrer, G. S. Influence of Surface Orientation on the Photochemical Reactivity of CaTiO<sub>3</sub>. *J. Am. Ceram. Soc.* **2020**, *103* (8), 4498–4506. <https://doi.org/10.1111/jace.17107>.
- (45) Li, N.; Liu, M.; Zhou, Z.; Zhou, J.; Sun, Y.; Guo, L. Charge Separation in Facet-Engineered Chalcogenide Photocatalyst: A Selective Photocorrosion Approach. *Nanoscale* **2014**, *6* (16), 9695–9702. <https://doi.org/10.1039/C4NR02068E>.
- (46) Li, P.; Zhou, Y.; Zhao, Z.; Xu, Q.; Wang, X.; Xiao, M.; Zou, Z. Hexahedron Prism-Anchored Octahedral CeO<sub>2</sub>: Crystal Facet-Based Homo Junction Promoting Efficient Solar Fuel Synthesis. *J. Am. Chem. Soc.* **2015**, *137* (30), 9547–9550. <https://doi.org/10.1021/jacs.5b05926>.
- (47) Xie, X.; Li, Y.; Liu, Z.-Q.; Haruta, M.; Shen, W. Low-Temperature Oxidation of CO Catalysed by Co<sub>3</sub>O<sub>4</sub> Nanorods. *Nature* **2009**, *458* (7239), 746–749. <https://doi.org/10.1038/nature07877>.
- (48) Wang, L.; Ge, J.; Wang, A.; Deng, M.; Wang, X.; Bai, S.; Li, R.; Jiang, J.; Zhang, Q.; Luo, Y.; et al. Designing P-Type Semiconductor–Metal Hybrid Structures for Improved Photocatalysis. *Angew. Chemie Int. Ed.* **2014**, *53* (20), 5107–5111. <https://doi.org/10.1002/anie.201310635>.
- (49) Li, G.; Yi, Z.; Bai, Y.; Zhang, W.; Zhang, H. Anisotropy in Photocatalytic Oxidation Activity of NaNbO<sub>3</sub> Photocatalyst. *Dalt. Trans.* **2012**, *41* (34), 10194–10198. <https://doi.org/10.1039/C2DT30593C>.
- (50) Giocondi, J. L.; Salvador, P. A.; Rohrer, G. S. The Origin of Photochemical Anisotropy in SrTiO<sub>3</sub>. *Top. Catal.* **2007**, *44* (4), 529–533. <https://doi.org/10.1007/s11244-006-0101-y>.
- (51) Giocondi, J. L.; Rohrer, G. S. Structure Sensitivity of Photochemical Oxidation and

- Reduction Reactions on SrTiO<sub>3</sub> Surfaces. *J. Am. Ceram. Soc.* **2003**, *86* (7), 1182–1189. <https://doi.org/10.1111/j.1151-2916.2003.tb03445.x>.
- (52) Pisat, A. S.; Salvador, P. A.; Rohrer, G. S. The Facet Structure and Photochemical Reactivity of Arbitrarily Oriented Strontium Titanate Surfaces. *Adv. Mater. Interfaces* **2019**, *6* (16), 1900731. <https://doi.org/10.1002/admi.201900731>.
- (53) Yu, J.; Low, J.; Xiao, W.; Zhou, P.; Jaroniec, M. Enhanced Photocatalytic CO<sub>2</sub>-Reduction Activity of Anatase TiO<sub>2</sub> by Coexposed {001} and {101} Facets. *J. Am. Chem. Soc.* **2014**, *136* (25), 8839–8842. <https://doi.org/10.1021/ja5044787>.
- (54) Liu, X.; Dong, G.; Li, S.; Lu, G.; Bi, Y. Direct Observation of Charge Separation on Anatase TiO<sub>2</sub> Crystals with Selectively Etched {001} Facets. *J. Am. Chem. Soc.* **2016**, *138* (9), 2917–2920. <https://doi.org/10.1021/jacs.5b12521>.
- (55) Lin, H.; Li, L.; Zhao, M.; Huang, X.; Chen, X.; Li, G.; Yu, R. Synthesis of High-Quality Brookite TiO<sub>2</sub> Single-Crystalline Nanosheets with Specific Facets Exposed: Tuning Catalysts from Inert to Highly Reactive. *J. Am. Chem. Soc.* **2012**, *134* (20), 8328–8331. <https://doi.org/10.1021/ja3014049>.
- (56) Morris Hotsenpiller, P. A.; Bolt, J. D.; Farneth, W. E.; Lowekamp, J. B.; Rohrer, G. S. Orientation Dependence of Photochemical Reactions on TiO<sub>2</sub> Surfaces. *J. Phys. Chem. B* **1998**, *102* (17), 3216–3226. <https://doi.org/10.1021/jp980104k>.
- (57) Lowekamp, J. B.; Rohrer, G. S.; Morris Hotsenpiller, P. A.; Bolt, J. D.; Farneth, W. E. Anisotropic Photochemical Reactivity of Bulk TiO<sub>2</sub> Crystals. *J. Phys. Chem. B* **1998**, *102* (38), 7323–7327. <https://doi.org/10.1021/jp982721e>.
- (58) Ohno, T.; Sarukawa, K.; Matsumura, M. Crystal Faces of Rutile and Anatase TiO<sub>2</sub> Particles and Their Roles in Photocatalytic Reactions. *New J. Chem.* **2002**, *26* (9), 1167–1170. <https://doi.org/10.1039/B202140D>.
- (59) Xie, Y. P.; Liu, G.; Yin, L.; Cheng, H.-M. Crystal Facet-Dependent Photocatalytic Oxidation and Reduction Reactivity of Monoclinic WO<sub>3</sub> for Solar Energy Conversion. *J. Mater. Chem.* **2012**, *22* (14), 6746–6751. <https://doi.org/10.1039/C2JM16178H>.

- (60) Li, G.; Yi, Z.; Wang, H.; Jia, C.; Zhang, W. Factors Impacted on Anisotropic Photocatalytic Oxidization Activity of ZnO: Surface Band Bending, Surface Free Energy and Surface Conductance. *Appl. Catal. B Environ.* **2014**, *158–159*, 280–285. <https://doi.org/10.1016/j.apcatb.2014.04.034>.

## **Appendix II: Investigating the Effect of High Temperature Photochromism Treatment on the Photochemical Properties of Fe-doped SrTiO<sub>3</sub>**

The impact of UV irradiation on the optical properties of Fe-doped SrTiO<sub>3</sub> single crystal has been reported.<sup>1</sup> It was found that a UV illumination together with a thermal treatment leads to the incorporation of oxygen into the single crystals and decreased oxygen vacancy concentration. The incorporated oxygen will oxidize Fe<sup>3+</sup> to Fe<sup>4+</sup>, and the crystal color changed to black. UV-vis spectra implied that the crystal absorbance at visible light region was significantly enhanced, and the band gap was reduced to about 2.74 eV when the heating temperature was 440 °C. Meanwhile, the treatment increases the electrical conductivity as well as the oxygen chemical potential in bulk. More importantly, this change of absorbance permanently remains at room temperature.

This change of light absorbance is known as photochromism, a phenomenon that the color and stoichiometry of the material change upon illumination.<sup>2</sup> This idea was first introduced by Tatsuma's et al. in TiO<sub>2</sub> film loaded by Ag nanoparticles.<sup>3</sup> And similar effects have been observed on numerous oxides, such as TiO<sub>2</sub>,<sup>4</sup> SrTiO<sub>3</sub>,<sup>5</sup> Zn<sub>2</sub>GeO<sub>4</sub>.<sup>6</sup> For Fe-doped SrTiO<sub>3</sub>, this behavior has been found decades ago. In 1976, Blazey et al. observed the enhanced absorption in the region of 400 nm to 700 nm on Fe-doped SrTiO<sub>3</sub> crystals due to the formation of Fe<sup>4+</sup> induced by irradiation.<sup>7</sup> In 1996, the study by Huang et al. implied that two defect states Fe'<sub>Ti</sub> and (Fe<sub>Ti</sub>-V<sub>O</sub>)' were introduced and served as hole and electron trappers, so that irradiation less than band gap can be absorbed.<sup>8</sup> In 2001, Maier et al. reported the use of UV light to accelerate the rate of oxygen incorporation into Fe doped SrTiO<sub>3</sub>, but the exorporation rates weren't affected.<sup>9</sup> In most of the studies, this photochromism behavior is reversible. In other word, if the illumination was removed, the material will be bleached soon. But the method introduced by Fleig et al.<sup>1</sup> is irreversible at room temperature, making it promising to the field of photocatalytic water splitting.

In this study, Fe-doped (100) SrTiO<sub>3</sub> single crystal substrates were purchased from MTI company (0.01 wt %, 5x5x0.5mm, 1sp). The crystal was first annealed at 1100 °C for 6 h to obtain the enough oxygen vacancy concentration for photochromism. Next, the crystal was illuminated under a 150 W UV lamp and heated at 440 °C for 6 h simultaneously. After the treatment, the

crystal color changed from yellow to dark brown. UV-vis spectra of the prepared samples are plotted in Figure 12-1. It is found that light absorbance at 400 nm of the Fe-doped crystal is obviously higher than the undoped crystal, consistent with previous report.<sup>7,10</sup> And the photochromism treatment further improved the optical property.

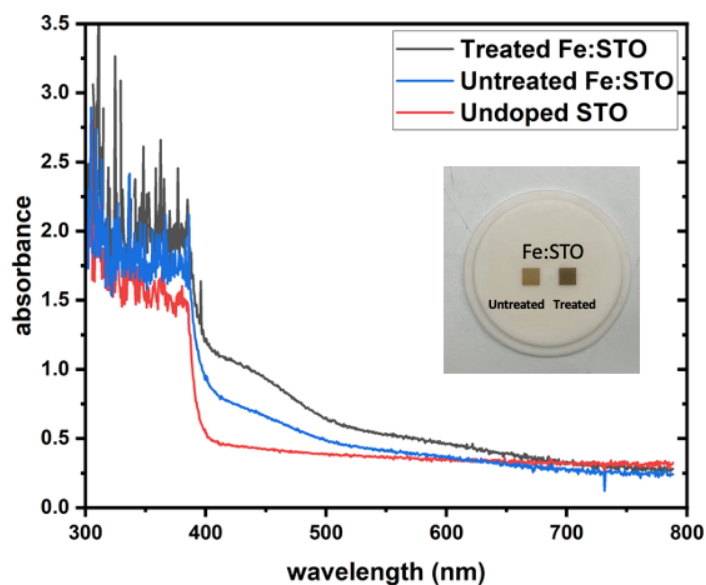


**Figure 12-1:** UV-vis spectra of undoped SrTiO<sub>3</sub> single crystal and Fe-doped SrTiO<sub>3</sub> single crystal with and without the photochromism treatment.

The photochemical property of the photochromism treated Fe-doped (100) single crystal surface was investigated with Ag<sup>+</sup> marker reaction. The illumination was provided by a 150 W Xe lamp (Newport). AFM images of the crystal surface after reaction is shown in Figure 12-2 (a) and (b). It is found that many long edges cross the surface, being roughly perpendicular to each other. And the silver deposits prefer to accumulate along these edges. There are small silver particles showing on the flat surface region as well, but the reactivity is generally lower compare with normal undoped (100) surface (see Chapter 7). The photochemical reactivity under visible light was studied by employing a long-pass filter to block UV light ( $\lambda < 400$  nm). After illumination, topography AFM images of the surface are shown in Figure 12-3 (c) and (d), and no silver deposits are observed on the surface, indicating a low reactivity under visible light.

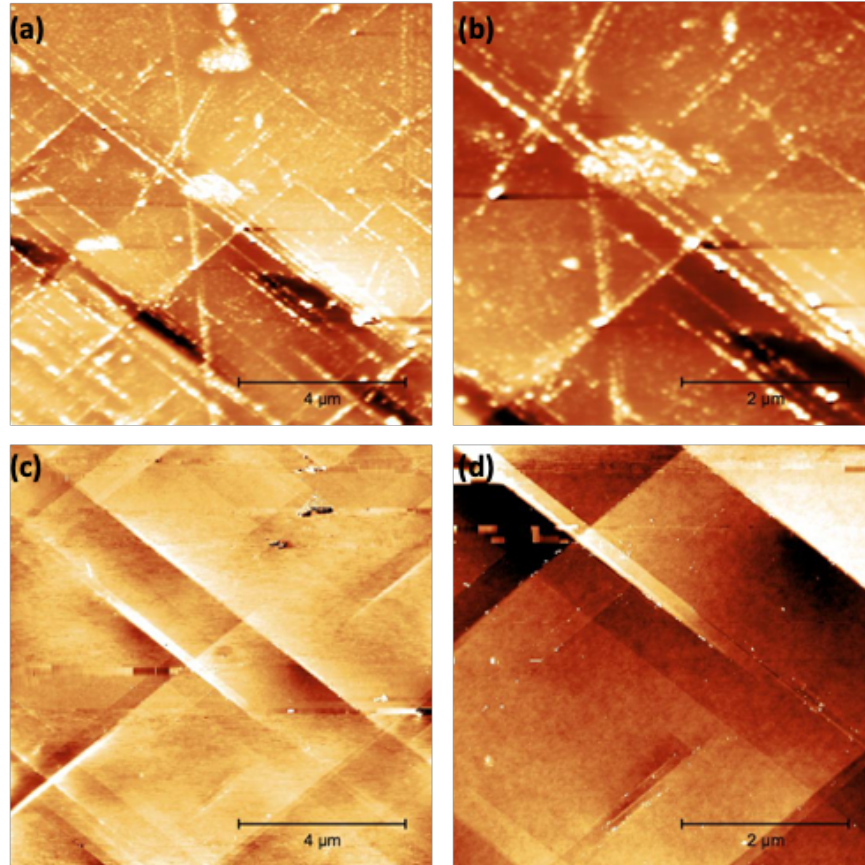


**Figure 12-2:** Photoreduction of  $\text{Ag}^+$  on the surface of a Fe-doped  $\text{SrTiO}_3$  single crystal that has undergone a photochromism treatment. The maker reaction was carried out under UV illumination for (a) and (b) and visible light illumination for (c) and (d). The dark to bright contrast is (a): 30 nm, (b): 30 nm, (c): 10 nm, (d): 6 nm.

Fe-doped  $\text{SrTiO}_3$  particles were prepared via a direct solid-state method by heating  $\text{SrTiO}_3$  with specific amount of  $\text{Fe}_2\text{O}_3$  at  $1200\text{ }^\circ\text{C}$  for 12 h to yield a doping concentration of 0.01%, 0.02%, 0.05% and 0.1%.  $\text{RhCrO}_x$  was loaded on the samples with an impregnation method. However, the photocatalytic hydrogen production was low and cannot be detected by the PAPCR. Inspired by previous results, the  $\text{SrCl}_2$  flux treatment was carried out on all samples at  $1150\text{ }^\circ\text{C}$  for 10 h in alumina crucibles to improve their reactivity. The SEM images of the flux treated particles are shown in Figure 12-3. The particle morphologies are relatively irregular compared with Al-doped samples (see Chapter 6 to 9). Photochromism treatment has been carried out by illuminating the powders under 150 W UV light at  $440\text{ }^\circ\text{C}$  for 6 hours. After the irradiation, the powders seem to turn slightly darker. But this change of color is reversible and would be bleached to the original color overnight in air.

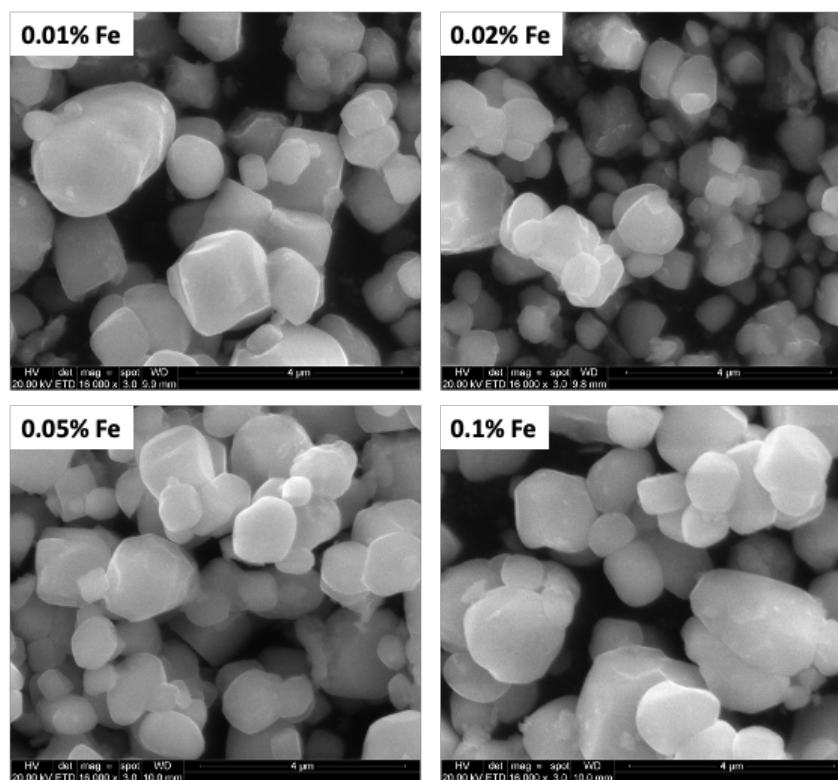


**Figure 12-3:** SEM images of 0.01%, 0.02%, 0.05% and 0.1% Fe doped SrTiO<sub>3</sub>. The samples were prepared with a solid-state method and then heated in the molten SrCl<sub>2</sub> flux.

Photocatalytic water splitting reactions have been carried out on the SrCl<sub>2</sub> flux treated Fe-doped powders with and without photochromism treatment using the PAPCR under 380 nm and 400 nm illumination. The hydrogen generation rates under 380 nm are shown in Figure 12-4. It is found that the sample without Fe incorporated has the highest reactivity. For the Fe-doped samples, it is found that 0.05% doped ones are the most reactive either in methanol solutions or in DI water. The pH effect is like the results in Chapter 6. However, under 400 nm illumination, no hydrogen production was detected from these samples by the PAPCR.

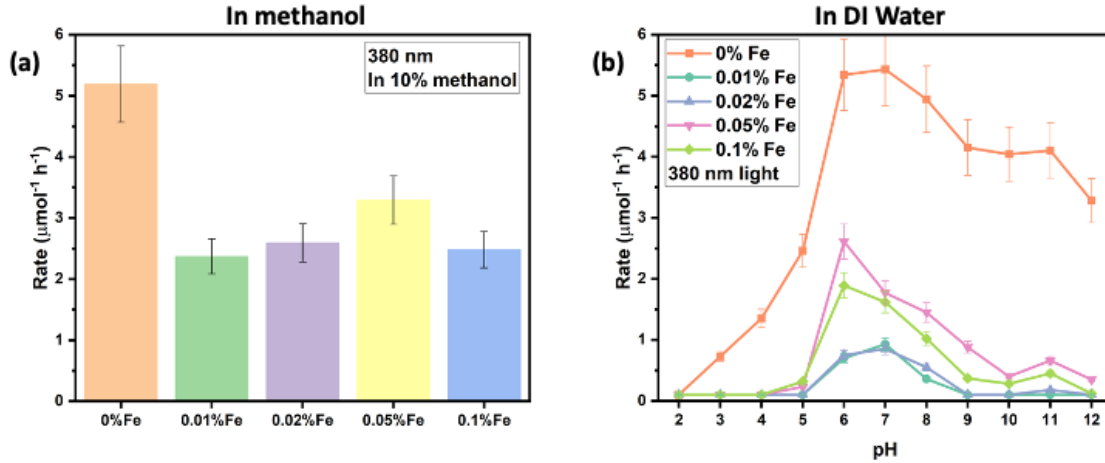


**Figure 12-4:** Photocatalytic hydrogen production rates of SrCl<sub>2</sub> flux treated Fe-doped SrTiO<sub>3</sub> with different Fe additions in (a) 10% methanol solutions and (b) pure water.

The color change is caused by the increasing Fe<sup>4+</sup> concentrations, expressed as:<sup>1</sup>



In this study, the photochromism effect has been observed on large single crystal substrates and the change of color is found to be stable over time. It is indicated that the UV illumination significantly increases the diffusion rate of oxygen, a situation closes to high pO<sub>2</sub>, and changes the oxygen stoichiometry of the entire bulk. The holes formed during the oxygen incorporation were trapped by Fe'\_{Ti} acceptors, and this will change the optical property. However, this effect is much weaker in powders. One possible explanation is that the different size scales for bulk crystal and powders. The bulk crystal is 0.5 mm thick, a roughly 1000 times larger than powders. When the illumination is removed, the environment changes back to low pO<sub>2</sub> situation, the trapped oxygen from the surface might escape from the surface, but the oxygen in the bulk are difficult to diffuse such a long range. Powders are much smaller crystals, and the trapped oxygen might easily leave the crystal by diffusion, explaining why we cannot observe an obvious blackening on the powders.

It is noted that the crystals in Fig. 12-4 were doped with Al<sup>3+</sup> as well during the SrCl<sub>2</sub> flux treatment. It is concluded that Fe<sup>3+</sup> is not an effective dopant like Al<sup>3+</sup>, and co-doping Fe<sup>3+</sup> into Al-doped SrTiO<sub>3</sub> will reduce its photochemical reactivity. Although the optical property is improved by the introduce of Fe<sup>3+</sup> and the photochromism treatment, this does not contribute to the photochemical

reactivity in the visible light region, determined from both marker reactions and water splitting. Previous defect studies have shown that Fe-doped SrTiO<sub>3</sub> might have a stronger p-type characteristic,<sup>11,12</sup> therefore, co-doping Al<sup>3+</sup> will only increase the p-type characteristic. Considering our compensation model discussed in Chapter 8, introducing a second donor dopant might be helpful to improve the photochemical reactivity of Fe-doped SrTiO<sub>3</sub>. Hence, doping La<sup>3+</sup>, Y<sup>3+</sup> and Nb<sup>3+</sup> at A-site might be promising.

## References

- (1) Viernstein, A.; Kubicek, M.; Morgenbesser, M.; Walch, G.; Brunauer, G. C.; Fleig, J. High-Temperature Photochromism of Fe-Doped SrTiO<sub>3</sub> Caused by UV-Induced Bulk Stoichiometry Changes. *Adv. Funct. Mater.* **2019**, *29* (23), 1900196. <https://doi.org/10.1002/adfm.201900196>.
- (2) Fleig, J.; Kubicek, M. Light May Harm or Help. *Nat. Mater.* **2018**, *17* (5), 389–391. <https://doi.org/10.1038/s41563-018-0052-2>.
- (3) Ohko, Y.; Tatsuma, T.; Fujii, T.; Naoi, K.; Niwa, C.; Kubota, Y.; Fujishima, A. Multicolour Photochromism of TiO<sub>2</sub> Films Loaded with Silver Nanoparticles. *Nat. Mater.* **2003**, *2* (1), 29–31. <https://doi.org/10.1038/nmat796>.
- (4) Tobaldi, D. M.; Hortigüela Gallo, M. J.; Otero-Irurueta, G.; Singh, M. K.; Pullar, R. C.; Seabra, M. P.; Labrincha, J. A. Purely Visible-Light-Induced Photochromism in Ag–TiO<sub>2</sub> Nanoheterostructures. *Langmuir* **2017**, *33* (20), 4890–4902. <https://doi.org/10.1021/acs.langmuir.6b04474>.
- (5) Faughnan, B. W. Photochromism in Transition Metal Doped SrTiO<sub>3</sub>. *Phys. Rev. B* **1971**, *4* (10), 3623–3636. <https://doi.org/10.1103/PhysRevB.4.3623>.
- (6) Jin, Y.; Hu, Y.; Fu, Y.; Mu, Z.; Ju, G. Reversible White and Light Gray Photochromism in Europium Doped Zn<sub>2</sub>GeO<sub>4</sub>. *Mater. Lett.* **2014**, *134*, 187–189. <https://doi.org/10.1016/j.matlet.2014.07.084>.
- (7) Blazey, K. W. Optical Absorption of SrTiO<sub>3</sub>:Fe<sup>4+</sup>. *Phys. status solidi* **1976**, *38* (1), K97–K99. <https://doi.org/10.1002/pssa.2210380171>.

- (8) Huang, M.-H.; Xia, J.-Y.; Xi, Y.-M.; Ding, C.-X. Study on Photochromism in SrTiO<sub>3</sub>:Fe Ceramic Powder. *J. Eur. Ceram. Soc.* **1997**, *17* (14), 1761–1765. [https://doi.org/10.1016/S0955-2219\(97\)00009-5](https://doi.org/10.1016/S0955-2219(97)00009-5).
- (9) Merkle, R.; De Souza, R. A.; Maier, J. Optically Tuning the Rate of Stoichiometry Changes: Surface-Controlled Oxygen Incorporation into Oxides under UV Irradiation. *Angew. Chemie Int. Ed.* **2001**, *40* (11), 2126–2129. [https://doi.org/10.1002/1521-3773\(20010601\)40:11<2126::AID-ANIE2126>3.0.CO;2-K](https://doi.org/10.1002/1521-3773(20010601)40:11<2126::AID-ANIE2126>3.0.CO;2-K).
- (10) Blazey, K. W.; Weibel, H. Optical Absorption Spectra of Reduced Transition-Metal Ion-Doped SrTiO<sub>3</sub>. *J. Phys. Chem. Solids* **1984**, *45* (8), 917–922. [https://doi.org/10.1016/0022-3697\(84\)90134-3](https://doi.org/10.1016/0022-3697(84)90134-3).
- (11) Wang, J.-J.; Huang, H.-B.; Bayer, T. J. M.; Moballegh, A.; Cao, Y.; Klein, A.; Dickey, E. C.; Irving, D. L.; Randall, C. A.; Chen, L.-Q. Defect Chemistry and Resistance Degradation in Fe-Doped SrTiO<sub>3</sub> Single Crystal. *Acta Mater.* **2016**, *108*, 229–240. <https://doi.org/10.1016/j.actamat.2016.02.022>.
- (12) Rothschild, A.; Menesklou, W.; Tuller, H. L.; Ivers-Tiffée, E. Electronic Structure, Defect Chemistry, and Transport Properties of SrTi<sub>1-x</sub>Fe<sub>x</sub>O<sub>3-y</sub> Solid Solutions. *Chem. Mater.* **2006**, *18* (16), 3651–3659. <https://doi.org/10.1021/cm052803x>.

## Appendix III: Synthesizing $\text{AgNb}_x\text{Ta}_{1-x}\text{O}_3$ Solid Solution for Visible Light Driven Water Splitting

$\text{AgNbO}_3$  with a band gap of about 2.8 eV is an attractive candidate for visible-light-driven photocatalytic water splitting. Its conduction band edge mainly compose of Nb 4d orbitals, and the hybrid of Ag 4d and O 2p orbitals formed the valence band at a more negative level than the O 2p orbitals, resulting in a decrease in the band gap.<sup>1</sup> Arney et al. synthesized  $\text{AgNbO}_3$  in a  $\text{Na}_2\text{SO}_4$  flux, and the catalysts can produce hydrogen in an aqueous methanol solution under visible light ( $\lambda > 420$  nm).<sup>2</sup> Gao et al. prepared  $\text{AgNbO}_3$  nanocubes using a hydrothermal approach and demonstrated an enhanced visible-light-driven photocatalytic performance in the photodegradation of tetracycline.<sup>3</sup> Li et al. showed that polyhedron-shaped  $\text{AgNbO}_3$  by solvothermal and liquid–solid methods is favorable for the photocatalytic  $\text{O}_2$  evolution under visible light.<sup>4</sup>

In this study,  $\text{AgNbO}_3$  powders were prepared with a solid-state method.  $\text{Ag}_2\text{O}$  and  $\text{Nb}_2\text{O}_5$  were mixed at a molar ratio of 1:1 in an agate mortar. The mixture was then pressed into a pellet and heated at 900 °C for 10 hours and at 1050 °C for another 20 hours in a furnace. After the furnace was cooled to room temperature, the pellet was ground to powders. The XRD pattern of the obtained powders is shown in Figure 13-1 (a), and all peaks are attributed to  $\text{AgNbO}_3$ . 1 wt% Pt or 0.1 wt%  $\text{RhCrO}_x$  cocatalysts was loaded on the samples. Photocatalytic water splitting experiment has been carried out on the  $\text{AgNbO}_3$  samples using the PAPCR in 10% methanol solutions or DI water whose pH was adjusted to be pH 2, pH 7 and pH 12. However, no hydrogen generation was detected in any samples here under 380 nm or 400 nm, as shown in Figure 13-1 (b). One possible interpretation of the poor reactivity is that the conduction band edge of  $\text{AgNbO}_3$  is just slightly above the reduction potential of proton so that the overpotential might not be enough to drive the reaction. The band gap of  $\text{AgTaO}_3$  about 0.6 eV larger than  $\text{AgNbO}_3$ , which is owing to the energy difference between Ta 5d orbital and Nb 4d orbital.<sup>1</sup> Inspired by this, it is considered that  $\text{AgNb}_x\text{Ta}_{1-x}\text{O}_3$  solid solution should have an intermediate band gap and a slightly higher conduction band edge.

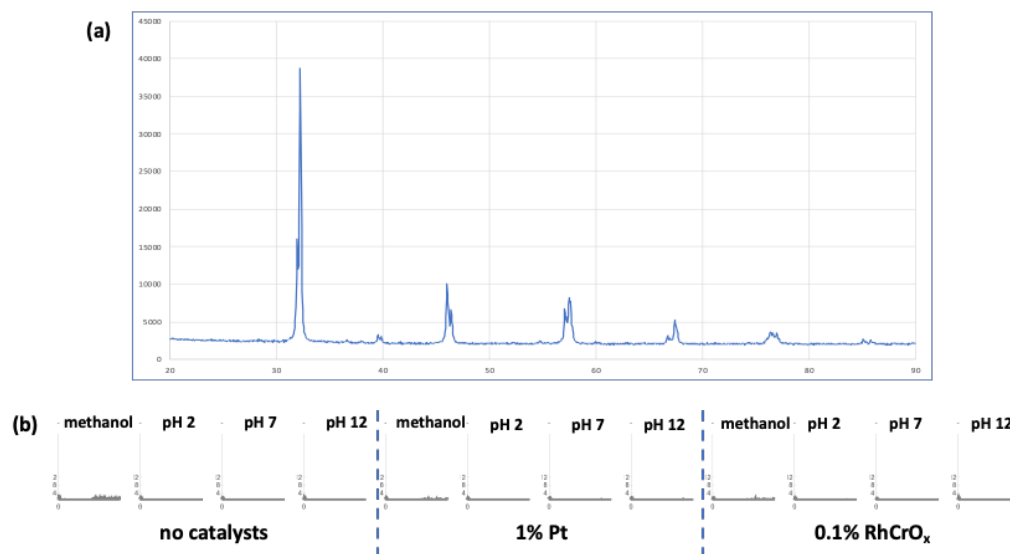


**Figure 13-1:** (a) XRD pattern and (b) photocatalytic hydrogen generation under 380 nm light from the prepared  $\text{AgNbO}_3$  powders.

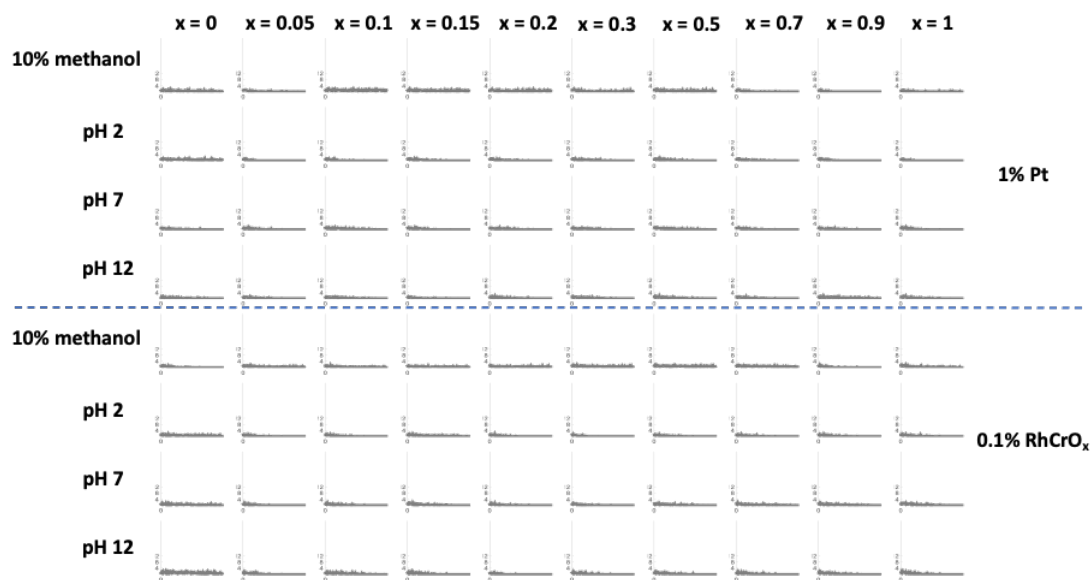


**Figure 13-2:** Photocatalytic hydrogen generation from  $\text{AgNb}_x\text{Ta}_{1-x}\text{O}_3$  solid solutions under 380 nm illumination.

$\text{AgNb}_x\text{Ta}_{1-x}\text{O}_3$  solid solutions were prepared by mixing  $\text{Ag}_2\text{O}$ ,  $\text{Nb}_2\text{O}_5$  and  $\text{Ta}_2\text{O}_5$  using ball milling to yield compositions where  $x = 0, 0.05, 0.1, 0.15, 0.2, 0.3, 0.5, 0.7, 0.9, 1$ . Again, the mixture was dried and pressed into a pellet, followed by heating at  $900\text{ }^\circ\text{C}$  for 10 hours and  $1050\text{ }^\circ\text{C}$  for another 20 hours in a furnace. The pellets were then ground into powders, and either 1 wt% Pt or 0.1 wt%  $\text{RhCrO}_x$  was loaded as cocatalyst. Photocatalytic water splitting experiment has been

carried out on the as prepared solid solution samples under 380 nm, as shown in Figure 13-2. Unfortunately, no hydrogen generation was detected from these samples.

Watanabe et al. reported that AgTaO<sub>3</sub> is an efficient photocatalysts whose apparent quantum yield reaches about 40% under 340 nm.<sup>5</sup> It is not clear why our AgNb<sub>x</sub>Ta<sub>1-x</sub>O<sub>3</sub> solid solution samples has such poor reactivity. One explanation is that the particle morphology is irregular since the particles were made by grinding a pellet in a mortar. A lot of defects might be introduced to both the surface and the bulk during grinding and serve as charge carrier recombination centers. To solve this, molten salt synthesis and hydrothermal synthesis could be employed to prepare high crystallinity materials in future. Another explanation is that free Ag<sup>+</sup> impurities exist in the samples. Under illumination, Ag<sup>+</sup> cations are easier to be reduced than protons due to the lower reduction potential. This will also limit the water splitting performance.

## References

- (1) Kato, H.; Kobayashi, H.; Kudo, A. Role of Ag<sup>+</sup> in the Band Structures and Photocatalytic Properties of AgMO<sub>3</sub> (M: Ta and Nb) with the Perovskite Structure. *J. Phys. Chem. B* **2002**, *106* (48), 12441–12447. <https://doi.org/10.1021/jp025974n>.
- (2) Arney, D.; Hardy, C.; Greve, B.; Maggard, P. A. Flux Synthesis of AgNbO<sub>3</sub>: Effect of Particle Surfaces and Sizes on Photocatalytic Activity. *J. Photochem. Photobiol. A-Chemistry* **2010**, *214* (1), 54–60. <https://doi.org/10.1016/j.jphotochem.2010.06.006>.
- (3) Gao, B.; Hu, D.; Xiao, C.; Li, D.; Lin, B.; Chen, Y.; Zheng, Y. Enhanced Visible-Light-Driven Photocatalytic Performance of AgNbO<sub>3</sub> Cubes with a High-Energy (001) Facet. *J. Phys. Chem. Solids* **2019**, *135*, 109083. <https://doi.org/10.1016/j.jpcs.2019.109083>.
- (4) Li, G.; Yan, S.; Wang, Z.; Wang, X.; Li, Z.; Ye, J.; Zou, Z. Synthesis and Visible Light Photocatalytic Property of Polyhedron-Shaped AgNbO<sub>3</sub>. *Dalt. Trans.* **2009**, No. 40, 8519–8524. <https://doi.org/10.1039/b906799j>.
- (5) Watanabe, K.; Iwase, A.; Kudo, A. Solar Water Splitting over Rh<sub>0.5</sub>Cr<sub>1.5</sub>O<sub>3</sub>-Loaded AgTaO<sub>3</sub> of a Valence-Band-Controlled Metal Oxide Photocatalyst. *Chem. Sci.* **2020**, *11* (9), 2330–2334. <https://doi.org/10.1039/C9SC05909A>.

## Appendix IV: Parallelized and Automated Photochemical Reactor (PAPCR)

**Reactor assemble.** The bottom part of the reactor is an aluminium plate. Two 100 W LED chips are fixed on the top of the plate with screws and thermal paste, providing constant illumination to the catalyts. The LED chips were purchased from Chanzon with various wavelengths. 380 nm and 400 nm are the most widely used wavelength in our lab to study the photocatalytic reactivity under UV light and visible light, respectively. Note that the number of photons from the LED chip depend on wavelength, and a 400 nm LED is supposed to emit more photons per second than a 380 nm LED. Each LED is connected to a 3000 mA Chanzon LED driver that can provide a constant electric current. Two fans are employed to cool the LEDs and the drivers. A cold plate is fixed on the backside of the aluminate plate, connected to a benchtop chiller, providing circulating chilled water ( $\sim 14\text{ }^{\circ}\text{C}$ ) to maintain the work temperature for the LEDs. One should pay attention that the LEDs should not be turned on unless the fan and the chiller is on, otherwise they will burn in minutes. To change the LEDs, hexane is used to dissolve the thermal paste.

The mid part is the reactor array where 108 1 mL borosilicate glass shell vials (JG Finneransit) sit on an aluminum plate with small holes drilled at the bottom, through which illumination from the LEDs can transmit into the vials. The diameter of each small hole is about 2.5 cm. The vials were covered with a layer of hydrogen sensitive film (DetecTape, Midsun Specialty Products) whose color changes from light to dark with an increase in the local hydrogen concentration. The tape is perforated by the vendor; thus, one should note that the holes should not be on the top of any vial. A fluorinated ethylene propylene (FEP) film was placed on the top of the hydrogen sensitive film to create a gas-impermeable environment. Next, a flexible silicone rubber sheet and a rigid plexiglass plate were placed on the top of the FEP film to seal and cover the whole reactor array. A rectangular aluminum frame is placed on the plexiglass plate. And 6 threaded rods are employed to connect the entire array and fixed under a pressure between 43 lbs and 44 lbs per inch<sup>2</sup>. A pair of aluminum U-channels is fixed on the aluminum plate to support the reactor array. Before running the reactor, a stream of compressed air is used to clean the surface of the plexiglass plate. And the four sides of the reactor array are covered with black tapes for enhanced image contrast.

The top part of the reactor is the camera. An acrylic housing, composed of five laser cut acrylic plates, serves as the camera holder. The camera (Raspberry Pi Camera Board v2 - 8 Megapixels) is fixed on the top of the acrylic housing, whose focus plane has been adjusted to locate on the hydrogen sensitive film. Two rows of white LED strips (JUNWEN, 3 W) are pasted inside the housing, to illuminate the hydrogen sensitive tape from above while the image is captured. The brightness and contrast of the image captured strongly influence the result so that the white LEDs should be warmed up prior to the experiment.

The two LED chips and the camera are connected to a Relay module and the entire system is controlled by a Canakit Raspberry Pi. Every six minutes, the LEDs are switched off, and the camera takes a picture of the hydrogen sensitive film. After the picture was taken, the LEDs were switched on for another 6-minute cycle. It is noted that the reactor runs through a Python 2 program, and the images captured during the experiment are automatically collected. Schematic illustration of the reactor setup is shown in Figure 14-1.

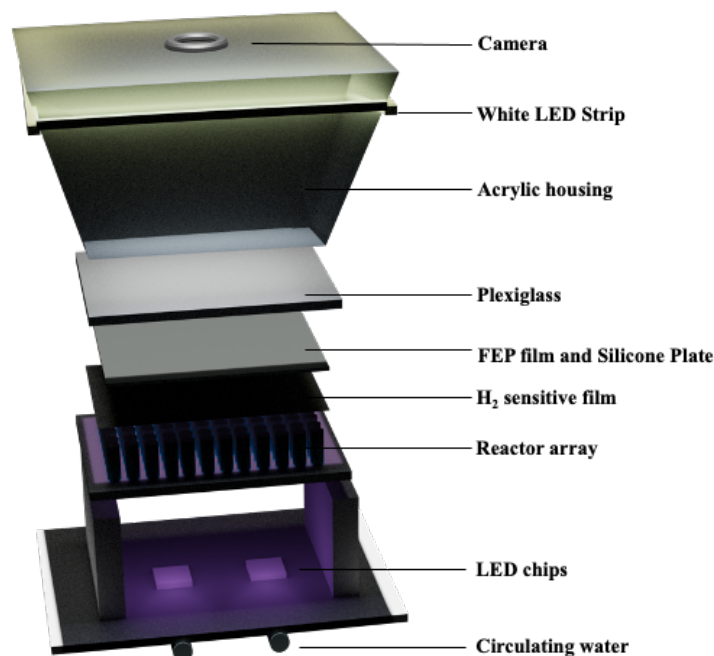


**Figure 14-1:** Schematic illustration of the PAPCR.

**Image processing.** First, a mask image is required to determine the locations of the pixels to be extracted and processed. The mask is prepared by selecting an image and painting a 54 pixels black circle on the top of each vial with GUN Image Manipulation Program. The mask image

color value is then inverted, and the threshold is set to maximum. A Mathematica script is employed to process the mask and all captured pictures to track the darkness change of the film. These values were then subtracted from the darkness value from the first image. The averaged RGB values are used as the darkness. Based on the calibrated relationship between local hydrogen concentration and the darkness of the film, it is possible to calculate the amount of H<sub>2</sub> production every 6 min

**Reactor calibration.** The colorimetric response of the tape to hydrogen was calibrated by injecting known amount of H<sub>2</sub> into vials covered by the tape. The procedure for calibration is basically the same as the normal reaction experiment. The only difference is that 15 vials have been replaced with special ones with holes drilled in the bottom and placed in the reactor array randomly. A gas-tight syringe was used to inject known amounts of H<sub>2</sub> into those vials. After injection, the vials were left for 10 min and then a picture of tape was taken. The RGB values were extracted from the 15 vials and then averaged. This procedure was repeated from 0% H<sub>2</sub> to 50% H<sub>2</sub>, summarized in Table 14-1. The images of the films exposed to different amount of H<sub>2</sub> are shown in Figure 14-2. It is found that the normalized intensity for the 15 vials decreased linearly with the amount of injected H<sub>2</sub> from 0% to 31%, but the linearity is less perfect at higher H<sub>2</sub> concentration. The fitting of the normalized intensity is plotted in Figure 14-3.

**Table 14-1:** The volume (ml) of hydrogen injected for calibration and the corresponding percentage of hydrogen (H<sub>2</sub>%) as well as the amount of hydrogen (μmol) calculated.

NO.	Volume injected (ml)	Total volume (ml)	Amount (μmol)	Percentage
0	0	0	0	0%
1	0.05	0.05	2.0	4%
2	0.05	0.1	4.1	8%
3	0.05	0.15	7.0	12%
4	0.05	0.2	8.2	15%
5	0.05	0.25	11.5	19%
6	0.05	0.3	12.3	21%
7	0.1	0.4	18.5	27%
8	0.1	0.5	20.4	31%
9	0.1	0.6	24.1	35%
10	0.1	0.7	28.6	39%
11	0.1	0.8	32.6	42%
12	0.1	0.9	36.8	45%
13	0.1	1.0	41.5	48%
14	0.1	1.1	45.0	50%

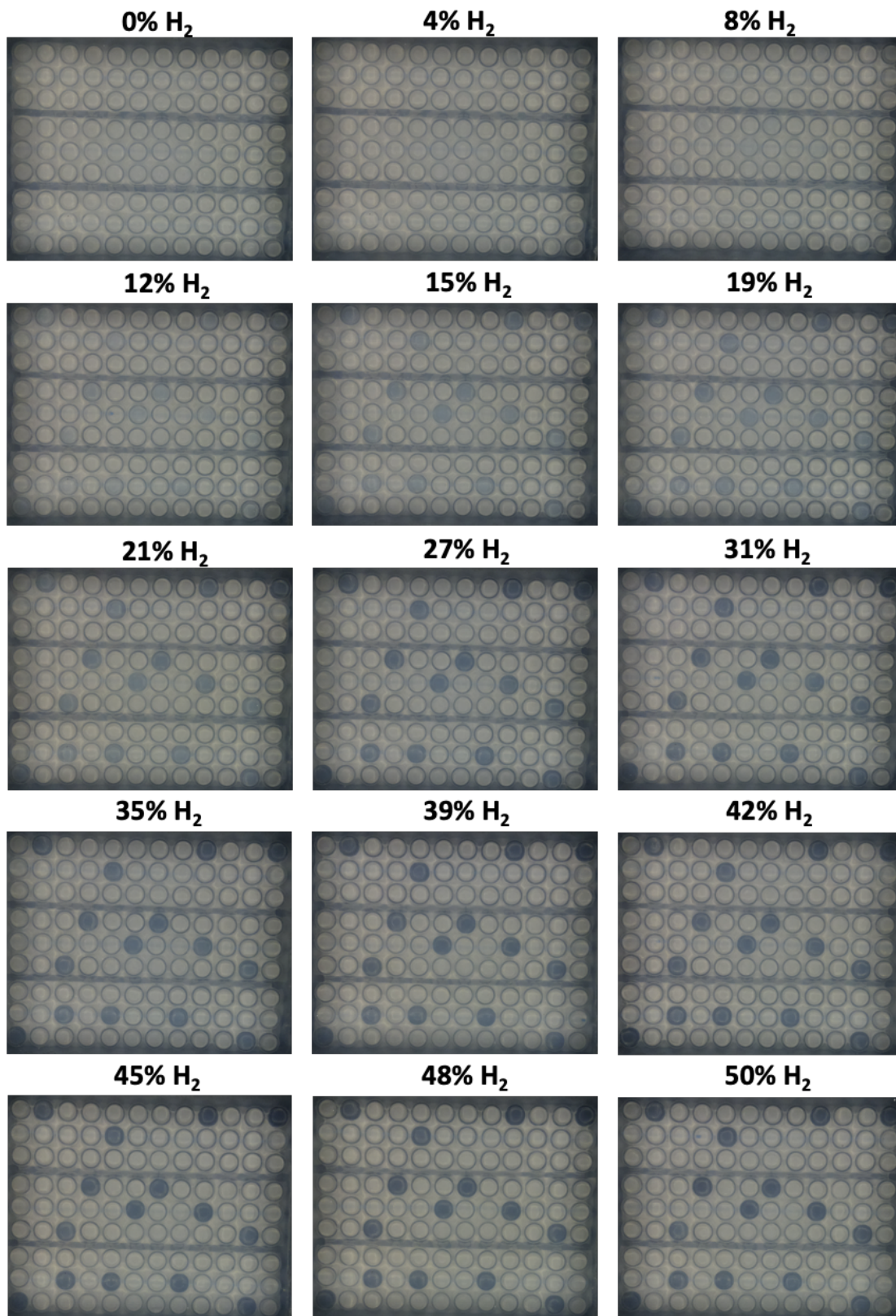


**Figure 14-2:** Pictures of the reactor array taken after injecting specific amount of hydrogen.

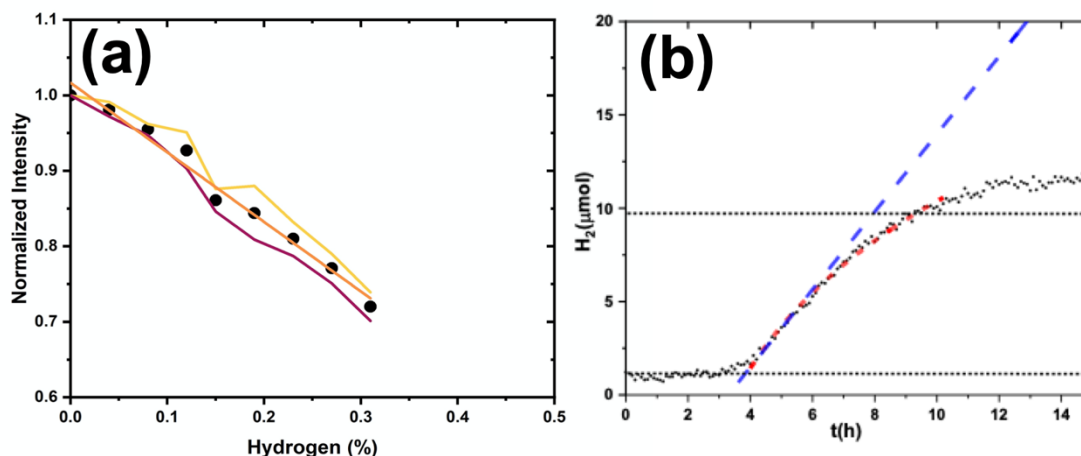


**Figure 14-3:** (a) The linear fitting for the average normalized intensity in the range of 0 to 31% hydrogen. The average of the 15 vials are represented by the black dots, and standard deviation are represented by the yellow and the purple lines, and the orange line shows the best fit. (b) Plot of the hydrogen production versus reaction time from one of the vials.

**Identical experiment.** An identical experiment has been carried out to determine the systematic error. A homogeneous catalyst mixture, containing 0.25 mM Ru(bpy)<sub>3</sub>(PF<sub>6</sub>)<sub>2</sub>, 0.125 mM methyl viologen dichloride, and 0.125 mM K<sub>2</sub>PdCl<sub>4</sub> was dissolved in a 6% TEOA 4:1 DMSO/water solution and was added to all 108 vials and illuminated by two 300 W 400 nm LED chips to produce hydrogen for 6 hours. The average amount of H<sub>2</sub> product was 11.70 μmol at 240 min, and the standard deviation was 14.91%. The hydrogen production from the 108 vials is given in Figure 14-4. Note that this experiment can be used to adjust the position of the two LED chips to ensure that the light uniformly covers the entire reactor array.

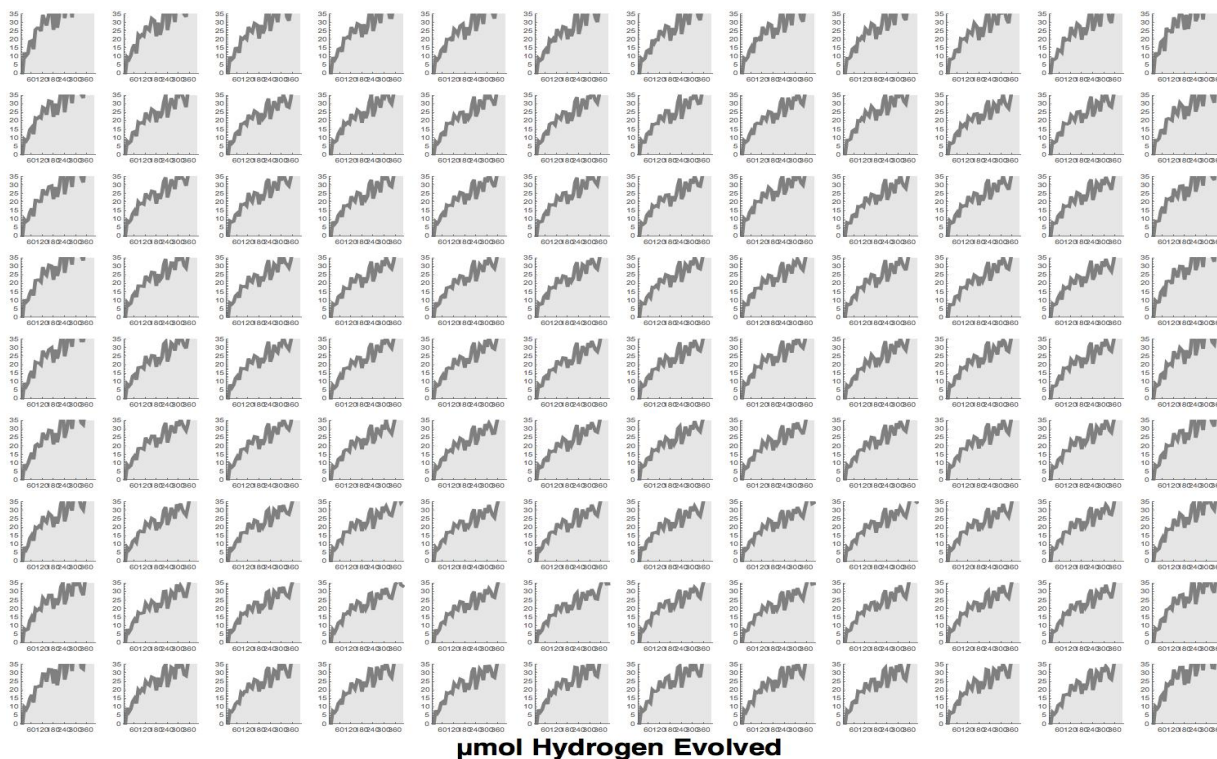


**Figure 14-4:** Hydrogen production from  $\text{Ru}(\text{bpy})_3(\text{PF}_6)_2$  catalysts in the identical experiment.

**Photocatalytic experiment.** In a typical experiment, specific amount of catalysts powders are weighted and transferred to the vials. Then specific solution, such as DI water and methanol solutions are injected into the vials with a pipet. It is noted that the detect range is correlated to the volume of the head space. For a 0.4 ml headspace, corresponding to 0.6 ml solution added, the detect range is about 0.9  $\mu\text{mol}$  to 9.6  $\mu\text{mol}$  for 4% to 31%  $\text{H}_2$ . Decreasing the headspace will improve the detect sensitivity of the reactor. A typical example of the hydrogen produced in a single vial is shown in Figure 14-3 (b): The black dots correspond to the amount of  $\text{H}_2$  product every six minutes; The red curve is the fitted logarithmic function and the region between the two horizontal dashed lines correspond to the calibrated range. The maximum  $\text{H}_2$  generation rate is determined by finding the maximum slope of the curve in the calibrated range, illustrated by the blue line in Figure 14-3 (b). The reason for the logarithmic fit is based on the assumption that the rate of hydrogen generation decreased with the pressure in the headspace because of the increasing rate of back reactions. From the reports by Song et al. on the same reactor,<sup>1</sup> the mass specific hydrogen generation rates increase with headspace, as the additional headspace reduces the pressure built up. And the logarithmic fitting that results from the pressure build-up model is

consistent with the shape of the hydrogen production versus time data. And there is an impregnation region at the beginning of the hydrogen generation curve. One explanation on this is that the hydrogen needs to first saturate the water before releasing to the headspace. Another explanation is based on the reports by Pan et al. that the concentrations of species dissolved in solution also affect the surface potential.<sup>2</sup> The presence of O<sub>2</sub> reduced the band bending in SrTiO<sub>3</sub>:Al/Pt, which reduced the electric field between SrTiO<sub>3</sub>:Al/Pt and bare SrTiO<sub>3</sub>:Al sites, made charge separation less effective, and thus reduced the charge separation efficiency. The presence of H<sub>2</sub> would behave in the opposite way. Considering our 1-ml small reactor, as H<sub>2</sub> and O<sub>2</sub> are generated at a 2:1 ratio, the H<sub>2</sub> concentration in the solution would increase with time. This would increase the reactivity. And this theory might be useful to understand why there is an impregnation time in the H<sub>2</sub> evolution curves measured by the PAPCR, as the increasing H<sub>2</sub> concentration activates the surface.

To maintain that the results could be compared from panel to panel, P25 TiO<sub>2</sub> was used as a reference catalyst and included in all panels. P25 powders were loaded with 1 wt% Pt by the impregnation method. Since the hydrogen production rate of P25 is known, we can determine if the reactor is running correctly. And the hydrogen detect tapes used in the experiment are in the same lots as the ones used in the calibration to maintain the accuracy of the colorimetric detection.

## References

- (1) Song, W.; Lopato, E. M.; Bernhard, S.; Salvador, P. A.; Rohrer, G. S. High-Throughput Measurement of the Influence of pH on Hydrogen Production from BaTiO<sub>3</sub>/TiO<sub>2</sub> Core/Shell Photocatalysts. *Appl. Catal. B Environ.* **2020**, *269*, 118750. <https://doi.org/10.1016/j.apcatb.2020.118750>.
- (2) Pan, Z.; Yanagi, R.; Wang, Q.; Shen, X.; Zhu, Q.; Xue, Y.; Röhr, J. A.; Hisatomi, T.; Domen, K.; Hu, S. Mutually-Dependent Kinetics and Energetics of Photocatalyst/Co-Catalyst/Two-Redox Liquid Junctions. *Energy Environ. Sci.* **2020**, *13* (1), 162–173. <https://doi.org/10.1039/C9EE02910A>.